# Representative characterisation of inorganic materials using cryo-electron microscopy

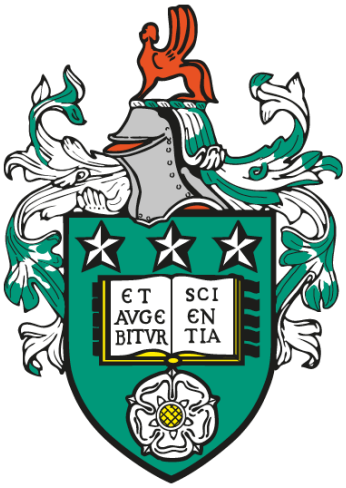


**Dario Luis Fernandez Ainaga**

School of Chemical and Process Engineering

University of Leeds

Submitted in accordance with the requirements for the degree of

*Doctor of Philosophy*

**April 2025**

I confirm that the work submitted is my own, except where work which has formed part of jointly authored publications has been included. My contribution and the other authors to this work has been explicitly indicated below. I confirm that appropriate credit has been given within the thesis where reference has been made to the work of others.

The work in **Chapter 5** of this thesis has been published in the following journal, and can be seen in **Appendix A**:

D L Fernandez Ainaga, T Roncal-Herrero, M Ilett, Z Aslam, C Cheng, J P Hitchcock, O J Cayre, N Hondow, “Native state structural and chemical characterisation of Pickering emulsions: A cryo-electron microscopy study”, *Journal of Microscopy*, 2025, **298** (1), 92-105, DOI: 10.1111/jmi.13391

The candidate carried out the majority of the experimental work and all the data analysis and writing. Cheng Cheng and James P. Hitchcock prepared the Pickering emulsion samples. All authors contributed to writing the final manuscript.

The work in **Appendix B** has been published in the following journal:

J Hooper, D Budhadev, D L Fernandez Ainaga, N Hondow, D Zhou, Y Guo, “Polyvalent Glycan Functionalized Quantum Nanorods as Mechanistic Probes for Shape-Selective Multivalent Lectin-Glycan Recognition”, *ACS Appl. Nano Mater.* 2023, **6**, 4201-4213. DOI: 10.1021/acsanm.2c05247

The candidate carried out the cryo-sample preparation and (S)TEM imaging.

The work in **Appendix C** has been published in the following journal:

S Ding, D L Fernandez Ainaga, M Hu, B Qiu, U Khalid, C D’Agostino, X Ou, B Spencer, X Zhong, Y Peng, N Hondow, C Theodoropoulos, Y Jiao, C M A Parlett, X Fan, “Spatial segregation of catalytic sites within Pd doped H-ZSM-5 for fatty acid hydrodeoxygenation to alkanes”, *Nat Commun*. 2024, **15**, 7718. DOI: 10.1038/s41467-024-51925-2

The candidate carried out the HAADF STEM electron tomography, 3D reconstruction, and visualisation of the resulting tomogram.

## Acknowledgements

I would like to thank my supervisor Dr Nicole Hondow for her guidance during the project and her help and support when writing this thesis.

I would like to thank Zabeada Aslam for her help when using the TEM, and Stuart Micklethwaite for his help when using the SEM and for preparing the lamellae for cryo lift-out.

I would like to thank the members of the Leeds Electron Microscopy and Spectroscopy Centre for their help discussing characterisation techniques and image processing techniques.

I would like to thank everyone who helped prepare the samples used in this thesis: Dr Olivier Cayre's research group in the School of Chemical and Process Engineering in the University of Leeds, including Cheng Cheng and Dr James Hitchcock for their help providing the Pickering emulsion samples. Dr Darshita Budhadev from the research group of Professor Dejian Zhou in the University of Leeds for providing the gold core-satellite samples. Dr Teresa Roncal-Herrero and Hafis Mehraliyev from the research group of Professor Andy Brown, in the School of Chemical and Process Engineering, University of Leeds for providing the titanium dioxide samples.

## Abstract

Nanoparticles have become increasingly common in a wide variety of application areas from medicine to materials science due to their appealing properties. Nanoparticle characterisation require the use of multiple techniques to analyse physical and chemical properties; among these techniques, electron microscopy is an essential high-resolution imaging technique that is routinely used to inspect nanoparticle size and agglomeration. However, high-resolution analysis of aqueous soft materials such as nanoparticle dispersion, hydrogels, and emulsions is often challenging because conventional dry sample preparation techniques can introduce artefacts affecting particle agglomeration and the overall structure of the sample. Cryogenic sample preparation and cryogenic electron microscopy are extensively used in the life sciences but are not as developed for their application to inorganic samples.

This thesis aims to representatively characterise inorganic materials using cryo-electron microscopy, employing a range of techniques found in biology and materials science including spectroscopy techniques, tomography, and dark field imaging. Cryo-transmission electron microscopy and cryo-scanning electron microscopy were used for the imaging of inorganic nanoparticles and Pickering emulsions. The spherical 3D structure of Pickering emulsions was seen to be preserved following cryogenic sample preparation using plunge-freezing, which was found suitable for the preparation of sample droplets up to ~600 nm in diameter, which were then analysed using cryogenic transmission electron microscopy, energy dispersive X-ray spectroscopy, and electron energy loss spectroscopy. The 3D nature of frozen hydrated samples allowed for the application of cryo-electron tomography, which was used to successfully visualise nanoparticles and emulsion droplets in 3D space, giving insight on the 3D position and shape of the particles. Lastly, spectroscopy techniques were used together with cryogenic electron tomography to obtain 3D elemental information of the oil and water phases in the emulsion.

Electron beam-induced damage to the sample and ice thickness remain the largest limiting factors to the cryo-transmission electron microscopy imaging of Pickering emulsions, affecting especially the size of emulsion droplets that can be analysed through tilt tomography without encountering issues with low signal-to-noise ratio (at low electron fluence) or sample damage (at high electron fluence). The imaging of

sections from Pickering emulsion samples with large droplets (>1 μm) was possible using cryo-focused ion beam-scanning electron microscopy, with the focused ion beam being used for both the 3D imaging of large volumes and the milling a frozen lamella that was transferred to the cryo-transmission electron microscope for high-resolution imaging.

## Table of Contents

Acknowledgements ..... III
Abstract ..... IV
Table of Contents ..... VI
List of Tables ..... VIII
List of Figures ..... VIII
Abbreviations ..... XIII
Chapter 1 Introduction ..... 1
1.1 Characterisation of Challenging Nanoparticle Systems ..... 1
1.2 Chapter Overview ..... 3
Chapter 2 Literature Review ..... 6
2.1 Characterisation of Challenging Nanoparticle Systems ..... 6
2.2 Pickering Emulsions ..... 7
2.2.1 Properties of Pickering Emulsions ..... 9
2.2.2 Characterisation Strategies for Pickering Emulsions ..... 14
2.3 Cryogenic Electron Microscopy ..... 20
2.3.1 Effects of Plunge-Freezing on the Sample ..... 23
2.3.2 Cryogenic- (Scanning) Transmission Electron Microscopy and Sample Damage ..... 26
2.3.3 Cryo-FIB-SEM and Transfer to the cryo-TEM ..... 34
2.4 Summary ..... 39
2.5 Project Aims and Objectives ..... 40
Chapter 3 Materials and Methods ..... 42
3.1 Nanoparticle-based systems ..... 42
3.1.1 Pickering Emulsions ..... 42
3.1.2 Zinc Oxide Nanoparticles ..... 43
3.1.3 Titanium Dioxide System ..... 45
3.1.4 Gold core-satellite nanoparticles ..... 45
3.1.5 General characterisation using Dynamic Light Scattering ..... 46
3.2 Electron Microscopy ..... 47
3.2.1 Transmission Electron Microscopy ..... 47
3.2.2 Conventional TEM Sample preparation ..... 52
3.2.3 Energy Dispersive X-Ray Spectroscopy ..... 53
3.2.4 Electron Energy Loss Spectroscopy ..... 54

3.2.5 Cryogenic Electron Microscopy ..... 58
3.2.6 Cryogenic Scanning Electron Microscopy ..... 62
3.2.7 Electron Tomography ..... 70
3.3 Image Analysis ..... 79
3.3.1 Shape and Size Measurements for Pickering Emulsions ..... 79
3.3.2 Size Measurements for Nanoparticles ..... 79
3.3.3 Nearest Neighbour Distances ..... 80
3.4 Summary ..... 80
Chapter 4 Development of Experimental Approaches via Case Studies ..... 81
4.1 ZnO Nanoparticle System ..... 81
4.1.1 Dynamic Light Scattering Analysis ..... 82
4.1.2 Initial Comparison Between Sample Preparation Methods ..... 85
4.1.3 Cryo-(S)TEM Particle Analysis ..... 90
4.1.4 Volume Analysis of Frozen ZnO NP Samples ..... 92
4.1.5 Agglomerate Size Analysis of ZnO NP Samples ..... 95
4.1.6 ZnO NP System Summary ..... 97
4.2 Gold Nanoparticle Core-Satellite System ..... 98
4.2.1 Plunge-Frozen Vacuum Dried Samples and Cryo-TEM ..... 99
4.2.2 Cryo-Tilt Tomography of the gold nanoparticles ..... 102
4.2.3 Au NP core-satellite summary ..... 106
4.3 $TiO_2$ coated in biological media ..... 107
4.3.1 Cryo-(S)TEM Imaging ..... 108
4.3.2 Cryo-HAADF STEM Tilt Tomography ..... 110
4.3.3 3D Elemental Analysis using EDX SI Tomographic Reconstruction ..... 112
4.3.4 $TiO_2$ coated in biological media summary ..... 116
4.4 Initial Ice Thickness Analysis ..... 117
4.5 Summary ..... 120
Chapter 5 Cryo-(S)TEM Analysis of Pickering Emulsion Samples ..... 122
5.1 Preliminary Sample Analysis ..... 122
5.1.1 DLS Measurements ..... 123
5.1.2 Dry Sample TEM Imaging ..... 125
5.2 Cryo-(S)TEM Imaging ..... 128
5.2.1 Initial Observations ..... 128
5.2.2 Comparisons Between Dry and Cryo-Prepared Samples ..... 133
5.2.3 Spectroscopy using EELS and EDX ..... 137

5.3 Electron Tomography ..... 143
5.3.1 Considerations for Electron Tomography ..... 148
5.4 Cryo-EELS Tomography ..... 153
5.5 Observations on Sample Damage ..... 157
5.6 Limits to the sample analysis and future directions for cryo-imaging and analysis of Pickering emulsions ..... 163
5.7 Summary ..... 163
Chapter 6 Cryo-SEM Analysis of Pickering Emulsion-Based Systems ..... 166
6.1 Cryo-FIB-SEM Analysis of Pickering Emulsion-Based Systems ..... 167
6.1.1 FIB Milling and “Slice and View” ..... 167
6.1.2 “Slice and View” Tomography ..... 170
6.2 Cryo Lift-Out and transfer to cryo-(S)TEM ..... 173
6.2.1 Cryo-SEM Imaging and Lamella Preparation ..... 173
6.2.2 Cryo-(S)TEM Imaging ..... 177
6.2.3 Cryo Lift-Out Limitations and Future Work ..... 183
6.3 Summary ..... 185
Chapter 7 Conclusions and Future Work ..... 187
7.1 Conclusions ..... 187
7.2 Opportunities for Future Work ..... 191
References ..... 193
Appendix A ..... 213
Appendix B ..... 227
Appendix C ..... 240

## List of Tables

*Table 2.1 – Cryogenic sample preparation techniques and literature examples.* ..... 22
*Table 3.1 – Description of the preparation methods for the ZnO NP samples.* ..... 44
*Table 4.1 – DLS intensity measurements for the two samples.* ..... 84
*Table 5.1 – Electron fluence values and sample thickness for the area in Figure 5.24 at different time points.* ..... 160

## List of Figures

Figure 2.1 – Cryo-high angle annular dark field STEM (cryo-HAADF STEM) images of a Pickering emulsion droplet and different stages of gold film growth. ..... 9

Figure 2.2 - Position of a spherical particle on a planar water-fluid interface. ..... 10
Figure 2.3 - Contour plot for equal detachment energies ..... 13
Figure 2.4 - Packing of the stabilising particles ..... 14
Figure 2.5 – Confocal light microscopy images of a swelling Pickering emulsion droplet. ..... 15
Figure 2.6 – Cryo-SEM and dry TEM images of emulsion droplets covered by silica NPs. ..... 16
Figure 2.7 – Confocal laser microscopy and cryo-TEM images of Pickering emulsion droplets. ..... 17
Figure 2.8 – Cryo-SEM images of a FIB-milled droplet section and models generated from tomographic data of the imaged region. ..... 18
Figure 2.9 – Cryo-TEM images of negatively stained droplets. ..... 19
Figure 2.10 – Phase diagram of non-crystalline water including amorphous ice phases LDA, HDA, and VHDA. ..... 21
Figure 2.11 - Particle distribution after plunge freezing. ..... 24
Figure 2.12 – Cryo-TEM images showing sample damage after exposure to the electron beam. ..... 27
Figure 2.13 – Comparison between STEM and TEM imaging in tomogram reconstruction and sample damage. ..... 30
Figure 2.14 – Cryo-STEM and cryo-TEM imaging of a 1 µm thick yeast cell sample at different tilt angles. Scalebars above the images represent a 5 µm distance. Tilt angle for the images is shown on the bottom of each column. ..... 33
Figure 2.15 – Sections and surfaces of tomograms reconstructed using bright field STEM versus HAADF STEM. ..... 33
Figure 2.16 - Schematic showing different strategies for FIB milling a sample for cryo-TEM. ..... 37
Figure 2.17 - Cryo-TEM image of a lamella after a successful lift-out and cryo-ET of a region in the lamella. ..... 38
Figure 3.1 – Simplified schematic of a DLS setup. ..... 46
Figure 3.2 – Schematic diagrams for (A) a transmission electron microscope and (B) the parallel beam operation in a TEM. ..... 49
Figure 3.3 – Schematic of the detector setup during STEM imaging. ..... 50
Figure 3.4 – Schematic of a TEM and EELS setup. ..... 55
Figure 3.5 – EEL spectrum of a 20 nm thin titanium carbide sample. ..... 56
Figure 3.6 – Blotting and Plunge-freezing steps for cryo-TEM preparation. ..... 58
Figure 3.7 - Schematic of a cryo-FIB-TEM ..... 64

Figure 3.8 – 3D diagram of a trench for serial block face “slice and view” FIB-milling. ..... 67
Figure 3.9 – Cryo-SEM BSE image of a FIB milled area for “slice and view”. ..... 68
Figure 3.10 – TEM transfer grid used for cryo lift-out. ..... 69
Figure 3.11 - Size ranges for different 3D imaging techniques ..... 71
Figure 3.12 – Schematic detailing the steps for cryo-ET in TEM. ..... 72
Figure 3.13 – Schematics showing the missing wedge (left) and pyramid (right) in a tilt series ..... 73
Figure 4.1 – DLS measurements for the ZnO dispersions ..... 83
Figure 4.2 – TEM images comparing samples prepared through drop casting, PF-VD, and plunge-freezing for cryo-TEM imaging. ..... 87
Figure 4.3 – TEM images of the dry ZnO 1.0 mg/mL samples. ..... 89
Figure 4.4 – Cryo-TEM and cryo-HAADF STEM images of ZnO nanoparticles. A) .. 90
Figure 4.5 – Diagram showing the possible effects of blotting to the nanoparticles in a dispersion. ..... 91
Figure 4.6 – Cryo-SEM images of the 0.1 mg/mL ZnO nanoparticles. a) and b) show backscattered images of the fractured sample. The black dots visible in both images are likely air bubbles or other artefacts arising from partial ice crystallisation due to slush nitrogen being the chosen cryogen. ..... 92
Figure 4.7 – 3D image of the 1.0 mg/mL ZnO cryo-FIB-SEM dataset. This ..... 93
Figure 4.8 – 2 µm thick slice of the 3D volume represented in Figure 4.7. ..... 94
Figure 4.9 - Diameter length for the 1.0 mg/mL ZnO nanoparticle agglomerates ..... 97
Figure 4.10 – TEM images of a drop cast Au-NP core-satellite sample showing ..... 99
Figure 4.11 - a) PF-VD and b) Cryo-TEM images of core-satellite gold nanoparticles. ..... 100
Figure 4.12 - TEM and HAADF STEM images of the sample prepared through PF-VD and for cryo-EM imaging. ..... 101
Figure 4.13 – Size distribution measurements for the Au-NPs in cryo-STEM, and for the same 3D particles created in the electron tomogram. ..... 103
Figure 4.14 – Images from an electron tomogram of the Au-NPs core-satellite sample ..... 105
Figure 4.15 – Schematic showing the possible positions and orientation of the core-satellite structures within the ice layer. ..... 106
Figure 4.16 - Cryo-HAADF STEM and EDX maps of the coated $TiO_2$ nanoparticles. ..... 109
Figure 4.17 - Cryo-ET reconstruction of a nanoparticle agglomerate consisting of coated $TiO_2$ particles. ..... 110

Figure 4.18 - 3D segmentation of the coated nanoparticles ..... 112

Figure 4.19 – Cryo-HAADF STEM and EDX elemental map of a sample with smaller coating thickness. ..... 113

Figure 4.20 – Cryo-HAADF STEM image of a $TiO_2$ cluster and 3D reconstruction from the HAADF STEM and EDX signals. ..... 115

Figure 4.21 – 3D reconstruction of the $TiO_2$ cluster in Figure 4.20-A, with manually generated surfaces from the HAADF STEM images. ..... 116

Figure 4.22 – Cryo-HAADF STEM image of a section of frozen ice and ice thickness estimated using low-loss EELS. ..... 118

Figure 4.23 – Cryo-HAADF STEM image of a section of ice near the TEM grid bars and ice thickness estimated using low-loss EELS. ..... 119

Figure 5.1 – DLS size measurements of the sunflower oil Pickering emulsion sample. ..... 124

Figure 5.2 - DLS measurements of the hexadecane Pickering emulsion ..... 125

Figure 5.3 – Electron microscopy images of a dry hexadecane oil Pickering emulsion sample. ..... 126

Figure 5.4 – EDX elemental analysis of dry a sunflower oil Pickering emulsion sample on a SiNx TEM grid. ..... 127

Figure 5.5 – Cryo-HAADF STEM images of Pickering emulsion droplets. ..... 130

Figure 5.6 – Cryo-HAADF STEM images showing imperfections in the sample. ... 131

Figure 5.7 – Cryo-HAADF STEM of a hexadecane oil Pickering emulsion with large droplet size (>1 μm) after plunge-freezing. ..... 132

Figure 5.8 – EELS elemental maps of a plunge-frozen Pickering emulsion sample with large droplets. ..... 133

Figure 5.9 – Comparison between dry and plunge-frozen sunflower oil Pickering emulsions. ..... 134

Figure 5.10 – Graphs showing the size distribution and circularity of 500 Pickering emulsion droplets prepared through drop casting and plunge-freezing. ..... 136

Figure 5.11 – Comparison between dry droplets and cryogenically prepared hexadecane-in-water emulsion droplets with different sizes. ..... 137

Figure 5.12 – EDX elemental analysis of a single sunflower oil-in-water emulsion droplet ..... 138

Figure 5.13 – Cryo-EELS elemental analysis of a droplet cluster. ..... 140

Figure 5.14 - Maps of the estimated absolute ice thickness (in nm) from EEL low-loss spectra ..... 142

Figure 5.15 – HAADF STEM images of a plunge-frozen and drop cast emulsion samples and images from the corresponding electron tomograms. ..... 144

Figure 5.16 – Electron tomogram images of a droplet cluster. ..... 146

Figure 5.17 – Schematic showing a cross-section of ice containing the Pickering emulsion sample. ..... 147

Figure 5.18 – Electron tomogram images of a droplet cluster that has received significant beam-induced damage. ..... 150

Figure 5.19 – Schematic showing the change in distance travelled by the beam through the sample after tilting. ..... 152

Figure 5.20 – Images from an electron tomogram including reconstructions from cryo-HAADF STEM and EELS signals. ..... 154

Figure 5.21 – Selection of images from the tilt series used for Figure 5.20. ..... 156

Figure 5.22 – Cryo-HAADF STEM images showing beam-induced damage to a droplet. ..... 157

Figure 5.23 – Images from a cryo-HAADF STEM tilt series corresponding to Figure 5.22 and Figure 5.18. ..... 158

Figure 5.24 – Cryo-HAADF STEM images of a droplet after beam exposure and corresponding EEL maps of the estimated sample thickness (in nm) at different time points ..... 159

Figure 5.25 – Selection of cryo-HAADF STEM images from an image series showing droplets expanding and bursting due to beam damage ..... 161

Figure 5.26 – Schematic showing the speculated mechanism for droplet deformation due to beam-induced damage. ..... 162

Figure 6.1 – BSE images from a “slice and view” image series. ..... 169

Figure 6.2 – Stills of 3D models from the “slice and view” dataset. ..... 172

Figure 6.3 – SE images showing the process of creating a sample lamella. ..... 175

Figure 6.4 – Cryo-(S)TEM images of the lamella after being transferred to the TEM. ..... 178

Figure 6.5 – Cryo-HAADF STEM images of the droplet and Pt-NPs in the sample lamella. ..... 179

Figure 6.6 – EDX of the droplet surface in the ~400 nm thick region of the lamella. ..... 180

Figure 6.7 – Cryo-HAADF STEM image of the area used for EDX analysis. ..... 182

Figure 6.8 – Schematic drawing depicting the possible droplet cross-section at the droplet surface after corresponding cryo-HAADF STEM images. ..... 183

## Abbreviations

| | |
|---|---|
| ADF | Annular Dark Field |
| AFM | Atomic Force Microscopy |
| ART | Algebraic Reconstruction Technique |
| Cryo- | Cryogenic |
| DLS | Dynamic Light Scattering |
| DMEM | Dulbecco's Modified Eagle Medium |
| EDX | Energy Dispersive X-ray |
| EEL(S) | Electron Energy Loss (Spectroscopy) |
| EM | Electron Microscopy |
| ET | Electron Tomography |
| FIB | Focused Ion Beam |
| HAADF | High Angle Annular Dark Field |
| HPF | High Pressure Freezing |
| ML | Machine Learning |
| NP | Nanoparticle |
| PF-VD | Plunge-Freezing Vacuum-Drying |
| SEM | Scanning Electron Microscopy |
| SIRT | Simultaneous Iterative Reconstruction Technique |
| SNR | Signal-to-Noise Ratio |
| STEM | Scanning Transmission Electron Microscopy |
| TEM | Transmission Electron Microscopy |
| WBP | Weighted Back Projection |

# Chapter 1 Introduction

## 1.1 Characterisation of Challenging Nanoparticle Systems

Nanoparticles (NPs) have found extensive use in a wide variety of areas such as medicine, electronics, and food science due to their highly tuneable properties [1, 2]. Examples of these applications can be seen in the medical field for targeted drug delivery [3, 4], use in the manufacture of semiconductors using silica nanoparticles [5], and as pigments such as zinc oxide and titanium dioxide nanoparticles in sunscreen [6-11]. Although there is no formal definition for nanoparticles, this is a term generally applied to particles with diameter between 1 nm and ~100 nm, a size range within which they exhibit unique properties compared to the bulk material [2, 12]. The electronic, optical, physical and chemical properties of nanoparticles are crucial to their effectiveness in the aforementioned applications and are dependent on the size of particles or any resulting agglomerates [13]. As such, the size, concentration, surface properties, and materials of nanoparticles need to be closely monitored during synthesis to ensure their suitability to the given applications.

The extensive use of nanoparticles requires knowledge on the best techniques and protocols for characterisation in order to ensure the nanoparticles adhere to the required standards in regard to physical and chemical properties, and, if relevant, biocompatibility [14, 15]. A range of different characterisation techniques are commonly employed for the analysis of nanoparticles, especially for particle size measurements. Dynamic light scattering (DLS) is a commonly used technique for particle size analysis to measure the hydrodynamic radius of the primary particles or clusters in bulk nanoparticle dispersions. Electron microscopy (i.e. transmission electron microscopy, TEM and scanning electron microscopy, SEM) provides high-resolution imaging capabilities that can be used for the imaging of primary particles and clusters, giving information on both the particle size and shape. Atomic force microscopy (AFM) is also used for the characterisation of nanoscale particles and is useful for the collection of size measurements of bimodal nanoparticle systems [16, 17]. Additionally, X-ray diffraction (XRD) [18], Fourier transform infrared spectroscopy (FTIR) [19] and Raman spectroscopy [20] are frequently used to determine the size, crystal structure and chemical composition of bulk nanoparticle systems [1, 21, 22].

No individual characterisation technique is sufficient for the collection of meaningful results, partly due to the need to analyse various properties, but also due to the various artefacts and biases to measurements associated with these techniques [2, 23]. In fact, despite being necessary for the full characterisation of nanoparticle systems, the above techniques all have biases and limitations that need to be taken in consideration. DLS is useful to measure the hydrodynamic radius of bulk systems but can give poor results when analysing multimodal systems as the scattering intensity of larger particles tends to mask that of smaller particles [2, 17, 22]. Electron microscopy is often vital for the characterisation of nanoparticles due to its high-resolution but presents several challenges. The high magnifications used in EM imaging can be a source of characterisation bias, as only a small portion of the sample can be imaged at once. This may make it difficult to image samples with a low concentration of nanoparticles and can lead to the measurements taken not being representative of the bulk sample due to human bias in the selection of areas to image [24]. Additionally, samples are required to undergo specialised preparation procedures due to the high vacuum in electron microscopes. Drying the sample on a TEM grid is a routine sample preparation method for nanoparticles but can introduce artefacts as nanoparticles tend to agglomerate during the drying process [1, 14, 22].

These issues can be resolved by employing a variety of techniques for the characterisation of any given system, thus allowing to compare measurements and minimise bias. However, issues in sample preparation and characterisation remain prevalent for soft matter, hydrated samples such as gels, emulsions, biological samples, and some nanoparticle dispersions. For these systems, characterisation in their native hydrated form is essential for understanding their performance as drying results in changes to their structure, behaviour, and overall properties [17, 25, 26]. This limits the characterisation techniques and sample preparation methods suitable for their characterisation and poses significant challenges for the high-resolution imaging of these systems. Cryogenic sample preparation is routinely used for the imaging of biological samples in their native state with electron microscopes, allowing for the 2D and 3D imaging of samples at high resolutions [27]. Cryogenic imaging has also been used for the preparation and imaging of inorganic, soft matter samples in materials science, but the methodologies used for inorganic samples still lag behind the state-of-the-art available in the life sciences.

The aim of this thesis is to successfully characterise Pickering emulsions in their native state by using cryogenic electron microscopy (Cryo-EM) techniques. To achieve this, a combination of techniques developed for biological and materials science imaging were used, to allow for the imaging of plunge-frozen Pickering emulsion samples of different droplet sizes for the analysis of the samples in 2D and 3D. An additional aim of this thesis is the exploration of 3D imaging and analysis using electron tomography in cryo-STEM and cryo-FIB-SEM. Electron energy loss spectroscopy (EELS) is also used in conjunction with cryo-high angle annular dark field scanning transmission microscopy imaging for the collection of tilt series for the reconstruction of tomograms containing 3D information on the elemental composition of the sample. The characterisation of frozen hydrated samples is essential to analyse the position, size, and shape of nanoparticles in 3D space while retaining the native sample structure, thus providing information on the performance of these difficult to characterise materials.

## 1.2 Chapter Overview

**Chapter 2:** Literature review. This chapter presents the challenges associated with the characterisation of hydrated soft matter nanomaterials and state of the art solutions for these challenges. Cryogenic sample preparation and electron microscopy imaging techniques for hydrated frozen samples are focused on due to their outstanding development within the life sciences. Cryogenic sample preparation, cryo-electron tomography, focused ion beam milling, and cryogenic-transmission electron microscopy are described and discussed within the scope of characterising biological and materials science samples, with an emphasis on Pickering emulsions as a nano-sized systems that require cryogenic imaging for representative sample characterisation. The thesis aims and objectives are clearly stated at the end of this chapter.

**Chapter 3:** Materials and methods. This chapter describes the methods used for the synthesis of the samples used within this thesis, the preparation methods used before analysis, and the analysis techniques used. Some

background on sample preparation methods and analysis techniques are also presented.

**Chapter 4:** Development of experimental approach via case studies. This chapter presents the results of the analysis of case studies systems displaying the characterisation techniques that are later used in Chapter 5 and Chapter 6. The systems presented are in order: zinc oxide nanoparticles, gold core-satellite nanoparticles, titanium oxide nanoparticles with a calcium and phosphorus coating, and ice without any additives.

**Chapter 5:** Cryogenic (scanning) transmission electron microscope (cryo-(S)TEM) analysis of Pickering emulsion samples. This chapter presents and discusses the results of cryogenic transmission electron microscopy analysis of hexadecane-in-water and sunflower oil-in-water Pickering emulsions with 3-5 nm platinum nanoparticles stabilisers and droplet size <1 μm. The viability of cryo-(S)TEM imaging, energy dispersive X-ray spectroscopy (EDX), electron energy loss spectroscopy (EELS), and electron tomography for the characterisation of Pickering emulsions are discussed. Lastly, a combined electron tomography and EELS method is presented for the 3D imaging and elemental analysis of the sample.

**Chapter 6:** Cryo-SEM analysis of Pickering emulsions. This chapter presents and discusses the analysis of a Pickering emulsion sample with droplet size >1 μm, achieved using cryo-FIB-SEM. The sample is cryogenically frozen and imaged in cryo-FIB-SEM, which allows for sample milling to image the sample cross-section and allows for serial tomography of the emulsion droplets. Lasty, a thin lamella is FIB-milled and transferred for cryo-TEM imaging, allowing for the application of the techniques presented in Chapter 6.

**Chapter 7:** Conclusions and future work. The results obtained from the sample analysis in Chapter 4, Chapter 5, and Chapter 6 are described and discussed, commenting to what extent the thesis aims and objectives were accomplished. Comments are given on possible avenues for future work to continue the work done in this thesis, and possible improvements on the techniques used.

# Chapter 2 Literature Review

All materials require appropriate characterisation to determine sample properties. Depending on the sample type and specific characteristics desired, a limited number of characterisation techniques and sample preparation methods are available for use. This is especially true for nanoparticles and soft materials, which often require high-resolution imaging techniques to measure the size, shape, and agglomeration of particles. Soft materials including biological particles, emulsions, gels, and electron beam sensitive materials will additionally require specific sample preparation methods to retain their native structure (i.e. remaining hydrated). This chapter discusses the characterisation requirements for these difficult systems and the use of state-of-the-art cryogenic electron microscopy as a useful characterisation technique for the imaging of hydrated nanomaterials.

## 2.1 Characterisation of Challenging Nanoparticle Systems

The difficulty in characterising nanoparticle systems is often exacerbated in soft matter and hydrated samples which include nanoparticle dispersions, gels, emulsions, and hydrogels [1]. All of these systems can contain nano-sized particles or structures which require a high-resolution characterisation technique, and if imaging is necessary, high-resolution imaging techniques such as TEM, SEM, and AFM are needed as part of the samples characterisation protocol. Unfortunately, in conventional imaging sample drying is often required, which can affect the samples structure due to the formation of agglomerates and loss of liquid [17, 25, 26, 28].

Alternative approaches, including imaging and sample preparation methods, have been developed through the years. Environmental SEM and TEM allow sample imaging in near-native conditions by either using specialised closed-cell holders to separate the sample from the high vacuum, or by using a differential pumping scheme [29-31]. However, these techniques are not without drawbacks, as imaging can be poor at higher resolution and damage to the sample often cannot be avoided [30]. Alternative sample preparation methods to avoid drying or loss of structure include chemical fixation and resin embedding, which consist in first freezing the sample followed by substituting the chemical fixatives into the sample [32, 33]. Extra

components such as bovine serum albumin can be added to prevent particle agglomeration [28], and finally cryogenic fixation consists in the rapid cooling of samples to cryogenic temperatures [27]. This thesis will focus on the use of cryogenic sample preparation techniques for the imaging of soft matter samples, as this technique is well-developed and has seen long term success for the preparation of samples in the life sciences [34]. Pickering emulsions have been chosen as a soft matter system to focus on in this thesis due a variety of factors: their nature as liquid systems requiring cryogenic EM for imaging, the possible size variation for the emulsion droplets and stabilisers which can be found in the nanoscale, and the three-dimensionality of the droplets which are suitable for the application of electron tomography.

## 2.2 Pickering Emulsions

Pickering emulsions are emulsions (mixtures of two immiscible liquids) stabilised by solid particles including nanoparticles, organic crystals, and proteins [35]. Unlike conventional emulsions, where surface-active polymers are added to the system to decrease the surface tension between phases, in Pickering emulsions solid particles are included to stabilise the emulsion droplets as was found from experiments by Pickering and Ramsden [35, 36]. These emulsions can be composed of a wide range of liquids and stabilising particles, chosen to fine-tune the emulsion's properties for a given application. Pickering emulsions see use in a range of areas due to the unique stabilisation method, giving these systems advantages in their stability and low toxicity compared to conventional, surfactant-stabilised emulsions [37-40].

Various properties within Pickering emulsion systems need to be monitored depending on the systems specific application. Overall, emulsion droplet size is consistently monitored (e.g. optical and fluorescence microscopy, DLS) to ensure long-term stability of the emulsion. Characterisation of the stabilising particles is often done independently of the stabilised emulsion, with the nanoparticle size, shape, and wettability being analysed after nanoparticle synthesis but outside of emulsion (prior to their inclusion in the emulsion). This allows for the use of high-resolution techniques such as AFM and EM without the use of specialised sample preparation methods.

Pickering emulsions have been used for the lubrication of metal surfaces, with the particle stabilisers being a more environmentally friendly alternative to surfactants and easier to control [38, 41]. In this area of application, the oil phase is chosen for its tribological properties, while the particles function mostly as a simple stabiliser. An example of this can be seen in Taheri *et al.* [42, 43] where a vegetable oil and water emulsion was chosen as a lubricant, with 35 nm $TiO_2/SiO_2$ composite NPs used to stabilise the emulsion. The focus for this system was the critical NP weight fraction needed to stabilise the emulsion without overloading the system with NPs, as high NP concentrations were seen to instead increase surface damage due to abrasion from NP agglomerates [42]. NP and droplet size are important in this type of system as a marker for emulsion stability and were measured with XRD and fluorescence microscopy within the study. Here, XRD was used to measure the size of dry NPs using their crystallite size as an alternative to other measurement techniques such as DLS or imaging techniques.

When considering Pickering emulsions for applications in medicine, emulsion stability and biocompatibility of the system components are of importance. For example, in Asfour *et al.* [44] a Pickering emulsion system was created to aid in wound healing using especially chosen materials (oleic acid for the oil phase and 287 nm chitosan stabilising particles) together with the presence of rutin dissolved in the oil phase. In this system, special importance was given to the biocompatibility and wound-healing properties of the oil phase and stabilisers. In addition, long-term emulsion stability remains important to ensure a long shelf life for the emulsion and to prevent the loss of rutin from within the oil droplets [44].

There are cases where the behaviour of the stabilisers needs to be observed in their native state while dispersed in the continuous phase. This can be seen in the Pickering emulsions in Hitchock *et al.* [40], which were used for the creation of gold nanocapsules for drug delivery. In this study, sunflower oil-in-water emulsions were stabilised by ~3 nm platinum NPs which also functioned as seed points for the growth of a gold capsule, used for the contain drugs dissolved in the oil phase for an extended period of time without drug leakage. In such as system, the size of the droplets needs to be monitored to allow for the creation of nanocapsules of appropriate size. In addition, the platinum nanoparticles on the oil-water interface need to be evenly spaced to ensure the growth of an appropriately thick gold shell. To obtain accurate

data on the distribution of stabilisers on the droplet's surface, the droplets must be characterised in their native state without drying the sample. This was accomplished by cryogenically freezing the sample using plunge-freezing and then imaging the sample at high-resolution using cryogenic TEM. This approach allowed the imaging of the stabilising nanoparticles on the droplet surface the gold film at different stages of growth (Figure 2.1). 3D analysis of the droplets through the use electron tomography techniques could help visualise the surface coverage of the NPs and the uniformity of the gold capsule, as visualising these aspects of the sample using only 2D imaging can be very challenging due to the inherent three-dimensionality of the droplets and capsules.

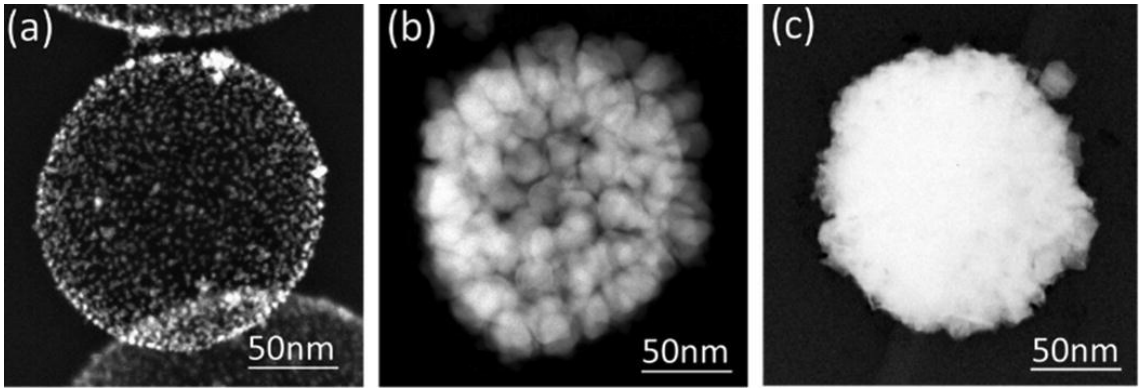


***Figure 2.1 –*** *Cryo-high angle annular dark field STEM (cryo-HAADF STEM) images of a Pickering emulsion droplet and different stages of gold film growth. Cryogenic imaging of frozen Pickering emulsions allows for the imaging of the stabilising nanoparticle distribution on the droplet surface (A), and the growth of the gold film (B) until a nanocapsule is produced (C). From Hitchcock et al. [40].*

### 2.2.1 Properties of Pickering Emulsions

Pickering emulsions use solid particles adsorbed onto the liquid-liquid interface to stabilise the system through a mixture of steric effects and capillary forces which prevent the particles from being detached from the interface, therefore stabilising it [35, 38, 45-47]. The detachment energy for the particles can be given by the following equation seen in Sjoo *et. al.* [47]:

$$E = r^2 \pi \gamma (1 - \cos\theta)^2 \quad (2.1)$$

Where:

- $E$ Is the detachment energy of the particle;
- $r$ Is the radius of the particle;
- $\gamma$ Is the surface tension (assuming a flat surface);
- $\theta$ Is the contact angle relative to the water phase;

From (2.1) it can be seen that the detachment energy is dependent on both the contact angle and the radius of the stabilising particle. The stabilising particles will be attracted preferentially to either the oil or water phase depending on their wettability. To obtain a stable system, the particles need to therefore have a contact angle close to 90° to maximise the detachment energy and ensure the particle do not disperse in the water phase (if too hydrophilic) or in the oil phase (if too hydrophobic) [38, 47, 48].

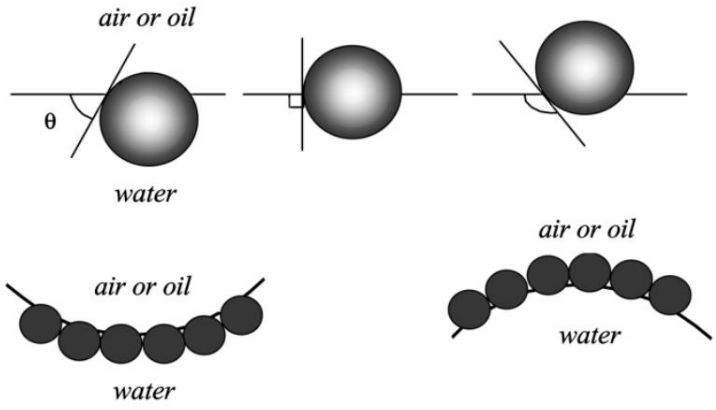


***Figure 2.2*** *- Position of a spherical particle on a planar water-fluid interface. Particles with a wetting angle below 90° (hydrophilic) will be close to the water phase, while particles with contact angles above 90° (hydrophobic) will be closer to the oil interface. Figure from Binks et al. [49].*

The stability of the emulsions droplets is also given by the concentration of particles adsorbed on the liquid-liquid interface. From studies by Nan *et al.* [50] it was found

that given a contact angle of 90°, the number of particles required to stabilise a system is given by:

$$n_p = \frac{4{r_e}^2 n_e}{r_p} \tag{2.2}$$

Where:

- $n$ Is the number of particles needed to stabilise the system
- $r_p$ Is the radius of the particles
- $r_e$ Is the radius of the emulsion droplets
- $n_e$ Is the number of droplets in the system

From this, assuming spherical particles, the mass required to stabilise the system is given by:

$$m_p = \frac{16}{3}\pi r_p \rho_p {r_e}^2 n_e \tag{2.3}$$

Where:

- $m_p$ Is the mass of particles needed to stabilise the system
- $r_p$ Is the radius of the particles
- $\rho_p$ Is the particle density
- $r_e$ Is the radius of the emulsion droplets
- $n_e$ Is the number of droplets in the system

Therefore, for emulsion systems with the same number of droplets ( $n_e$ ), the concentration of particles required to stabilise the system increases with increasing particle and droplet radius. It can therefore be seen that not only the stabiliser properties, but also the droplet size is important to create a stable Pickering emulsion system. As the solid stabiliser concentration increases (assuming a stable ratio of oil to water) the particle concentration on the droplet interface increases and causes a decrease in droplet size. Droplet size continues to decrease as more solid stabiliser is added, increasing in turn the stability of the emulsion, until a critical droplet size is reached after which the size remains unaffected. Any additional particles added

beyond this point will be dispersed in either phase depending on the surface properties of the particles [49].

For the solid particles to be suitable for stabilising the system they need to be wetted by both liquids simultaneously, which creates a drive to manufacture a wide variety of particles tailored for specific Pickering emulsion systems. Silica nanoparticles are often used as stabilisers due to their ease of manufacture and control over the particle properties, as seen in studies such as Binks *et al.* [51]. A solution for the necessity of the stabilising to be wetted by both phases simultaneously can be found in the use of Janus particles, which have surfaces with two or more physical properties. These allow the particle's surface to be half hydrophobic and half hydrophilic, therefore increasing the detachment energy of the system. Stabilising particles are not required to be spherical, with various studies showing the use of rod-like or disc-shaped particles. Wei *et al.* [52] used Halloysite nanotubes to stabilise an emulsion of dichloromethane in water, while studies such as Fujii *et al.* [53] show droplet stabilisation using hydroxyapatite stabilisers in the form of spheres, rods, and fibres. Pickering emulsion droplets are mostly spherical [38], though different shapes can be obtained depending on the properties of particles and the liquid phases used [38, 54, 55]).

In addition to the stabilising particle's surface properties, the particle size also contributes greatly to the particle's ability to stabilise the system. A higher detachment energy can be obtained from particles with very low or very high contact angles provided the radius is sufficiently high, as shown in Figure 2.3 [47, 49, 56, 57]. Given this, it is preferable for the stabilising particles in a Pickering emulsion system to be as large as possible, though the emulsion droplets need to be at least one order of magnitude larger than the stabilising particles used, providing a limit to the particle size [48].

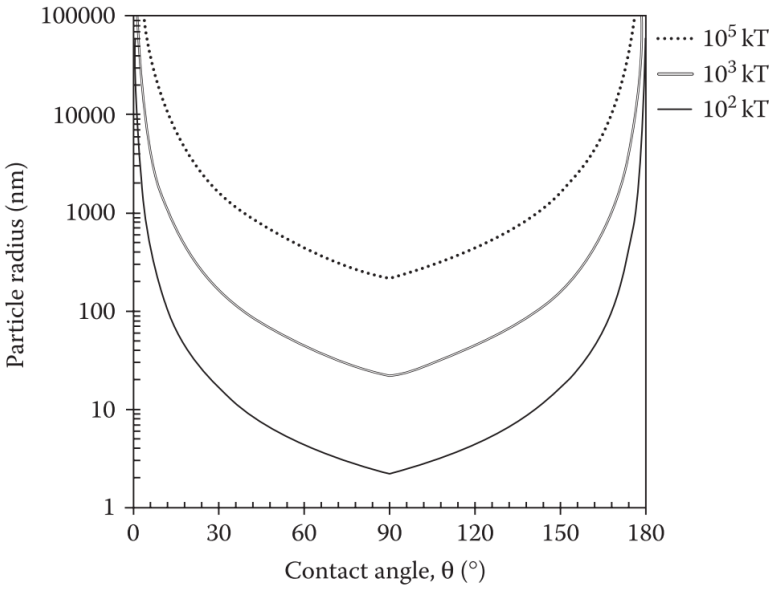


***Figure 2.3*** *- Contour plot for equal detachment energies as the contact angle and particle radius varies [47]. A ~2 nm nanoparticle with a 90° contact angle will have the same detachment energy as a ~200 nm nanoparticle with a ±30° contact angle. Figure from Binks et al. [58].*

Particles within a successfully stabilised Pickering emulsion system have a strong preference to adsorb into the liquid-liquid interface to form an ordered monolayer at the droplet surface; however, it is also possible for the stabilising particles to be found in the continuous phase depending on the contact angle of the stabilising particles. This is especially relevant to cases where the droplets have formed agglomerates, or are in the process of coalescing, as depicted in Figure 2.4 [47]. Coalescence in Pickering emulsion droplets results from a low detachment energy for the particles, which allows for liquid bridges to form between droplets that contribute to an increase in emulsion droplet size which can affect the emulsion stability and the suitability of the system for some applications.

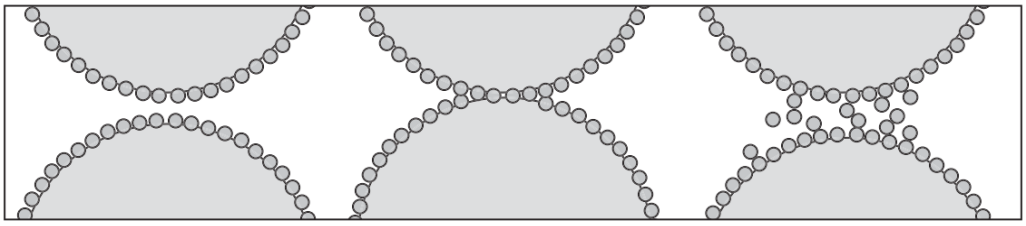

***Figure 2.4*** *- Packing of the stabilising particles. The droplets on the left are stabilised by a particle monolayer, while the central droplets are stabilised by particles bridging between the droplets. The last example shows aggregation of the particles in the continuous phase preventing droplet coalescence. Figure from Sjoo et al. [47].*

Sedimentation and creaming can occur when the droplets are large enough to be affected by gravity, leading to the system separating into a continuous phase and a region with a high concentration of droplets, which can drastically shorten the emulsion's shelf life [47]. Simulations for sedimentation of droplets by Pal [59] show that droplet size, size of nanoparticles, contact angle of the nanoparticles, and packing density of nanoparticles contribute to sedimentation and creaming.

### 2.2.2 Characterisation Strategies for Pickering Emulsions

Due to the importance of both the droplet and particle sizes and shape, Pickering emulsions are carefully monitored during and after their manufacture, often using imaging techniques [57]. Optical microscopy is used as a routine imaging technique to monitor droplet size, aggregation, and shape at any point during the manufacturing process. This, together with dynamic light scattering for droplet and particle size measurements [57, 60, 61] are the most commonly used routine bulk characterisation techniques for Pickering emulsions. Confocal laser scanning microscopy is commonly used as a supplemental imaging technique to distinguish the liquid phases and visualise the stabilising particles with the use of fluorescent dyes [62, 63]. An example of the use of confocal fluorescence microscopy can be found in a study by Douliez *et al.* [64], where this technique was used to image colloidosomes and track in 3D their ability to swell in a controlled manner. The Pickering emulsion system characterised in this study was engineered to be able to encapsulate and release material in a controlled manner (e.g. to capture biomolecules and cells), therefore needing

characterisation techniques that would allow to monitor the 3D structure of the droplets and the presence of captured material within the droplet itself after swelling (see Figure 2.5). Confocal fluorescence microscopy was suitable for this task sue to the ability to identify fluorescence markers associated with the stabilisers and captured material, while allowing for imaging in a hydrated state [64]. Optical, confocal, and fluorescence microscopy are all widely used for the imaging of Pickering emulsion droplets as they allow for rapid imaging with minimal sample preparation at any point during the synthesis of the Pickering emulsion system.

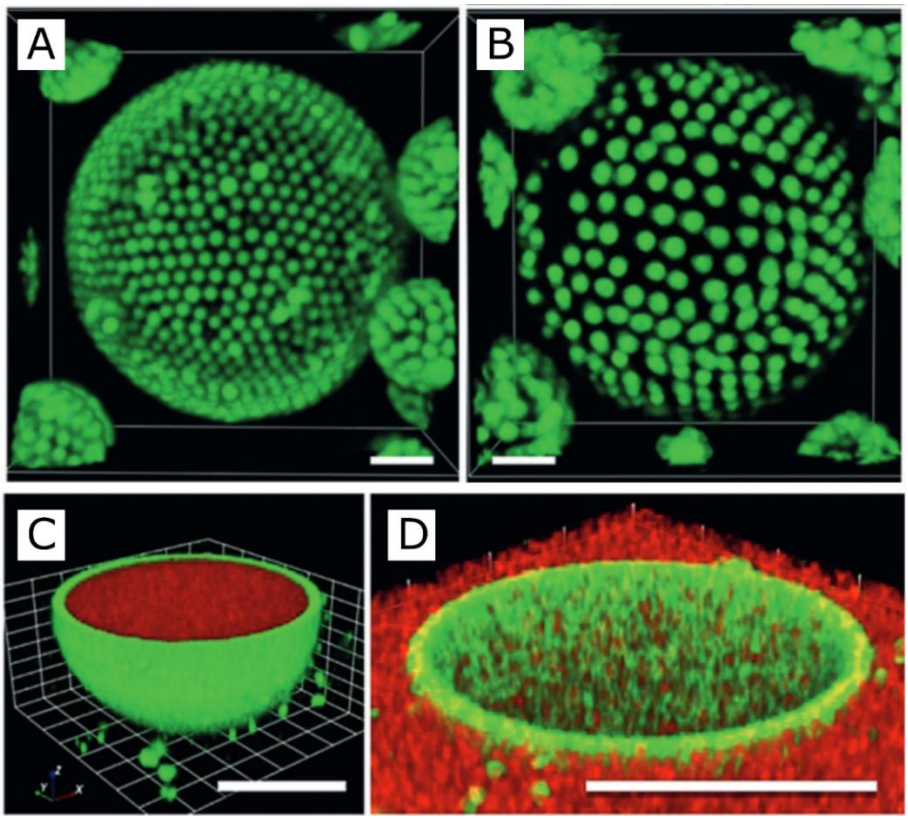


***Figure 2.5 –*** *Confocal light microscopy images of a swelling Pickering emulsion droplet. A) and B) 2D images of a droplet before and after swelling, showing the stabilising particles moving further apart as the droplet volume increases. C) and D) 3D tomograms generated from tilt tomography showing a droplet pre- and post-swelling. Fluorescence microscopy as used here can track the movement of marked material from the inside to the outside of the droplet during swelling. Figure modified from Douliez et al. [64]. A), B) and C) scale bar = 5 µm. D) scale bar = 20 µm.*

However, the imaging of Pickering emulsions can become challenging with systems using nanosized droplets or stabilising particles, as neither the structure of the stabilising particles nor the droplet shape can be easily imaged through conventional microscopy for emulsions composed of small droplets below the micrometre size (1-100 nm) [57, 65]. In these cases, a variety of characterisation techniques need to be used, with optical and fluorescence microscopy allowing for low resolution imaging, DLS being used for particle and droplet size measurement, and electron microscopy techniques being used for the imaging of the stabilising nanoparticles and their interactions with the oil-water interface. Cryogenic electron microscopy can be used to image the droplet structure and stabilising particles in Pickering emulsion samples by preventing the droplets from drying using cryofixation, which additionally prevents the loss in sample structure that may happen with traditional fixation methods [57]. Cryo-SEM and cryo-TEM have both seen use for the imaging of the stabilising particles on the emulsion droplet's surface, with studies such as Sihler *et al* (2015) showing the ability to image the presence of particles (12-22 nm silica NPs) on the droplet (<500 nm) surface and the particle coverage using cryo-SEM, while using dry TEM for size measurements as shown in Figure 2.6.

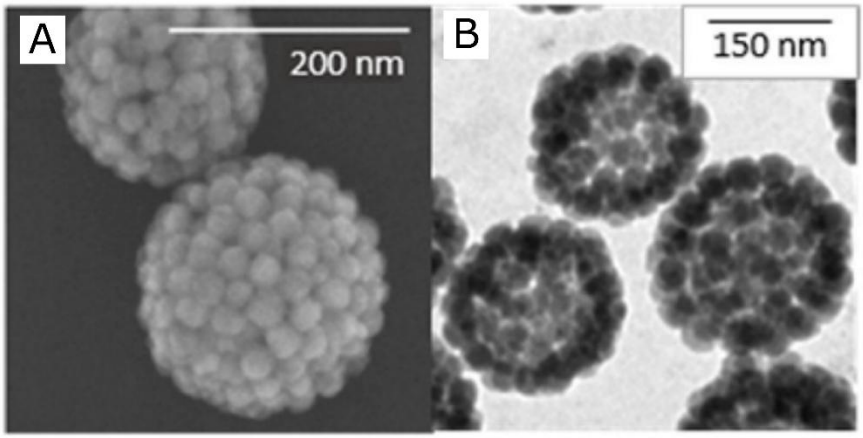


***Figure 2.6 –*** *Cryo-SEM and dry TEM images of emulsion droplets covered by silica NPs. A) Cryo-SEM image of cryogenically frozen Pickering emulsion droplets stabilised by silica NPs. The droplets retain their spherical shape due to having been cryogenically cooled in liquid ethane. B) TEM image of the dried Pickering emulsion. As the liquid components have evaporated, the NPs have been deposited on the carbon film in the TEM grid, thus losing the hydrated droplet structure. Images from Sihler et al. [66].*

Cryo-TEM can likewise be used to image both droplets and stabilising particles [67]; Zhai *et al.* [67] used cryo-TEM both for the imaging of cellulose stabilising nanofibers alone (30-80 nm diameter and >100 nm length), and for the imaging of the droplets. Cho *et al.* [68] shows the use of cryo-TEM for the imaging of water-in-silicone Pickering emulsion stabilised by bacterial cellulose nanofibrils and cationic nanoplatelets. This system was synthesised to show the possibility to form a tightly fitting double layer at the droplet interface, formed by the nanofibrils and nanoplatelets. Here, confocal laser scanning microscopy was used to confirm the presence of the stabiliser layers at lower magnifications. Conventional TEM was used for the characterisation of the stabiliser sizes, while plunge-freezing of the sample and cryo-TEM (in HAADF STEM mode) was necessary to image this double layer structure at the droplet interface, shown in Figure 2.7 [68].

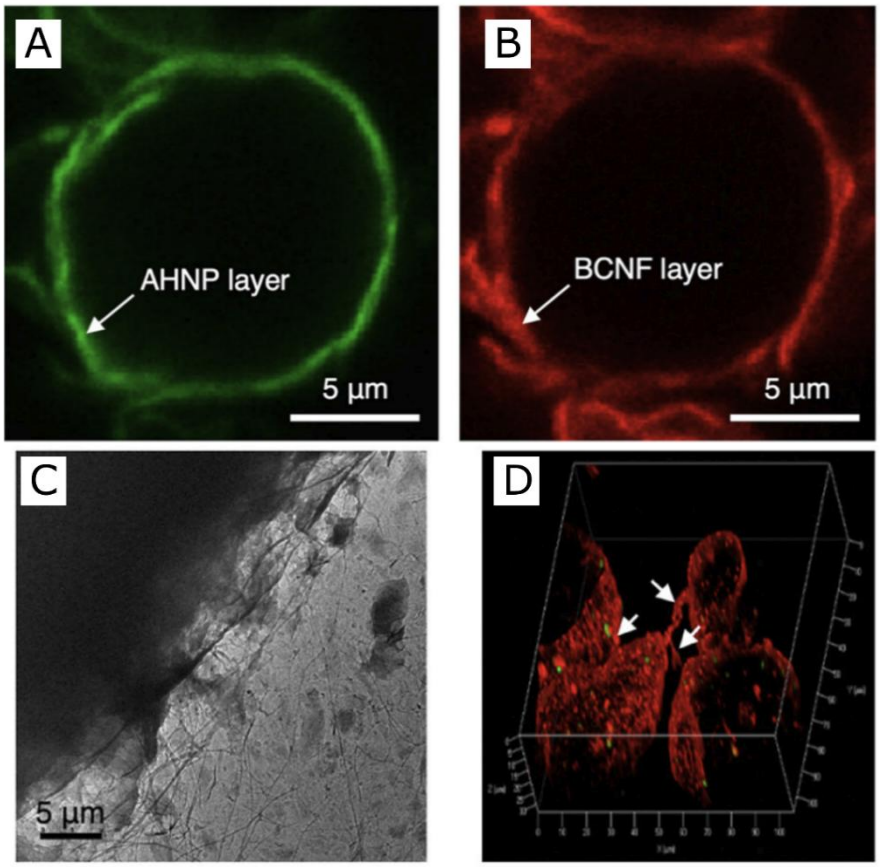


***Figure 2.7 –*** *Confocal laser microscopy and cryo-TEM images of Pickering emulsion droplets. A) and B) confocal laser micrographs of a droplet with the platelets stained in green (A) and fibrils stained in red (B). C) cryo-TEM image of the droplet interface showing the fibrils on the droplet interface. D) 3D confocal laser tomogram showing*

*fibril bridges forming between droplets. Note that the sample in (C) was plunge-frozen and imaged in cryo-TEM despite showing a droplet size much larger than what would be traditionally suitable for plunge-freezing (usually below ~200 nm). Figures modified from Cho et all. [68].*

Cryo-SEM and focused ion beam milling have been used by Elbers *et al.* [69] to image the non-touching surface interactions between water droplets and poly(methyl-methacrylate) (PMMA) particles (2.8 µm). Cryo-SEM imaging is necessary in this case due to the large particle and droplet size, while FIB-milling is useful for the analysis of the droplet-particle cross-section. Elbers *et al.* [69] also shows the use of serial FIB sectioning to obtain a tomogram of the droplet-particle interaction. Figure 2.8 shows the ability to expose specific sample features using FIB milling.

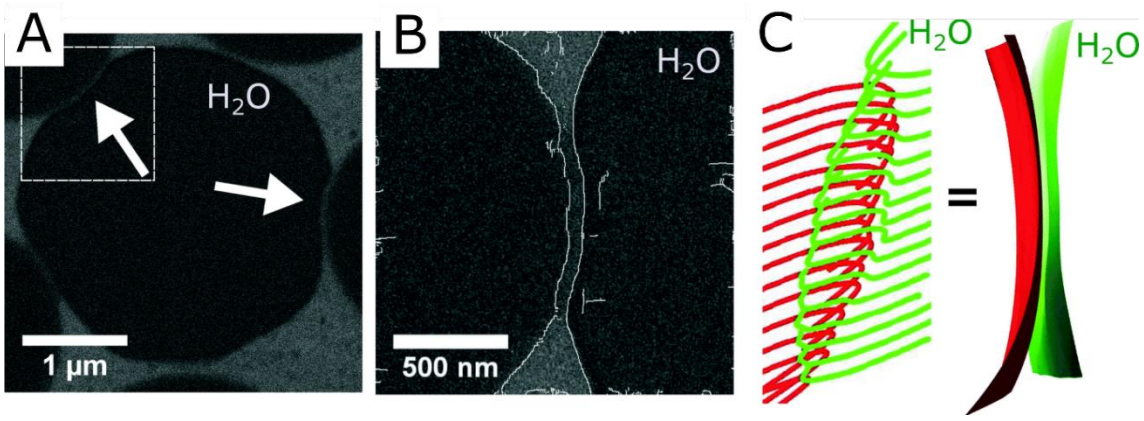


***Figure 2.8 –*** *Cryo-SEM images of a FIB-milled droplet section and models generated from tomographic data of the imaged region. A) and B) cryo-SEM images of a FIB-milled droplet cross-section showing the non-touching interaction between the water droplet (labelled as $H_2O$) and a PMMA particle (unlabelled). C) 3D reconstruction of the imaged region. Figure modified from Elbers et al. [69].*

However, the lack of sample staining together with the lack of contrast between the liquid phases of the emulsions in cryo-TEM leads to an inability to distinguish between the oil and water phase. In contrast, negative staining of samples can be seen for nano emulsions in dry samples as in Schalbart *et al.* [70] and in cryo-prepared samples as in Klang *et al.* [71] and Persson *et al.* [72], which are shown in Figure 2.9. Staining can

be used to improve contrast by the addition of heavy metal particles, which easily allow for the visualisation of both the stabilising particles and oil phase simultaneously. Limitations can be found to the use of negative stains, some of which can be found in a review of stains for both dry and frozen hydrated samples by De Carlo and Harris [73]. For a sample to be suitable for staining it first must endure the exposure to high concentrations of the salt used, and then the stain must be able to penetrate the sample fully otherwise there is a risk of losing information on the internal structure of the particles stained.

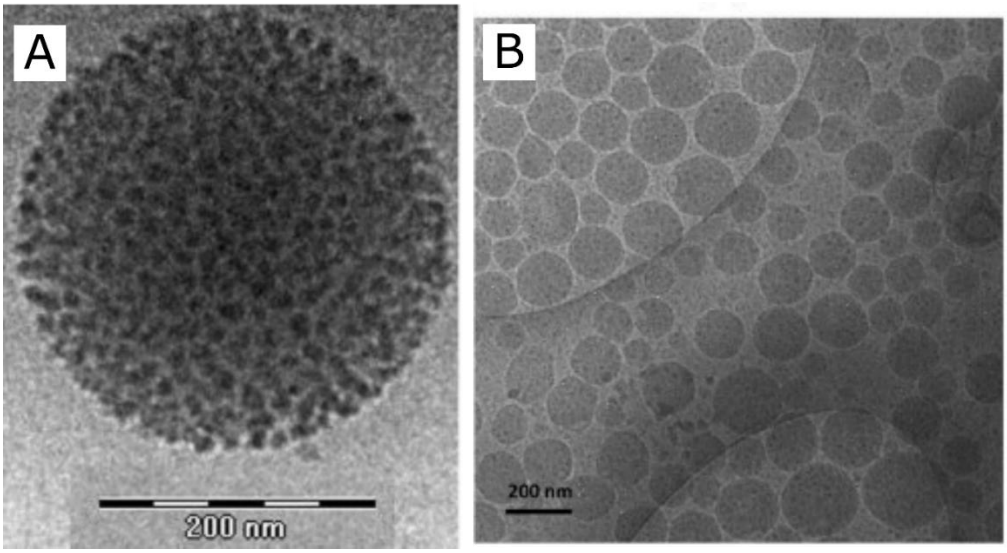


***Figure 2.9 –*** *Cryo-TEM images of negatively stained droplets. A) cryo-TEM image of a negatively stained Pickering emulsion droplet (squalene-in-water with silica NPs) from Presson et al. [72]. B) cryo-TEM image of sucrose stearate nano-emulsions negatively stained from Klang et al. [71]. Both samples were stained with uranyl acetate to improve contrast of the oil phase.*

An alternative strategy for the visualisation of the two liquid phases can be found in the use of elemental analysis techniques such as energy dispersive X-ray spectroscopy (EDX) and electron energy loss spectroscopy (EELS) [40, 65]. These allow the oil and water phases to be identified by detecting the carbon and oxygen signals in the sample, without the need for sample staining.

The use of multiple characterisation techniques for the analysis of Pickering emulsion systems is vital to obtain accurate measurements. The use of optical microscopy and

fluorescence microscopy are ubiquitous in Pickering emulsion studies due to their relative ease of use for bulk sample imaging and for tracking components in the system. However, while high-resolution imaging techniques such as AFM and EM are present in studies analysing nano-sized emulsions and stabilisers, they are not as well-developed as optical microscopy methods. 3D imaging and spectroscopy techniques in cryo-EM is nearly absent in the analysis of Pickering emulsions, even in cases where they may be of benefit. Meanwhile electron tomography, EELS and EDX are often used during electron microscopy in biology and in materials science and could be also applied for the characterisation of Pickering emulsions.

## 2.3 Cryogenic Electron Microscopy

Complex hydrated samples such as nanoparticle dispersions, cells, and tissue samples often need to be characterised using methods that retain their native structure. When the characterisation goal is high-resolution imaging of nano-sized structures these samples become problematic, as high-resolution imaging techniques such as electron microscopy require the samples to be vacuum-resistant. This has led to the development of a wide variety of sample fixation techniques, which aim to “fix” the sample structure in place using chemical agents (e.g. formaldehyde) at room temperature or using rapid freezing. Chemical fixation methods can cause tissue to contract, cause volume changes, and might fail to properly fix certain regions in the sample, leading to the use cryogenic fixation becoming more common for EM imaging of biological samples as research groups acquire the required equipment and knowledge for the use of cryogenic fixation [34].

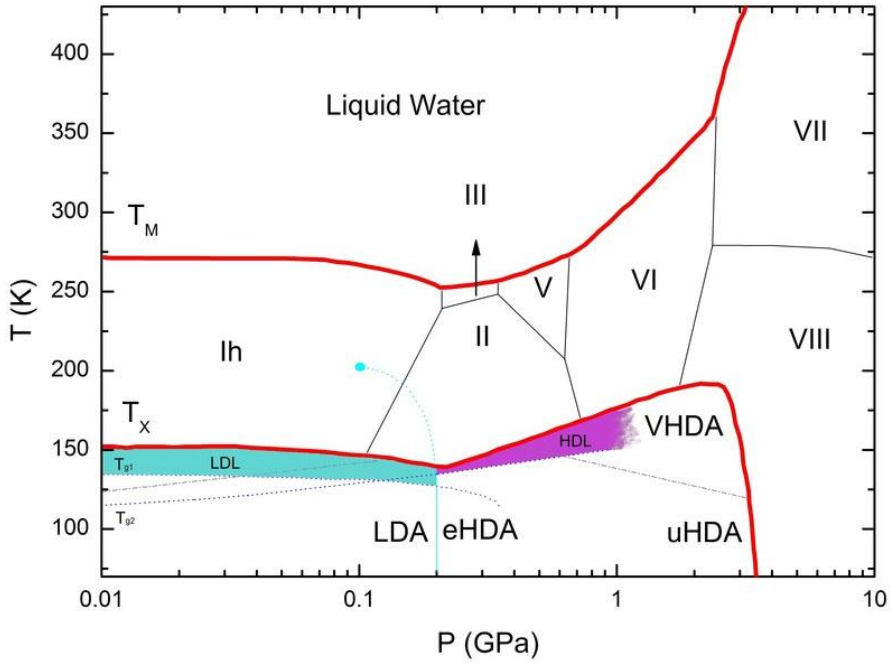


***Figure 2.10 –*** *Phase diagram of non-crystalline water including amorphous ice phases LDA, HDA, and VHDA.The solid red lines indicate the crystallisation temperature, with the amorphous ice phases found below the crystallisation temperature $T_x$. Water needs to be cooled below the glass transition temperature ($T_{g1}$, approximately -137°C) to prevent crystallisation. Diagram from Ruiz et al. [74].*

The main scope of cryogenic sample preparation as a fixation technique is to preserve the sample in the native state [34]. This is accomplished by cooling down the sample below the glass transition temperature of water, transforming the liquid water to its solid amorphous (vitreous) state, as seen in Figure 2.10. Cooling water below its nucleation temperature prevents the nucleation and growth of ice crystals, which can displace material within the sample [27, 75, 76]. Different cryogenic sample preparation techniques are used depending on sample size and target imaging technique, some of which are described in Table 2.1.

***Table 2.1 –*** *Cryogenic sample preparation techniques and literature examples.*

| Technique | Brief Description | Size of Samples | Imaging Techniques | Literature Examples |
|---|---|---|---|---|
| Plunge Freezing | A drop of the liquid sample is deposited on a TEM grid, which is blotted to obtain a thin liquid film and then plunged into liquid ethane. | Small particles (generally below ~200 nm) | TEM, SEM | Membrane proteins (~1 nm) [77]; $CaCO_3$ particles (~5 nm) [78] |
| Spray Freezing | A small portion of the sample is spayed through a nozzle onto a TEM grid as it is being plunged in liquid nitrogen. | Small particles (generally below ~200 nm) | TEM, SEM | Erythrocyte vesicles (~100 nm) [79] |
| Metal Mirror / Impact Freezing | A metal plate is cooled to cryogenic conditions and pressed against the sample. | Bulk samples up to 20 μm | SEM | Nerve tissue [80] |
| Plunging | A small volume of liquid sample is put in a rivet and plunged into liquid ethane or liquid or slush nitrogen. The sample can then be freeze-fractured to expose objects within. | Bulk samples up to 200 μm | SEM | Yeast cells (*Saccharomyces Cerevisiae*) [81] |
| High Pressure Freezing | The sample is put in a chamber where it is put under high pressures (~2100 bar) while being cooled in liquid nitrogen. | Bulk samples up to 200 μm | TEM, SEM | Hydrogels [82]; Emulsions (oil-in-water and water-in-oil emulsions) [83] |

| Technique | Brief Description | Size of Samples | Imaging Techniques | Literature Examples |
|---|---|---|---|---|
| Cryo Lift-Out | Not a freezing technique but consists in the fabrication of a thin lamella of a sample frozen with one of the abovementioned techniques. The lamella is cut with a cryo-ultramicrotome or milled with a focused ion beam in an SEM and then transferred to a TEM. | Bulk samples up to 200 µm, but can deliver lamellae of the desired thickness | TEM | Neuronal aggregates (>10 µm) [84] |

Among the techniques presented in the Table 2.1 plunge-freezing is employed very frequently for the preparation of both biological and inorganic samples with small sizes (generally below ~200 nm, but up to ~600 nm) due to its reliability in generating vitreous ice for cryo-(S)TEM imaging. Note that in this thesis, “plunge-freezing” will always refer to blotting a sample on a TEM grid followed by rapid plunging in a cryogenic coolant. Other instances of sample preparation consisting of plunging a sample in a cryogenic coolant will simply be referred to as “plunging”. Cryo-prepared samples can be imaged while kept at low temperatures using TEM and SEM setups. Both cryo-TEM and cryo-SEM allow for the imaging of samples at high resolutions and spectroscopic analysis (EDX and EELS in the TEM, EDX in the SEM). Cryo-SEM fitted with a focused ion beam can additionally be used to mill sections of the sample to expose new cross-sections for imaging or to prepare thin sections (lamellae) that can be transferred to a cryo-TEM. Sample imaging using cryo-(S)TEM and cryo-SEM will be discussed in the following sections.

### 2.3.1 Effects of Plunge-Freezing on the Sample

Despite the promise of plunge-freezing and cryo-EM to maintain structural integrity, subtle changes during the sample preparation process can greatly change the particle

distribution after freezing (Figure 2.11), and the production of high-quality cryo-EM samples where particle distribution and overall sample structure remain unaffected is limited by the user skill in preparing the sample [75]. Even in a well-prepared sample, artefacts can arise because of contamination of the sample surface by frost collected during sample transfer to the cryo-electron microscope, obscuring the sample being imaged. For this, the room the transfer is being made in must be kept dry and during the transfer process the sample must be exposed to the air for as little as possible [85, 86].

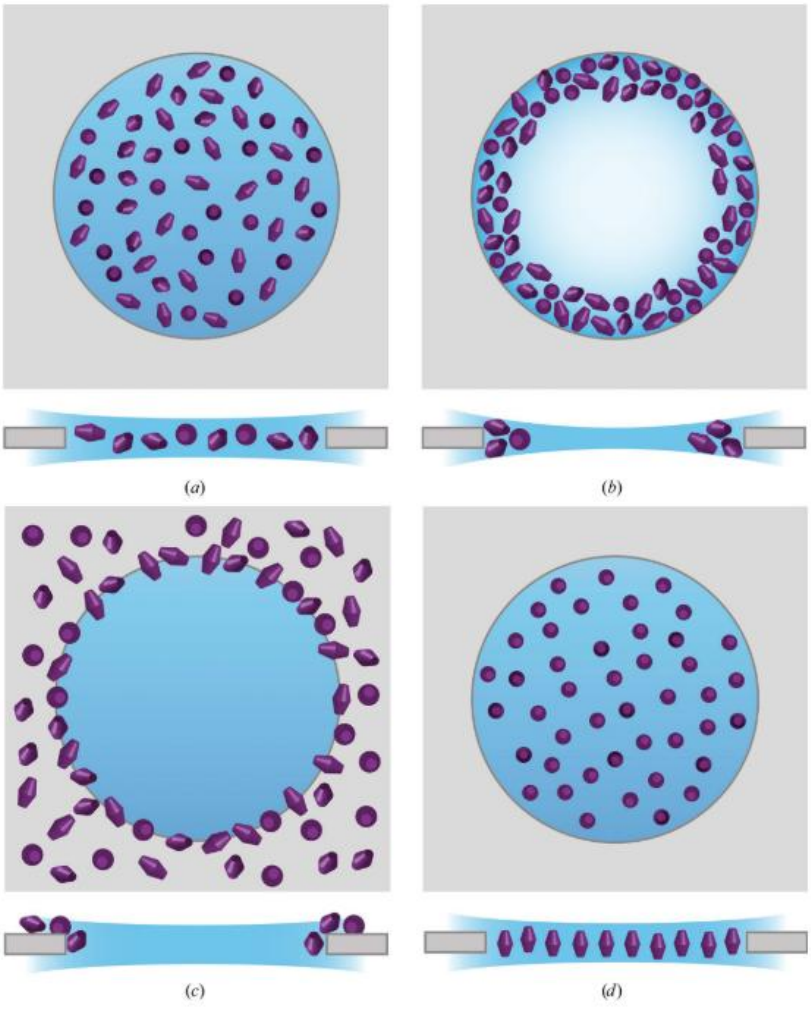


***Figure 2.11*** *- Particle distribution after plunge freezing. (a) shows an ideal sample where the particles retain their original position within an homogeneous vitreous ice layer; (b) shows particles agglomerating in regions where the ice layer is thicker; (c) shows particles that have a higher affinity for the substrate used and therefore do not appear in the hole with vitrified ice; (d) shows particles adopting a preferred orientation. Figure from Drulyte et al. [75].*

Some of the possible factors affecting the particle distribution in a plunge-frozen sample are shown in Figure 2.11 and include:

- Hydrophilicity of the TEM grid: the solution droplet added to the TEM grid needs to wet the entire surface to ensure the presence of ice in the entire grid area.
- Local thickness of the ice layer: in cryo-TEM the sample tends to be more visible when in the holes in the carbon film. However, local ice thickness within the carbon holes is variable and larger holes may be completely devoid of ice. This forces particles to cluster in areas where ice is thicker, which in turn are more difficult to image and more prone to being crystalline [75, 85].
- Particle affinity for different substrates, and their propensity to be found at the air-water interface after blotting [75, 77].

Vitrification of a plunge-frozen sample is highly dependent on the ability of heat to flow out of the sample at a fast enough rate to prevent crystal nucleation; this is in turn limited by the heat capacity and temperature of the liquid the sample is plunged into, and by the time taken for the heat to leave the liquid water entirely. Given this, the sample thickness will be crucial during plunge freezing, as larger samples can become too thick for heat to disperse before vitrification is allowed to happen. Practically, this means that plunge-freezing (as a surface cooling technique) can only be applied to samples of limited thickness (hence the blotting step), with an ideal thickness quoted to be approximately in the range of 100 nm by Friedrich *et al.* [87] for cryo-(S)TEM imaging. Much larger cell samples have been cryo-prepared via plunge-freezing, but these require prior sample preparation to ensure vitrification. Guo *et al.* [84] shows the plunge-freezing of neuronal aggregates incubated in glycerol to raise the glass transition temperature of the sample, thus allowing for full vitrification. It must be noted, however, that this sample was initially imaged in cryo-SEM, where thin lamellae were prepared through FIB-milling for further cryo-TEM imaging.

Cryogenic imaging of larger samples that are not applicable for plunge freezing can instead be imaged using a surface imaging technique (i.e. SEM) or by imaging thin slices cut from a larger frozen sample, which could be possible via either cryo-

ultramicrotomy or cryo-FIB-SEM. High pressure freezing (HPF) can be used to freeze these larger volumes up to 1 $mm^3$ [88-90].

### 2.3.2 Cryogenic- (Scanning) Transmission Electron Microscopy and Sample Damage

Cryogenic transmission electron microscopy (cryo-TEM) is widely used for the imaging of biological samples, as the cryogenic conditions can be used for sample fixation while the high resolutions available in TEM allow for the imaging of nano-sized biological material such as viruses, bacteria, and organelles. Besides 2D imaging, cryo-TEM has also been used extensively for 3D imaging using electron tomographic techniques (ET). Cryo-TEM has also seen use for the imaging of hydrated or beam-sensitive materials within materials science, with self-assembled structures, catalytic materials, and polymers being some of the possible systems that benefit from cryogenic imaging [87, 91]. Lobling *et al.* [92], for example, shows the use of cryo-TEM and electron tomography for the imaging of self-assembling micelles in high detail. Such micelles need high structural complexity to encapsulate selected objects in applications in nanoreactors and medical applications; however, this high complexity requires high-resolution characterisation techniques to properly analyse the suitability of the sample for its application.

Sample damage needs to be considered when imaging frozen electron beam-sensitive samples to prevent damage to the sample or to the ice, which can create artefacts in the sample (Figure 2.12). Exposure of the vitrified ice to the electron beam can cause sample drift and an increase in the local temperature of the ice. This first leads to devitrification of the exposed area, with the growth of cubic or hexagonal ice crystals which disrupts imaging due to Bragg scattering [76, 87]. After further exposure to the beam the ice can sublimate, causing small objects in the sample to be displaced and forming holes in the ice. Although cryogenic conditions increase the threshold for damage for the sample being imaged, the sample can still be directly affected by the beam before devitrification or sublimation occurs. Damage to beam-sensitive particles is often observed as “bubbling” on the rim of the particles as can be seen in Figure 2.12-A [85-87]. Micro- and nanopores within porous particles can also be damaged by the beam even under cryogenic conditions [93].

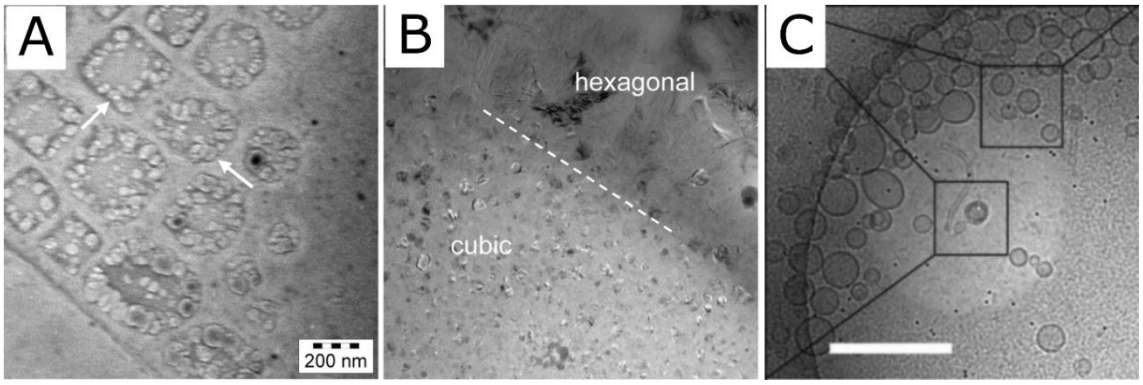


***Figure 2.12 –*** *Cryo-TEM images showing sample damage after exposure to the electron beam. A) "Bubbling" appearing at the edge of particles [86]. B) Hexagonal and cubic ice forming as the ice is warmed up [86]. C) Circular sample region (appearing brighter than the surrounding ice) showing damage after exposure to the electron beam [87]. Note the damaged region in (C) is circular due to the parallel beam in conventional TEM imaging. When imaging in cryo-STEM mode, damaged regions will instead be rectangular, corresponding to the area scanned by the electron probe. A) and B) from Kuntsche et al. [86]; C) from Friedrich et al. [87].*

Imaging at low total number of electrons is always necessary to minimise sample damage, but for especially sensitive or small samples, further approaches are needed. The biological sciences have pioneered numerous techniques for minimising damage: imaging of the TEM grid at low magnifications allows users to find important features without the need to use high electron doses to visualise the sample. Meanwhile, when imaging the sample, images can be created from the averaging of multiple frames. Numerous images can be collected with low exposure times and then averaged to form a single improved image, thus obtaining an image with sufficient contrast but with a lower total exposure of the sample to the electron beam [94]. This is especially useful when imaging small identical particles, as this approach allows for the averaging of images of different particles, thus yielding high-resolution images without having to expose any single particle to the beam for long time periods [94].

The vitrified ice needed for cryo-TEM imaging is metastable and will devitrify and sublime as the temperature increases [87], therefore making cryogenically frozen samples highly susceptible to the high-energy electron beam in TEM. This beam-induced damage is observed in vitrified ice (~100 nm thick) even at relatively low

electron fluence (<100 $e^{-}/\text{Å}^2$), though the damage increases as the fluence increases [95]. The amount of electrons in the imaged area (electron fluence) and the amount of electrons in the imaged area in a given period of time (electron flux) are given by [95]:

$$fluence\left(\frac{e^{-}}{\text{Å}^2}\right) = \frac{N_e}{A} \tag{2.4}$$

$$flux\left(\frac{e^{-}}{\text{Å}^2\,\text{s}}\right) = \frac{fluence}{t} \tag{2.5}$$

Where:

$N_e$ Is the sum of electrons in an image

$A$ Is the total relevant image area

$t$ Is the acquisition length

This susceptibility to beam-induced devitrification is especially problematic as the resolution in TEM is limited by the electron dose; according to Glaeser [96] to be able to resolve an object, the contrast must be larger than the local fluctuation given by a minimum acceptable value for signal-to-noise ratio (SNR). Therefore, the product of the contrast and resolution must be equal to or greater than a constant:

$$Cd \geq \frac{SN}{\sqrt{fD_C}} \tag{2.6}$$

Where:

$C$ Is the contrast

$d$ Is the size of the smallest resolvable distance

$SN$ Is the minimum acceptable SNR

$\mathrm{D_C}$ Is the critical electron dose

$f$ Is the fraction of electrons that enter the lens aperture and contribute to the image

From equation (2.6), to increase the image resolution it is necessary to increase the overall electron dose [96, 97]. In addition, techniques such as energy dispersive X-ray (EDX) spectroscopy and electron energy loss spectroscopy (EELS), which inherently

require higher electron fluences to function, are therefore unavailable for standard cryo-TEM imaging [98].

As seen in Ilett et al. [99], the beam-induced damage can be decreased when imaging in STEM mode. In STEM the electron flux (as either the probe flux received at each pixel ($F_p$), and average electron flux averaged over the whole frame ($F_{av}$)) can be calculated as [98]:

$$F_p = \frac{I}{(eA_p)} \tag{2.7}$$

$$F_{av} = \frac{I}{eA_f} \tag{2.8}$$

Where:

$I$ Is the probe current in coulomb per second

$e$ Is the electron charge (e=1.602×10$^{-19}$ C)

$A_p$ Is the area of the probe

$A_f$ Is the total scan area of the frame

From the average electron flux, the electron fluence is:

$$\text{total accumulated fluence} = \frac{\mathrm{It}}{\mathrm{eA_f}} \tag{2.9}$$

Where:

$I$ Is the probe current in coulomb per second

$t$ Is the total scan time (in seconds, which is taken from the pixel dwell time and number of pixels)

Following this, it was found that at similar amounts of electron fluence per frame imaging in STEM mode has caused less damage to vitrified ice compared to conventional TEM. Using cryo-STEM, electron fluences of at least 1000 $e^-/\text{Å}^2$ are necessary before damage to ice was observed [98]. The use of STEM can allow for EDX, EELS, and electron tomography to be used on a cryo-TEM sample with higher electron fluences and without risking devitrification, therefore greatly expanding the possible analysis techniques available in cryo-TEM.

Cryo-STEM has seen some use in biology, where it is used for the imaging of thick samples and for the ability to also use EDX and EELS [89, 100, 101]. Bright field cryo-STEM has been used as an alternative to defocus phase contrast in conventional TEM due to the signal acquisition in STEM being more flexible more accurately representing the mass density of the sample [102, 103]. In Figure Elbaum *et al.* [103] shows poor image resolution after reconstruction of TEM defocus images even with the use of SIRT when compared to STEM images.

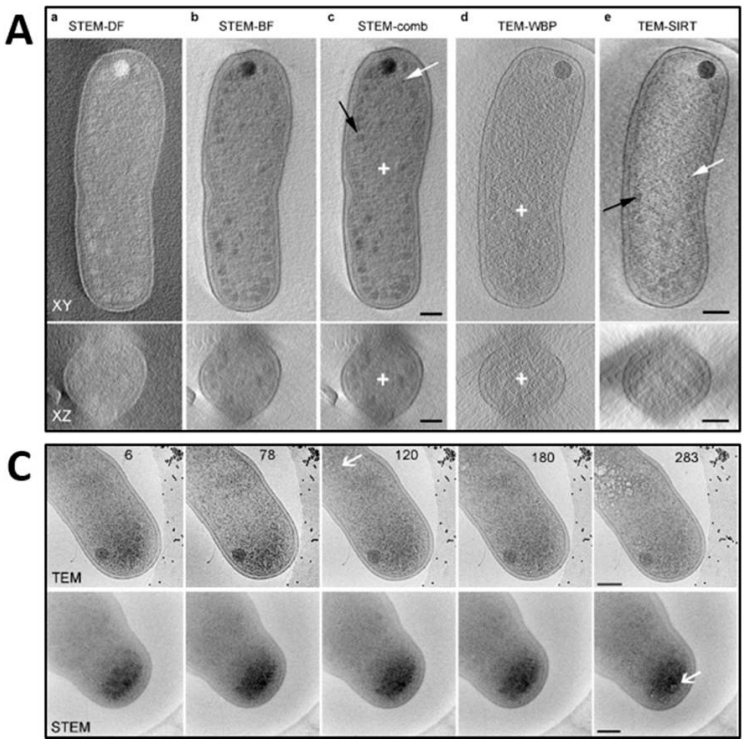


***Figure 2.13 –*** *Comparison between STEM and TEM imaging in tomogram reconstruction and sample damage. A) Tomograms reconstructed from STEM and TEM images, showing a lower image resolution in the tomograms obtained from the defocus TEM images. B) Visible damage to the sample with increased exposure (number in the top-right shows the accumulated exposure in* $e^{-}/Å^{2}$*). The damage threshold is higher in STEM. Image modified from Elbaum et al. [103].*

The ability to image thick biological samples in bright field STEM has been well-studied, with studies such as Aoyama *et al.* [104] showing the ability to image and successfully obtain tilt tomograms of samples up to 1 µm thick, which were previously high pressure

frozen and substituted. Figure 2.14 presents results from this study, showing that conventional cryo-TEM is unable to image high thickness samples that are instead suitable for cryo-STEM imaging. As a sample encased in ice is tilted, the effective sample thickness increases, as the distance the electrons must travel through the sample increases. This can cause issues when collecting tilt series for electron tomography, resulting in lower-resolution reconstructions. As Figure 2.14 shows, STEM imaging is suitable for the imaging of thick samples at larger tilt ranges than conventional TEM. This makes STEM mode suitable to be used together with electron tomography for the 3D imaging of biological samples, as seen in studies such as Aoyama *et al.* [104], Hofmann-Marriott *et al.* [105], Wolf *et al.* [106], which were successful in the imaging of cells, bacteria, and organelles in samples up to 1 μm thick [104, 105, 107].

In materials science, cryo-STEM has been used with annular dark field (ADF) and high-angle annular dark field (HAADF) imaging. These imaging modes allow for atomic contrast imaging, which aids in the imaging of nano-structures with high atomic numbers. Yoshida *et al.* [108] used cryo-STEM electron tomography for the 3D imaging of the nanostructure in porous titania photocatalyst particles and silver nanoparticles. The very small pore size requires high-resolution imaging, while cryogenic conditions are necessary to prevent damage to the titania structure and coalescence of the nanoparticles. In this case, the sample was cooled using liquid nitrogen during imaging, rather than cryogenic preparation prior to transfer to the TEM, as the sample does not need to be imaged in hydrated conditions. Reducing the specimen temperature has been proven to decrease the specimen's radiation sensitivity, increasing the critical dose needed before the start of beam-induced damage; it is critical to note however, that this process is not related to thermal decomposition, as heat-induced damage is often minimal at low electron doses [109]. Miszta *et al.* [110] shows the use of cryo-STEM and cryo-HAADF STEM electron tomography for the 3D imaging of 3D nanocrystal assemblies dispersed in toluene. Here the 3D structures only exist when dispersed in a solution and therefore need to be cryogenically frozen before imaging.

Meanwhile, cryo-HAADF STEM (with or without the additional use of ET) is not generally used for the imaging of biological samples, with bright field imaging remaining the standard. Aoyama *et al.* [104] suggests the use of HAADF for the

imaging of negatively stained samples, by taking advantage of HAADF providing higher contrast for materials with high atomic number. However, both Aoyama *et al.* [104] and Hofmann-Marriott *et al.* [105] ultimately show that HAADF STEM imaging is largely unsuitable or the imaging of thick biological samples, while not showing the distinct advantages that would be expected from atomic contrast imaging. This is due to biological samples being predominantly composed of elements with low atomic numbers (mostly carbon, with traces of nitrogen and oxygen). HAADF STEM therefore becomes ineffective in increasing contrast without the addition of negative stains, and remains more suitable for the imaging of non-biological, inorganic materials.

In contrast, in the past years cryo-HAADF STEM tomography has been used for the imaging of inorganic samples such as catalysts and battery materials, making use of the lack of diffraction contrast for more accurate reconstructions [111-113]. Koneti *et al.* [113] shows the limitations of bright field imaging for the (dry) electron tomography of palladium nanoparticles on an α-$Al_2O_3$ grain (used as a case study sample), where the diffraction contrast present in bright field images lead to some nanoparticles missing from a bright field tomogram, while being present in a HAADF STEM tomogram (see Figure 2.15). Padgett *et al.* [114] used cryo-HAADF STEM electron tomography for the 3D analysis of platinum nanoparticle catalysts on a carbon porous support, with the sample being cooled down with liquid nitrogen to cryogenic conditions to prevent sample damage. In this case HAADF STEM electron tomography is needed for the 3D analysis of the sample to visualise the position of the catalytic nanoparticles on and within the support material. HAADF STEM allowed for accurate imaging of the nanoparticles without interference from diffraction contrast.

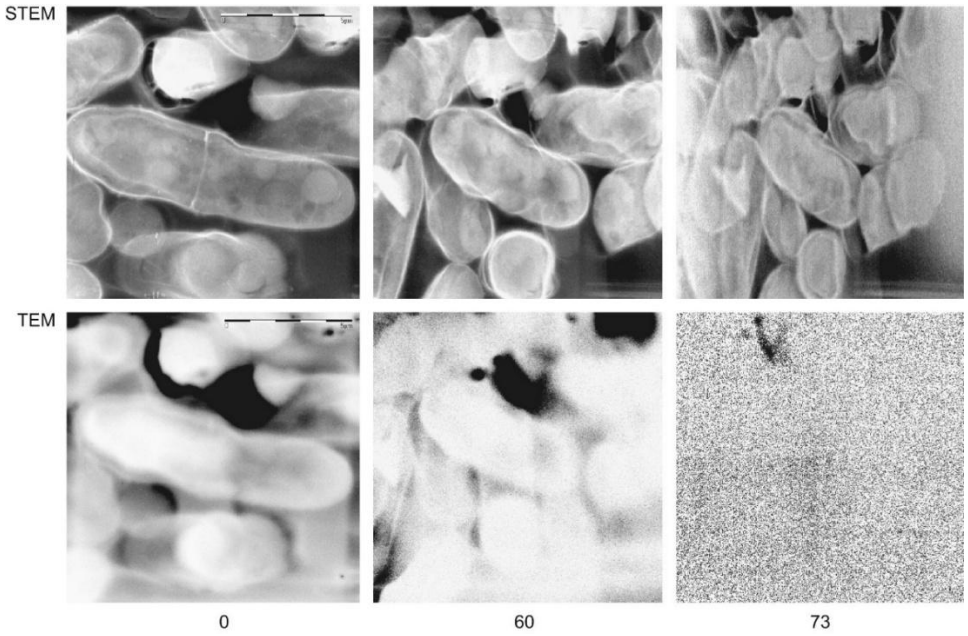


***Figure 2.14 –*** *Cryo-STEM and cryo-TEM imaging of a 1 µm thick yeast cell sample at different tilt angles. Scalebars above the images represent a 5 µm distance. Tilt angle for the images is shown on the bottom of each column. Figure from Aoyama et al. [104].*

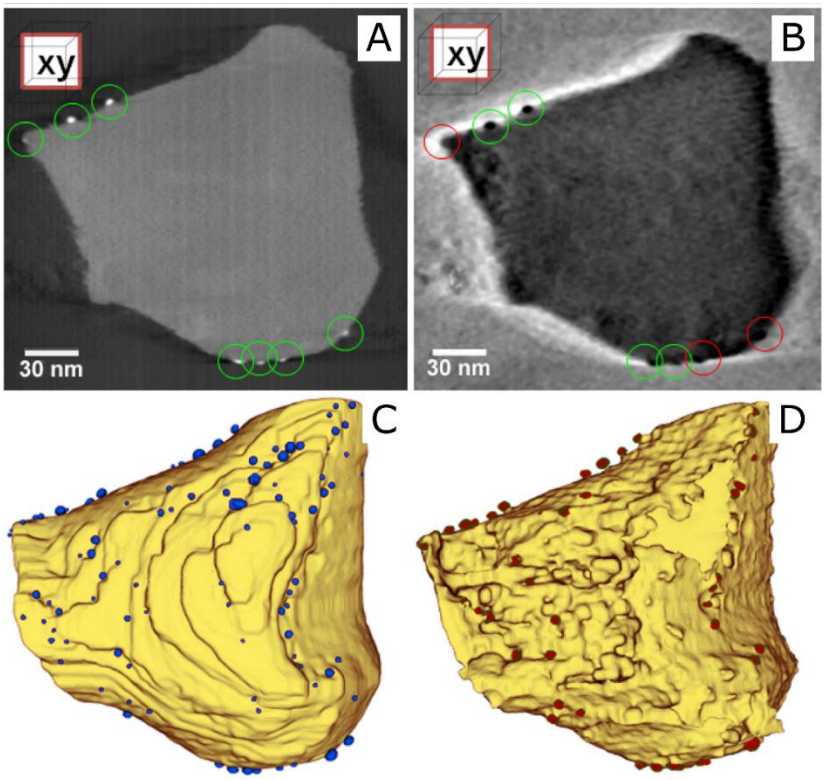


***Figure 2.15 –*** *Sections and surfaces of tomograms reconstructed using bright field STEM versus HAADF STEM. A) and B) tomogram sections in a sample imaged in (A)*

*HAADF STEM mode and (B) bright field STEM. Visible Pd NPs are circled in green. Some NPs are not visible in the bight field STEM section (circled in red). C) and D) segmented tomogram surface for the (C) HAADF STEM and (D) bright field STEM modes. Diffraction contrast in the bright field STEM results in the NPs being more difficult to distinguish from the α-$Al_2O_3$ grain. Image modified from Koneti et al. [113].*

Despite the recent improvements to cryo-HAADF STEM imaging with ET in materials science, this technique is still relatively novel and has only been applied to few materials, with cryo-techniques often being used to cool down the samples to prevent damage, rather than being applied to hydrated samples. There is potential in the segmentation of 3D volumes collected in cryo-HAADF STEM using the elemental analysis techniques available to STEM imaging (i.e. EELS and EDX). Moreover, high-resolution capabilities are missing from cryo-STEM tomography in materials science. Subtomogram averaging is used in biological samples to increase the resolution of tomograms for samples containing similar structures but is unfortunately unavailable for the reconstruction of many nanoparticle systems. Future improvements in imaging equipment and image processing might allow for sub-nanometre resolution cryo-tomograms.

### 2.3.3 Cryo-FIB-SEM and Transfer to the cryo-TEM

Cryo-TEM provides excellent imaging resolution for aqueous and biological samples and is routinely used in the life sciences to obtain images and 3D models with sub-nanometre resolution. However, TEM requires samples to be thin enough for the electrons to transmit through the sample for an image to be formed, which greatly limits the range of samples suitable for cryo-TEM imaging. The high-resolution imaging of large volumes of aqueous samples has been routinely performed using sample fixation in paraffin or cryofixation, which allows for imaging of thin slices in an SEM using ultramicrotomy, which consists in the sectioning of solid samples using a diamond knife [32, 115]. Ultramicrotomy is a staple for the preparation of thin biological samples for TEM imaging that would otherwise be too large for plunge-freezing (e.g. cells and tissue samples, which would not fit within a ~200 nm thick ice layer), but has also seen use in materials science for the section of soft materials such as polymers

[32, 116]. A study by Denk and Horstmann [117] pioneered the use of an ultramicrotome within an SEM, allowing for the serial sectioning and imaging of resin embedded samples. This process, named serial block face ultramicrotomy, allows for the collection of 3D microscopy data of volumes much larger than those accessible through tilt tomography or single particle reconstruction in TEM samples (see Chapter 3 for more detail on tomographic techniques). Unlike tilt tomography which needs several sample slices to obtain 3D reconstructions of thick samples, serial block face ultramicrotomy allows for the 3D analysis of much larger volumes in a single session [117]. This technique has since been used for the 3D analysis of dry embedded samples in materials science, and also cryogenically frozen hydrated samples (i.e. cryo-ultramicrotomy) where the 3D imaging is done inside [116] or outside [118] of the cryo-SEM.

As an alternative to cryo-ultramicrotomy, focused ion milling has been observed by Marko *et al.* [119] to not induce devitrification of the sample using plunge-frozen water samples with 200 nm polystyrene latex sphere to help maintain a uniform frozen layer. Ice devitrification was observed using electron diffraction in a cryo-TEM as the sample was heated; devitrification was not observed in the sample after FIB-milling of the ice. The lack of heat-induced devitrification of ice by FIB-milling therefore allows for the preparation of thin sample slices (200-150 nm) from bulk cryogenically frozen samples. This “cryo-FIB thinning” technique has been since used successfully to image cells, and tissue samples within cryo-SEM [120-122]. (Cryo-) ultramicrotomy requires extensive sample preparation before sectioning and can only be used on soft samples, limiting its use for harder materials such as metals, ceramics and bone [123]. On the other hand, FIB-milling can be applied to a much larger range of materials, and allows for thinner slices (2-20 nm against 30-50 nm for ultramicrotome slices). Despite this, ultramicrotomy finds uses for the sectioning of larger samples due to the larger sample volume available for ultramicrotomy [124].

FIB-milling has been used on frozen hydrated samples for block face serial milling of samples larger than what would normally be suitable for cryo-TEM or X-ray tomography. The development of automated FIB-milling and SEM scanning procedure has allowed for the collection of large volume data for the 3D analysis of biological samples such as cells [81, 125]. As such, FIB-milling is not only useful for cross-sectional imaging and preparation of sample slices, but also finds use in 3D imaging.

Schertel *et al.* [125] shows the application of serial block face imaging using FIB-milling on high pressure frozen samples of mouse optic nerves and dormant *Bacillus subtilis* spores. Cryo-FIB-SEM was pivotal in allowing the imaging of dormant spored, which would otherwise be activated during the chemical fixation process. Overall, Schertel *et al.* [125] found that serial block face milling using FIB was suitable for the high resolution imaging of samples that require staying hydrated (or are in any way unsuitable for chemical fixation) while providing a fast method for the analysis of substantially large volumes (when compared to the capabilities of cryo-TEM tomography) without the need of further processing steps after freezing. Spehner *et al.* [126] used serial block face imaging for the acquisition of 3D data on high pressure frozen protein samples, using gold labelling identify the position of the proteins. Spehner *et al.* [126] shows the suitability of this technique for the imaging of proteins in a cellular context due to the ability of cryo-FIB-SEM serial block face imaging to analyse larger volumes than what is normally possible with cryo-TEM, especially with the added use of image processing algorithms to denoise the images and remove artefacts.

The ability to thin bulk frozen samples to lamellae with less than 200 nm thickness has opened the possibility to prepare these samples for TEM cryo-imaging and cryo-electron tomography, thus uniting the bulk sample preparation ability of cryo-SEM with the high spatial resolution of TEM. Marko *et al.* [127] successfully showed the viability of this characterisation process applied to plunge-frozen *E. coli* cells. The study showed the ability of FIB milling a cell sample to a size suitable for low-dose cryo-TEM imaging and cryo-tomography without the need for adjusting the electron dose to accommodate for thick samples [127].

This process has since been applied to a range of biological samples and has evolved to prepare samples of varying sizes. Initial “on-grid” thinning procedures such as those shown in Marko *et al.* [119, 127] consist of the thinning of plunge-frozen samples on a TEM grid without removing the thinned section (Figure 1.15A). Although this process created a sample that is readily loaded into a TEM, it also requires for the sample to be suitable for plunge-freezing, which is only applicable to smaller samples such as bacteria and small cells.

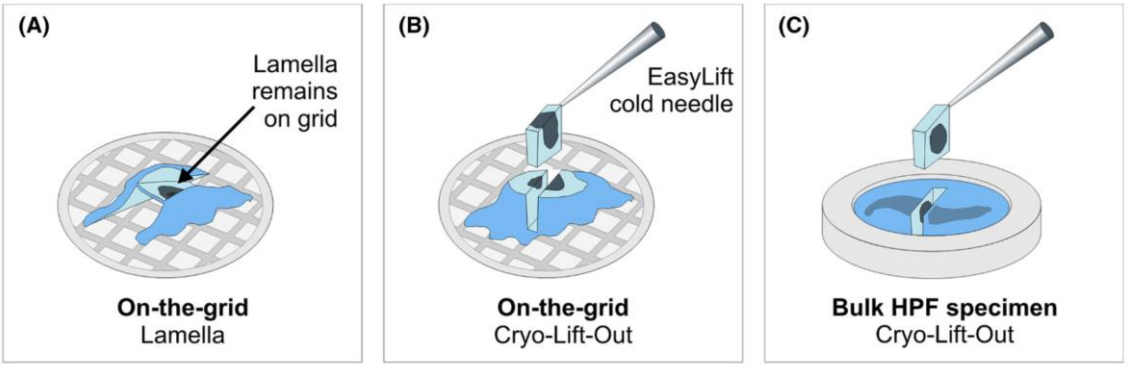


***Figure 2.16 -*** *Schematic showing different strategies for FIB milling a sample for cryo-TEM. "On-grid" thinning as shown in (A) is limited to smaller samples that can be plunge-frozen, while bulk in situ thinning followed by lift-out can be applied to samples of any size, thus allowing thinning of both samples on a TEM grid (B) and bulk frozen samples (C). Image from Kuba et al. [128].*

*In situ* FIB thinning and subsequent lamella lift-out has been routinely used in materials science for the TEM analysis of room-temperature samples and was recognised as an alternative thinning process for cryogenically frozen samples [129]. The lift-out of frozen lamellae has been made possible in studies by Parmenter *et al.* [130-132] with the use of cryo-manipulators to physically move the lamella onto a TEM grid (Figure 2.16-B and Figure 2.16-C, showing the lift out of the FIB-milled lamella from on-grid samples and bulk-frozen samples). In the past decade, efforts have been made to streamline the cryo lift-out process by producing detailed methodologies and by creating bespoke equipment to facilitate the lift-out and transfer of the frozen lamella [132].

In recent years, cryo lift-out has seen used successfully for the imaging of both biological and inorganic samples. Zens *et al.* [133] and Kuba *et al.* [128] both show the use of confocal microscopy for the imaging of the bulk sample before lamella preparation correlative targeting to identify areas of interest in the sample. This approach allows for straightforward identification of areas for FIB milling, therefore reducing the time needed to identify areas with sufficient concentration of the sample without additional information that are suitable for further imaging. In both Zens *et al.* [133] and Kuba *et al.* [128], areas were chosen to then perform cryo-electron tomography. Cryo lift-out has been used to obtain high-resolution tilt series

reconstructions of tissue samples as shown by Schaffer et al. [134], where cryo-lift out was used for the preparation of a lamella of a *C. elegans* tissue sample. Figure 2.17 shows the results of this study including slices of the reconstructed tomogram, which was obtained with images collected with an image pixel resolution below 1 nm [134].

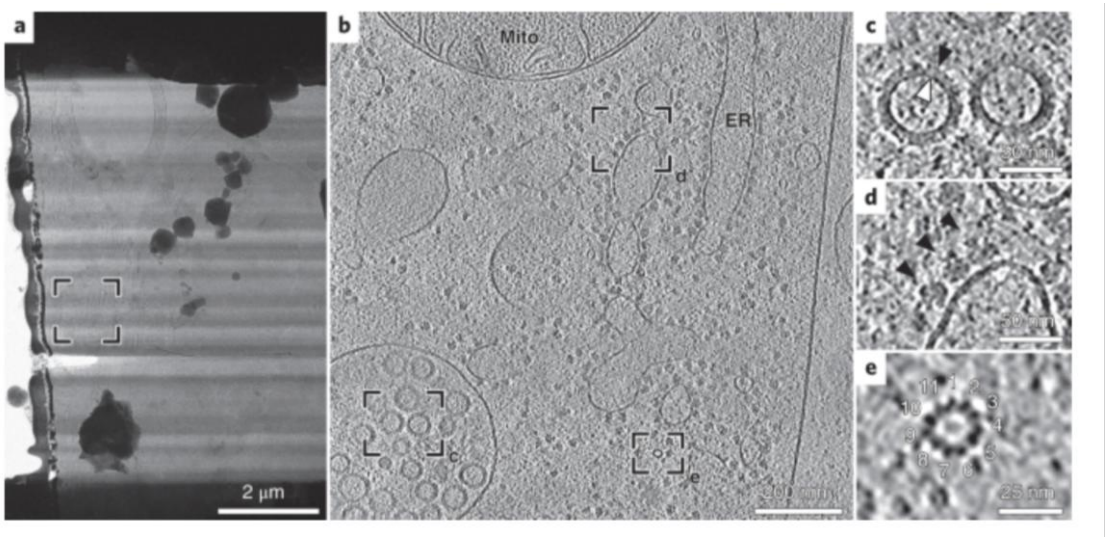


***Figure 2.17 -*** *Cryo-TEM image of a lamella after a successful lift-out and cryo-ET of a region in the lamella.(A) Frozen lamella containing C. elegans tissue and tomogram slices (B, C, D) of a selected region in the lamella [134]. The TEM image in (A) also shows some standard artefacts associated with cryo lift-out, namely curtaining as a result of FIB milling, and the presence of frost on the lamella surface.*

Cryo lift-out can also be used for the imaging of inorganic samples when a thin sample section is needed. Long *et al.* [135] shows the application of the cryo lift-out method for cryo-STEM imaging of the solid-electrolyte interphase in a liquid electrolyte sample [135]. It is important to note, however, that despite the advancements in the approaches for cryo lift-out, there are challenges associated with this procedure. Sample preparation and imaging are often a day-long procedure and cannot be repeated often as the SEM stage and cryo-manipulator need to be kept at cryogenic temperatures. Issues remain in the transfer process itself, as frost can accumulate on the sample while it is being loaded, covering up part of the lamella. Efforts have been made to reduce these issues by increasing the number of lamellae that can be delivered per transfer [136], while further efforts can be made using bespoke

equipment to keep the sample under a vacuum in cryogenic conditions during transfer, though in both cases specialised equipment is needed.

## 2.4 Summary

There is a need for the representative characterisation of nano-sized soft materials (e.g. nanoparticle dispersions and Pickering emulsions), as the properties of these materials in their native hydrated state are indicative of their performance. Among the characterisation techniques needed for proper sample analysis, high-resolution imaging using electron microscopy is important for the imaging of the size and shape of nanomaterials. Despite its usefulness, imaging using conventional electron microscopy is often problematic when applied to soft matter samples such as Pickering emulsions due to the need for sample drying, which disrupts the sample structure, making imaging no longer representative.

Cryo-EM has significant use in biological fields as it allows for imaging of hydrated frozen materials without disrupting the native sample structure and is currently being used increasingly often in material science together with HAADF STEM to improve the contrast of particles with high atomic numbers. A variety of cryo-EM techniques have been developed by taking from pre-existing techniques within materials science and biological fields to allow for the imaging of increasingly large samples at increasingly higher resolutions. Cryo-electron (tilt) tomography in TEM and serial sectioning using either cryo-ultramicrotomy or FIB-milling in a cryo-SEM allow for the 3D imaging of different ranges of sample volumes. Meanwhile, cryo-STEM can be used for the imaging of relatively thick samples and allows for the use of spectroscopy techniques for quantitative elemental analysis. Cryo-HAADF STEM tomography and spectroscopic analysis of frozen hydrated samples is however rarely seen and could be useful for the 3D imaging and tracking of nanomaterials such as Pickering emulsions, where the imaging of nanoparticle stabilisers on the droplet’s surface is an indicator of sample stability and performance.

## 2.5 Project Aims and Objectives

The aim of this thesis is to undertake the native state characterisation of Pickering emulsions using cryogenic electron microscopy (Cryo-EM) techniques. The application of cryo-EM imaging, elemental analysis and tomography will serve to bridge the gap between the cryo-EM imaging techniques found in the life sciences and the characterisation techniques routinely employed for the analysis of inorganic samples. This will result in the high-resolution imaging of Pickering emulsion stabilising particles and droplets of different size in 2D and 3D without the need for sample staining to visualise the different structures in the sample. Additionally, the project aims to explore 3D imaging and analysis using electron tomography in cryo-STEM and “slice and view” in cryo-FIB-SEM to accurately image the droplet shape and position of sample particles in 3D space. Native state characterisation of these systems in the liquid environment is essential to extract information on the position, size, and shape of particles in 3D space, which link to the performance of the materials.

The objectives for this project are:

- To use test systems to develop the application of cryogenic imaging techniques including plunge-freezing, cryo-TEM and cryo-SEM imaging, EDX, EELS, tilt tomography and the combination of elemental analysis techniques together with tilt tomography. A zinc oxide nanoparticle system, a gold nanoparticle system, and a titanium dioxide nanoparticle system are used as case studies to test these techniques.
- To image a Pickering emulsion sample with cryo-(S)TEM and cryo-SEM, confirming whether it is possible to obtain representative images of the sample.
- To apply EDX and EELS as elemental analysis techniques to the cryogenically frozen Pickering emulsion sample.
- To use tomographic techniques to observe the 3D structure of the droplets/Pt-NPs. Tilt tomography is used in STEM HAADF mode in cryo-TEM, while “slice and view” using FIB-milling is used for the collection of a slice image stack in cryo-SEM.
- To use elemental analysis techniques together with tomographic techniques to obtain 3D elemental data of the emulsion samples, thus allowing for the visualisation of the oil and water phases in 3D.

- To apply the abovementioned characterisation techniques to Pickering emulsion samples with large droplet sizes by preparing the sample in a cryo-FIB-SEM, then using FIB-milling to prepare a frozen sample lamella that will be lifted out and transferred to a cryo-TEM.

# Chapter 3 Materials and Methods

This chapter contains the preparation methods for the systems analysed in this study, an explanation of the equipment used, and the techniques and protocols used to characterise the samples. Four different types of systems and their preparation methods are presented in this chapter: Pickering emulsions, zinc oxide nanoparticles, titanium dioxide particles, and gold core-satellite nanoparticles. Chapter 5 and Chapter 6 will focus on the analysis of the Pickering emulsions, while the remaining three systems were used to test the characterisation methods to be applied to the Pickering emulsion systems (Chapter 4). Further background information on these case study systems will be provided in Chapter 4.

These systems were analysed using the following characterisation methods: general bulk sample size analysis was carried out using dynamic light scattering (DLS). Sample imaging was carried out using transmission electron microscopy (TEM), cryogenic transmission electron microscopy (cryo-TEM), and cryogenic scanning electron microscopy (cryo-SEM). Elemental analysis of the sample was performed using energy dispersive X-ray spectroscopy (EDX) and electron energy loss spectroscopy (EELS). 3D datasets were collected using “slice and view” cryo-FIB-SEM tomography and by reconstructing tilt series collected in cryo-TEM. This chapter will cover the background for these techniques and how they were used.

## 3.1 Nanoparticle-based systems

### 3.1.1 Pickering Emulsions

Two similar Pickering emulsions were examined in this work: a sunflower oil-in-water emulsion stabilised by 3-5 nm diameter platinum nanoparticles (Pt-NPs), and a hexadecane-in-water emulsion stabilised by the same 3-5 nm Pt-NPs. The two oils used in these emulsions have broadly similar properties as far as their behaviour is concerned and are therefore used interchangeably as the focus of this work is the characterisation procedure. The droplets in these two samples are typically < 1 μm. An additional hexadecane-in-water Pickering emulsion stabilised by 3-5 nm Pt-NPs sample with droplet size >1 μm was prepared for analysis using cryo-SEM and for the cryo lift-out procedure. These emulsions were prepared by Cheng Cheng and Dr

James Hitchcock from the research group of Dr Olivier Cayre, in the School of Chemical and Process Engineering, University of Leeds.

- The sunflower oil emulsion was prepared by first hand-shaking a 20 mL sample tube containing 2 mL of oil and 8 mL of the pre-prepared Pt-NPs aqueous suspension.
- The emulsion was then immediately prepared using a sonic dismembrator ultrasonic processor (Fisher Scientific) for 1 min (40% amplitude) in a large water bath (at room temperature) to avoid dramatic increase of the sample temperature.
- The hexadecane emulsion was prepared by hand-shaking a 10 mL sample tube containing 20 µL of hexadecane oil and 4.98 mL of Pt-NPs in suspension. This resulted in an emulsion with 0.04 vol% oil concentration.
- The same Pt-NPs were used in both samples and were synthesised by the reduction of platinum salt in the presence of a reducing agent at room temperature as detailed in Hitchcock *et al.* [40].
- A gold metal shell was deposited onto the Pickering emulsion droplets to form metal capsules by adding the sunflower oil-in-water Pickering emulsion solution to the following gold plating solution; 1 mL PVP solution (0.2 wt%), 10 mL of Milli-Q water, 2 mL of 12 mM gold salt (HAuCl4) and 1 mL of $H_2O_2$ (60 mM).
- The samples were then agitated on the carousel for 30 min. Capsules were then allowed to settle under gravity for 24 h and were subsequently washed by removal and replacement of the supernatant with Milli-Q water, as detailed in Hitchcock *et al.* [40].

### 3.1.2 Zinc Oxide Nanoparticles

Two zinc oxide (ZnO) nanoparticle dispersions were prepared using commercially available NanoGard Zinc Oxide nanoparticles without surfactants (Alfa Aesar, lot number 44898), with concentrations of 0.1 mg/mL and 1.0 mg/mL following the methods of Wallace [137]. The samples were sonicated for 15 minutes after the dispersions were prepared. These two concentrations were prepared to test the sample concentration necessary to guarantee the presence of nanoparticles during cryo-TEM imaging. Both samples were prepared using the methods in Table 3.1.

Before sample preparation the dispersions were sonicated for 15 minutes, while the TEM grids used were plasma cleaned for 20 seconds.

***Table 3.1 –*** *Description of the preparation methods for the ZnO NP samples. All TEM grids were plasma cleaned for 20 seconds before sample preparation. The ZnO samples were sonicated for 15 minutes prior to beginning each the preparation procedure.*

| Sample | Preparation Procedure | Additional Notes |
|---|---|---|
| Drop-cast | A 3.5 µL drop of sample was dropped on a continuous carbon TEM grid on top of filter paper. | Standard TEM sample preparation procedure for TEM imaging of nanoparticle dispersions. |
| Drop-cast and air dried | A 3.5 µL drop of sample was dropped on a continuous carbon TEM grid held by tweezers and allowed to dry naturally. | This procedure prevented any of the sample in the drop from being lost to the filter paper. |
| Blotted and dried | A 3.5 µL drop of sample was added to a continuous carbon TEM grid in a Vitrobot, then blotted and allowed to dry naturally. | This follows the blotting and plunge-freezing procedure used for the preparation of cryo-TEM samples without cryogenically freezing the sample to allow for standard TEM imaging. |
| Plunge-frozen and vacuum-dried | A 3.5 µL drop of sample was plunge-frozen in a Vitrobot and then dried using a high vacuum. | As detailed in section 3.2.5.2 Plunge-Freezing and Vacuum-Drying. |
| Plunge-frozen | A 3.5 µL drop of sample was plunge-frozen in a Vitrobot. | as detailed in the section 3.2.5.1 Plunge-Freezing. |
| Frozen for cryo-FIB-SEM | The samples for cryo-FIB-SEM were prepared by plunging the sample in slush nitrogen. | as detailed in the section 3.2.6.1 Cryo-SEM Sample Preparation. |

### 3.1.3 Titanium Dioxide System

The titanium dioxide ($TiO_2$) system analysed in this study was prepared by Dr Teresa Roncal-Herrero and Hafis Mehraliyev from the research group of Professor Andy Brown, in the School of Chemical and Process Engineering, University of Leeds. A stock solution of 1 mg/ml fg-$TiO_2$ (untreated food-grade $TiO_2$ powder, supplied by AgResearch Limited) in Milli-Q water was prepared and subsequently used to produce dispersions of 100 µg/ml $TiO_2$ in a Gibco Dulbecco's Modified Eagle's Medium (DMEM) cell culture media (Thermo Fisher Scientific). The pH of the dispersion was measured to be pH = 6.8 immediately after mixing. After mixing, the $TiO_2$ – DMEM dispersion was sonicated for ~ 2 hours until the pH of the solution was pH = 8.0 (for the first sample) and pH = 7.8 (for the second sample).

After sonication, the samples were cryo-prepared via plunge-freezing onto lacey carbon TEM grids using a Vitrobot, using the plunge-freezing process detailed in section 3.2.5.1 "Plunge-Freezing".

### 3.1.4 Gold core-satellite nanoparticles

The gold core-satellite nanoparticles (Au-NPs) were prepared by Dr Darshita Budhadev from the research group of Professor Dejian Zhou, as described in Budhadev *et al.* [138] and Basaran *et al.* [139]. Au-NP-glycans (nanoparticles capped with the α-1-mannose-α-1,2-mannose glycan ligands) were prepared by incubation of a 5 nm citrate stabilized Au-NPs with DHLA-glycan ligands in water for 24 h to complete the GNP glycosylation via self-assembly. Any free unbound ligands were removed by ultrafiltration using 30K MWCO filter tubes and washing with pure water. The LA–EG 4–DiMan ligand was synthesised by Cu-catalysed click chemistry between a LA–EG4–acetylene linker and N 3–EG2–DiMan and purified by using a P2 biogel column. The constructed DC-SIGN and DC-SIGNR were expressed, purified by affinity column chromatography, and then site-specifically labelled with maleimide modified Atto-643. The samples were then cryo-prepared using plunge-freezing for cryo-(S)TEM imaging as detailed in section 3.2.5.1 "Plunge-Freezing".

The gold core-satellite system consists of ~5 nm and ~10 nm Au-NPs. The surface modification of the Au-NPs ensured that the larger (~10 nm) NPs would be surrounded by a number of smaller Au-NPs (~5 nm), in a "core-satellite" formation.

### 3.1.5 General characterisation using Dynamic Light Scattering

General bulk sample characterisation was performed using dynamic light scattering (DLS). DLS is based on two principles related to colloids: light scattering off the particles (Tyndall effect) and Brownian motion of the particles. In a DLS setup, a laser source is pointed at the liquid sample within a cuvette. The particles will scatter the coherent monochromatic light, which is then collected by a detector (Figure 3.1). As the particles move randomly (Brownian motion), the relative intensity of the scattered light will vary with time. A normalised autocorrelation function can be obtained by taking the scattered intensity at an arbitrary time I(t) and the intensity after a delay time τ as I(t+τ), which can give us quantitative information on the time scale of the intensity fluctuations. The decay time of the correlation function will depend on particle size, therefore allowing to quantitatively measure the hydrodynamic radius of colloidal particles and aggregates [140].

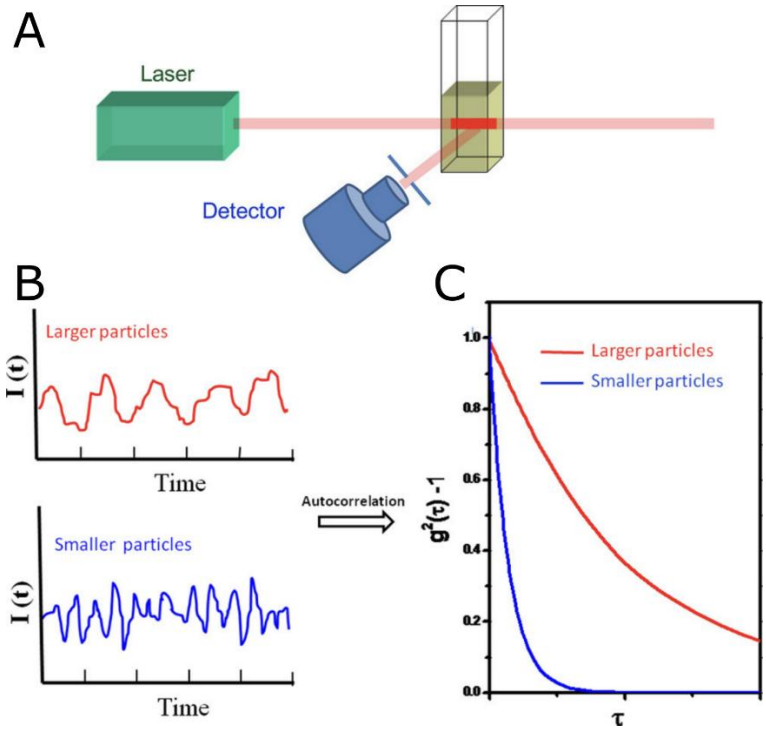


**Figure 3.1 –** *Simplified schematic of a DLS setup. A) simplified DLS setup, where a laser is pointed at a sample within a cuvette. The scattered light is then collected by a detector after passing through a polariser. B) Changes in the intensity of the scatted light depending on particle size. C) Autocorrelation function resulting from the intensity fluctuations in (B). Schematics taken and modified from Hassan et al. [140].*

Within this work, for sub-micron emulsion droplets and nanoparticle dispersions, a NanoSeries Zetasiser (Malvern Nano-ZS) (DLS) fitted with a He-Ne laser source (633nm wavelength, 4mW power) was used to measure emulsion droplets in suspension. 4 repeats were collected per sample and analysed using the DTS Nano software. For emulsion droplets larger than 1μm, droplet size distribution was measured using the Benchtop C70 Series FlowCAM imaging flow cytometry instrument used in AutoImage mode using a 20x objective, FC50 flow cell in a reverse flow configuration.

## 3.2 Electron Microscopy

The instruments and methods used for electron microscopy will be discussed here, including cryogenic electron microscopy, spectroscopic techniques, and tomography. The standard sample preparation methods used within this thesis are also described here.

### 3.2.1 Transmission Electron Microscopy

Transmission electron microscopy (TEM) is one of the techniques of choice for imaging samples at the nanometre level as it can reach resolutions down to the angstrom and sub-angstrom level [87]. One of the main limiting factors for the imaging of smaller samples is the microscope resolution:

$$d = \frac{\lambda}{2NA} \tag{3.1}$$

Where:

$d$ Is the minimum resolvable distance

$\lambda$ Is the incident wavelength used to characterise the sample

$NA$ Is the numerical aperture of the microscope

From Equation (3.1), it can be seen that a decrease in the wavelength of the incident rays will allow for imaging at better resolutions. By using electrons in the imaging beam electron microscopy (EM) allows for high-resolution imaging by increasing the energy

of the incident electron beam therefore decreasing the electron wavelength. A TEM operating at an accelerating voltage of 200-300 kV will result in electrons with a wavelength of approximately 0.0020-0.0030 nm using the de Broglie relation between the momentum and wavelength of the electron. Using (3.1, for a TEM with an assumed numerical aperture of 0.1, these electron wavelength would correspond to a resolving power of ~0.1 nm. However, this is not seen in practice due to aberrations caused by the magnetic lenses used in EM [141, 142]. TEM, specifically, consists of an electron beam transmitted through a sample, with the forward scattered electrons being then collected by an electron detector.

Generally, a TEM setup contains various components, described here from the top of the TEM column (and visualised in the schematic in Figure 3.2-A) [142, 143]:

- The electron gun, which generates the electron beam;
- Lenses (condenser and objective) to focus the beam;
- Apertures;
- Sample stage, where a sample is inserted using a TEM sample holder;
- The plate or electron detector, where the image is formed.

The entire column is kept under a high vacuum ($10^{-4}$–$10^{-5}$ Pa) to prevent interactions between the electrons and objects other than the sample (e.g. atoms in the air).

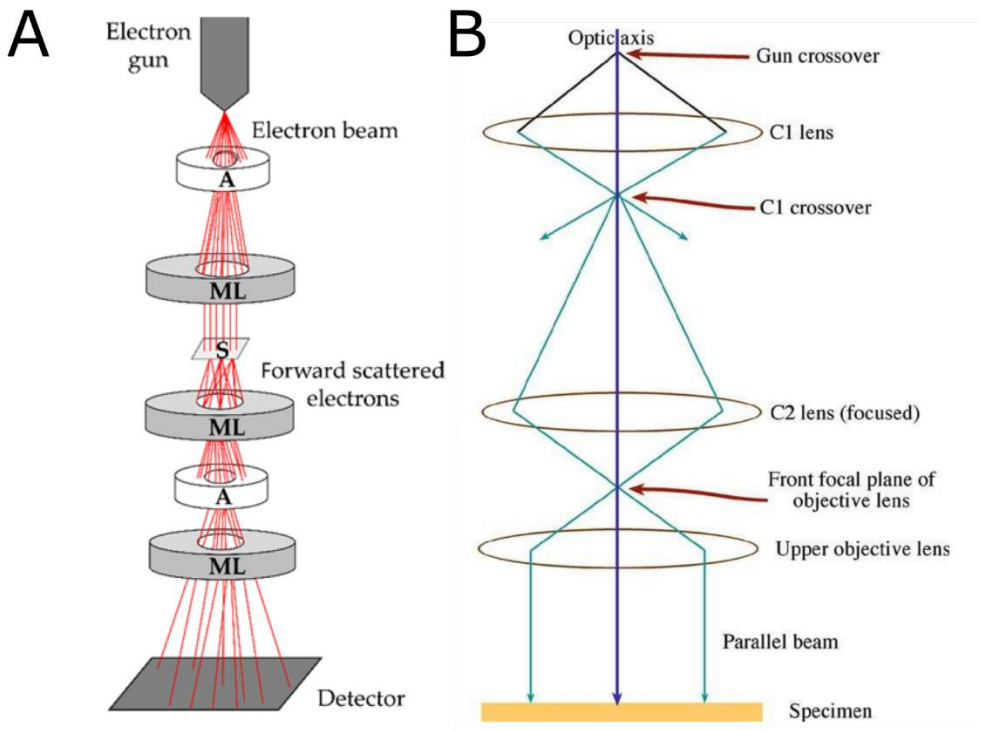


***Figure 3.2 –*** *Schematic diagrams for (A) a transmission electron microscope and (B) the parallel beam operation in a TEM. A: aperture, ML: magnetic lens, S: sample. (A) From Malenica et al. [144], (B) from Williams and Carter [142].*

In conventional TEM operation a parallel beam is formed at the sample plane (as seen in Figure 3.2-B), with electrons simultaneously irradiating a large sample area to form an image. The electron beam can be converged to form an electron probe, which can be used to localise the signals coming from the sample. With the beam focused to make a probe, the probe must be scanned across the sample to create a useful image. Sample imaging using this imaging mode is called scanning transmission electron microscopy (STEM). Unlike parallel beam TEM where apertures are used to create bright field and dark field images, STEM uses different detectors located at different scattering angles; these are the bright field detector, the annular dark field detector (ADF), and the high angle annular dark field detector (HAADF), as shown in *Figure 3.3*. This setup allows for most of the electrons scattered at high angles to be detected by the ADF or HAADF detectors, contributing to a high SNR that can be useful for the imaging of samples that are too thick for parallel beam TEM [142].

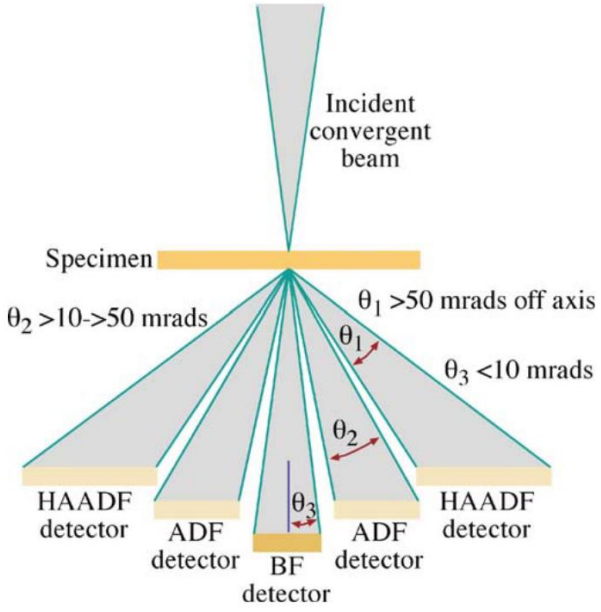


***Figure 3.3 –*** *Schematic of the detector setup during STEM imaging. The BF and ADF detectors collect electrons at smaller scattered angles ($\theta_3$ and $\theta_2$), while the HAADF detectors collect electrons at high scattering angles ($\theta_1$ > 50 mrads). Schematic from Williams and Carter [142].*

Contrast in TEM is given by the scattering of the incident beam. Two mechanisms can contribute to contrast in TEM: phase contrast (will not be discussed here due to its low impact on this work) and amplitude contrast. Amplitude contrast is the result of variations in the sample's mass and thickness and is divided into diffraction and atomic contrast. Diffraction contrast is generated by the electrons scattering when interacting with crystalline materials, resulting in a diffraction pattern formed from the constructive interference of electrons scattered at specific angles (Bragg angles) given by the crystalline structure of the sample:

$$n\lambda = 2d \sin\theta \quad (3.2)$$

Where:

- $n$ Is the diffraction order of the crystal structure
- $\lambda$ Is the wavelength
- $d$ Is the crystal lattice spacing
- $\theta$ Is the Bragg angle, the angle between the incident ray and the crystal plane which is required for constructive interference

Denser, thicker, or higher-mass areas of the sample will appear darker in bright field imaging (while appearing brighter in dark field), forming what is known as atomic contrast [142, 144]. Given the lack of diffraction contrast in non-crystalline samples, mass-thickness contrast becomes the main contrast mechanism for the imaging of polymers and biological samples. During conventional bright field TEM imaging, both atomic and diffraction contrast contribute to the final image, but changing operational parameters such as the collection angle can allow for greater contribution from one type of contrast.

High angle annular dark field (HAADF) imaging uses an ADF detector with an aperture angle of >50 mrad and is used to only collect Rutherford scattered electrons (angle change of the electrons due to interactions with the atoms in the sample, as opposed to the Bragg scattered electrons), therefore forming images that are greatly affected by atomic number [142]. This can be used to decrease diffraction contrast in the image when this would contribute negatively to image formation, making the sample difficult to visualise. In this thesis, HAADF STEM imaging was used to decrease diffraction contrast when imaging crystalline samples, but also to exploit atomic contrast when imaging samples with high atomic numbers such as the Pt-NPs in the Pickering emulsion samples. In this case, the high atomic number for platinum, together with the use of dark field imaging, allows for the collection of images where the small (3-5 nm) Pt-NPs are highly visible even at the low probe currents necessary to prevent sample damage.

The samples used in TEM must be thin enough to allow for the electrons to pass through for an image to be formed. This leads to a need to prepare the sample before imaging by cutting or milling the sample down to a thin enough slice [143] if the sample

is otherwise too thick (i.e. larger than approximately 200 nm, but dependent on the material). Further limitations to sample imaging are exist for aqueous samples (including nanoparticle dispersions, emulsions, and many biological samples), which cannot be imaged through conventional TEM due to the presence of a vacuum that causes the water to evaporate. It is therefore necessary to dry the samples before imaging, which may result in a change in structure or morphology, and thus limit the representative data that can be collected.

The high resolutions attainable using TEM are ideal for the imaging of small nanoparticles such as the 3-5 nm Pt-NPs present in the Pickering emulsions used in this work. Within this work, a FEI Titan Themis$^3$ TEM operated at 300 kV with a monochromator, multiple STEM detectors, Gatan One-View CCD, Super-X 4-detector silicon drift EDX system and a Gatan GIF Quantum 965 EELS was used. The monochromator allowed continuous beam current control in STEM when not excited and the X-FEG source provided an energy spread of ~1.1 eV (FWHM of zero loss peak) in this condition. STEM was run with a 1.4 Å probe diameter of 10 mrad convergence semi angle. HAADF images were collected over the scattering semi-angle range of 35-150 mrad. Probe currents were varied using the monochromator and ranged from 5–100 pA depending on the imaging and mapping mode.

### 3.2.2 Conventional TEM Sample preparation

Different sample preparation procedures exist for TEM samples depending on the nature of the sample, with the focus to deliver a thin, electron transparent and vacuum-resistant sample. In the context of non-magnetic nanomaterials such as nanoparticles and nanotubes, a sample drop (2–5 µl) can be applied to a TEM grid and dried. This approach, called drop-casting, requires the particles to be suspended in a liquid that can dry at room temperature, and is suitable for stable materials [85, 145, 146]. Soft materials such as hydrogels or emulsions cannot however retain their native structure after drying, and need alternative fixation methods such as freezing. Cryo-fixation methods will be discussed in more detail within section 3.2.5 “Cryogenic Electron Microscopy”.

Within this work, for conventional, dry TEM observations 3.5 µl of the Pickering emulsion suspension was deposited onto a lacey carbon film supported on 400 mesh

copper grids (EM Resolutions), 200 mesh continuous carbon film copper grids or SiNx grid (EM Resolutions), which were plasma cleaned for 20 seconds prior to sample deposition. SiNx grids were solely used for the (S)TEM imaging of dry Pickering emulsion samples. Copper grids with continuous carbon film were used for all other dry and PF-VD samples, while copper grids with lacey film were used for all plunge-frozen samples imaged in cryo-(S)TEM.

### 3.2.3 Energy Dispersive X-Ray Spectroscopy

Energy dispersive X-ray spectroscopy (EDX) is a spectroscopy technique used to obtain quantitative elemental information on the sample from X-rays emitted from the sample because of beam-sample interactions. When the TEM electron beam interacts with the atoms in the sample, the inner-shell electrons in can be ejected from the shell. This creates an electron vacancy which can be filled by a higher-energy electron from an outer shell. This decay process results in the emission of a characteristic X-ray with energy between the two energy levels. Since the difference in energy between levels is discrete and unique between atoms of different elements, it is possible to associate the energy of the X-rays detected with specific elemental compositions in the sample [147, 148].

In this study, EDX spectra were collected during (S)TEM imaging to obtain elemental information for a wide range of samples, as EDX allows to easily obtain signals from elements such as platinum and titanium without the need to increase the total electron fluence used (as is the case for obtaining signals for EEL edges at high energy loss values). Throughout this study, EDX and EELS were used as complementary elemental analysis techniques, as each technique will be more suitable to analyse specific elements in different sample conditions. EDX spectra were processed using VELOX and Hyperspy. The spectra acquisition and processing steps used are as follows, assuming the microscope is in STEM imaging mode:

1. An area of interest was identified;
2. An image of the area was collected using the VELOX software;
3. Using the VELOX software, an acquisition area for EDX was selected;
4. The image acquisition parameters were set depending on the sample to ensure a sufficiently high SNR without risking sample damage;

5. EDX spectra was continuously collected until sufficient signal was collected, or until the sample began being damaged;
6. Individual EDX spectra were processed using the VELOX software, adjusting the post-processing filters within the software to ensure the elemental maps are easily identifiable.

For the processing of EDX tilt series, the EDX spectra were processed using Hyperspy:

1. The spectra were loaded in Hyperspy:
2. The signal was rebinned to endure each pixel contains sufficient signal for elemental analysis and tomography reconstruction;
3. Signal decomposition was used to remove noise from the vitreous ice;
4. A model was created containing the elements that are needed for analysis, and was then applied to the spectra;
5. The background was removed and the signal from the analysed elements was used to create elemental maps.

### 3.2.4 Electron Energy Loss Spectroscopy

Electron energy loss spectroscopy (EELS) is a spectroscopic technique which is used to obtain elemental and structural information in a sample by measuring the loss of kinetic energy of the electrons transmitted through the sample [149, 150]. When an electron beam is incident on a sample the electrons will interact with the atoms and electrons in the sample in a variety of ways, with the inelastic scattering of the incident electrons being of interest for EELS. The distribution of all the inelastically scattered electrons provides information on the sample's atomic electrons, which is related to the chemical and physical properties, including quantitative and qualitative information on the elements present, electromagnetic properties, and molecular structure of the sample [149-151].

In a TEM-EELS setup, a thin sample is exposed to an electron beam which passes through the sample. A magnetic prism behind the image-viewing chamber allows for the creation of a uniform magnetic field that functions as a spectrometer that focuses and disperses the electrons according to their energy (see Figure 3.4) [149].

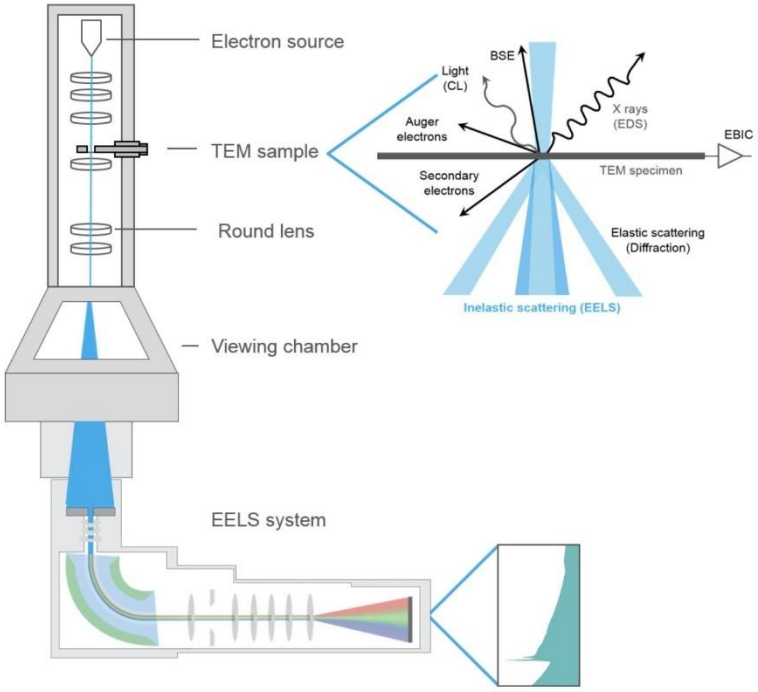


***Figure 3.4 –*** *Schematic of a TEM and EELS setup. As the electron beam passes through the TEM sample, the electrons interact with the sample. The electrons scattered inelastically are separated using a homogeneous magnetic field and then collected. The resulting data is a spectrum containing the electron counts detected at each energy loss. Diagram from Gatan [152].*

The typical EEL spectrum is shown in Figure 3.5 and is divided in two sections: the low-loss region (including electron energy losses up to ~50 eV) and the core-loss region (energy losses above ~50 eV).

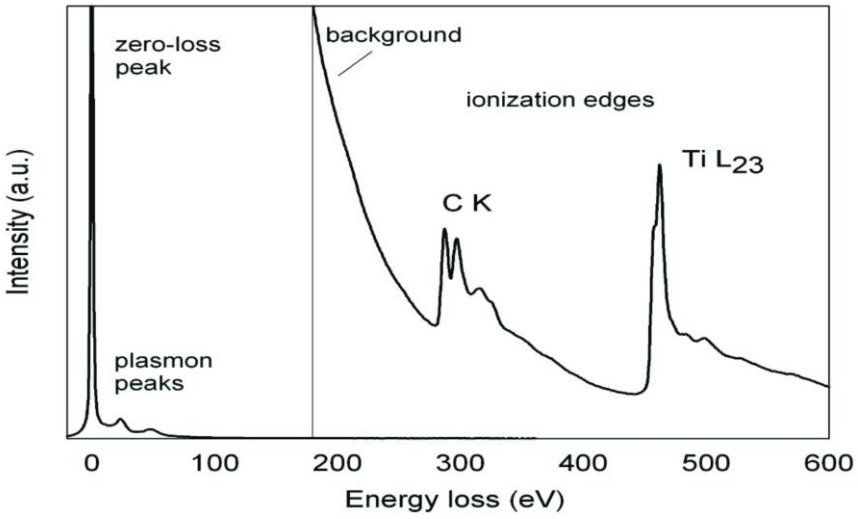


***Figure 3.5 –*** *EEL spectrum of a 20 nm thin titanium carbide sample. Several features can be seen within an EEL spectrum; the zero-loss peak and plasmon peaks are seen at low energy losses (the low-loss region), while at higher energy losses (the core-loss region) it is possible to obtain quantitative and qualitative elemental on the sample's elemental composition. Figure from Hofer et al. [149].*

The zero-loss peak within the low-loss region is comprised of electrons that have been scattered elastically, or with minimal energy loss and can be used to determine the relative (or absolute) sample thickness according to [153]:

$$\frac{t}{\lambda} = -\ln\left(I_0/I_t\right) \tag{3.3}$$

Where:

- t Is the sample thickness
- λ Is the inelastic mean free path of the sample
- $I_0$ Is the area under the zero-loss peak
- $I_t$ Is the total area under the energy-loss spectrum

The core-loss region of the spectrum is the most important for elemental analysis as it contains edges formed due to inner shell excitations of the sample atoms [151]. These edges allow for the extraction of quantitative and qualitative elemental information.

Due to the basic principle behind EELS being the collection of forward inelastically scattered electrons, this technique is especially sensitive to sample thickness and cannot yield quantitative data above particular thickness thresholds dependent on the sample's inelastic mean free path. Samples thinner than approximately 2-3 times the inelastic mean free path are needed to collect a low-loss EEL spectrum suitable for thickness estimation [154]. Additionally, elemental quantification ideally requires samples thinner than the inelastic mean free path to avoid multiple scattering.

In this study, STEM-EEL spectra were collected with a 20.2 mrad collection semi-angle to obtain information on sample thickness and to perform elemental analysis for the Pickering emulsion samples, as EELS allows to easily obtain information on the oxygen and carbon K-edges. EEL spectra were analysed using the Gatan DigitalMicrograph software and Hyperspy. The STEM-EEL spectra collection and processing steps used are as follows, assuming the microscope is set to STEM mode:

1. An area of interest was identified;
2. The DigitalMicrograph software was used to select the EELS detector and operate the Gatan Imaging Filter;
3. The probe was positioned over a hole in the sample to set up safe exposure time to prevent damage to the detectors;
4. The zero loss peak was centred and the beam was focused with the aid of the DigitalMicrograph software;
5. The SNR acquisition mode was selected to aid in the collection of weak signals due to added noise from the vitreous ice;
6. Energy loss, dispersion, exposure, and sum time were then fine-tuned for the given sample depending on the sample material and thickness;
7. The EEL low-loss and core-loss spectra were collected;
8. The spectra were loaded onto Hyperspy;
9. The zero loss peak was centred if found to not be properly centred;
10. Fourier-ratio deconvolution was applied;
11. A model was created including the elements that need to be analysed, and was then applied to the spectra;
12. Using the model results, the background was subtracted and the edge signal for the analysed elements was extracted and used to create elemental maps.

### 3.2.5 Cryogenic Electron Microscopy

Despite the high-resolution imaging possible through TEM, the 2-dimensional images obtained are not necessarily representative of the *in vivo* structural organisation of the sample. For conventional TEM and SEM imaging, the samples are dried in order to be compatible with the vacuum in the microscopes; this drying procedure not only limits the range of suitable samples but additionally induces drying artefacts and leads to the re-distribution of particulates [95, 155].

Cryogenic electron microscopy (cryo-EM) presents the opportunity to image wet samples (and including biological samples, colloidal suspensions and other soft materials) without the need for a drying procedure, by instead freezing the sample and thus retaining its 3D structure. Moreover, freezing the sample lowers the diffusion rate of particles within the sample, generally slowing down the rate of reactions [156], and allowing for the imaging of samples at specific steps along a reaction [155]. Samples for cryo-(S)TEM imaging must be thin enough to allow for the electrons to pass through the sample [143]. Plunge-freezing aqueous samples (Figure 3.6) allows for the preparation that is thin enough for TEM imaging through a blotting step, while preventing any possible structural change as a result of crystal formation by vitrifying the water in the sample by plunging it in liquid ethane [27, 87, 157].

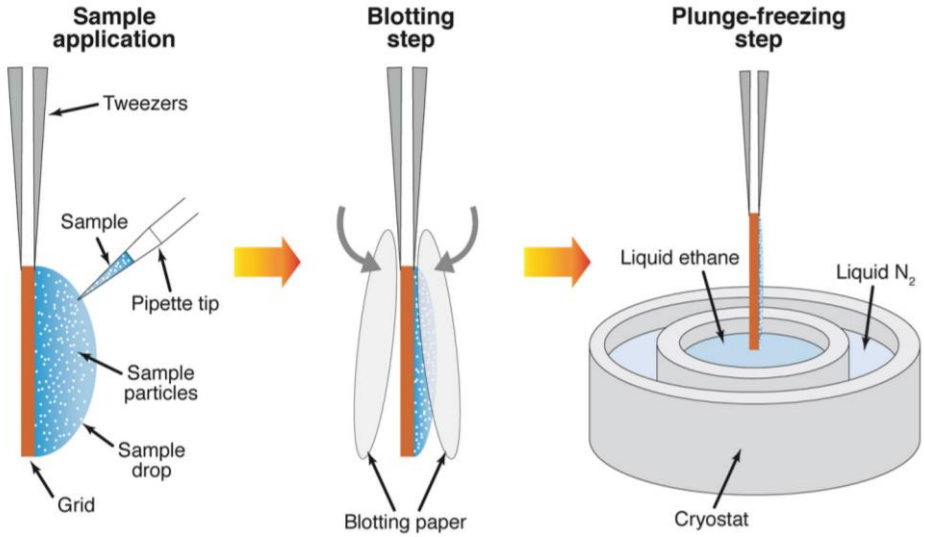


***Figure 3.6*** *– Blotting and Plunge-freezing steps for cryo-TEM preparation. Figure from Sgro and Costa [157].*

#### 3.2.5.1 Plunge-Freezing for cryo-(S)TEM

Cryogenic preparation can be used to retain the native sample structure, but depending on the freezing procedure used new artefacts can be introduced [75]. The most immediate issue that has to be addressed is the ice crystallinity, which affects cryo-TEM imaging due to the increase in the general difficulty to properly image the sample and diffraction contrast from the crystalline ice.

An problem has been indicated by Dubochet [27], as the formation of crystalline ice creates osmotic pressure which in turn leads to movement of particles in the solution and eventually phase segregation [88]. As crystalline ice dendrites form from nucleation sites, water molecules diffuse towards the forming crystal phase and are recruited in order to further grow the crystals. This movement of water molecules inevitably causes an increase in the concentration of the remaining liquid solution; in addition, salts and other particles will be displaced away from the crystalline phase until the crystallisation process is terminated [27]. The resulting structure is comprised of crystalline ice and regions with concentrated particles; such result is not only undesirable for biological samples [27], but also damaging for inorganic samples as the concentration, shape and size of particle agglomerates will be affected.

It is therefore necessary to fully vitrify the ice to prevent the formation of crystals. For vitrification, the water needs to be cooled rapidly to avoid the nucleation and eventual growth of ice crystals. Vitreous ice is metastable, being prone to forming cubic ice crystals on warming [27]; frozen samples therefore need to be continuously kept at low temperatures during storage, transport procedures, and during imaging as the sample is exposed to the electron beam in electron microscopes, as devitrification will occur if the sample is not kept below approximately -140°C [87]. High cooling rates can be achieved using a variety of techniques depending on the overall size of the volume frozen: two main techniques that have been applied to both organic and inorganic samples are plunge-freezing and high-pressure freezing [87, 88].

Therefore, cryogenically prepared samples for cryo-TEM must satisfy two main requirements:

- The sample must be thin (electron transparent).
- The ice must be vitreous.

Plunge-freezing is a cryo-preparation technique that satisfies both of these requirements by first blotting the sample using filter paper to ensure a thin liquid layer, and then quickly plunging the sample in liquid ethane (is cooled down by liquid nitrogen to approximately $-183$°C) to rapidly cool down the sample and avoiding crystallisation. The thinness of the sample after blotting together with the high heat capacity and boiling point of ethane allows for a much faster sample cooling rate compared to plunging in liquid nitrogen [87].

In this study, plunge-freezing was carried out using the following steps [87, 157], using a FEI Vitrobot© mark IV plunge freezer:

1. TEM grids were plasma cleaned for 20 seconds;
2. The Vitrobot chamber was prepared by lowering the chamber temperature to 12°C and adjusting the chamber humidity to 100%. This reduces evaporation, which is especially important after the blotting step as the liquid sample volume is decreased drastically compared to its surface area;
3. A 3.5 µl drop of sample was added to the TEM grid;
4. The liquid is blotted on both sides for 4 seconds with filter paper to create a thin liquid layer, allowing for the liquid to cool rapidly enough to vitrify (and additionally allowing to resolve the image in TEM);
5. The grid is quickly plunged into cooled down liquid ethane.
6. The grid was then quickly transferred into a Gatan 914 cryo-holder for TEM while maintaining the sample temperature below -170 °C to prevent devitrification. This was accomplished by leaving the grid submerged in liquid nitrogen.

Within this work, samples for cryo-(S)TEM imaging were plunge-frozen before being transferred to the TEM. The sample solution was deposited onto a lacey carbon film supported on 400 mesh copper grids (EM Resolutions) or onto a SiNx grid (EM Resolutions).

Beyond using a suitable freezing procedure and a cryo-compatible TEM, it is also important to take into account the type of TEM holder used. Cryo-holders used for cryo-TEM are capable of regulating the sample temperature using liquid nitrogen or liquid helium as a cryogen, and are needed to maintain the sample temperature below the glass transition temperature to prevent crystal formation. Three main aspects for

cryo-holders have to be taken into consideration for cryo-TEM electron tomography [158, 159]:

- Temperature control capability: the ability of the holder to maintain the sample at a given temperature. For this work, the cryo holder is required to maintain a temperature of -170°C to prevent vitrification [158].
- Holding time: the amount of time the holder is able to maintain a given temperature without any major fluctuations.
- Tilting capabilities. Tilt holders are required to tilt beyond 45° to reduce the severity of missing wedge artifacts following tilt tomography [159]. The Gatan 914 cryo-holder used in this work allows for a tilt range of ±60°C, suitable for tilt tomography.

#### 3.2.5.2 Plunge-Freezing and Vacuum-Drying

TEM can be used for the imaging of dried colloidal solutions to obtain particle size measurements. However, the conventional drop-casting technique for sample preparation cannot give a representative view of the sample structure due to drying artefacts [85, 160]. This is because, while primary particle size can still be measured after sample drying, agglomerate sizes cannot be accurately measured due to drying-induced agglomeration [161, 162]. Usually, particle sizing is confirmed using DLS, but it is reliant on knowledge of the refractive index of the sample and is not reliable for measuring wide particle size distributions. In these cases, neither DLS nor conventional TEM can guarantee the size measurements are representative of native sample. A study by Hondow *et al.* [163] shows that TEM quantum dot samples prepared by plunge-freezing a blotted grid into liquid ethane followed by warming to room temperature in a rotary pumped vacuum desiccator successfully maintained the native dispersion state of the quantum dots. This plunge-freeze vacuum-drying (PF-VD) method has since been successfully used for the size analysis of ZnO nanoparticles by Wallace [137].

Within this work, PF-VD was used to retain the native dispersion of nanoparticle systems. The same plunge-freezing procedure used for cryo-TEM was followed, using TEM grids with continuous carbon films (200 mesh Copper, EM Resolutions) to ensure the nanoparticles do not fall through the holes in the carbon film. After the specimen

was successfully plunge-frozen, it was then warmed to room temperature using a vacuum desiccator, subliming the vitrified ice. The sublimation steps allows for nanoparticle clusters to retain the structure seen in vitrified ice (in regions where the ice thickness is lower than 100 nm), as the particles do not move significantly and instead are deposited directly on the carbon film [163].

Separate to the research presented in this thesis, this approach was used to capture functionalised quantum rods to examine how the surface functionalisation impacted the groupings of the quantum rods. This work, published in ACS Applied Nano Materials [84] and included in Appendix B, showed how with appropriate sample preparation, imaging and image analysis, different binding modes of quantum rods would result from changes in proteins covering the surfaces of those particles. These samples were examined in training on this experimental approach and consequently applied to samples in Chapter 4.

### 3.2.6 Cryogenic Scanning Electron Microscopy

Cryogenic scanning electron microscopy (cryo-SEM), similarly to cryo-TEM, is used for the imaging of cryogenically frozen samples; for this research project, the additional use of a focused ion beam (FIB) in cryogenic conditions is useful for the 3D imaging of samples as the ion beam can be used to cut slices by serial sectioning [164]. Cryo-SEM allows for the imaging of larger sample volumes compared to cryo-(S)TEM as there is no thickness limitation for electrons to pass through the sample.

Scanning electron microscopy (SEM) is a high-resolution surface imaging technique which uses the electrons scattered off the sample surface to form an image down to nanometre resolution. Similar to the TEM design shown in Figure 3.2, the SEM is composed of an electron gun that is used to accelerate an electron beam down a column. Here, a series of lenses and apertures are used to control beam size and focusing. The beam then reaches the sample positioned on a sample stage. A detector position above the sample is used to collect backwards scattered electron (also known as backscattered electrons, BSE) and electrons expelled from the sample (known as secondary electrons, SE) [165, 166]. As with TEM, the SEM column must be kept under high vacuum to prevent unwanted electron interactions.

Secondary and backscattered electrons, together with X-rays emitted from the sample can be detected to obtain valuable sample information from different sample depths [167]:

- Secondary electrons are detected in the 1-30 nm range below the sample surface, and can be used to obtain information on the sample topology;
- Backscattered electrons (BSE) are detected from at least 10-100 nm below the sample surface and can help capture information on the atomic weight of the materials being imaged, making BSE useful to differentiate between materials [168-170];
- X-rays can be collected from further below the surface (compared to BSE) and can provide information on the elemental composition of the sample.

These penetration depths are dependent on both the accelerating voltage used and the material analysed.

As the name SEM suggests the electron beam is focused to form a probe which is used to scan the sample, but unlike transmission techniques like STEM, SEM only collects information from the sample surface. This method of sample imaging allows for the imaging of large sample (as the beam does not need to pass through the sample), meaning that SEM can be used as an alternative EM imaging technique to TEM when the sample cannot be thinned.

Cryogenic scanning electron microscopes (cryo-SEM) present important additions (see Figure 3.7) to the standard SEM setup to allow for the transfer and imaging of cryogenically frozen samples [171]:

- A cryostage is needed to maintain the sample well below the devitrification temperature of −137°C.
- An anticontaminator is kept near the sample at a temperature of lower than the sample itself to prevent sample contamination.
- A cryogenic sample transfer system is needed to provide a method to transfer the sample in and out of the microscope. This consists of a sample shuttle and a transfer chamber separated from the microscope sample chamber and outside by a cryo airlock. A cryo-fracturing device in the transfer chamber can be used to fracture samples, while a sputter coater is used to coat the sample.

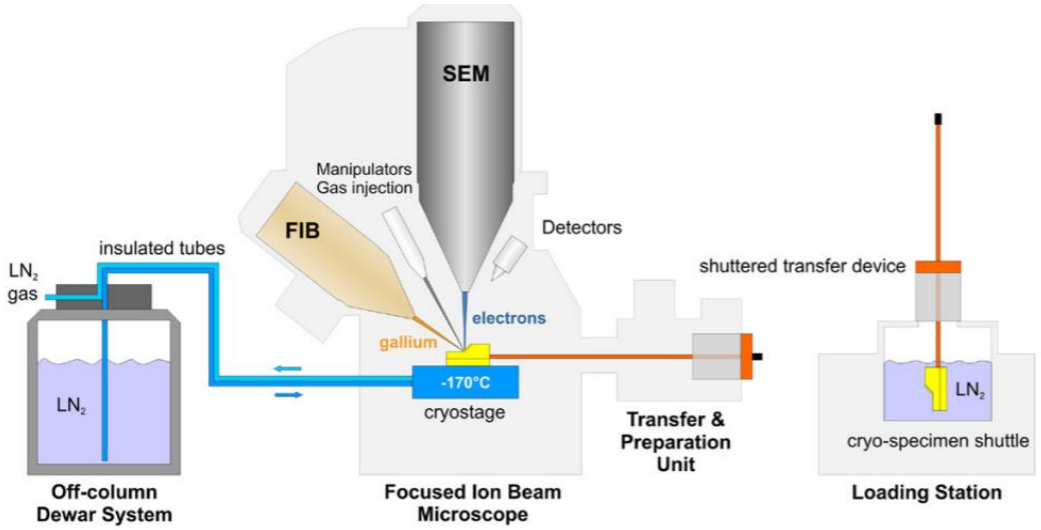


***Figure 3.7*** *- Schematic of a cryo-FIB-TEM. Additions such as cryostage and transfer unit. This diagram contains a focused ion beam (FIB) which interacts with the sample at an angle. Figure from Rigort et al. [171].*

In this study, cryo-SEM was undertaken using a FEI Helios G4 CX DualBeam scanning electron microscope, equipped with a gallium focused ion beam and Oxford Instruments EDX. Cryogenic sample preparation was carried out using a quorum technologies PP3010 cryo preparation system, as explained in the next section.

#### 3.2.6.1 Cryo-SEM Sample Preparation

The image formation mechanism used in SEM imaging allows for the analysis of samples much thicker than those used in cryo-TEM; as such, a wide range of cryogenic preparation methods are available for cryo-SEM.

For smaller samples (e.g. nanomaterials, bacteria, etc.) the sample can be frozen onto a TEM grid using plunge-freezing (as described in prior sections) [85, 86, 172]. When larger sample volumes (e.g. plant or animal tissue, hydrogels, etc.) need to be cryo-fixated, alternative procedures can be found with plunging in liquid, slush nitrogen or ethane, and high-pressure freezing being some of the more commonly seen

techniques [87, 88, 172]. High-pressure freezing allows for the vitrification of larger sample volumes (up to 1 $mm^3$) placed in a metal tube or planchet by cooling down the sample at high pressures [88, 173]. Plunge-freezing can be applied to smaller sample volumes, with plunging into liquid ethane allowing for better vitrification due to the higher heat capacity of ethane.

In this study, samples for cryo-FIB-SEM were prepared by plunging in slush nitrogen. The sample was placed in a brass rivet, and frozen by plunging the liquid sample into a slush nitrogen bath. This freezing method can be used for sample volumes up to 200 µm, though in practice the heat capacity of slush ethane does not allow for proper vitrification beyond the range of a few micrometres. As such, it is expected for some areas of the sample to show signs of crystallisation. Despite this drawback, this freezing method was choses due to the unavailability of a high pressure freezer. The frozen sample was placed in the cryo-SEM sample chamber where it was fractured using a cold knife to expose the sample which was then sputter coated with a thin layer of iridium. Before using acquiring the “slice and view” data, a further platinum coating was applied to the area of interest to minimise charging.

#### 3.2.6.2 Focused Ion Beam Milling and “Slice and View” Serial Block Face Tomography

Cryo-SEM provides good depth of field while still being a high-resolution imaging technique; moreover, as a surface imaging technique cryo-SEM allows for the imaging of samples with no inherent thickness limitation. The addition of a focused ion beam (FIB) allows for the generation of new cross-sections by milling the surface of the sample, therefore allowing for the serial imaging of large volumes [81, 89] such as hydrogels [174] and cells [175, 176]. FIB-milling can also be used to cut sample lamellae for materials that would otherwise be difficult to cut [97, 164]; these lamellae can be lifted out of the SEM and transferred to a TEM for further imaging [177].

As can be seen from Figure 3.7 FIB-SEM setups contain an ion gun (usually gallium ions) pointed towards the sample at an angle [81], thus requires the sample stage to be tilted before use. This ion beam is capable of depositing material, surface etching, and sample milling to expose new surfaces for imaging or fabricate lamellae for lift-out. When using FIB-milling to prepare samples for TEM imaging, a sample

manipulator is needed to grip and move the lamellae, which then need to be attached to a TEM grid for transfer. The ion beam in cryo-capable FIB-SEM generates a lower amount of volatile components (when compared to FIB in non-cryogenic conditions) and can be used to remove frost accumulated on the sample surface (given lower operating voltages) [81, 97].

Serial imaging of FIB-milled sample slices can be used to reconstruct the milled volume in 3D. This serial tomography technique will be referred to as “slice and view” within this thesis. The thickness of the “slice and view” slices needs to be decided depending on the material and the size of the structures that needs to be imaged [116]; the slices need to be thin enough to allow for the imaging of the smallest features of interest, but simultaneously, the depth that the electrons will travel inside the material needs to be considered. Therefore, a biological sample imaged with secondary electrons at low accelerating voltages can use thin slices, but inorganic materials characterised using EDX will use a slice thickness above 50 nm due to the interaction volume for X-rays [116, 178]. When performing serial block face FIB-milling, the sample stage is tilted to 52° and the ion beam is used to mill a trench around a sample cross-section that will be used for imaging. Figure 3.8 shows a diagram of the FIB-milled trench around a volume of the sample that will be used for tomography, with the red surface being the sample cross-section that will be imaged. After imaging, this surface will be FIB-milled to expose a new cross-section for imaging, until the entire volume is imaged. Slice tomography is available for large samples, as in this technique images are collected from slices of the samples. FIB-milling has been used to slice samples to obtain image stacks of the sample volume, which can then be reconstructed to form a tomogram.

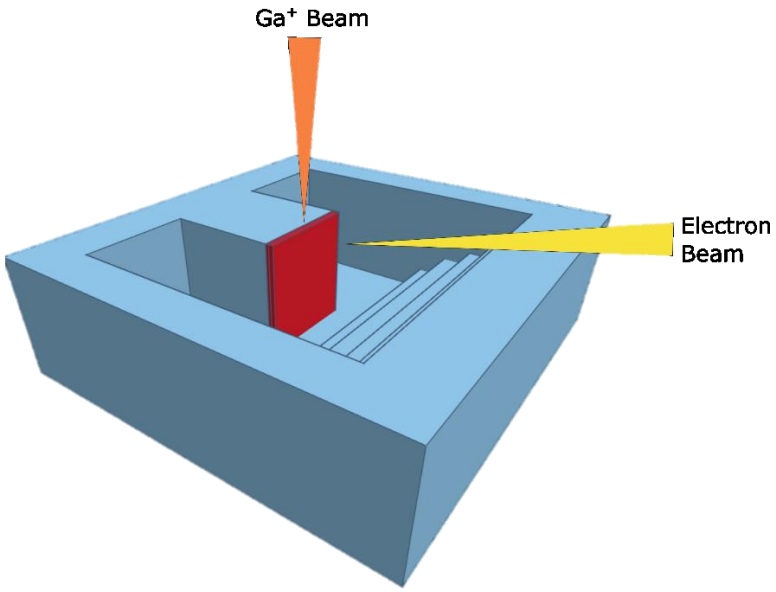


***Figure 3.8 –*** *3D diagram of a trench for serial block face "slice and view" FIB-milling.*

In this study, the "slice and view" method was used to obtain tomograms of frozen samples. When a suitable area was found in cryo-SEM (i.e. an area on the sample surface where particles are present), the eucentric height was then found and the sample is tilted to begin FIB milling. Material was removed from the front and sides of the area of interest as seen in Figure 3.9. Before imaging, the FIB was used to remove any redeposited material, then a marker was etched on the sample surface to ensure proper image alignment during imaging. Backscattered electron images were taken with a 5kV accelerating voltage, then a slice with thickness of 50 nm was milled to expose new sample surface. The last two steps were repeated until the full volume was imaged.

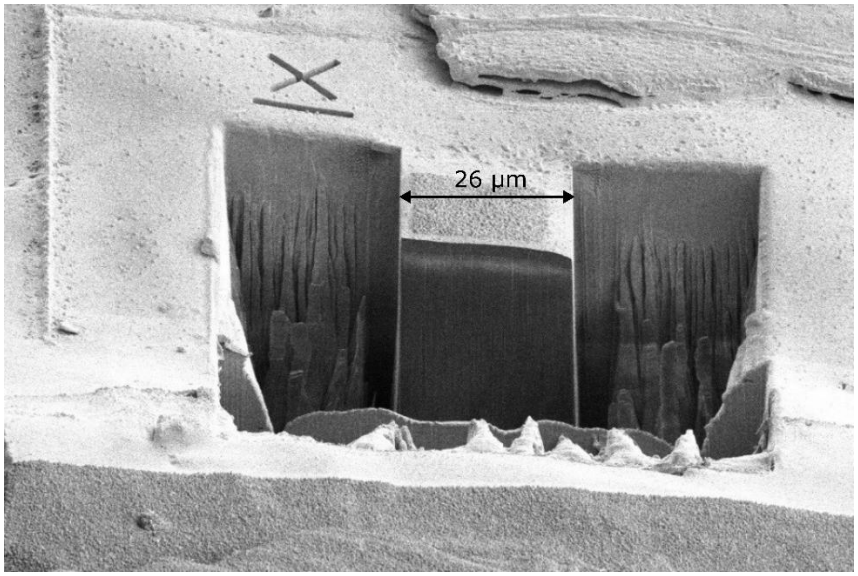


***Figure 3.9*** *– Cryo-SEM BSE image of a FIB milled area for "slice and view". The sample is milled in front and on the sides of the area of interest to clear the view. A fiducial marker is visible on the sample surface, used to track the image alignment during "slice and view".*

Slice series taken in cryo-FIB-SEM were first aligned using the "Linear Stack Alignment with SIFT" plugin in ImageJ [179] to correct the camera drift during the "slice and view" stack acquisition. Visualisation in 3D and generation of 3D surfaces was carried out using the Imaris software.

#### 3.2.6.3 Cryo Lift-Out

One of the uses of FIB was to cut lamellae for materials that would otherwise be difficult to cut [97, 164]; these lamellae can be lifted out of the SEM and transferred to a TEM for further imaging. This process is also applicable to cryogenic samples, therefore allowing for the imaging of larger sample volumes initially in a cryo-SEM, and then in cryo-TEM once a lamella of the appropriate thickness has been produced, provided it is transferred while preventing frosting and maintaining temperatures below -140°C [88, 132].

Samples for cryo lift-out were prepared and imaged using the same preparation process described in the previous section. After finding an area of interest, the sample was coated with a thin layer of Pt coating and tilted to operate the focused ion beam.

A large slice of the sample was milled using the FIB to ensure the area contains the sample of interest and to allow for enough space to operate the cryo-grippers once a lamella is created. After finding a suitable cross-section, the area around the section of interested was milled to obtain a lamella, which was lifted using a Kleindiek cryoFIB lift out manipulator ("cryo-grippers") and deposited onto a bespoke TEM transfer grid (see Figure 3.10). A single-slot TEM support grid was FIB-milled to remove a one-quarter slice above the slot (Figure 3.10-B). This modification is necessary to allow for the manipulation of the cryo-grippers; this design also allows for easy manipulation with tweezers during the grid transfer to the cryo-holder. Within the grid slot, a slot was FIB-milled to allow the secure fit of frozen lamellae; this allows to mechanically secure the lamella without having to redeposit material to attach the lamella to the grid, thus simplifying the transfer procedure. The lamella on the TEM transfer grid was then removed from the cryo-FIB-SEM and submerged in liquid nitrogen for transport to the cryo-TEM. The grid was then loaded into a cryo-holder and inserted into the cryo-TEM for cryo-(S)TEM imaging.

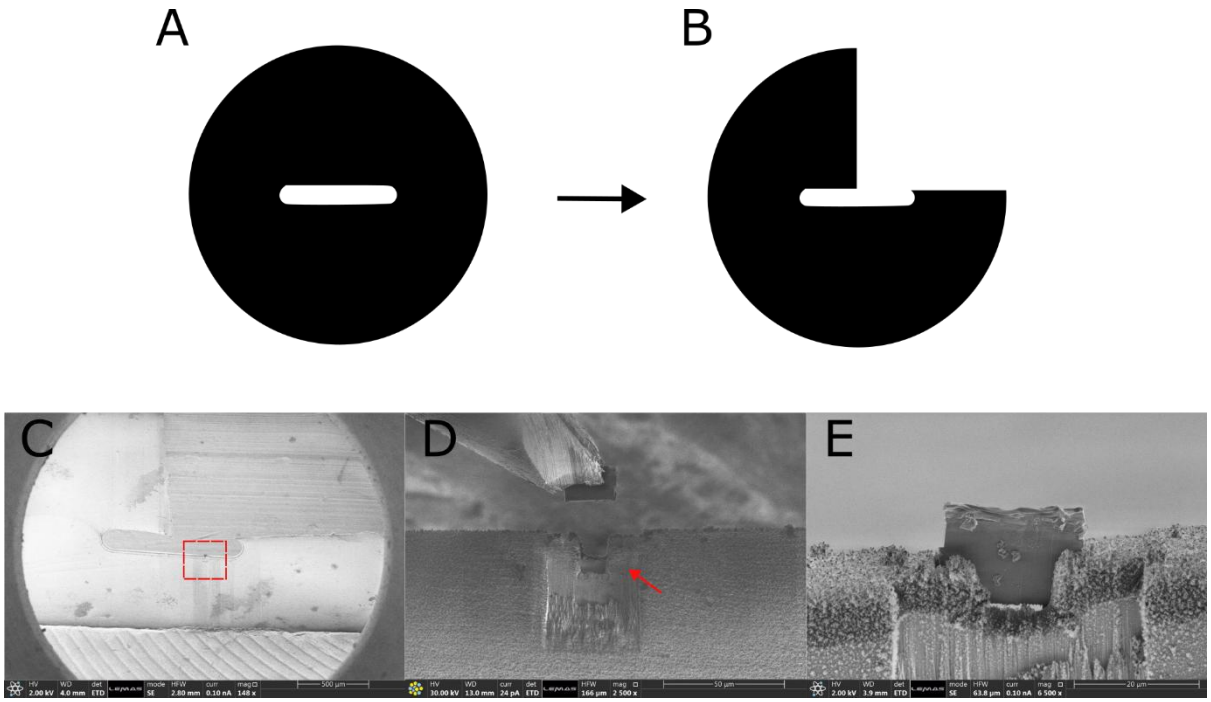


***Figure 3.10 –*** *TEM transfer grid used for cryo lift-out. A) Simplified schematic of a single-slot TEM support grid. B) Milled TEM grid; the removal of a quarter of the grid allows to manoeuvre the cryo grippers within the lamella slot, while retaining enough*

*surface area for easy gripping of the grid itself during the transfer process, and allowing to more easily orientate the grid within the cryo holder. D) Secondary electron SEM image of the slot in a modified grid, with a milled opening for a lamella within the grid slot (within the red box). D) Secondary electron SEM image of the highlighted area in (C), showing the FIB-milled slot. E) Frozen lamella resting within the slot.*

### 3.2.7 Electron Tomography

Cryo-electron tomography (cryo-ET) refers to a series of techniques where a series of sample images is collected and then processed using 3D reconstruction algorithms to produce a 3D image stack, thereby generating 3D datasets from a series of 2D images.

For small biological particles (including viruses and proteins, among others) single particle reconstruction is often for the generation of 3D models of particles while minimising the beam-induced damage to the sample [94]. This method consists in reconstructing a tomogram from images of a large amount of single objects. If the objects imaged all have the same structure, it is then possible to treat objects with different orientations as projections of that object at different angles, which can be in turn reconstructed to form a tomogram. This approach allows for the creation of high-resolution tomograms of small particles from a large quantity of images taken with very low electron fluence, thus preventing sample bubbling or devitrification [94, 180, 181]. However, the objects imaged are required to be identical in structure, but beyond a certain size objects cannot be identified as identical copies, and will require electron tomography techniques to collect 3D datasets, as seen in Figure 3.11 [94]

Above this size, tilt tomography and slice tomography are often used for electron tomogram, and will be focused on in this thesis. Tilt tomography requires the collection of a series of images at a range of tilt angles (a tilt series), meaning sample tilting is needed. This technique can be applied to TEM and SEM [182] imaging of samples up to a few microns, thus being applicable to a wide range of inorganic and biological samples. The main advantage of tilt tomography its high-resolution, together with the ability to obtain a tomogram from a single object. The TEM imaging mode used for tilt series collection can vary depending on the sample requirements: amorphous

biological samples can be imaged using conventional TEM imaging, while HAADF STEM can be used for the tomography of strongly scattering crystalline samples [183].

In this thesis, cryo-ET was used to visualise cryogenically frozen samples in 3D, allowing for the imaging of a wide range of sample sizes (Figure 3.11). This large characterisation range is especially useful when analysing the Pickering emulsion samples, allowing to image both the stabilising nanoparticles (3-5 nm) and the oil droplets (50-600 nm). Two main methods for generating 3D images will be employed: cryo-electron tomography (cryo-ET) where a 3D image is reconstructed from a cryo-TEM tilt series (Section 1.2.7.1), and 3D image reconstruction from cryo-FIB-SEM slice stacks (previously detailed in Section 1.2.6.2).

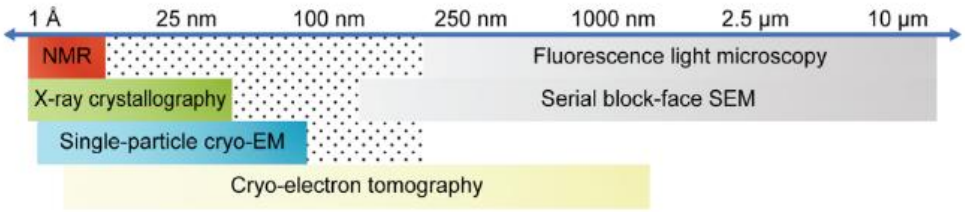


***Figure 3.11*** *- Size ranges for different 3D imaging techniques*[184].

### 3.2.7.1 Cryo-TEM Electron Tomography

Cryo-electron tomography (cryo-ET) is a high-resolution (down to the 2-20 nm scale) 3D imaging technique where a 3D volume is reconstructed from a series of images recorded at different angles (see Figure 3.12) [185, 186]. This technique is suitable for high-resolution 3D imaging for structures that cannot be reconstructed with other techniques such a single particle reconstruction [87].

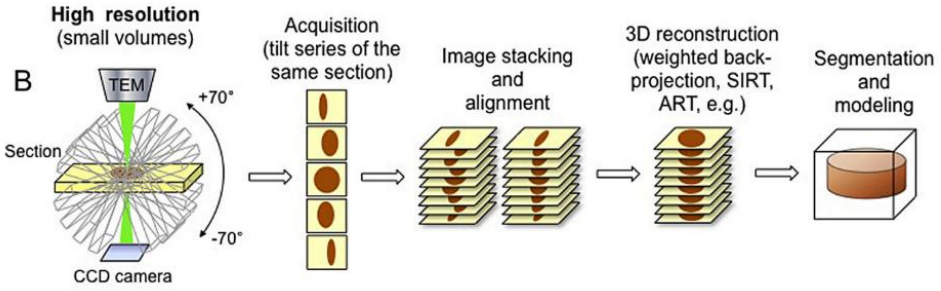


***Figure 3.12*** *– Schematic detailing the steps for cryo-ET in TEM. After the collection of a tilt series, the images are aligned and reconstructed to form a 3D image. In this project, a HAADF detector was used to collect STEM data for the tilt series (instead of a CCD camera), though the other steps remain unchanged. Figure from Miranda et al [187].*

Data collection for electron tomography is generally carried out following the steps [184]:

1. The eucentric height is set;
2. The stage is tilted mechanically along a tilt axis (the tilt axis used depends on the sample stage and sample holder used);
3. Centring of the image;
4. Focusing;
5. Recording of the image.

This process is then repeated for every tilt angle. The ideal tilting range for a full series is ±90°, but in reality the stage can only shift up to a maximum of ±60-78° [185] due to interference from the TEM grid and sample thickness. This limit in the collection range leads to a “missing wedge”, encompassing the positions that cannot be reached by tilting the stage [185, 188]. This missing data issue can be improved by collecting a further tilt series following a tilt axis perpendicular to that used in the first series; although this procedure transforms the “missing wedge” (single tilt axis) into a “missing pyramid” (double tilt axis, see Figure 3.13) [189]. This is complicated, as specialised equipment is needed that allows for two tilting directions, and moreover, prolonged exposure to the electron beam can exacerbate the damage to the sample. In fact, the beam damage issue explored in the use of cryo-TEM remains relevant in cryo-ET; the tilt series is therefore recorded in HAADF STEM mode rather than TEM to remove

diffraction contrast (as this prevents proper 3D reconstruction of crystalline samples) [185] and to reduce damage to the ice, though the radiation damage remains a limiting factor for obtaining high-resolution images with a low SNR [188].

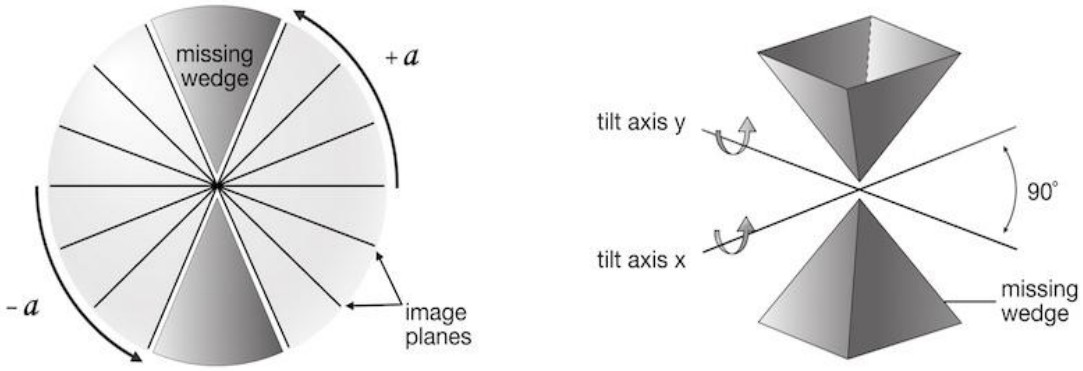


***Figure 3.13*** *– Schematics showing the missing wedge (left) and pyramid (right) in a tilt series [189].*

An additional challenge during image capture relates to the sample thickness: the already restrictive thickness limit for TEM is even more restrictive in cryo-ET as the effective length the electrons have to penetrate increases at higher tilt angles. At 70° angles the sample thickness will be approximately 2.9 times the original thickness, meaning that higher electron voltages will be needed to penetrate the sample and collect high-resolution images [185, 188].

As seen in Figure 3.12, after the tilt series is collected the images need to be aligned as a pre-reconstruction step and finally reconstructed into a 3D image. Alignment of the images is vital to ensure the a good quality reconstruction and will be necessary even if the detector is automatically aligned during image collection, as the magnification used will need to readjust as the stage is tilted to maintain the sample centred and focused [188]. Alignment can be done either manually or by automatic/semi-automatic tracking of markers within the sample. For biological samples high-contrast particles (e.g. 5-20 nm gold NPs) can be used and automatically tracked, while for inorganic high-contrast samples tracking points can be automatically generated throughout the tilt series [189, 190].

The image stack is then used to reconstruct the 3D image by using Fourier's slice theorem (projection theorem), stating that the projection of an object at a specific angle θ is equivalent to the central plan of the object's 3D Fourier transform at that same angle θ [188, 189]. The simplest reconstruction method is the weighted back-projection (WBP). WBP directly applies Fourier's slice theorem, assuming that the tilt images are projections representing the mass density encountered by the electron beam. The 2D images are simply re-projected at the angles at which they were originally collected (i.e. backprojected). A high-pass filter is applied to the projections to properly represent high frequency information (i.e. weighting). Despite the computational simplicity of this method, weighted back-projections tend to be blurry as the low frequency information (corresponding to data for larger spatial detail) tends to be oversampled, while the high frequency information tends to be under-sampled. This is especially detrimental for cryo-ET, where the low SNR contributes to low tomogram resolution [191].

Alternatively, iterative reconstruction algorithms can also be used to improve the quality of the resulting image. Simultaneous iterative reconstruction technique (SIRT) and algebraic reconstruction technique (ART) are examples of iterative reconstruction methods, where the 3D reconstruction is re-projected along the collection angles and resulting projections are then compared to the original tilt series [189, 191]. This process is repeated for a number of iterations, generally 30-50 [191] to minimise the calculated error between experimental projections and those computed from the generated volume.

Lastly, the discrete algebraic reconstruction technique (DART) is an iterative algorithm that requires knowledge of the grey levels in the imaged object and projections. In DART, an iterative reconstruction algorithms (e.g. SIRT) is initially used to form a reconstructed volume, which is then thresholded. The result is improved in each iteration through the use of reconstruction and segmentation steps, to obtain a reconstruction that contains only grey levels from a previously-known set. This results in a straightforward algorithm with less missing wedge artefacts compared to SIRT [192]. However, DART is only applicable to datasets with known and fixed grey levels, and therefore the use of DART can be challenging in samples with different chemical compositions or when the regions containing grey levels are particularly small (e.g. nanoparticles) [192, 193].

In this thesis, cryo-HAADF STEM tilt series were collected and then reconstructed using SIRT according to the procedures detailed in section 3.2.7.2 “Cryo-HAADF STEM Tomography”, section 3.2.7.3 “Cryo-Electron Tomography in conjunction with Electron Energy Loss Spectroscopy”, and section 3.2.7.4 “Cryo-Electron Tomography in conjunction with Energy Dispersive X-Ray Spectroscopy”.

In addition to the research presented in this thesis, electron tomograms were collected, reconstructed, visualised and analysed for two catalyst systems. This allowed the processes detailed below to be learnt and developed on a non-cryogenic and electron beam stable sample. The results showed the distribution of palladium nanoparticles through two catalysts, identifying the different locations depending upon catalysts support (distributed through meso- and micropores, or in mesopores and the external surface only). This research has been published in Nature Communications [194] and is included in Appendix C. The approaches and analysis learnt through studying this system were subsequently used in the examination of cryogenically prepared samples in Chapter 4 and Chapter 5.

#### 3.2.7.2 Cryo-HAADF STEM Tomography

Cryo-ET was performed by collecting a series of images in cryo-HAADF STEM mode while tilting the sample (tilt series). The use of cryo-HAADF STEM helped mitigate the beam-induced damage accumulating as multiple images are collected [98]. Additionally, the ability to selectively collect Rutherford scattered electrons at high angles using HAADF conditions eliminates diffraction contrast while increasing atomic contrast. The advantages of this within the context of serial cryo-imaging of Pickering emulsions is twofold. The lack of diffraction contrast removes any visual contamination from crystalline regions in the ice, oil, and Pt-NPs, which helps distinguish important features such as the Pt-NPs even in thicker ice. In addition, atomic contrast favours the Pt-NPs as these have a high atomic number, thus making their imaging easier even at higher sample thicknesses and lower probe currents (which needed to ensure the sample is not damaged during serial imaging). STEM imaging is also less negatively influenced by variations in sample thickness, which can help in imaging during tilt series collection.

The tilt series were collected with a probe current of 5 – 20 pA every 3°-5° with a tilt range from α = -60° to α = +60°. Although the ideal tilt range for a full series is ±90° [185, 188], the equipment used only allowed for a full tilt range of ±60° when using the cryo-TEM holder.

The specific tilt series collection parameters for the tilt series presented in this thesis vary depending on the sample imaged and will be discussed in more depth in the results chapters. Image collection was carried out using the following steps, as outlined in other publications such as Turk and Baumeister (2020):

1. The eucentric height was set;
2. The stage was tilted mechanically along the tilt axis;
3. The image was centred to ensure the sample of interest was positioned in the middle of the camera;
4. The sample was focused;
5. The image was recorded.

This process was repeated from tilt angles -60° to +60°. Focusing was done manually for all Pickering emulsion samples, focusing on the Pt-NPs in the central slice of the droplet whenever the droplets were too large to focus on their entirety. For each tilt series acquired, a cryo-HAADF STEM image of the tilt series area was collected before and after tilt series acquisition to document damage to the sample, and to serve as a reference for the analysis of the resulting tomogram. Tilt series acquisition was aided by the use of the FEI STEM Tomography software which was used for tracking the stage position after each tilt step and for applying the correct defocus at each point of the image at the different tilt angles.

The images in the tilt series were then processed in ImageJ to adjust the brightness and contrast of the sample when needed to ensure an effective 3D reconstruction. The Inpect3D software was used to align the tilt series and reconstruct a tomogram using simultaneous iterative reconstruction technique (SIRT) (100 iterations). The tomograms were visualised in the Imaris software (version 9.5.0), which was used to create surfaces to better visualise the oil droplets and Pt-NPs. For the Pt-NPs, the automatic stop creation function in Imaris was used to generate spots corresponding to the nanoparticles and were manually inspected after generation using a cryo-HAADF STEM image of the area as a reference. This was done to ensure the correct

nanoparticle position. The surface creation tool in Imaris was used to manually generate surfaces to represent the oil phase of the droplets, using the position of the stabilising Pt-NPs as a reference for the oil surface. This process assumes that these Pt-NPs are found exactly on the oil-water interface and is therefore only an approximation of the real droplet.

#### 3.2.7.3 Cryo-Electron Tomography in conjunction with Electron Energy Loss Spectroscopy

Cryo-ET was performed alongside electron energy loss elemental maps to allow for the collection of elemental data to enhance the 3D reconstructions of Pickering emulsions. EEL low-loss and core-loss spectra in conjunction with HAADF STEM tracking images were collected at various tilt angles alongside a HAADF STEM tilt series, using a modified version of the procedure used in 3.2.7.2 Cryo-HAADF STEM Tomography:

1. A region of interest was identified;
2. The eucentric height was set;
3. EEL low-loss and core-loss spectra were collected for the region of interest;
4. The EEL spectra were briefly analysed to estimate the sample thickness and presence of carbon film near the sample;
5. The stage was tilted mechanically along the tilt axis;
6. The sample was focused;
7. EEL low-loss and core-loss spectra were collected;
8. The image was centred to ensure the sample of interest was positioned in the middle of the camera;
9. The image was recorded.

Steps 5 through 9 were repeated until the end of the tilt series, acquiring EEL spectra only when needed. A total of 9 EELS elemental were thus acquired at tilt angles 0°, ±18°, ±27°, ±39°, and ±51°, while 51 HAADF STEM images were acquired with a 3° tilt step and ~3 nm/px pixel size at ~10 pA. This was done to decrease the amount of electron fluence required for the acquisition of the full tilt series, therefore decreasing the amount of beam-induced damage on the sample. This image collection process resulted in a total electron fluence of ~200 $e^-/Å^2$ depending on the specific pixel size

and probe current used. Image centring was performed after the acquisition of the EEL spectra to allow for minor movements in the stage when setting the new parameters for EELS acquisition at new tilt angles.

Hyperspy was used to analyse the EELS data and generate elemental maps using the carbon K-edge signal corresponding to the Pickering emulsion droplet's oil phase. These elemental maps were then processed by adding a gaussian blur filter. Both the elemental maps and the cryo-HAADF STEM tilt series were then aligned and reconstructed using SIRT using the Insppect3D software. The resulting tomograms were simultaneously loaded on the same Imaris dataset as separate channels. As the two tomograms differ in size, they were then manually aligned using the cryo-HAADF STEM reference images and HAADF tracking image at 0° tilt.

#### 3.2.7.4 Cryo-Electron Tomography in conjunction with Energy Dispersive X-Ray Spectroscopy

Cryo-ET in conjunction with EDX was used for the elemental analysis in 3D of the $TiO_2$ coated in biological media sample. EDX spectral map were collected in conjunction with cryo-HAADF STEM tilt series using the same general method used for EELS detailed in the previous section. A total of 51 cryo-HAADF STEM tilt images were collected every 3° in a ±60° tilt range. EDX spectra were collected alongside these at tilt angles 0°, ±9°, ±21°, ±30°, ±39°, ±51°, and ±60°. More acquisition steps were used for EDX (compared to EELS) due to the higher damage threshold of the $TiO_2$ sample this technique was applied to. Both images and spectra were collected with a probe current of ~10 pA at low tilt angles below ±50°, and with a probe current ~20 pA above ±50° to allow for a sufficiently high SNR at high angles where the sample thickness increases.

The EDX spectra were processed in Hyperspy, where the dataset was re-binned and processed to obtain elemental maps for the titanium and calcium signals. A gaussian blur filter was applied to the elemental maps for both elements. These elemental maps together with the cryo-HAADF STEM images were aligned and reconstructed using SIRT using the Inspect3D software. The resulting tomograms were loaded into Imaris as separate channels and aligned using the cryo-HAADF STEM images collected during the tilt series as a reference.

## 3.3 Image Analysis

### 3.3.1 Shape and Size Measurements for Pickering Emulsions

The shape of the emulsion droplets was measured using ImageJ in a population of 500 emulsion droplets. Using the STEM images, the shape of the droplets was underlined and an ellipsoid was adjusted to the shape. In this way, the diameter of the emulsion has been chosen to be the major axis of the ellipsoid. The circularity is defined by Equation (3.4):

$$Circ = 4\pi \frac{Area}{Perimeter^2} \tag{3.4}$$

The circularity ranges from 0 (infinitely elongated polygon) to 1 (perfect circle).

### 3.3.2 Size Measurements for Nanoparticles

Size measurements of nanoparticles in TEM images was done using ImageJ (Fiji), using the built-in particle analysis tool. The brightness and contrast of the images were changed when higher contrast was needed, then a threshold was applied before obtaining the Feret diameter using the particle analysis tool. In all cases, particles on the edges of images were excluded. The particle size measurement steps used are as follows:

1. An image was loaded to ImageJ;
2. The image scale was set;
3. A median filter and background subtraction were applied in that order to remove background noise;
4. Automatic thresholding was applied using Otsu's method, then a mask was applied to the image;
5. ImageJ's automatic particle analysis function was applied to the masked image to obtain the ferret diameter of the particle, ensuring that the particles near the image's perimeter were excluded from the analysis.

### 3.3.3 Nearest Neighbour Distances

Nearest neighbour distances were measured in ImageJ using the BioVoxxel Toolbox plugin when analysing TEM images. For the nearest neighbour analysis of tomograms, spots were created in Imaris using the automatic spot creation tool, which were then manually checked to ensure the spot diameter was consistent with the reference cryo-HAADF STEM images. The MATLAB plugin to Imaris was then used to measure the distance between the spots.

## 3.4 Summary

This chapter has provided an overview of the samples and electron microscopy approaches used in this work. In two instances, training samples were used to develop the required skills to approach the samples detailed in later chapters; each of these resulted in publications not further discussed in this thesis, but that are included in Appendix B and Appendix C. A focus on cryo-electron microscopy is presented, with the results of this shown in the following chapters.

# Chapter 4 Development of Experimental Approaches via Case Studies

In order to fully implement cryogenic approaches to the study of Pickering emulsions, experimental approaches encompassing cryogenic sample preparation, cryo-TEM, cryo-STEM, cryo-electron tomography (ET), cryo-EDX and cryo-EELS have been undertaken on a series of cases studies. This initial analysis was conducted to test the limitations of plunge-freezing and cryo-(S)TEM imaging before characterising the main Pickering emulsion samples. The case studies comprise:

1. Zinc oxide nanoparticles;
2. “Core-satellite” gold nanoparticles;
3. Titanium dioxide nanoparticles in culture media;
4. Vitreous ice produced through plunge-freezing.

These systems provide a varying level of complexity for applying the characterisation techniques that were later used on the Pickering emulsion samples, namely cryo-(S)TEM imaging, EDX, EELS, and cryo-ET.

## 4.1 ZnO Nanoparticle System

The first system discussed in this chapter consists of zinc oxide (ZnO) nanoparticles (NPs). ZnO NPs have found applications in a variety of areas that include human contact with the NPs such as in sunscreen and as supplement in the food and agricultural industries [6-8]. Analysis of particle and agglomerate size, shape, and dissolution mechanisms are important to understand and monitor the potential toxicity of ZnO in humans [7, 195, 196]. Wallace [137] provides a protocol for the synthesis and analysis of ZnO nanoparticles to test for particle agglomeration, size and toxicity, including results from electron microscopy imaging [197]. This extensive study of ZnO NP size and agglomeration was used as a control for the effects of cryogenic sample preparation techniques on nanoparticle dispersions. This will in turn be used as a reference for the preparation of the Pickering emulsion samples to ensure the sample is well-distributed and the droplets are not compressed.

Two ZnO nanoparticle dispersions in water were prepared, with concentrations of 0.1 mg/mL and 1.0 mg/mL following the methodology in Wallace (2013), to test the sample

concentration necessary to guarantee the presence of nanoparticles during cryo-TEM imaging. Both samples were prepared using the approach described in the Materials and Methods.

The choice of suitable sample preparation methods before EM imaging is vital for the collection of accurate particle size measurements as different preparation methods can result in increased agglomeration compared to the native sample conditions. This section focuses on the comparison between ZnO samples prepared using a range of approaches, for both 2-D projection imaging TEM and 3-D volume SEM.

As explained in Chapter 3, these preparation methods are expected to yield different agglomerate sizes as nanoparticles tend to agglomerate as the sample dries, while cryogenic freezing is expected to retain the native agglomerate sizes due to the rapid freezing. This section aims to inspect whether these preparation methods will result in significantly different agglomerate sizes, which could affect the distribution and agglomeration of Pickering emulsion droplets.

### 4.1.1 Dynamic Light Scattering Analysis

DLS measurements for both ZnO concentrations (Figure 4.1, Table 4.1) were acquired approximately 40 minutes after the samples were sonicated, replicating the preparation time before plunge-freezing. The average particle size (taken from the peak centre) was found to be ~461 nm (PDI: 0.21) for the 0.1 mg/mL sample and ~435 nm (PDI: 0.22) for the 1.0 mg/mL sample. The polydispersity indexes (PDI) measured here show that both systems are moderately polydisperse, being between 0.1 and 0.4 (with a lower PDI indicating a more monodisperse system, and vice versa) [198]. This indicates that a wide distribution of particle sizes are present, as can be seen by the peak widths in Figure 4.1, which indicate the presence of particles with sizes within 200 – 1000 nm in the main peaks. Preliminary DLS measurements are similar to the results in Wallace (2013) and thus suggests that microscopy analysis should also be similar. Given the similarity between the average sizes in both concentrations it can be assumed that during microscopy, differences in agglomerate sizes in the two samples will be solely due to the preparation method. The secondary peaks in the two distributions are possibly due to contamination or presence of large agglomerates. DLS measures the particles' hydrodynamic radius, which becomes non-representative

when looking at non-spherical particles – this is the case with the particles in this system, as the primary particles are elongated, and the agglomerates are not necessarily spherical. Lastly, the polydispersity of these systems could make the evaluation of the effects of sample preparation challenging, as any particle agglomeration induced during sample preparation might result in agglomerates with sizes within the size ranges found in DLS. Despite these drawbacks, DLS remain a fast technique for particle sizing that requires minimal sample preparation, therefore being a suitable reference point to ensure that TEM imaging results in accurate particle sizing.

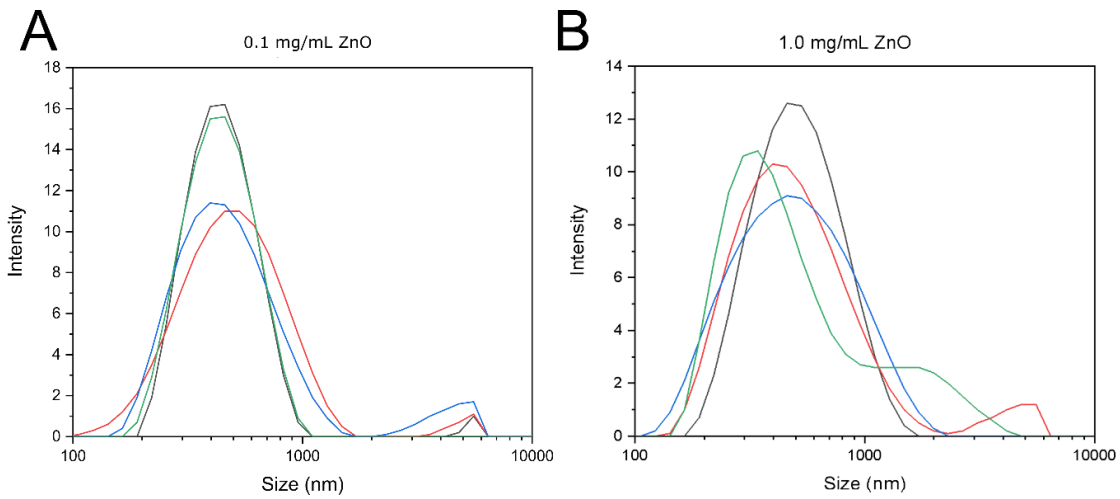


***Figure 4.1 –*** *DLS measurements for the ZnO dispersions, showing all four repeats per sample.*

***Table 4.1 –*** *DLS intensity measurements for the two samples.*

| | Intensity | | | | | | | |
|---|---|---|---|---|---|---|---|---|
| **Size (nm)** | **0.1 mg/mL ZnO** | | | | **1.0 mg/mL ZnO** | | | |
| 0.40 | 0 | 0 | 0 | 0 | 0 | 0 | 0 | 0 |
| 0.46 | 0 | 0 | 0 | 0 | 0 | 0 | 0 | 0 |
| 0.54 | 0 | 0 | 0 | 0 | 0 | 0 | 0 | 0 |
| 0.62 | 0 | 0 | 0 | 0 | 0 | 0 | 0 | 0 |
| 0.72 | 0 | 0 | 0 | 0 | 0 | 0 | 0 | 0 |
| 0.83 | 0 | 0 | 0 | 0 | 0 | 0 | 0 | 0 |
| 0.96 | 0 | 0 | 0 | 0 | 0 | 0 | 0 | 0 |
| 1.12 | 0 | 0 | 0 | 0 | 0 | 0 | 0 | 0 |
| 1.29 | 0 | 0 | 0 | 0 | 0 | 0 | 0 | 0 |
| 1.50 | 0 | 0 | 0 | 0 | 0 | 0 | 0 | 0 |
| 1.74 | 0 | 0 | 0 | 0 | 0 | 0 | 0 | 0 |
| 2.01 | 0 | 0 | 0 | 0 | 0 | 0 | 0 | 0 |
| 2.33 | 0 | 0 | 0 | 0 | 0 | 0 | 0 | 0 |
| 2.70 | 0 | 0 | 0 | 0 | 0 | 0 | 0 | 0 |
| 3.12 | 0 | 0 | 0 | 0 | 0 | 0 | 0 | 0 |
| 3.62 | 0 | 0 | 0 | 0 | 0 | 0 | 0 | 0 |
| 4.19 | 0 | 0 | 0 | 0 | 0 | 0 | 0 | 0 |
| 4.85 | 0 | 0 | 0 | 0 | 0 | 0 | 0 | 0 |
| 5.62 | 0 | 0 | 0 | 0 | 0 | 0 | 0 | 0 |
| 6.50 | 0 | 0 | 0 | 0 | 0 | 0 | 0 | 0 |
| 7.53 | 0 | 0 | 0 | 0 | 0 | 0 | 0 | 0 |
| 8.72 | 0 | 0 | 0 | 0 | 0 | 0 | 0 | 0 |
| 10.10 | 0 | 0 | 0 | 0 | 0 | 0 | 0 | 0 |
| 11.70 | 0 | 0 | 0 | 0 | 0 | 0 | 0 | 0 |
| 13.54 | 0 | 0 | 0 | 0 | 0 | 0 | 0 | 0 |
| 15.69 | 0 | 0 | 0 | 0 | 0 | 0 | 0 | 0 |
| 18.17 | 0 | 0 | 0 | 0 | 0 | 0 | 0 | 0 |
| 21.04 | 0 | 0 | 0 | 0 | 0 | 0 | 0 | 0 |
| 24.36 | 0 | 0 | 0 | 0 | 0 | 0 | 0 | 0 |
| 28.21 | 0 | 0 | 0 | 0 | 0 | 0 | 0 | 0 |
| 32.67 | 0 | 0 | 0 | 0 | 0 | 0 | 0 | 0 |
| 37.84 | 0 | 0 | 0 | 0 | 0 | 0 | 0 | 0 |
| 43.82 | 0 | 0 | 0 | 0 | 0 | 0 | 0 | 0 |
| 50.75 | 0 | 0 | 0 | 0 | 0 | 0 | 0 | 0 |
| 58.77 | 0 | 0 | 0 | 0 | 0 | 0 | 0 | 0 |
| 68.06 | 0 | 0 | 0 | 0 | 0 | 0 | 0 | 0 |
| 78.82 | 0 | 0 | 0 | 0 | 0 | 0 | 0 | 0 |
| 91.28 | 0 | 0 | 0 | 0 | 0 | 0 | 0 | 0 |
| 105.70 | 0 | 0 | 0 | 0 | 0 | 0 | 0 | 0 |
| 122.40 | 0 | 0 | 0 | 0 | 0 | 0 | 0 | 0 |
| 141.80 | 0 | 0 | 0.3 | 0.1 | 0 | 0 | 0.1 | 0 |
| 164.20 | 0.5 | 0.8 | 1.4 | 0.8 | 0.1 | 0 | 1 | 1 |
| 190.10 | 2.2 | 3.1 | 3.3 | 2.2 | 1 | 0.7 | 2.6 | 3.6 |
| 220.20 | 5.3 | 6.3 | 5.6 | 4.3 | 2.8 | 2.3 | 4.7 | 6.6 |
| 255.00 | 8.9 | 9.6 | 8.1 | 6.7 | 5.5 | 4.6 | 6.8 | 9.2 |
| 295.30 | 12.3 | 12.1 | 10.2 | 9.1 | 8.6 | 7.3 | 8.5 | 10.6 |
| 342.00 | 14.6 | 13.3 | 11.7 | 11 | 11.4 | 9.7 | 9.7 | 10.8 |
| 396.10 | 15.3 | 13.1 | 12.3 | 12.2 | 13.5 | 11.6 | 10.3 | 9.9 |
| 458.70 | 14.2 | 11.8 | 11.9 | 12.5 | 14.2 | 12.6 | 10.2 | 8.4 |
| 531.20 | 11.6 | 9.7 | 10.6 | 11.8 | 13.6 | 12.5 | 9.5 | 6.7 |
| 615.10 | 8.1 | 7.3 | 8.6 | 10.2 | 11.6 | 11.5 | 8.4 | 5.2 |
| 712.40 | 4.6 | 4.8 | 6.4 | 8.1 | 8.7 | 9.7 | 7.1 | 3.9 |
| 825.00 | 1.8 | 2.7 | 4.2 | 5.7 | 5.5 | 7.5 | 5.6 | 3.1 |

| | Intensity | | | | | | | |
|---|---|---|---|---|---|---|---|---|
| Size (nm) | 0.1 mg/mL ZnO | | | | 1.0 mg/mL ZnO | | | |
| 955.40 | 0.3 | 1.2 | 2.3 | 3.4 | 2.7 | 5.1 | 4.2 | 2.7 |
| 1106.00 | 0 | 0.3 | 1 | 1.6 | 0.8 | 3 | 2.9 | 2.6 |
| 1281.00 | 0 | 0 | 0.2 | 0.4 | 0 | 1.4 | 1.8 | 2.6 |
| 1484.00 | 0 | 0 | 0 | 0 | 0 | 0.4 | 1 | 2.6 |
| 1718.00 | 0 | 0 | 0 | 0 | 0 | 0 | 0.5 | 2.6 |
| 1990.00 | 0 | 0 | 0 | 0 | 0 | 0 | 0.2 | 2.4 |
| 2305.00 | 0 | 0 | 0 | 0 | 0 | 0 | 0.1 | 2 |
| 2669.00 | 0 | 0 | 0 | 0 | 0 | 0 | 0.2 | 1.5 |
| 3091.00 | 0 | 0 | 0 | 0 | 0 | 0 | 0.5 | 1 |
| 3580.00 | 0 | 0.2 | 0.1 | 0 | 0 | 0 | 0.7 | 0.6 |
| 4145.00 | 0 | 0.7 | 0.3 | 0 | 0 | 0 | 1 | 0.2 |
| 4801.00 | 0 | 1.2 | 0.6 | 0 | 0 | 0 | 1.2 | 0 |
| 5560.00 | 0 | 1.7 | 0.9 | 0 | 0 | 0 | 1.2 | 0 |
| 6439.00 | 0 | 0 | 0 | 0 | 0 | 0 | 0 | 0 |
| 7456.00 | 0 | 0 | 0 | 0 | 0 | 0 | 0 | 0 |
| 8635.00 | 0 | 0 | 0 | 0 | 0 | 0 | 0 | 0 |
| 10000.00 | 0 | 0 | 0 | 0 | 0 | 0 | 0 | 0 |

### 4.1.2 Initial Comparison Between Sample Preparation Methods

The “dry samples” prepared using the methodologies described Chapter 3 were imaged using standard TEM, and can be seen in Figure 4.2 and Figure 4.3. In summary there are samples prepared via:

- Drop Cast Dry Sample; where a drop was placed onto a continuous carbon film TEM grid placed on a piece of filter paper.
- Plunge-freezing and vacuum drying (PF-VD); a sample which has been plunge frozen onto a continuous carbon film TEM grid and subsequently vacuum dried according to the protocol detailed in Hondow *et al.* [163] and subsequent publications.
- Plunge-Frozen Cryo-TEM; a sample which has been plunge frozen onto a lacey carbon film TEM grid and transferred to the TEM under cryogenic conditions.
- Blotted Dry Sample; where a drop was placed onto a continuous carbon film TEM grid and the grid was blotted using the Vitrobot.
- Air-Dried Droplet; where a drop was placed onto a continuous carbon film TEM grid held in the air using a pair of self-closing tweezers.
- Plunged into slush nitrogen for cryo-FIB-SEM imaging.

The cryo-TEM samples were initially compared to a dry and PF-VD sample on a continuous carbon film (Figure 4.2), showing the cryo-TEM images contain a higher

concentration of nanoparticles and larger agglomerates when compared to the other preparation methods for both sample concentrations. This might be due to a combination of the use of blotting prior to plunge freezing and the type of carbon film used. The presence of holes in the lacey carbon film might allow for a greater concentration of NPs to accumulate after the blotting step. Further work would be needed to verify this hypothesis, including measuring NP concentrations using support films with different hole sizes and different materials. These results should also be compared to more in-depth analysis of samples prepared through other methods such as high pressure freezing and spray freezing, though this goes outside this thesis.

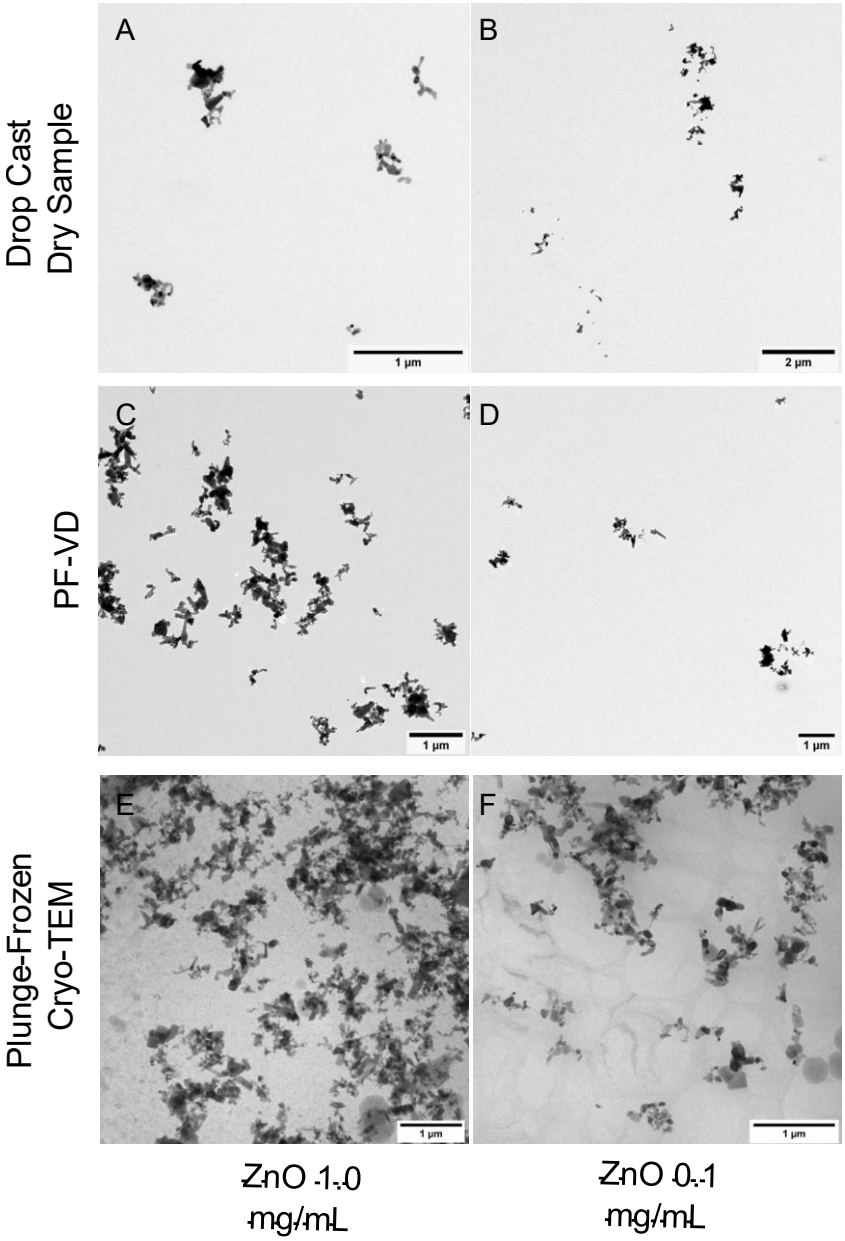

***Figure 4.2 –*** *TEM images comparing samples prepared through drop casting, PF-VD, and plunge-freezing for cryo-TEM imaging. Generally, the dry and PF-VD samples showed a lower presence of NPs compared to the cryo-TEM samples. Electron fluences: 7 $e^-/Å^2$ (E), 10 $e^-/Å^2$ (F).*

A 1.0 mg/mL sample was also prepared by air-drying a drop on a TEM grid, and by blotting a drop using the Vitrobot. It was originally expected that both these new preparation methods would produce samples with similar nanoparticle concentration as the cryo-TEM sample, but with different distributions and agglomerate sizes arising from particles agglomerating during the drying process. Figure 4.3 shows the results of these experiments. All samples except for PF-VD show very large agglomerates (>10 μm), likely generated during the drying process. As the liquid in a nanoparticle dispersion dries, the nanoparticles tend to form densely packed agglomerates following the receding air-water interface [28, 199]. *In situ* TEM imaging of NP dispersions in a liquid cell by Zheng *et al.* [200] shows that NPs are displaced by the advancing air-water interface as the liquid evaporated. The displacement of NPs ahead of the air-water interface results in the formation of agglomerates which are eventually deposited at a rate dependent on their solubility and evaporation rate [161]. Deposition of NPs ahead of the receding air-water interface can lead to concentric rings of deposited NPs (termed “coffee ring” effect) [26, 162]; although these “coffee rings” patterns were not observed in the samples shown in Figure 4.3, there is evidence of particle agglomeration. In particular, the presence of large agglomerates in the blotted and air-dried sample compared to the PF-VD sample shows an increase in agglomerate size due to drying. After both samples were blotted used a Vitrobot, the PF-VD sample was cryogenically frozen in liquid ethane and then placed in a vacuum desiccator to sublime the ice, allowing the ZnO NPs to be deposited onto the supporting film without further drying-induced agglomeration [163].

In contrast, the blotted and air-dried sample allowed to dry in air resulted in the formation of large agglomerates (>10 μm), which are otherwise absent in the PF-VD sample. When compared to the cryo-FIB-SEM results, the PF-VD sample shows similarly homogeneously distributed particles; despite this, the cryo-TEM sample resembles the air-dried droplet sample. This may be caused by the filter paper and blotting paper absorbing part of the droplet (including the dispersed nanoparticles). This is immediately evident in the dry sample, where excess sample was added to the

TEM grid, allowing the drops to be absorbed and dried by the filter paper; given a filter paper was not used for the air-dried drop sample, more nanoparticles remain on the grid. Likewise, the blotting paper may have absorbed some of the nanoparticles in the sample, causing the PF-VD sample to contain fewer nanoparticles. It remains unclear why the nanoparticles in the cryo-TEM samples are not being removed from the grid during the blotting step, though given a lacey carbon grid was used for cryogenic samples, the type of carbon grid may contribute to this effect. The increased presence of nanoparticles on the lacey carbon TEM grid after plunge-freezing could also be partially explained by the possible affinity of the particles to the carbon film. Particle affinity to the carbon film has been observed in plunge-frozen biological particles [75] which can lead to increased particle agglomeration, and preferential orientation of the particles. Alternative sample preparation strategies to address this issue include the use of continuous films (rather than holey or lacey films) [75], and the use chemically treated, or plasma treated graphene films [201, 202].

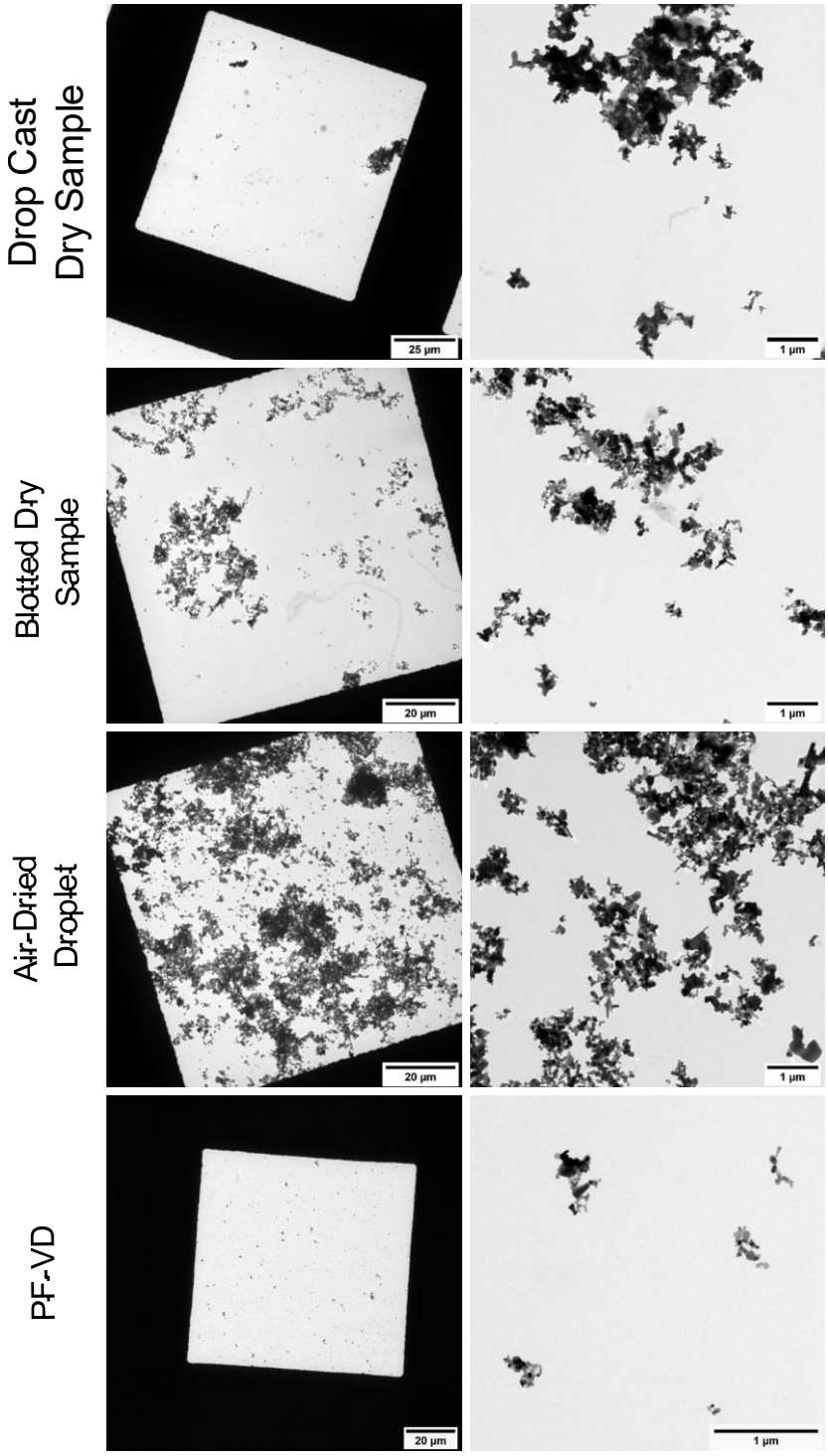


***Figure 4.3 –*** *TEM images of the dry ZnO 1.0 mg/mL samples.All samples except for PF-VD show drying artefacts in the form of large NP agglomerates; the air-dried droplet sample generated images that more closely resemble the nanoparticle concentrations seen in cryo-TEM.*

### 4.1.3 Cryo-(S)TEM Particle Analysis

Cryo-TEM and cryo-HAADF STEM were used to image 1.0 mg/mL and 0.1 mg/mL ZnO NPs plunge-frozen on a lacey carbon TEM grid and cryo-transferred to the TEM (Figure 4.4). Both samples showed the presence of large nanoparticle agglomerates. Agglomerates in both samples appear very close together, and due to the 3D nature of the sample, nanoparticle clusters that are positioned above each other appear as a single, larger agglomerate when viewed in 2D. Due to the ZnO NPs being enclosed within a layer of ice, it is difficult to interpret the agglomerates due to the possibility of out-of-plane particles which cannot be easily visualised through 2D imaging. Issues imaging these 3D structures can be mitigated by tilting the sample or employing tilt tomography to better visualise the position of out-of-plane particles. This approach can be used to visualise the three-dimensional structures such as NP agglomerates [199], NP assemblies [203], and the position of NPs in 3D space [113, 114, 204]. Frost particles are visible during cryo-(S)TEM imaging as a result from the transfer of the plunge-frozen sample into the microscope.

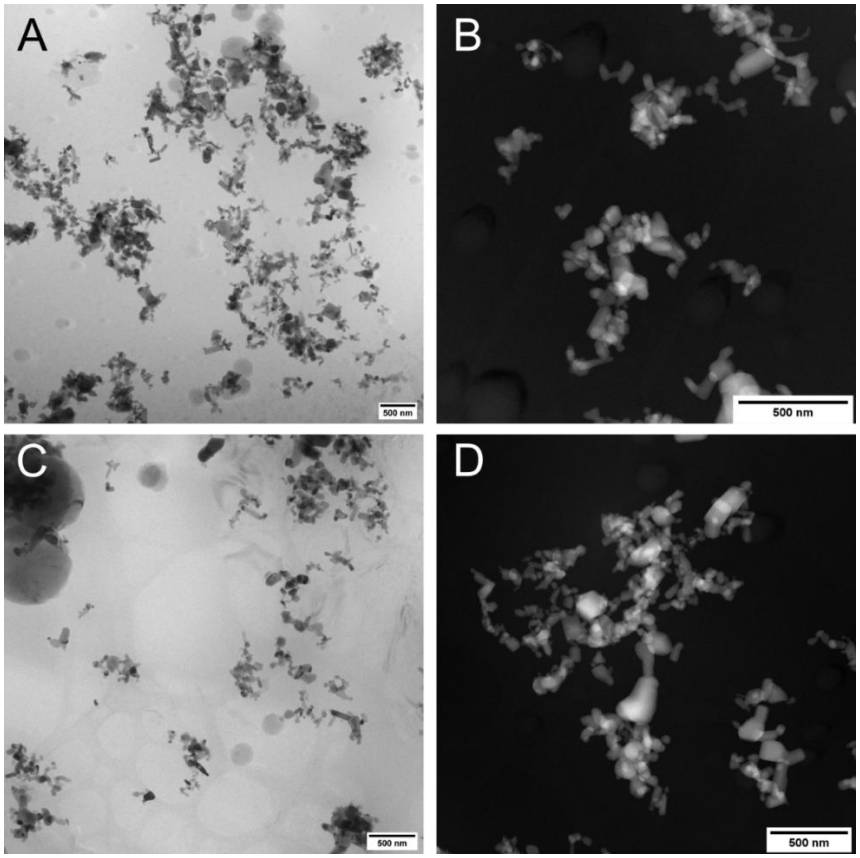


***Figure 4.4 –*** *Cryo-TEM and cryo-HAADF STEM images of ZnO nanoparticles. A) and B) show the 1.0 mg/mL sample in bright field cryo-TEM and cryo-HAADF STEM mode*

*respectively; C) and D) show the 0.1 mg/mL sample in bright field cryo-TEM and cryo-HAADF STEM mode respectively. It is difficult to interpret the nanoparticles in a) as forming either a large agglomerate, or agglomerates close to each other yet overlapping in the z-direction. Electron fluences: 0.7 $e^-/Å^2$ (a), 5.8 $e^-/Å^2$ (b), 0.7 $e^-/Å^2$ (c), and 3.9 $e^-/Å^2$ (d).*

Sample differences seen across the different preparation methods in Figure 4.2, Figure 4.3, and Figure 4.4 suggest that both the preparation methods (i.e. drying in air versus cryogenic freezing) and the supporting film in the TEM grids (i.e. continuous film versus lacey film) may affect the distribution of the NPs on the grid. In the dry samples shown in Figure 4.3 the particles are deposited onto the supporting film, therefore generating a mostly flat sample; large agglomerates may contain NPs overlapping in the z-direction, but separate NPs or agglomerates will deposit on the same plane, making the interpretation of agglomerate sizes straightforward. On the other hand, sample cryo-fixation generates a 3D sample wherein the NPs and agglomerates can be distributed within the entire ice thickness (Figure 4.5). Moreover, the type of support film used could affect the ice thickness and the size of agglomerates that can be contained within the ice, with holes in the film allowing for larger agglomerates (Figure 4.5-C and Figure 4.5-D).

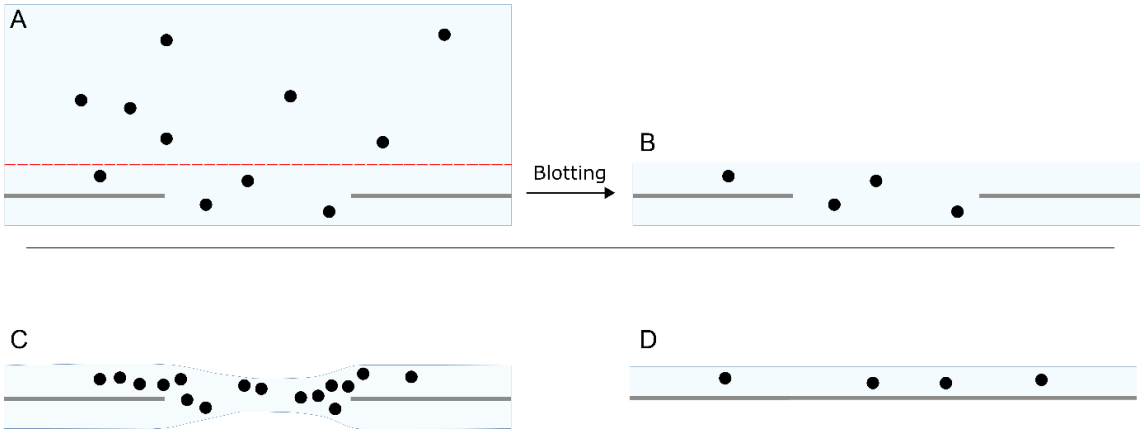


***Figure 4.5 –*** *Diagram showing the possible effects of blotting to the nanoparticles in a dispersion. A) idealised NP dispersion on a lacey TEM grid before blotting (TEM support film in grey). B) Idealised diagram of the thin liquid film after blotting. Here, part of the liquid volume is removed by the filter paper, leaving the NPs within a thin*

*film. C) Possible distribution of the NPs as observed in cryo-(S)TEM, where the NPs have enough space to form larger agglomerates. D) Possible distribution of the NPs after blotting on a continuous carbon TEM grid, as seen from the TEM imaging of PF-VD samples.*

### 4.1.4 Volume Analysis of Frozen ZnO NP Samples

The 1.0 mg/mL ZnO NP sample was appropriately prepared for cryo-SEM through being frozen, fractured, and sputtered as detailed in the Materials and Methods section. The fractured surface was imaged using cryo-SEM in preparation for “slice and view”. ZnO agglomerates were visible on the ice surface after fracturing using backscattered electron imaging (

Figure *4.6*). After fracturing, the ice surface was further sublimed to fully expose the nanoparticles, thus allowing for easier imaging.

When compared to the cryo-TEM images of the same samples, the ZnO nanoparticles were very difficult to find along the ice surface and showed no sign of larger agglomerates as seen in both cryo-TEM samples. BSE can be helpful for the imaging of smaller nanoparticles due to the higher penetration of BSE as opposed to SE, which allows to visualise the particles a few nanometres within the fractured ice surface [205].

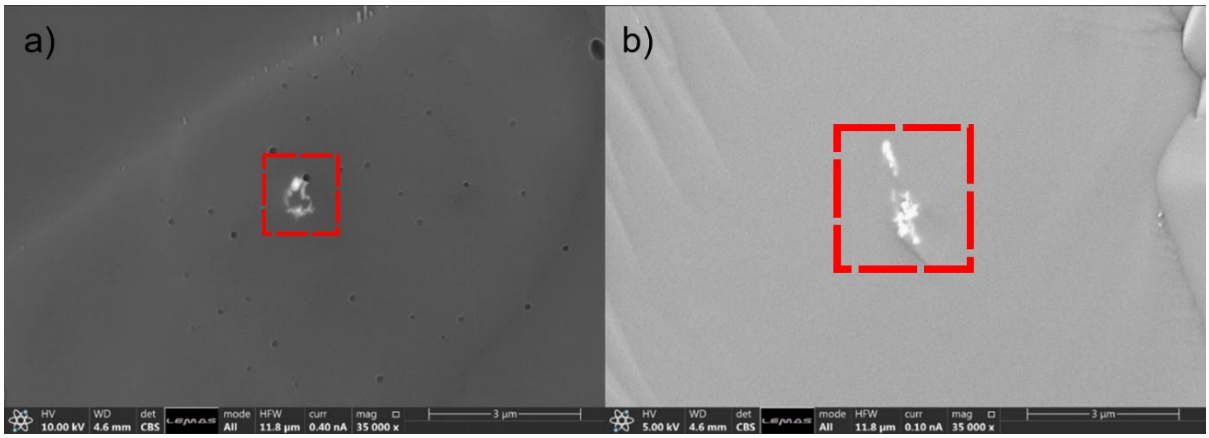


*Figure 4.6 – Cryo-SEM images of the 0.1 mg/mL ZnO nanoparticles. a) and b) show backscattered images of the fractured sample. The black dots visible in both images are likely air bubbles or other artefacts arising from partial ice crystallisation due to slush nitrogen being the chosen cryogen.*

A “slice and view” dataset was obtained for the 1.0 mg/mL ZnO nanoparticle sample, in an area where nanoparticles were located on the fractured ice surface. A focused ion beam was used to mill the selected area, exposing a sample cross-section. This section was then imaged using the “slice and view” method, imaging the exposed cross-section and then FIB milling to remove the surface of the cross-section to progressively expose more of the sample volume [81, 89, 116, 178]. The higher concentration sample was chosen for “slice and view” due to the higher chance of finding nanoparticles within the chosen volume, given the long wait time to obtain a full dataset. The resulting image stack was reconstructed into a full volume (approximately 23 x 26 x 37 µm) and visualised using Imaris software, which was also used to generate 3D objects for the nanoparticles (Figure 4.7).

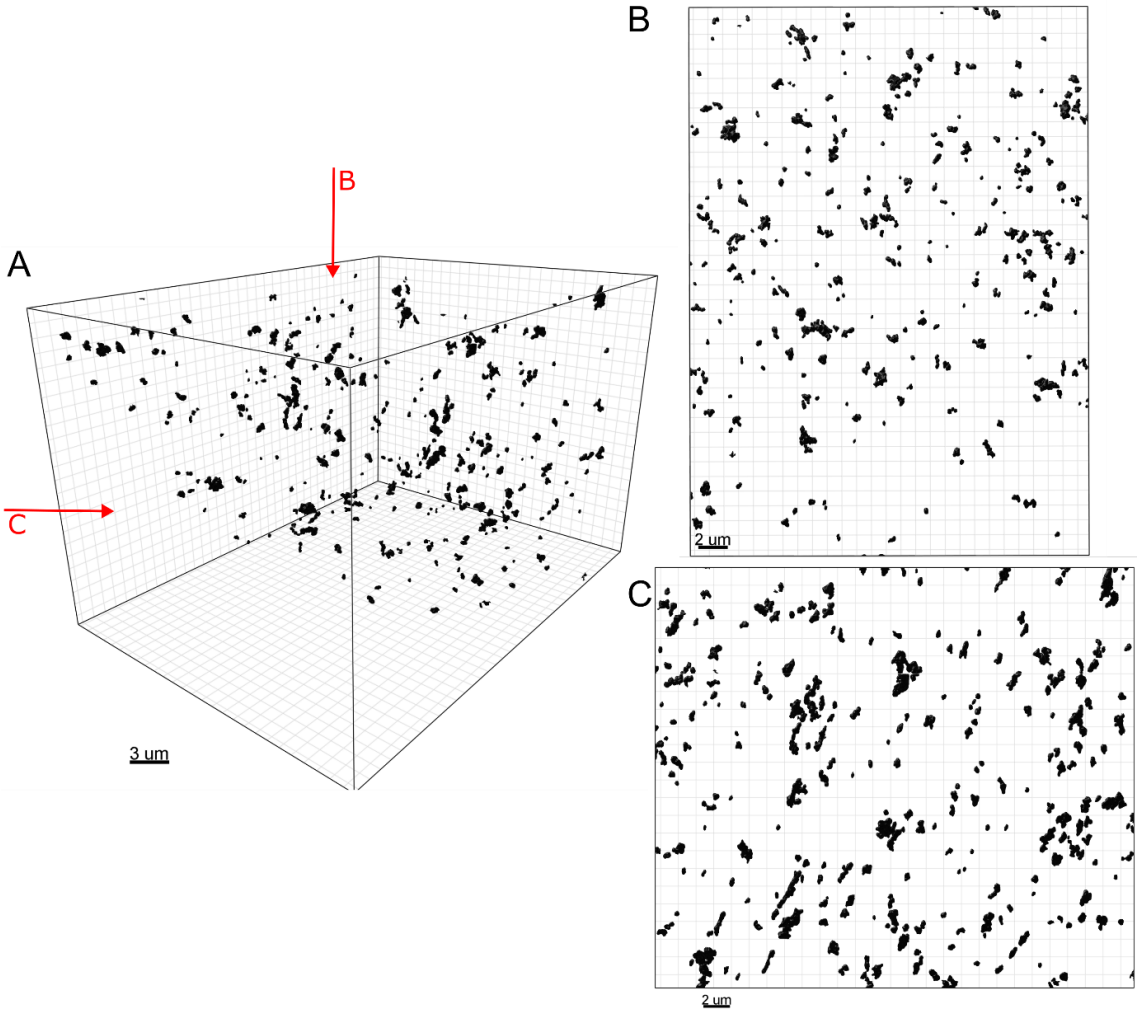


***Figure 4.7*** *– 3D image of the 1.0 mg/mL ZnO cryo-FIB-SEM dataset. This shows the full volume, with B) and C) being projections of the full volume from the top and frontal*

*planes (highlighted in red). Note the top plane (B) corresponds to the view in the "slice and view" stack.*

The 3D image of the sample volume shows the nanoparticles to be homogeneously distributed throughout the imaged volume, though the nanoparticle concentration and agglomerate size appear to be smaller than what is imaged in the cryo-TEM images for the same sample (see Section 4.1.5 "Agglomerate Size Analysis of ZnO NP Samples"). An orthogonal view of a 2 µm thick slice of the volume (Figure 4.8) was taken to better approximate the volume that would be present in a cryo-TEM sample. This thickness was chosen to ensure that none of the NP agglomerates within the slice were truncated. However, this view further shows the concentration of nanoparticles in the cryo-TEM sample (Figure 4.4-C and -D) was much higher.

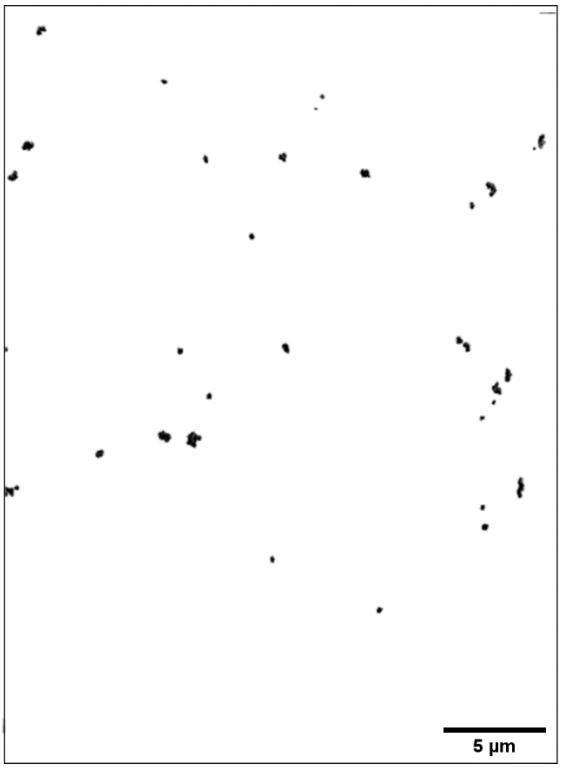


***Figure 4.8*** *– 2 µm thick slice of the 3D volume represented in Figure 4.7.Despite the slice thickness used here being larger than that of the ice in cryo-TEM, the particle density seen in cryo-FIB-SEM is much lower.*

The volume of the 3D object was recorded and used to approximate the ZnO concentration in this volume. The approximated volume was calculated to be 3.3 mg/mL; the difference in this result compared to the original 1.0 mg/mL dispersion may

be due to the creation of 3D objects overestimating the volume of the aggregates, which is necessary to ensure the smaller particles are also included within the threshold value used to create the 3D objects. Cryogenic freezing through plunging in slush nitrogen has limited uses as it is only suitable for freezing up to 2-5 μm thick samples [206]. Beyond this size, the rate of heat transfer for slush nitrogen is insufficient for the vitrification of water, thus resulting in the formation crystals and eutectic ridges that can cause structural changes to the sample by displacing particles [27, 206-208]. The apparent preferential orientation adopted by the ZnO NPs in Figure 4.7-C might be the result of improper vitrification, though it is unclear from this dataset alone if the agglomerate sizes might be affected by this. When attempting to cryogenically freeze samples beyond 2-5 μm in thickness, high pressure freezing is a more suitable sample preparation method. Studies such as Efthymiou *et al.* [206] show the displacement of material (in this case fibrils in a pectin gel network) when frozen using slush nitrogen; on the other hand, these artefacts are absent when freezing the sample using alternative methods such as propane jet freezing or high pressure freezing [207, 209, 210]. Unfortunately, freezing in slush nitrogen was chosen for this study due to the unavailability of a high pressure freezer.

### 4.1.5 Agglomerate Size Analysis of ZnO NP Samples

Measurements for all samples (Figure 1.9) show a higher mean diameter length compared to the DLS results (~435 nm), perhaps due to further agglomeration either due to the drying process or blotting. The cryo-FIB-SEM sample shows the most differences compared to other samples, given that no particles smaller than 100 nm or particles larger than 2.5 μm were measured, despite both sizes being observed frequently in other samples. The lack of smaller particles can be attributed to the resolution limit chosen for the cryo-SEM during “slice and view” acquisition, with voxel sizes of 27 x 34 x 34 nm for the x-, y-, and z-axis respectively. There are trade-offs to be made in selecting cryo-FIB-SEM conditions; with smaller voxel sizes potentially resolving small agglomerates or individual particles, however limiting the overall volume analysed, and vice versa. The presence of very large particles in conventional TEM can be attributed particle agglomeration during the drying process due to the capillary effect. The cryo-TEM samples presented very large agglomerates (as seen in Figure 4.2), though this is not reflected in Figure 4.9, as the large agglomerates

were often too large to fit entirely within the field of view and spanning the entire grid square. These large agglomerates were not included as it was challenging to determine when these were single large agglomerates or a collection of smaller agglomerates.

As previously stated, it is still unclear why the cryo-TEM sample contains these larger agglomerates, while the PF-VD sample does not; although this difference may be caused by the carbon film in the TEM grids, as the holes in the lacey film may allow for the presence of a thicker water film after blotting (compared to a continuous film grid) which would in turn result in the presence of larger agglomerates. The mean particle size as measured through EM imaging in Figure 4.9 was consistently higher than the ~435 nm average particle size measured in DLS, with mean particle sizes ranging from 521 nm in cryo-TEM to 680 nm (for cryo-FIB-SEM, and closer to the average sizes of the remaining samples). This discrepancy can be explained by the polydispersity of the system as seen in DLS, with most of the size distributions measured in EM being within the DLS peak width. This shows that the results shown here are inconclusive, with a more monodisperse system being a possible alternative to obtain more conclusive evidence of the extent of particle agglomeration using these sample preparation conditions.

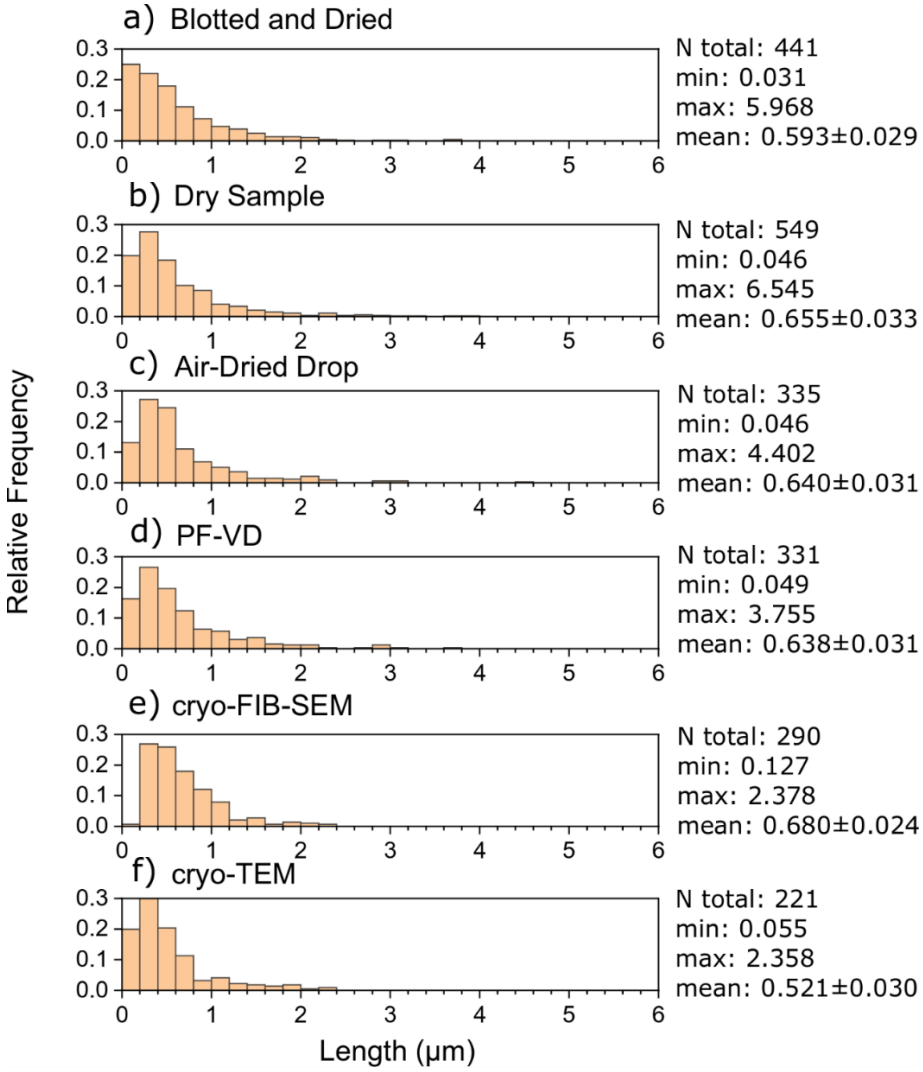


***Figure 4.9*** *- Diameter length for the 1.0 mg/mL ZnO nanoparticle agglomerates for a) the blotted dry sample, b) the dried sample, c) the air-dried drop sample, d) the PF-VD sample, e) the cryo-FIB-SEM sample, and f) the cryo-TEM sample. All measurements are in μm. Agglomerate sizes were taken as the feret diameter, measured using ImageJ's particle analysis function. Agglomerates near the edges of the images were excluded from the analysis, thus decreasing the amount of large (>10 μm) agglomerates measured in the plunge-frozen, cryo-TEM samples.*

### 4.1.6 ZnO NP System Summary

The results from this ZnO NP study are complicated as the suspension is not homogeneous; it is clear there are a range of differently sized NP agglomerates from the DLS and various EM imaging approaches. A simpler system, which perhaps was either monodisperse or formed regularly size agglomerates would have provided a

route to more conclusive results regarding the impact of sample preparation method. However, laboratory access at the time this experimental work was undertaken was limited.

Despite these challenges, TEM and cryo-STEM imaging of these ZnO NPs has shown a difference in the apparent sample concentration on the TEM grid depending on the preparation procedure and type of TEM grid used. The difference between the PF-VD sample on a continuous carbon TEM grid compared to the plunge-frozen samples on a lacey carbon TEM grid is especially useful, as the presence of large >1μm NP agglomerates could signify that cryo-TEM using lacey carbon TEM grids might allow for the presence of Pickering emulsion droplet clusters. This contrasts with the results found with continuous carbon grids where only NP agglomerates up to ~3μm were measured, thus would only accommodate individual droplets or small clusters of few droplets. This, however, does not inform us on the possible effects of sample blotting during the plunge-freezing process, which might cause the droplets to be deformed, especially if in large clusters. This will have to be tested by directly imaging Pickering emulsion samples with droplets of different sizes to check whether the droplets might collapse as a result of sample preparation. Cryo-FIB-SEM imaging appears to be more suitable when there is a need to image a larger sample volume in a cryogenically prepared sample, when there is a need to analyse interactions between larger agglomerates.

## 4.2 Gold Nanoparticle Core-Satellite System

The second system discussed in this chapter consists of gold nanoparticles (Au-NPs) coated in glycans that can bind with lectin viral receptors (DC-SIGN and DC-SIGNR) [138, 139, 211]. These nanoparticles can be used as probes for multivalent lectin-glycan interactions using the fluorescence of Au-NPs [211]. The specific Au-NP system examined in this section consists of ~5 nm and ~13 nm Au-NPs that are designed to form “core-satellite” structures with the ~13 nm Au-NPs surrounded by several ~5 nm nanoparticles, and were provided by the group of Professor Dejian Zhou, School of Chemistry, University of Leeds.

The main challenge presented by the preparation and imaging of this system is the preservation of nanoparticle clusters showing the core-satellite structure where a

larger nanoparticle is surrounded by smaller nanoparticle. Drop casting a drop of sample directly onto a TEM grid is a simple and effective preparation method that can be used for the imaging of nanoparticles but is unsuitable for this core-satellite system due to anticipated sample drying artefacts such as coffee stain artefacts resulting in the nanoparticles forming agglomerates near the receding air-water interface [28, 199]. As with the ZnO system, plunge-freezing followed by cryo-(S)TEM imaging, or vacuum-drying for standard dry TEM imaging are both promising techniques to preserve the sample's core-satellite structure while imaging.

Initial imaging consisted of preparing the sample through a simple drop casting method for standard TEM imaging as presented in Figure 4.10, which shows the presence of both core-satellite structures and areas with Au-NPs forming large agglomerates.

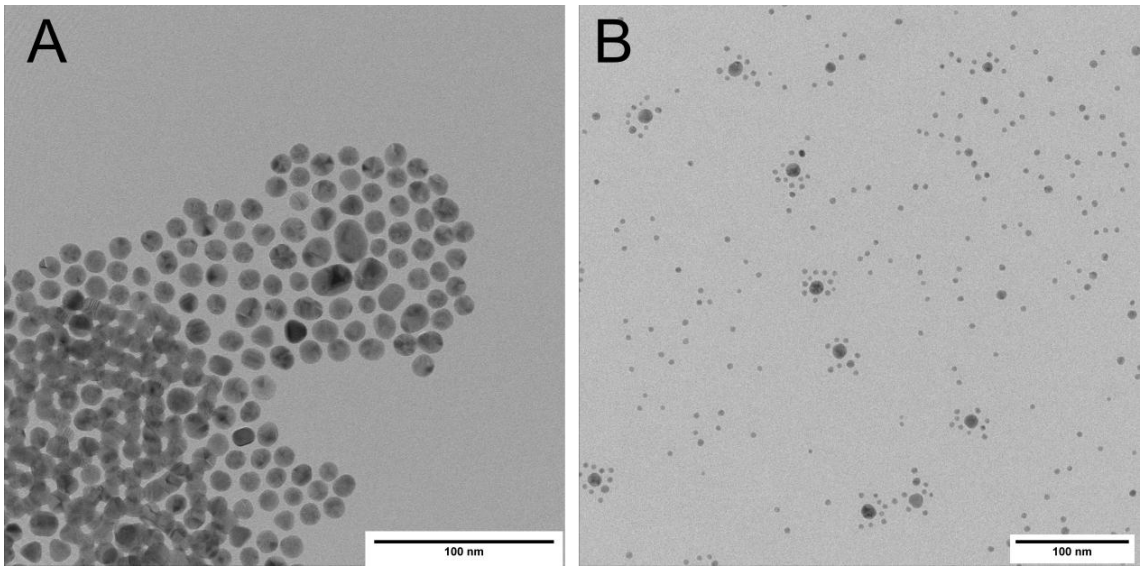


***Figure 4.10 –*** *TEM images of a drop cast Au-NP core-satellite sample showing A) an area with heavily agglomerated particles and B) an area showing some core-satellite structure but also a large number of Au-NPs found individually.*

### 4.2.1 Plunge-Frozen Vacuum Dried Samples and Cryo-TEM

To preserve the core-satellite structure during TEM imaging, the sample was prepared via plunge-freezing and then imaged in cryo-(S)TEM and standard TEM after being vacuum-dried (Figure 4.11). Although both preparation methods are expected to retain the native sample structure [180], there should still be differences between the two methods given the absence of an ice layer in the PF-VD sample. Specifically, the NPs

in the cryo-TEM sample are suspended within the ice and are therefore distributed not only on the x-y plane, but also on the z-axis throughout the ice thickness. In contrast, the particles in the PF-VD sample are deposited onto the carbon film, therefore the sample is not expected to retain any three-dimensionality. This can be partly seen when comparing the particle distributions in Figure 4.11-A (PF-VD) and Figure 4.11-B (cryo), as in the former the particles are seen to be separated from one another, even in the case of neighbouring particles, while in the latter some particles are seen to be overlapping. The apparent overlap between particles in cryo-TEM could be resulting from the particles being positioned on top of each other in 3D space, though it remains unclear from 2D imaging alone whether these particles touch each other.

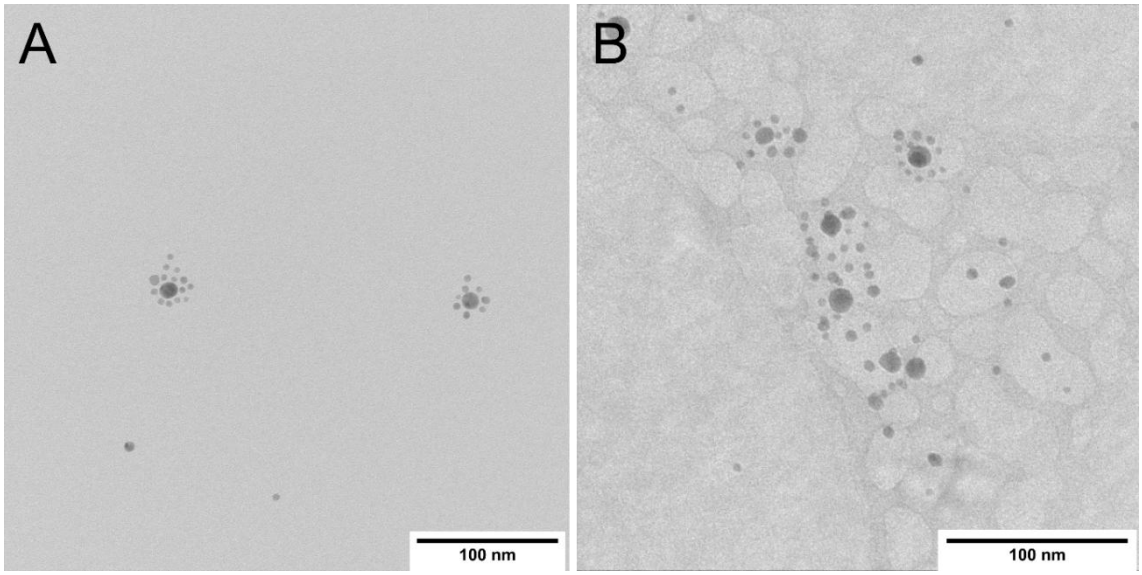


**Figure 4.11** - a) PF-VD and b) Cryo-TEM images of core-satellite gold nanoparticles. *Both the vacuum-dried and the cryogenically imaged samples retain the core-satellite structure, though there are more nanoparticles touching in the cryo-TEM sample. This might be due to the nanoparticles trapped in the vitreous being allowed to position themselves in 3D space rather than being deposited in a plane and therefore appearing to be overlapping.*

This effect becomes more apparent when attempting to measure the distance between neighbouring particles, including the distance between all particles, both core and satellite. Figure 4.12 shows the nearest neighbouring distance (NND), measured as the distance between the centre of the two closest particles for both cryo and PF-VD

samples. Both sample preparation methods show a mean NND larger than the ~5 nm sized Au-NPs (PFVD mean: 15.8+1.1 nm, cryo-EM mean: 11.4+0.5 nm), though the minimum distance between particles in cryo-EM is significantly lower than that of the PF-VD sample (PFVD minimum: 4.5 nm, cryo-EM minimum: 1.7 nm). Moreover, when manually counting the number of Au-NPs touching their nearest neighbour, it was found that in the PF-VD sample there were 16 cases of particles touching (across 23 images), while in the cryo-EM sample there were 209 cases (across 20 images). Both observations can be explained by the three-dimensionality of the cryo-EM sample. Electron tomography of the cryo-prepared sample will enable 3D visualisation of the sample, allowing for the analysis of the particle distribution in three dimensions. 3D imaging of nanoparticle samples through tilt tomography is often used to visualise particle orientation and observe the presence of particles out of plane [204, 212].

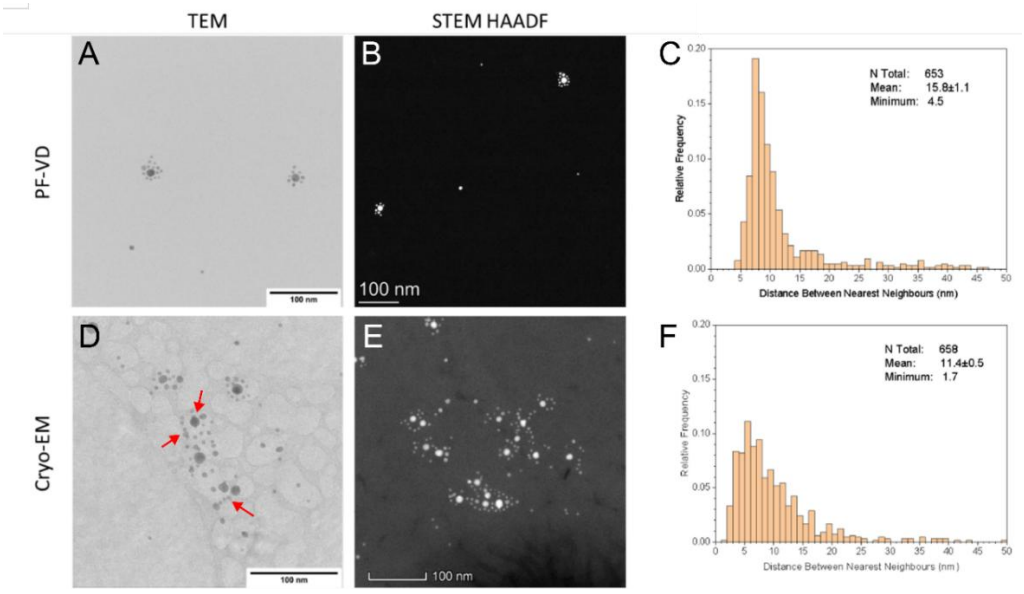


***Figure 4.12 -*** *TEM and HAADF STEM images of the sample prepared through PF-VD and for cryo-EM imaging. Graphs on the right show the distance between the nearest neighbouring particles for each sample preparation method. A) TEM image of a PF-VD sample. B) HAADF STEM image of the same PF-VD sample as in (A). C) Nearest neighbour distance between particles in the sample seen in (A) and (B). D) Cryo-TEM image of a plunge-frozen sample. E) Cryo-HAADF STEM image of the same plunge-frozen sample as in (D). F) Nearest neighbour distance between particles in the sample seen in (D) and (E). The red arrows in (D) indicate NPs that appear to be touching, in contrast with the particles in the PF-VD sample which do not touch each other.*

### 4.2.2 Cryo-Tilt Tomography of the gold nanoparticles

A cryo electron tomogram was produced from images collected in a tilt series in a ±60° range, with an image collected every 5°. The images were collected with a 0.39 nm/px resolution, and with a probe current of ~2 pA. This resulted in a total electron fluence of ~ 600 $e^-/Å^2$. Notably, this value is higher than what is generally reported for cryo-ET in biological studies, where electron fluence is kept below ~100-200 $e^-/Å^2$ [213-216]. This difference in total electron fluence without major sample damage is only possible because of the damage mechanisms experienced in biological samples versus inorganic samples. The Au-NPs themselves are not beam sensitive, therefore the only damage observed comes from ice sublimation. In contrast, biological samples are beam sensitive and often have a damage threshold below what would be needed for observable sublimation. The data set was reconstructed using SIRT, after which surfaces were created in the Imaris software using the particle creator function to better visualise the Au-NPs. The size of the particles was automatically created from the HAADF STEM signal and then adjusted to match the particle sizes measured from cryo-HAADF STEM images (Figure 4.13). This was done to ensure that the size of the surfaces created reflects accurately the size of the Au-NPs observed in cryo-(S)TEM images. The surfaces created through this function are always spherical regardless of the shape of the original particle, which was useful to eliminate the elongation along the z-axis arising as a missing wedge artefact. The particle size adjustment was additionally important to compensate for any inaccuracy from the missing wedge and low signal-to-noise ratio in the HAADF STEM images.

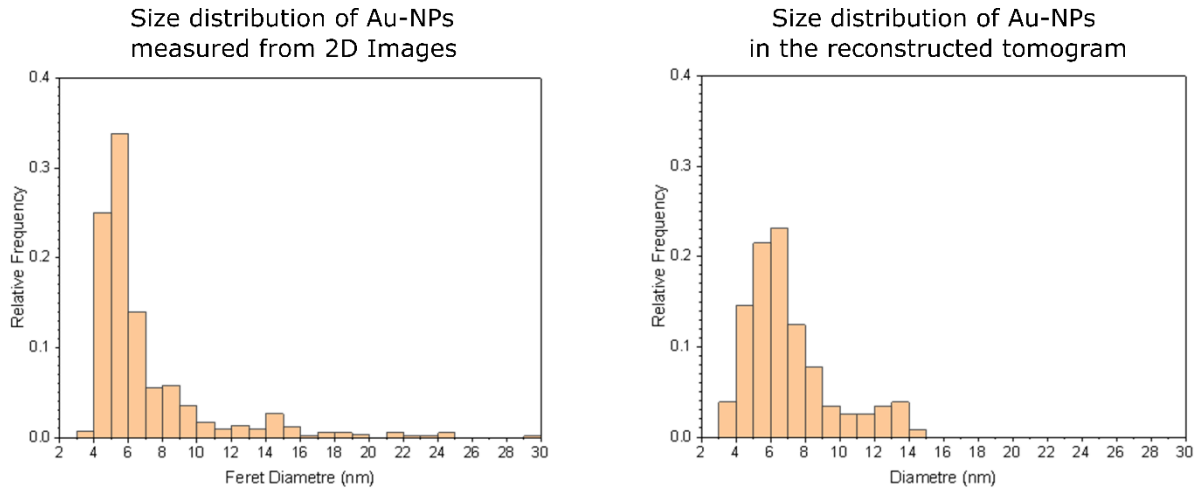


***Figure 4.13*** *– Size distribution measurements for the Au-NPs in cryo-STEM, and for the same 3D particles created in the electron tomogram. The size of the 3D spheres was tuned during their creation to follow the size distribution seen in the cryo-prepared sample.*

Figure 4.14 shows images from the electron tomogram and the original area of interest (Figure 4.14-A); as was seen from regular cryo-(S)TEM images, some Au-NPs appear to be touching when observed from an above view. A side view of the tomogram (Figure 4.14-C) shows the particles to be distributed along the thickness of the ice, confirming that the particles are not in direct contact with each other (as interpreted from the 2D images).

Overall, the core-satellite structure is retained in 3D, with the smaller Au-NPs surrounding the larger particles in all directions. A preference for particle distribution along the ice surface remains in this sample, with Figure 4.14-C showing a strong tilt likely caused by the local shape of the ice [217, 218]; the satellite particles are also preferentially distributed near the ice surface, though to a smaller extent, as some particles are still seen above and below the larger “core” particles. Preferential distribution of nanoparticles along the air-water interface is a well-known issue when plunge-freezing in biology, with Noble *et al.* [204] finding that approximately 90% of all particles are localised to the air-water interface (from 50 different grids) approximately 5-10 nm from the interface, as visualised using tilt tomography. This absorption onto the air-water interface has been observed in a wide range of nanoparticles including proteins [219], viruses [220], nanocrystals [221], and nanoparticles [217], all of which

may adsorb onto the air-water interface in preferred orientations [204, 217, 222, 223]. The plunge-frozen core-satellite structures appear to be preferentially orientated on-plane, i.e. the satellite NPs are mostly found on the same plane in-line with the plane of ice and perpendicular to the beam. This explains how the majority of core-satellite structures appear two-dimensional with the exception of some NPs that are further within the ice volume and therefore appear to overlap in 2D imaging (as visualised in the diagram in Figure 4.15). The adsorption of nanoparticles to specific interfaces occurs during the waiting period between sample blotting and vitrification; at this point the water film is only a few nanometres thick, and the nanoparticles can easily collide with the air-water interface multiple times before vitrification. Decreasing this waiting time to below ~200 ms by Noble *et al.* [224] has been shown to result in a 20-fold increase in “free-floating” particles within the ice volume, though such a drastic decrease in waiting time (compared to >1 seconds achieved by the Vitrobot) require the use of especially-made plunge-freezers such as microfluidic spray-plungers [220, 224-226].

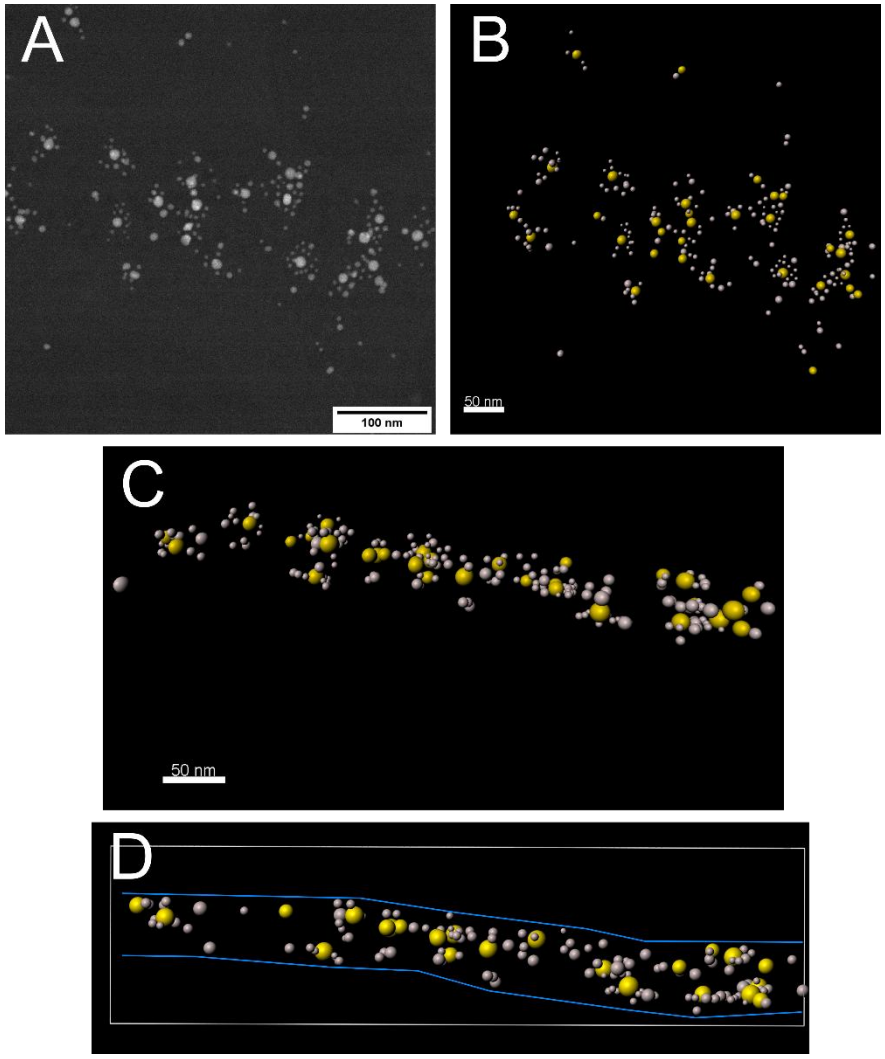


***Figure 4.14 –*** *Images from an electron tomogram of the Au-NPs core-satellite sample showing A) cryo-HAADF STEM image of the area of interest imaged for 3D reconstruction. B) Image from the reconstructed tomogram, taken from the same angle as the original HAADF image. C) Image from the tomogram taken perpendicularly from B. Particles with size above 13.0 nm are shown in yellow, while smaller particles are shown in grey. Note the particles in the tomogram appear perfectly circular as they were created using the particle creator function in Imaris; this does not reflect the real NP shape. D) Projected view along the same axis as C, showing the proposed ice layer (shown in blue). This proposed ice layer assumes the NPs at the top and bottom of the volume are near the air-water interface, as the ice itself could not be imaged due to lack in contrast [224]. Total electron fluence: 700* $e^{-}/Å^{2}$.

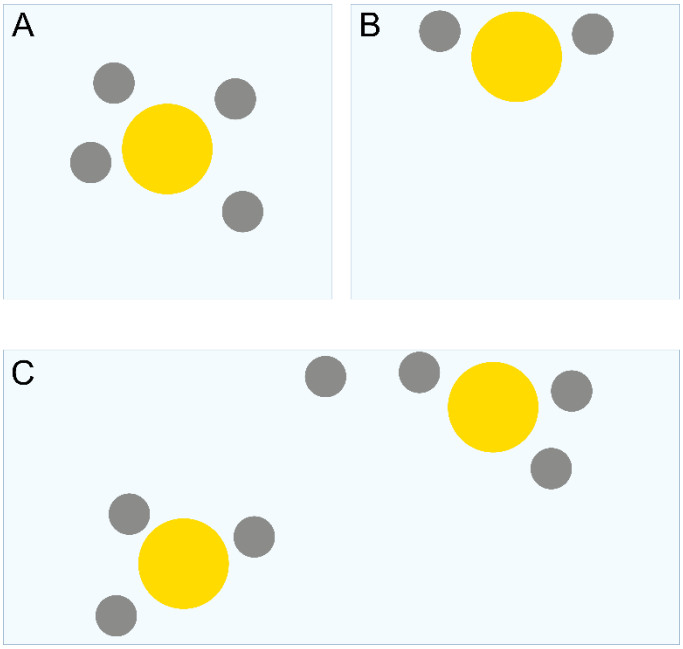


***Figure 4.15 –*** *Schematic showing the possible positions and orientation of the core-satellite structures within the ice layer. A) Idealised plunge-frozen sample where the NPs are within the ice volume and far from the air-water interface. Here the position of the NPs is solely given by the inter-particle forces resulting in 3D core-satellite structures. B) Sample with all NPs absorbed onto the air-water interface, with the core-satellite structure appearing "flat". C) Diagram more closely showing the position of the NPs as seen from tilt tomography. Here some of the NPs are adsorbed onto the air-water interface, while others are found deeper within the ice volume.*

### 4.2.3 Au NP core-satellite summary

Overall, it was possible to observe the core-satellite structure in the Au-NP system using plunge-freezing to instantly vitrify the sample. Cryo-HAADF STEM imaging shows the presence of these core-satellite structures in vitrified samples, as opposed to drop cast samples where particle agglomeration is a result of the drying process. Electron tomograms were successfully collected through the collection of cryo-HAADF STEM tilt series at a high enough resolution to be able to resolve the smaller ~5 nm Au-NPs, while simultaneously preventing beam-induced damage to the sample. This allowed for the visualisation of the nanoparticles in 3D while retaining their native structure.

Cryogenic preparation and imaging of the sample shows distinct advantages over plunge-freezing vacuum-drying as cryo-(S)TEM imaging allows for the observation of the sample structure in 3D, compared to PF-VD where the particles are deposited onto the TEM grid. Despite the preferential positioning of the Au-NPs near the ice surface, the overall core-satellite structure of the NP clusters is retained and can be seen through the entire ice thickness. Overall, these results that conventional drop-casting and air drying is unsuitable for the imaging of self-assembled structures in their native aqueous state, while PF-VD and cryo-(S)TEM can preserve these structures as seen with these core-satellite Au-NPs. After PF-VD NPs are deposited onto the supporting film on the TEM grid, thus resulting in a 2D projection of the sample's core-satellite structure. This can be beneficial for the measurement of particle size and distances between particles (including nearest-neighbour distances), while losing on the 3D aspects of the particle position. Meanwhile, cryo-(S)TEM can preserve these 3D structures, making measurements from 2D images more challenging due to out-of-plane NP overlap. This makes cryo-(S)TEM imaging especially desirable when using ET. The results obtained with this sample can be applied to the Pickering emulsions systems with 3-5 nm stabilising particles, as the cryo-ET procedure used for the Au-NP system could also be applied to collect tomograms of Pickering emulsion droplets and their stabilising particles.

## 4.3 $TiO_2$ coated in biological media

The third system discussed in this chapter consists of titanium dioxide nanoparticles in a cell culture medium ($TiO_2$–DMEM, Dulbecco's Modified Eagle Medium) prepared by the group of Professor Andy Brown, School of Chemical and Process Engineering, University of Leeds. $TiO_2$ is currently used in a wide variety of applications such as in paints, sunscreen, cosmetics and as additives in food and drugs due to its light-scattering properties and ability to confer whiteness and opacity [227]. $TiO_2$ has been proven to be biologically inert [228, 229] and approved for consumption as a food and pharmaceutical additive [9], but its overall toxicity is yet to be fully understood [227].

The formation of an amorphous coating containing calcium and phosphorus on $TiO_2$ particles has been observed when dispersed in DMEM and subjected to changes in pH [230-232]. $TiO_2$ particles that travel along the digestive tract would experience a

change in pH, and hence this coating may form. Therefore, it is important to understand this system, as any absorption or uptake of $TiO_2$ by cells in this situation may be due to the coating formed *in situ*. TEM imaging can be used to confirm the presence of a calcium and phosphorus coating surrounding particles. In this section, cryo-(S)TEM imaging was employed for the particle analysis to prevent drying artefacts [99], as this previous work has shown that in drying other components of the biological media (e.g., Na, Cl) precipitate out on the particles. EDX spectroscopy and mapping was used for the elemental analysis of the particles and coating. Cryo-ET was used to visualise the particles in 3D to ensure the coating fully surrounds the particles.

The characterisation of this sample using cryo-(S)TEM imaging and spectroscopy in 2D and 3D was used to test the more energy-intensive tilt series acquisition methods integrating spectral data. This sample was suitable for this task for two main reasons: first, the elements Ti (in the core nanoparticles), Ca, and P (in the nanoparticle coating) present in the sample can be identified by both EELS and EDX; second, the $TiO_2$ nanoparticles used in this sample are much larger (~150 nm) than the Pt nanoparticles present in the Pickering emulsion samples (3-5 nm) and are therefore less affected by the initial sublimation of the vitreous ice as a result of beam-induced damage. This means that a higher cumulative damage to the sample will be needed before the emergence of any observable change in the sample structure (i.e. particles drifting as the surrounding ice sublimates), thus allowing for a more generous total electron fluence range that can be used during imaging.

### 4.3.1 Cryo-(S)TEM Imaging

Initial cryo-HAADF STEM imaging of the sample in conjunction with EDX was performed on a plunge-frozen sample to ensure the presence of a particle coating containig calcium and phosphorus. Both cryo-(S)TEM imaging and EDX spectral maps confirm the presence of a coating (Figure 4.16), while EDX confirms the presence of Ca and P signals on the particle coat. EDX analysis of this sample was simple to perform even with a low electron beam current (~10 pA) with a sufficiently high signal-to-noise ratio due to the overall size of the particles (which were found in >400 nm clusters) and the thickness of the coating (~60 nm). This allowed for a strong Ti and

Ca signals, though the P signal was noticeably weaker (as can be partially seen in Figure 4.16-D). Coatings rich in calcium and phosphorus similar to those reported here have been observed in nanoparticle systems in cell culture including $TiO_2$, Au, $BaTiO_3$, ZnO, and $Fe_2O_3$ nanoparticles as seen in studies such as Ribeiro *et al.* [230] and Ilett *et al.* [232], where nanoparticle coatings were observed in nanoparticle systems after prolonged sonication or heating [230, 232, 233].

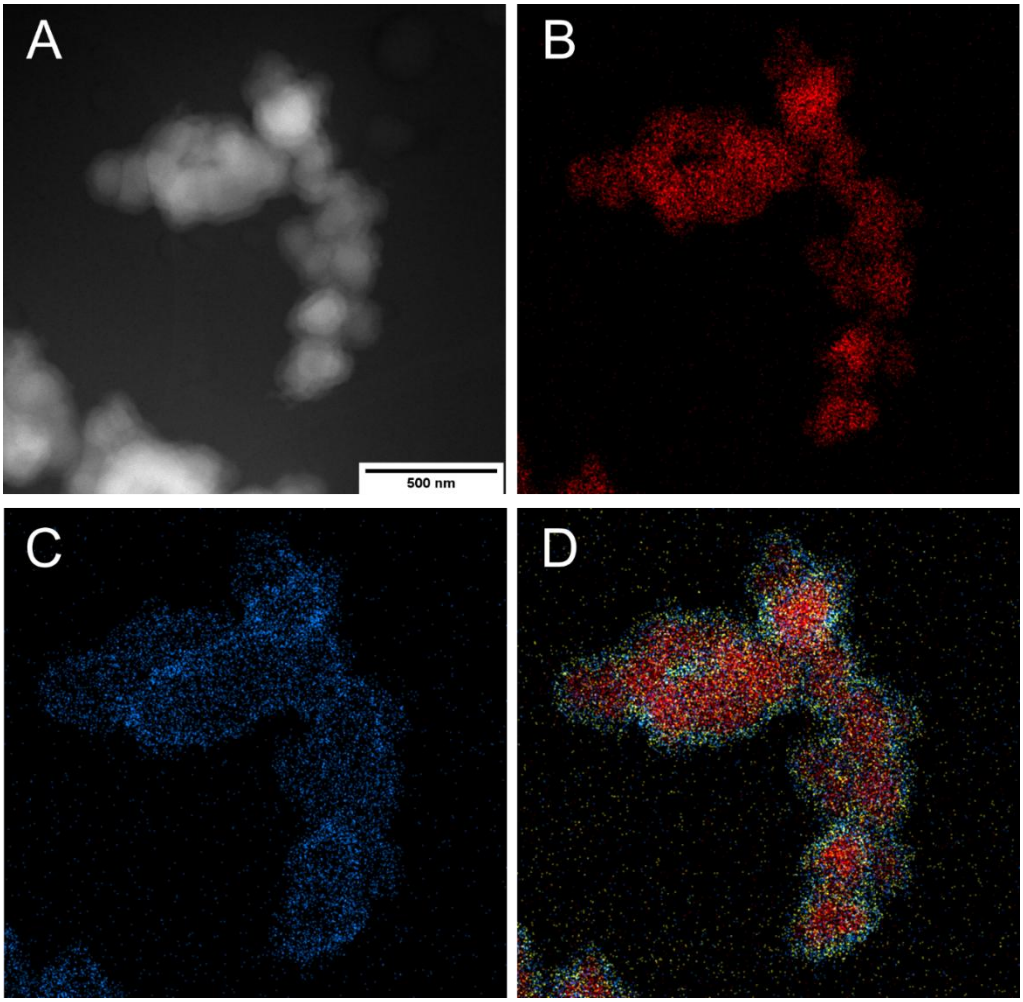


***Figure 4.16 -*** *Cryo-HAADF STEM and EDX maps of the coated $TiO_2$ nanoparticles. Though the coating is already visible with HAADF STEM, EDX mapping confirms the size of the coating and the presence of Ca and P in the coating. A) cryo-HAADF STEM image of a $TiO_2$ particle agglomerate. B) EDX map showing the Ti K$\alpha$ signal. B) EDX map showing the Ca K$\alpha$ signal. D) Composite EDX map showing the Ti K$\alpha$ (red), Ca K$\alpha$ (blue), and P K$\alpha$ (yellow) signals. Total electron fluence: 180 $e^-/Å^2$.*

### 4.3.2 Cryo-HAADF STEM Tilt Tomography

Initial tilt series were collected in cryo-HAADF STEM along a ±60° range with tilt interval of 3°. The resulting tilt series was reconstructed using SIRT. The reconstructed electron tomogram in Figure 4.17 shows that the coating seen in the cryo-HAADF STEM images remains distinguishable after 3D reconstruction even without the use of EDX or other elemental analysis techniques. When observing the particle cluster in 3D, the coating appears to surround the cluster itself rather than the individual particles. The $TiO_2$ particles in the tomogram in Figure 4.17-C appear to directly touch one another, suggesting that the particles might have already formed a cluster before the deposition of Ca and P on the cluster surface. This shows that the particles agglomerate prior to the pH change and remain agglomerated as the coating forms.

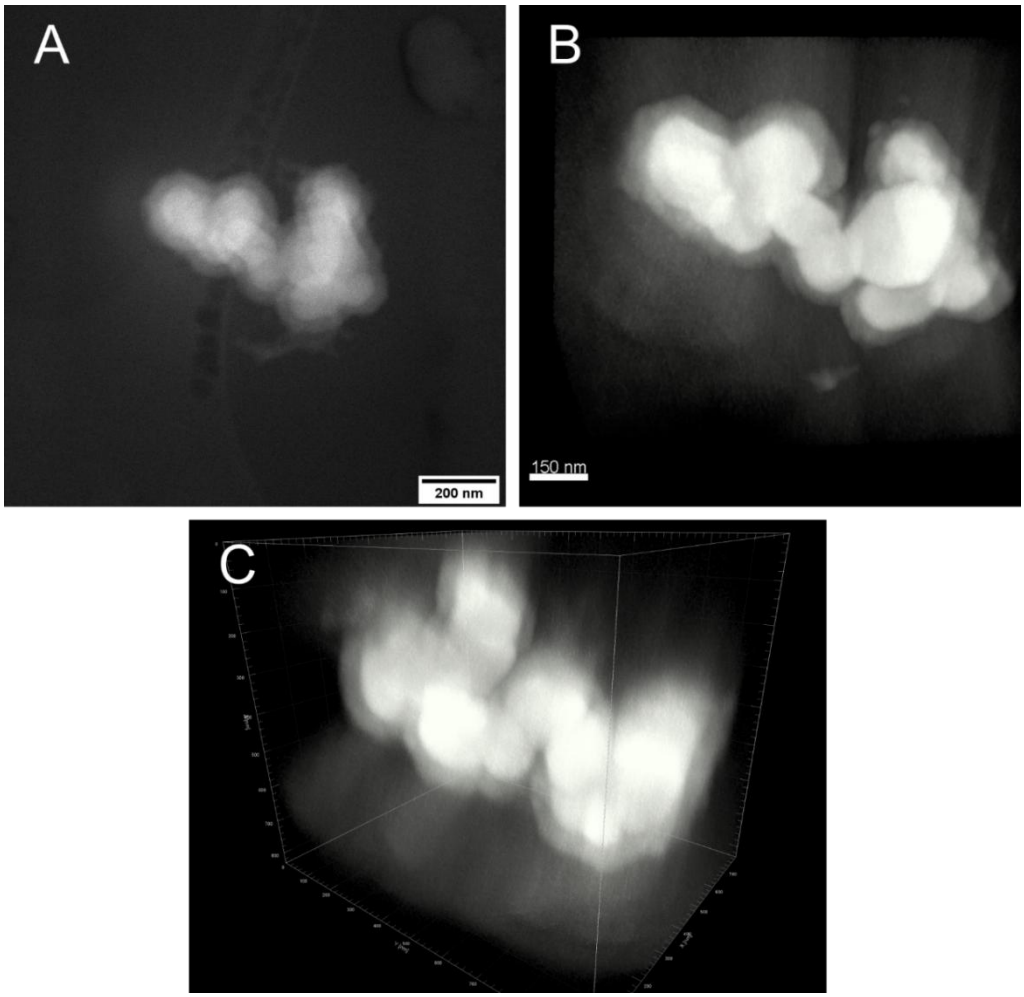


***Figure 4.17 -*** *Cryo-ET reconstruction of a nanoparticle agglomerate consisting of coated $TiO_2$ particles. A) cryo-HAADF STEM image of the area of interest. B) Above-*

*view of the reconstructed tomogram, showing the coating being clearly visible even after reconstruction. C) Tilted view of the tomogram, showing the presence of the coating around the entirety of the coated $TiO_2$ particles. Total electron fluence: 180 $e^-/Å^2$.*

Given the ease of distinguishing the coating from the $TiO_2$ particles and surrounding ice, it was possible to segment the tomogram by simply applying a threshold to the tomogram images. In order to confirm the presence and position of the coating, EDX was performed on the same particles used for electron tomography (Figure 4.18-A and Figure 4.18-B) after the completion of the tilt series. EDX data was collected solely at 0° tilt rather than performing another full tilt series to minimise exposure to the beam. However, EDX data collection should be performed together with the HAADF STEM tilt series to ensure that the elemental data obtained can be applied to a 3D dataset. The result of this image segmentation in Figure 4.18-D and Figure 4.18-E more clearly show the $TiO_2$ particles (shown in red) and the coating fully surrounding them (edge shown in blue). The image segmentation in Figure 4.18-D and -E highlights more clearly the position of the coating layer surrounding the larger cluster. This coating surrounds the entire agglomerate and appears to be consistent (~60 nm) within the centre of the tomogram in the x-y plane (orthogonal to the electron beam at 0° tilt). Coating measurements could not be performed in other planes or at the top or bottom of the agglomerate due to the inaccuracy of the reconstruction because of the missing wedge. It is important to note that the segmentation method presented here was only possible due to the clear contrast from the coating in the electron tomogram. Additionally, this method is limited in its accuracy, as the only elemental information on the sample was obtained at a 0° tilt and therefore does not provide information to segment the tomogram above and below the tilt axis. In the example presented in Figure 4.17 Figure 4.18, the coating can be seen throughout the entire tomogram as the effects of the missing wedge are minor, but in cases where coating is more difficult to distinguish (perhaps due to a lower signal-to-noise ratio or more artefacts) this segmentation method would not be suitable.

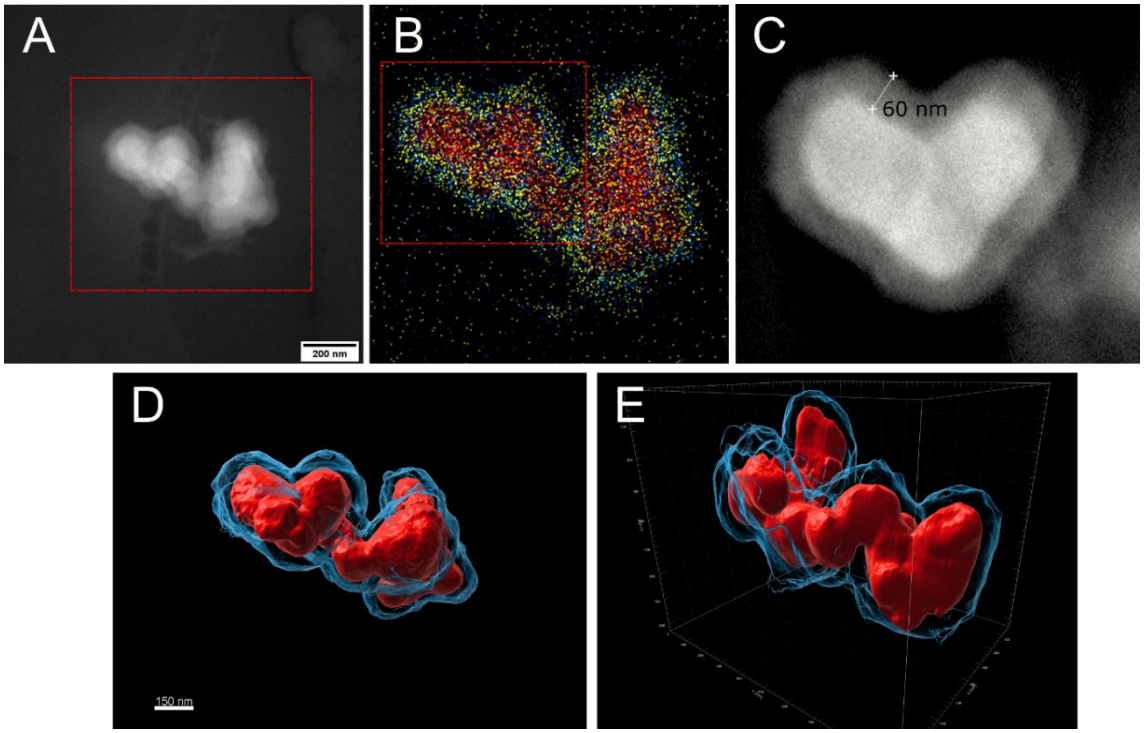


***Figure 4.18 -*** *3D segmentation of the coated nanoparticles using EDX as a reference. A) cryo-HAADF STEM image of the area of interest, with B) the equivalent EDX spectral map showing the Ti Kα (red), Ca Kα (blue), and P Kα (yellow) signals. C) Cross-section of the reconstructed tomogram showing the coating, line measuring 60 nm is shown on the coating. D) Above-view of the electron tomogram after segmentation, with the $TiO_2$ particles being coloured red and coating coloured blue. E) Tilted view of the segmented tomogram. Total cumulative electron fluence (ET and EDX): 300 $e^-/Å^2$.*

### 4.3.3 3D Elemental Analysis using EDX SI Tomographic Reconstruction

A second $TiO_2$ sample with thinner coating (pH = 7.8, see Chapter 3) was prepared for cryo-(S)TEM imaging by plunge-freezing. Cryo-HAADF STEM imaging and EDX as shown in Figure 4.19 confirm the presence of a much thinner coating (~10 nm) compared to the previous sample. In this case, the electron tomography and tomogram segmentation technique shown in the previous section are unsuitable due to the thinness of the coating and it was therefore decided to collect a tilt series composed of EDX elemental maps. This approach should allow for the collection of elemental information at multiple tilt angles, which, after 3D reconstruction, can aid

with the segmentation process by overlapping the tomograms obtained from the cryo-HAADF STEM signal and the EDX Ti Kα and Ca Kα signals. The P Kα signal was not used for further tomography due to the poor signal strength compared to titanium and calcium.

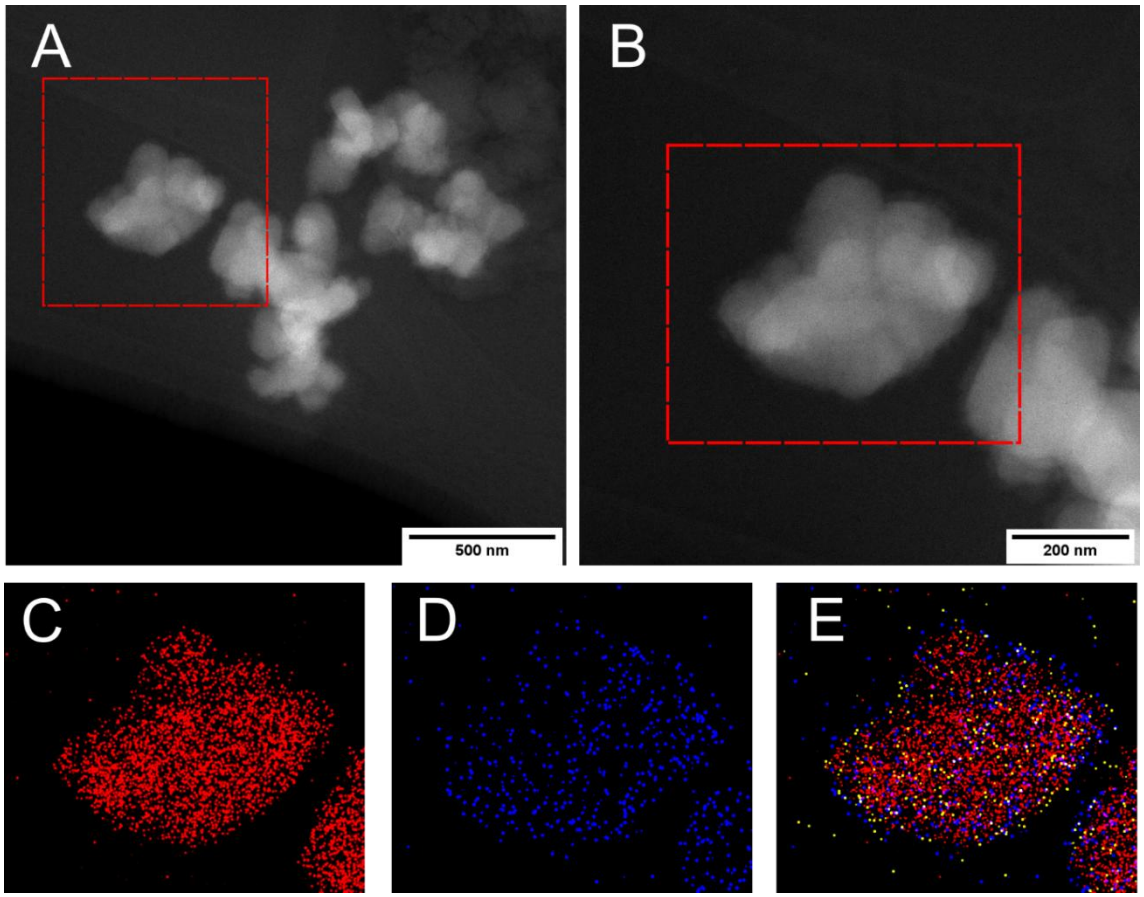


***Figure 4.19 –*** *Cryo-HAADF STEM and EDX elemental map of a sample with smaller coating thickness. A) and B) cryo-HAADF STEM images of a particle agglomerate. C) EDX elemental map showing the Ti Kα signal. D) EDX elemental map showing the Ca Kα signal. E) composite EDX elemental map showing the Ti Kα (red), Ca Kα (blue) and P Kα (yellow) signals. A thin coating containing Ca and P can be seen in E. Total electron fluence: 80* $e^{-}/Å^{2}$.

Cryo-HAADF STEM images of a $TiO_2$ particle cluster were collected every 3° in a ±60° tilt range. EDX data of the area of interest was collected at tilt angles 0°, ±9°, ±21°, ±30°, ±39°, ±51°, and ±60° together with the HAADF STEM tilt series to ensure proper image alignment after each stage tilt. Both images and spectra were collected with a probe current of ~10 pA at low tilt angles below ±50°, and with a probe current ~20 pA above ±50° to allow for a sufficiently high signal-to-noise ratio (SNR) at high angles where the sample thickness increases. Elemental maps for each of the available tilt angles were created from the Ti-K$\alpha$ and Ca-K$\alpha$ EDX signals, chosen as representative of the $TiO_2$ particles and coating, with a spatial resolution of 20 nm/px. The tomograms reconstructed from the HAADF STEM and EDX signals in Figure 4.20 shows the possibility of reconstructing tomograms from EDX images. As was seen in Figure 4.17, 3D reconstruction from cryo-HAADF STEM images remains a viable method to accurately visualise the particle cluster.

Figure 4.20-C and -D show the tomograms reconstructed from the Ti-Ka and Ca-Ka EDX signals respectively, which largely correlate with the HAADF STEM tomogram in Figure 4.20-B. Although this process was largely successful in creating tomograms from cryo-EDX data, the accuracy of the results is lacking due to the poor spatial resolution used for the elemental maps. The spatial resolution of the elemental maps and the signal-to-noise ratio for the EDX data collected in cryogenic conditions is correlated with the total electron fluence and therefore the potential damage to the sample. A higher electron dose per tilt angle, higher amount of tilt steps and higher spatial resolution are needed to obtain better quality tomograms, though these parameters all contribute to the total electron fluence for the tilt series. An equilibrium needs to be struck between tomogram quality and electron dose for each area that is being analysed based on the sample size and material. In the case of the $TiO_2$ particle cluster shown in Figure 4.20-A, the main limiting factor to take in consideration is the size of the individual $TiO_2$ particles, which contain features as small as ~50 nm. When compared to the spatial resolution of 20 nm/px for the elemental maps, some of the sample details are lost, including the thin coating.

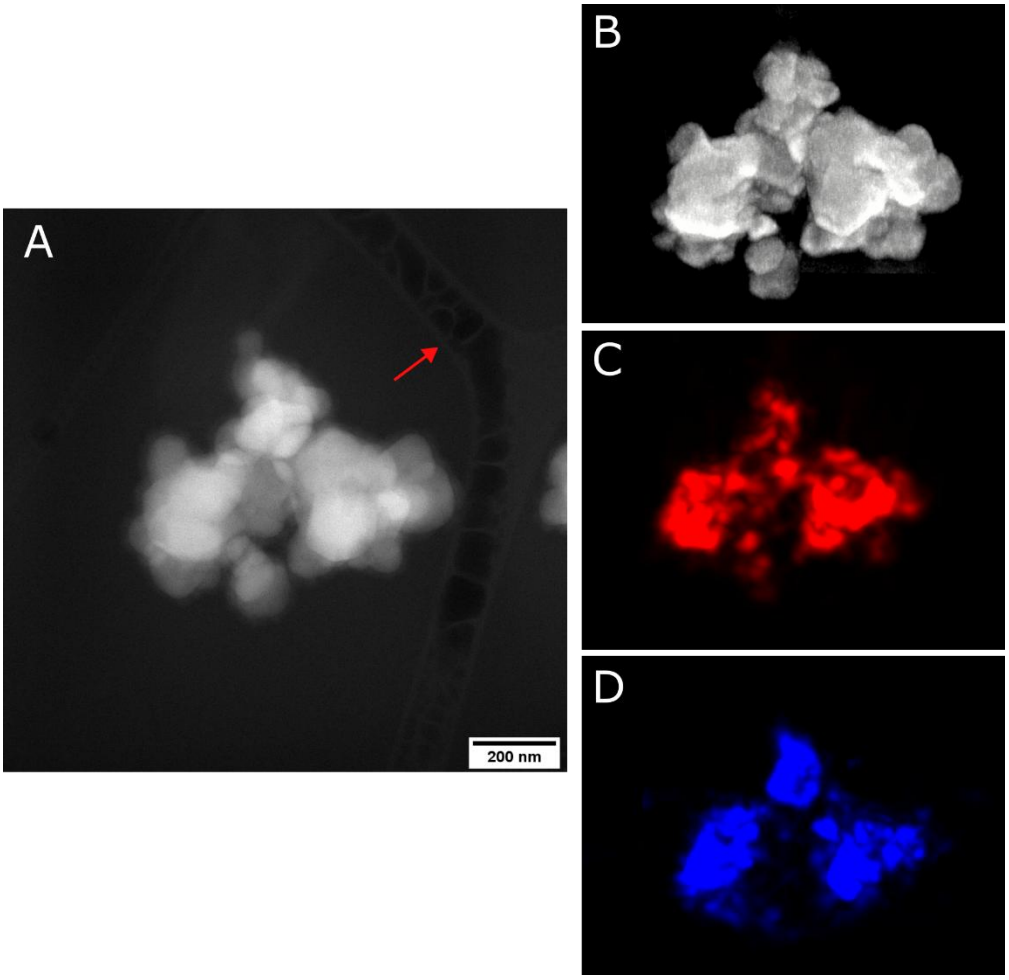


***Figure 4.20 –*** *Cryo-HAADF STEM image of a $TiO_2$ cluster and 3D reconstruction from the HAADF STEM and EDX signals. A) Cryo-STEM HAADF image of a $TiO_2$ cluster after the collection of the tilt series. Some damage to the area can be seen on the carbon film on the right of the particle cluster (where the ice has sublimed, indicated by the red arrow), though there was no visible damage to the particles. B) 3D reconstruction of the cluster in A, reconstructed from the cryo-HAADF STEM images collected in the tilt series. C) and D) show the 3D reconstruction of the elemental maps collected using EDX, with C) showing the tomogram reconstructed from the Ti K$\alpha$ signal and D) showing the tomogram reconstructed from the Ca K$\alpha$ signal. The tomograms B), C), and D) are shown at the same magnification, though C) and D) appear smaller due to the poor spatial resolution used for the collection of the EDX data. Total electron fluence for ET: 180 $e^-/Å^2$; for EDX: 80 $e^-/Å^2$.*

The same approach to image segmentation shown in Figure 4.18 (using image contrast) can also be applied to this tomogram, as the coating remains clear enough to be distinguished from the $TiO_2$ particles. The result of the segmentation as seen in Figure 4.21 shows the $TiO_2$ particle cluster in red and the coating in blue. Despite the segmentation process being more difficult as the coat is much thinner than the previous sample, this method remains more approachable than the EDX tomography.

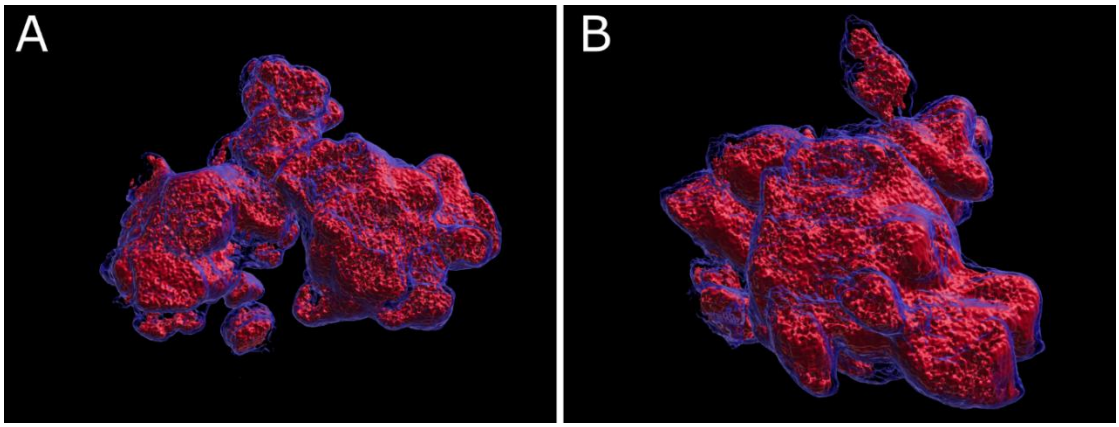


***Figure 4.21 –*** *3D reconstruction of the $TiO_2$ cluster in Figure 4.20-A, with manually generated surfaces from the HAADF STEM images. The $TiO_2$ nanoparticles are shown in red, while the coating is shown with a blue see-through surface.*

### 4.3.4 $TiO_2$ coated in biological media summary

In these cryo-fixed samples, segmentation of the tomograms is preferrable to the collection of additional spectral data in the tilt series. The segmentation approach is significantly less damaging to the sample, as it only requires a standard tilt series to be collected alongside an EDX elemental map to use as reference for the position of the coating. The biggest limitation to this approach is the need for every component that needs to be segmented to be sufficiently contrasting as to be distinguished from other components. This was the case in this $TiO_2$ sample, as only two components were present (the $TiO_2$ particles and the coating), which are both easy to distinguish from the vitrified ice and from one another. However, this is not the case for all systems, including the Pickering emulsion samples used in this study, where the oil is difficult to distinguish from the vitrified ice. In this case, collecting elemental data

together with a cryo-HAADF STEM tilt series remains a useful method to distinguish between different components in the system in 3D.

## 4.4 Initial Ice Thickness Analysis

Understanding the thickness of the vitreous ice is important for various aspects in cryo-(S)TEM. It is important for the vitreous ice to be sufficiently thick to allow for sample presence, in this case of the next chapter, the Pickering emulsion droplets. However, excessively thick ice can become an issue preventing the electrons from fully passing through the sample, thus affecting the image signal. The ice thickness was estimated in a lacey carbon TEM grid after plunge-freezing a hexadecane-in-water Pickering emulsion sample, although only selecting regions in the grid with no Pickering emulsion droplets. Two approaches to ice thickness measurement consist of using EELS and tilt tomography, both of which tend to be situational due to their suitability to different samples. The EELS method is straightforward as it uses low-loss EEL spectra to measure the sample thickness but requires knowledge of the mean inelastic free path of the sample, which can be challenging as it varies depending on the accelerating voltage used and exact sample composition and will therefore be unsuitable for samples that are not well-studied. The tilt tomography method allows for the measurement of sample thickness directly from a 3D tomogram using markers as points of reference. This method is more generally accessible, but in this case it was not used to avoid the addition of markers to the sample that may affect stability of the Pickering emulsions.

Estimations for the ice thickness were calculated in Hyperspy from low-loss EEL spectrum images. The value for the inelastic mean free path on vitreous ice at 300 kV was taken to be $\lambda_{in}$ = 356 nm, which was determined by Yan *et al.* [217] and previously predicted by Vulović *et al.* [234] from experimental results at different conditions. Analysis of the vitreous ice around the centre of the grid squares shows an ice thickness value in the 300-350 nm range. This estimated value is close to the inelastic mean free path for vitreous ice, indicating that the sample is unsuitable for quantitative elemental EELS analysis of high-loss edges. The ice thickness estimation was also performed near the grid bars, as ice is known to be thicker in this region. Figure 4.23 shows drastic increase in ice thickness nearing the grid bars, with the thickness

reaching 2 μm at a distance of 5 μm from the grid bars. The ice thickness continues increasing when nearing the grid bars, but at sample thickness values this far above $\lambda_{in}$ the portion of electrons passing through the sample is too small to obtain a proper signal for EELS.

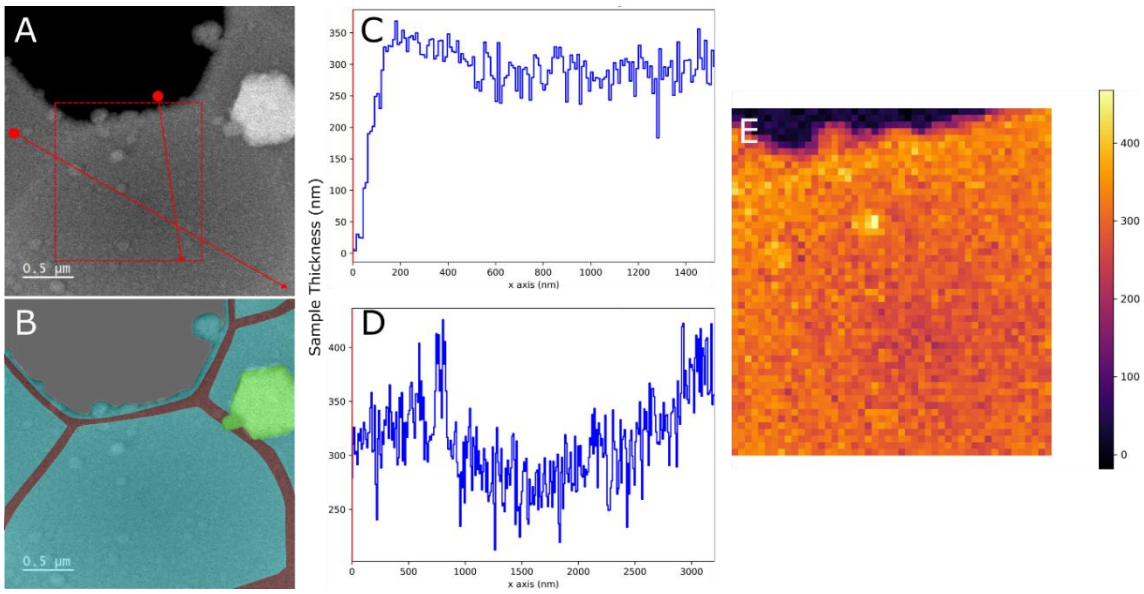


***Figure 4.22 –*** *Cryo-HAADF STEM image of a section of frozen ice and ice thickness estimated using low-loss EELS. A) HAADF STEM image of a region of ice in a lacey carbon TEM grid. The area imaged here shows part of the carbon film, several holes in the film filled with ice, and a hole without any ice. The lines show the position of line profiles taken, starting from the dot and terminating in the arrow. B) Position of the carbon film (red) ice (blue) and frost particles (green).C) and D) thickness estimation (in nm) for the line profiles shown in A). E) Estimated thickness (in nm) map of the area highlighted in A).*

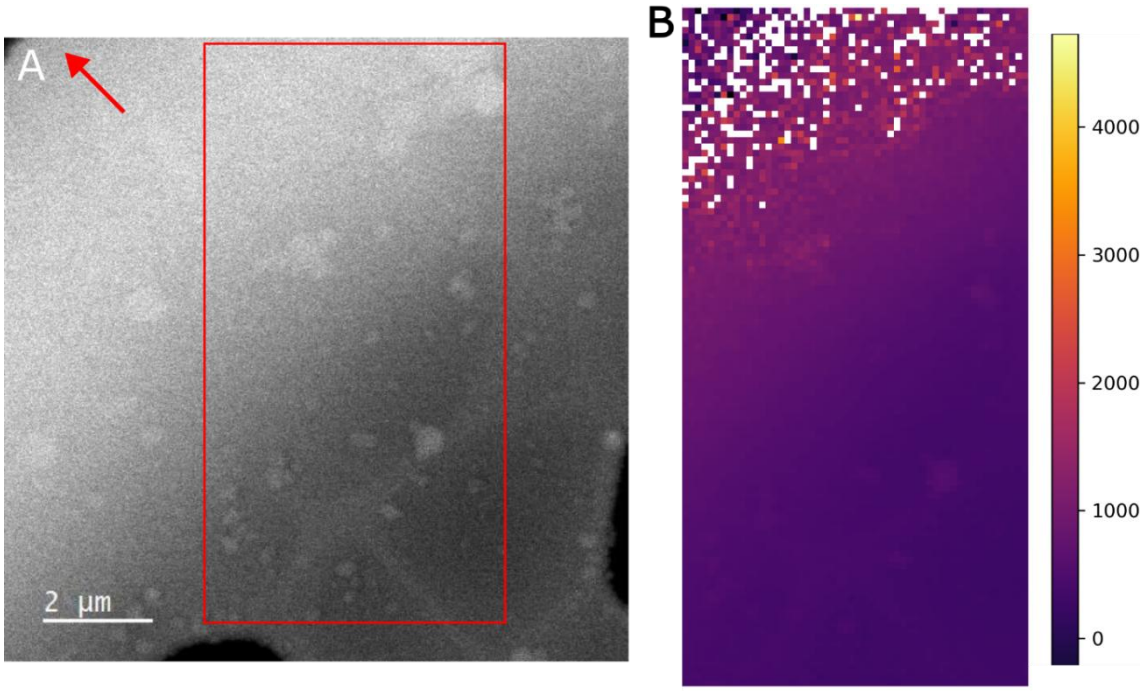


***Figure 4.23 –*** *Cryo-HAADF STEM image of a section of ice near the TEM grid bars and ice thickness estimated using low-loss EELS.A) ADF image of a region of ice near the TEM grid bars (visible in the top-left corner of the image and indicated by a red arrow). B) Estimated thickness map of the area highlighted in A).*

The thickness values for vitreous ice in a lacey carbon TEM grid prepared through plunge-freezing were estimated to be in the 300-350 nm range near the centre of the grid squares. The ice thickness was seen to increase above 2 µm when approaching the grid bars, at which point the ice reaches a critical thickness above which EELS thickness analysis cannot be applied and cryo-(S)TEM becomes unusable. Ice thickness as reported in the literature tends to vary depending on the sample used and ice region analysed. In Noble *et al.* [204] tilt tomography was not only used to investigate nanoparticle distribution within the ice, but also served to obtain ice thickness measurements for a wide range of plunge-frozen sample in holey TEM grids. In the data reported in this study, the ice was thinnest in the centre of the holes (~15-190 nm depending on the sample) and gradually became thicker near the edge of the holes (up to ~265 nm). These results are generally thinner than the estimations made in this thesis, but also in some cases larger than the ideal <100 nm ice thickness [67]. Ice thickness varies depending on the sample [67] and the particle size might also be

crucial for the determination of ice thickness, as thicker ice might be present near larger particles, meaning that samples larger than the average ice thickness could be found near the centre of the grid squares. This increases the possibility of finding samples in areas suitable for tilt series acquisition.

Low-loss EELS was found to be suitable for the estimation of the ice thickness in plunge-frozen samples, which is invaluable as a tool when analysing areas to perform tilt tomography. As the sample is tilted when collecting a tilt series, the effective thickness of the sample increases when approaching higher tilt angle [104], affecting the signal-to-noise ratio due to multiple scattering and ultimately negatively affecting the quality of the resulting tomogram.

## 4.5 Summary

ZnO NP dispersions were imaged in TEM, cryo-(S)TEM and cryo-FIB-SEM using a range of sample preparation methods to investigate the effects of sample drying and cryogenic freezing to the agglomeration of particles. Comparisons between preparation techniques are challenging due to the large mixture of agglomerate sizes even when dispersed in water as seen from DLS size measurements. Nonetheless, PF-VD on continuous carbon grids and cryo-(S)TEM of frozen samples in lacey carbon grids are seen as suitable techniques for the imaging of NP dispersions.

Cryogenic freezing using plunge-freezing was shown to be valuable for the retention of the core-satellite structures in the gold nanoparticle system. PF-VD was found suitable for sample imaging when particle size measurements are needed as the gold nanoparticles are deposited onto the carbon support film while maintaining the core-satellite structure. In contrast, results from a sample imaged in cryo-(S)TEM show overlap between nanoparticles was observed due to out-of-plane nanoparticles. Cryo-ET of core-satellite structures confirmed the nanoparticle overlap was due to the three-dimensionality of the core-satellite structures.

Cryo-HAADF STEM was used to image $TiO_2$ particles surrounded by a coating rich in calcium and phosphorus, as confirmed through EDX spectroscopy. Tilt tomography of a $TiO_2$ particle agglomerate showed the coating surrounding the agglomerate rather than the individual particles, indicating that agglomeration took place before the formation of the coating layer. Moreover, it was shown that EDX can be performed at different tilt angles simultaneously with cryo-HAADF STEM tilt tomography to obtain tomograms from elemental maps that track the elements in 3D space. This technique can help obtain 3D elemental information for structures that lack contrast in cryo-HAADF STEM such as the oil and water phases in a Pickering emulsion.

The ice in a plunge-frozen sample was found to vary in thickness depending on the distance from the grid bars and distance from the support film. Low-loss EELS was successfully used as a low-dose technique for the estimation of the ice thickness, which can be used to select areas suitable for tilt tomography to ensure the ice thickness at high tilt angles is thin enough to allow for cryo-(S)TEM imaging.

# Chapter 5 Cryo-(S)TEM Analysis of Pickering Emulsion Samples

This chapter includes the cryo-(S)TEM analysis of three different Pickering emulsion samples that were presented in Chapter 3:

1. A sunflower oil-in-water Pickering emulsion stabilised by 3-5 nm Pt-NPs, with ~100 nm droplet size;
2. A hexadecane-in-water Pickering emulsion stabilised by 3-5 nm Pt-NPs and ~100 nm droplet size;
3. A hexadecane-in-water Pickering emulsion stabilised by 3-5 nm Pt-NPs and > 1 μm droplet size.

Cryo-(S)TEM imaging was performed on Pickering emulsion samples prepared by using plunge-freezing, with droplet size and shape examined. Cryo-EDX and -EELS were used for the elemental analysis of the sample focusing on the carbon signal from the oil phase, oxygen signal from the water phase (and vitreous ice), and platinum signal from the Pt-NPs. Cryo-ET was used to visualise the sample droplets in 3D to ensure the spherical structure of the droplets is retained after plunge-freezing. Further cryo-ET with simultaneous EELS spectrum imaging (SI) was performed to obtain 3D elemental maps of the emulsion droplets as a stain-free method to visualise the oil phase.

The Pickering emulsion samples were prepared by the research group of Dr Olivier Cayre, in the School of Chemical and Process Engineering, University of Leeds. Part of the results presented in this chapter have been published in the Journal of Microscopy under the title “Native state structural and chemical characterisation of Pickering emulsions: A cryo-electron microscopy study” (see Appendix A).

## 5.1 Preliminary Sample Analysis

Pickering emulsions have been analysed using a wide range of techniques including optical microscopy, AFM, DLS, TEM and SEM. Among these, optical light microscopy is one of the simplest methods to visualise emulsions. Optical microscopy was used in previous work featuring these Pickering emulsion samples seen in Hitchcock *et al.* [40] to confirm the droplet size and shape. However, these observations are limited by the spatial resolution of light microscopy, restricting the ability to image the smaller

droplets in the system or the Pt-NPs [40]. For several of the samples presented here, the smallest droplets were too small to allow for representative characterisation using a light microscope and as would be expected, this method does not provide information on the Pt particles or their distribution on any of the Pickering emulsion droplets. Conventional TEM and SEM have been identified as important techniques to break through this resolution limit [57] but are both unsuitable for imaging Pickering emulsions and other soft matter samples due to the vacuum in the microscopes drying the samples. The drying of aqueous samples will affect their structure and create drying artefacts, which in turn affects sample imaging [17, 28, 235].

Initial analysis of the Pickering emulsion samples includes DLS analysis for bulk sample measurement in in the native state, and TEM imaging to visualise the emulsion droplets and stabilising nanoparticles. Both dry sample imaging and imaging of a cryo-fixated sample were used in this chapter to confirm the usefulness of cryo-fixation techniques in preserving the structure of soft matter samples. For this, plunge-freezing was chosen as a cryogenic preparation technique due to its ease of use and availability.

### 5.1.1 DLS Measurements

Preliminary DLS measurements were taken to verify the droplet size in its native, aqueous state before undergoing any changes during sample preparation for EM imaging. Using DLS the average particle size was measured to be ~100 nm for the sunflower oil Pickering emulsion (see Figure 5.1), though this is limited by DLS only measuring the hydrodynamic diameter of the droplets, and therefore unable to differentiate between individual droplets and any agglomerates of droplets.

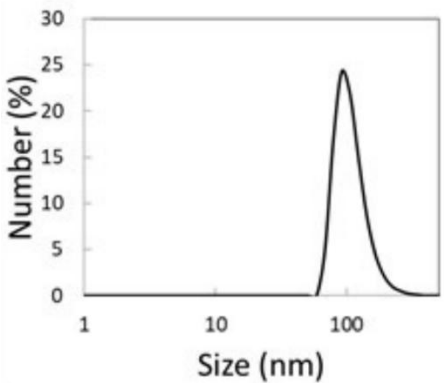


***Figure 5.1 –*** *DLS size measurements of the sunflower oil Pickering emulsion sample. The measurement shows an average droplet diameter of ~100 nm [236].*

The hexadecane oil Pickering emulsion sample used later in the chapter was similarly analysed using DLS, with results presented in Figure 5.2. DLS size measurements in Figure 5.2 show a number distribution with a main peak corresponding to ~100 nm, similar to the results seen in Figure 5.1. This suggests that the largest droplet population consists of ~100 nm droplets. The DLS volume distribution in Figure 5.2-B contains two peaks at ~100 nm and ~600 nm. This may suggest the presence of large droplet clusters, though it may be due to the presence of large droplets. When considering the size limitations for imaging samples in TEM, a sample with smaller primary particle size would be preferred, especially since the further limitations given by plunge-freezing would mean that larger droplets may collapse or be deformed during sample preparation. EELS thickness measurements for the ice formed through plunge-freezing seen in Chapter 4 showed an average ice thickness of 300-350 nm in the centre of the grid squares. Although emulsion droplets with sizes near the 100 nm diameter measured in DLS may be found in ice with this thickness, larger droplets or clusters are expected to be “pushed” to the thicker ice regions near the grid bars which are less accessible for imaging and electron tomography.

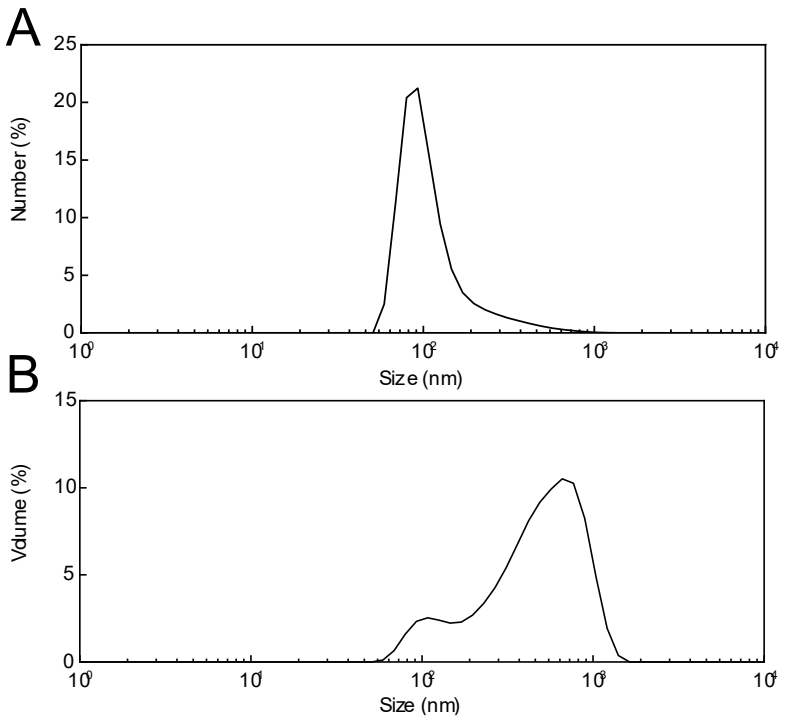


**Figure 5.2 -** *DLS measurements of the hexadecane Pickering emulsion, showing A) the number distribution and B) the volume distribution. The graph in A) shows that similarly to the sunflower oil sample in Figure 5.1, the hexadecane sample has an average diameter of ~100 nm. The volume distribution graph in B) instead shows two peaks, with a main peak around ~600 nm and a second peak at around ~100 nm [236].*

### 5.1.2 Dry Sample TEM Imaging

The hexadecane-in-water Pickering emulsion sample was drop-cast onto a continuous carbon TEM grid and left to dry, after which it was taken to the TEM for imaging. As the structure of Pickering emulsions is given by surface interactions between the oil and water phases, it is expected the droplets would collapse following drying and therefore not carry any information on droplet size, shape, or agglomeration. Similarly, it was expected for the NPs to not retain their native distribution and agglomeration.

TEM and HAADF STEM images of the dry sample in Figure 5.3 show the presence of collapsed droplets, delineated by the Pt-NPs. Here, the Pt-NPs on the droplet surface appear to have been directly deposited on the grid film during drying, thus functioning as a projection of the original droplets and providing some information on droplet

shape or aggregate size. This can be seen with dry droplets in Figure 5.3-A, Figure 5.3-B, and Figure 5.4-B where a projection of the droplet remains.

Dry (S)TEM imaging can be useful for basic particle analysis of the stabilising NPs if only information such as nanoparticle size or shape is needed. High magnification TEM imaging of the sample can be seen in Figure 5.3-C, where the particle size of the Pt-NPs has been measured to be 3-5 nm. It is however impossible to collect any information on droplet agglomeration or distribution as these are greatly affected by the droplet collapse and drying artefacts.

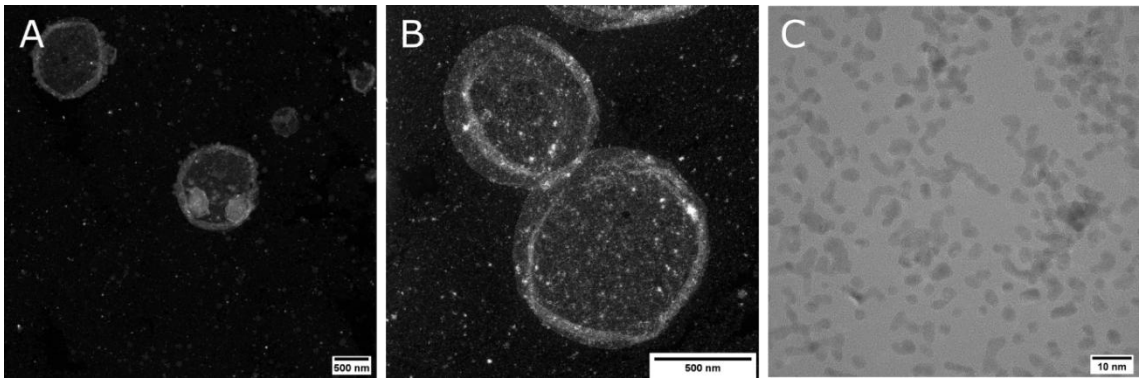


***Figure 5.3 –*** *Electron microscopy images of a dry hexadecane oil Pickering emulsion sample. A) and B) HAADF STEM images of collapsed droplets. C) TEM image of the Pt-NPs, with approximate particle size of 3-5 nm.*

Stabilising particles can naturally sit in the continuous phase in Pickering emulsion systems, therefore it is unclear from the imaging of a dry sample whether the position of the Pt-NPs is due to Pt-NPs in the water phase or as a result of the sample drying [237]. EDX analysis performed by Roncal-Herrero *et al.* [65] on a dry sample of sunflower-in-oil Pickering emulsion on a silicon nitride TEM grid confirms the absence of a defined carbon signal from the droplets, as the oil phase had fully evaporated during the drying process. The EDX results in an area including a collapsed droplet (Figure 5.4) show that although a carbon signal was detected, it does not correspond directly to the oil droplet. The platinum signal map in Figure 5.4-C confirms that the nanoparticles are platinum and are present both in the collapsed droplet and around it [65]. Overall, these results show that cryo-EM imaging is necessary to verify the position of the Pt-NPs in cryo-fixated Pickering emulsion samples.

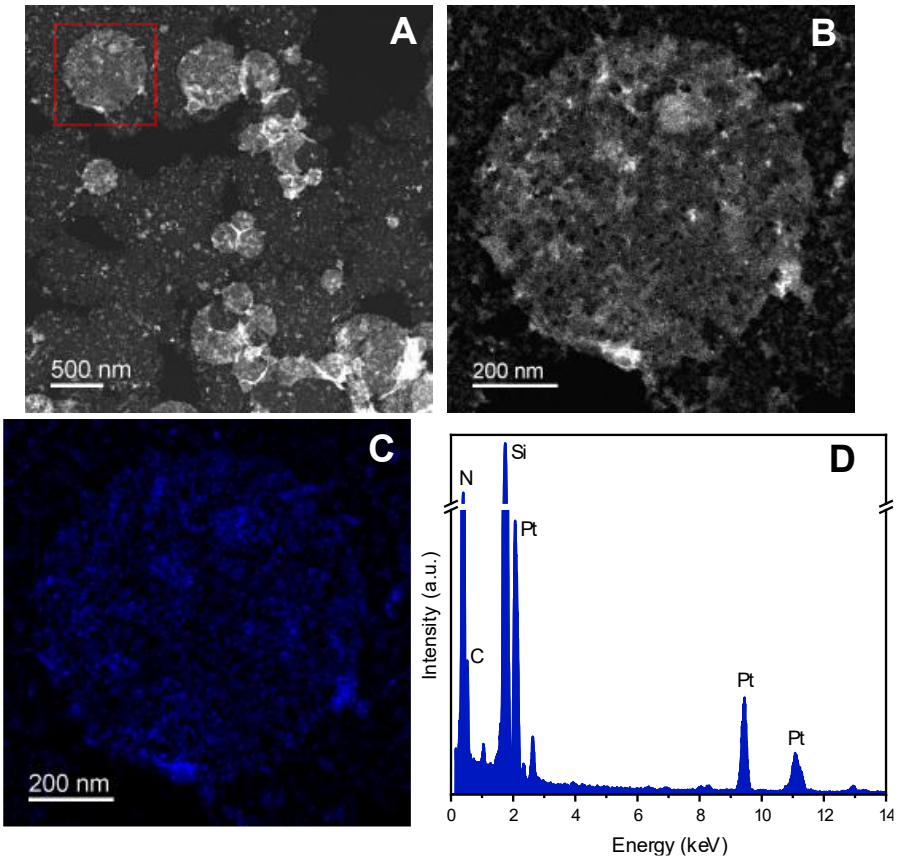


***Figure 5.4 –*** *EDX elemental analysis of dry a sunflower oil Pickering emulsion sample on a SiNx TEM grid. A) HAADF STEM image of a group of collapsed droplets. B) Higher magnification image of the area in A) showing a single collapsed droplet. C) EDX elemental map of the Pt signal, which corresponds to the remnants of the collapsed droplet. D) EDX spectrum with the main peaks labelled. The Si and N peaks are due to the $SiN_x$ TEM grid. The elemental maps in C) shows that while the Pt signal corresponds to the droplet in B), the C signal does not reflect the position of the droplet, thus demonstrating that the sample has completely collapsed and does not retain its native structure. Figure adapted from the data in Roncal-Herrero et al. [65].*

## 5.2 Cryo-(S)TEM Imaging

The two main Pickering emulsion samples used for cryo-(S)TEM imaging all possess droplets with an average diameter of ~100 nm, making the sample suitable for preparation through plunge-freezing. The Pickering emulsion samples were mainly imaged in cryo-HAADF STEM mode to make use of two key advantages for cryogenic imaging:

1. Higher electron fluences being needed before beam-induced damage occurs in STEM mode [95, 98];
2. Atomic number imaging in STEM mode allows to obtain good contrast for the Pt-NPs [108, 142, 144].

Further analysis was conducted using cryo-EDX, -EELS, and -electron tomography to fully characterise the sample in 2D and 3D. Cryo-imaging is useful for imaging the Pickering emulsion sample in a hydrated state, preventing the loss of structural integrity of the droplets as a result of drying artefacts.

### 5.2.1 Initial Observations

Initial imaging of the hexadecane-in-water emulsion (< 1µm) using cryo-HAADF STEM can be seen in Figure 5.5, showing individual droplets and clusters of droplets. The images in Figure 5.5 were collected near the centre of the TEM grid squares where the ice is thinnest, with the droplets not showing any evidence of deformation or collapse even within larger droplet clusters as seen in Figure 5.5-A. Higher magnification imaging resolved individual 3-5 nm Pt-NPs in Figure 5.5-B and Figure 5.5-D. These images show the Pt-NPs being arranged in chains, mostly at the oil-water interface on the droplet's surface. Some nanoparticles can be also seen in small clusters in the water phase (Figure 5.5-D). Cryo-HAADF STEM was used for high magnification imaging due to the higher threshold for ice damage associated with STEM imaging as was demonstrated in previous work by Ilett *et al.* [95] and Egerton [238], where damage in cryo-analytical STEM was seen to occur at higher electron fluences (<2000 $e^{-}/Å^{2}$) as compared to conventional cryo-TEM (<100 $e^{-}/Å^{2}$) [95, 238]. Although higher magnification imaging was possible in cryo-STEM, consideration of electron fluence is required to prevent sample damage from interfering with the imaging process. Electron fluence (the total number of electrons incident on the

sample per unit area) and dose (the rate of electrons per unit area) are critical parameters for cryo-EM observation. At high total electron fluences the sample will incur significant beam-induced damage in the form of ice subliming, but a minimum amount of electrons is also needed to generate enough contrast for imaging; this impacts the parameter needed for sample imaging, focusing, and navigation, as all these steps can impact the total electron fluence. The beam current was kept below 20 pA when imaging in HAADF STEM at image resolutions below 2 nm/px to keep the total electron fluence under a total of ~200 $e^-/Å^2$, within the safe range before incurring beam damage as reported by Ilett *et al.* [95] and Egerton [238]. However, damage remains at smaller pixel sizes due to diffusion limited damage by the radiolysis products generated in vitreous ice [95].

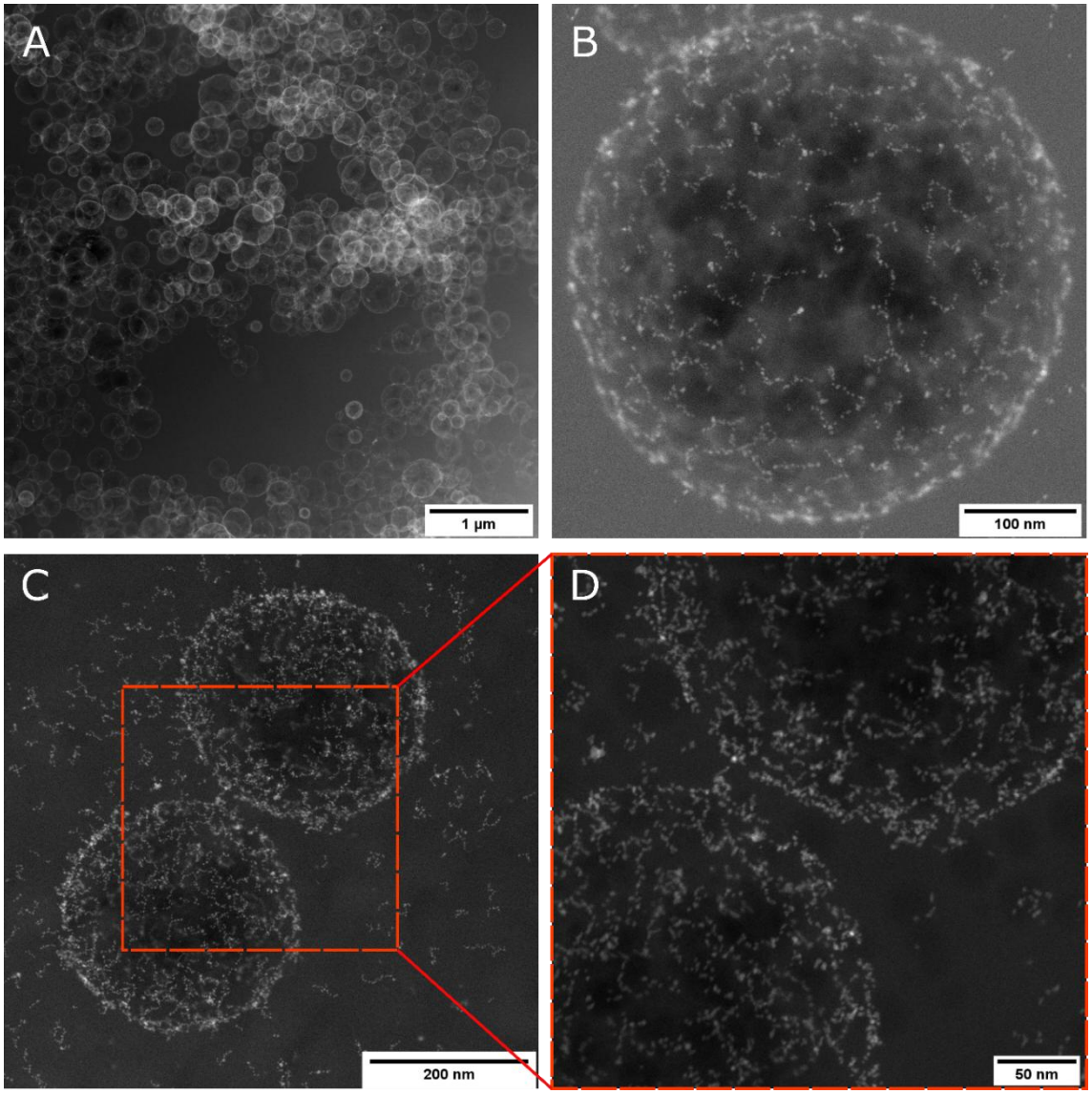


***Figure 5.5 –*** *Cryo-HAADF STEM images of Pickering emulsion droplets. A) Low magnification image of a large droplet cluster. B) Image of a single droplet with Pt-NPs visible on the droplet surface. C) and D) images of droplets at two magnifications, with D) showing a high magnification image of C) where individual Pt-NPs can be resolved. Total electron fluences: A) 10 $e^-/Å^2$, B) 63 $e^-/Å^2$, C) 66 $e^-/Å^2$, D) 270 $e^-/Å^2$ [236].*

Large droplets with diameter >500 nm can be occasionally identified, though not all of them are properly preserved. Figure 5.6-A shows an example of such droplets, which appear to have partially burst. Very large agglomerates and droplets (>1 µm) can be seen near the grid bars (Figure 5.6-B), where the ice thickness is anticipated to be higher as observed in the preliminary ice studies conducted in Chapter 4.

Unfortunately, sample imaging in these regions is difficult as the ice thickness approaches the maximum size for STEM imaging, and approaches sizes where ice is likely to have crystallised during plunge-freezing. This indicates that cryo-(S)TEM is therefore not suitable for the analysis of Pickering emulsion samples with large droplet sizes.

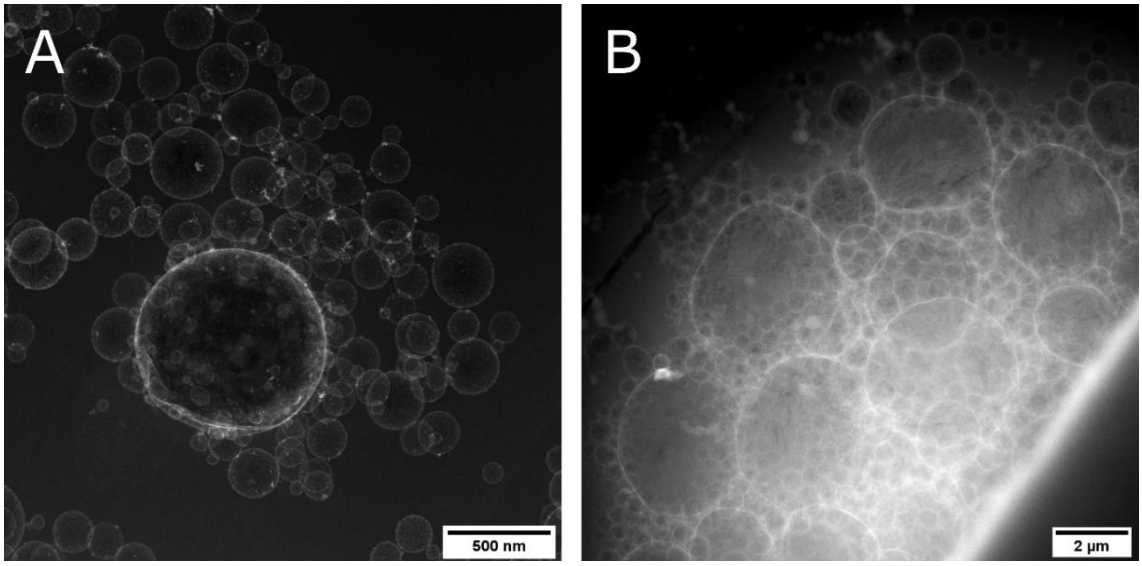


***Figure 5.6 –*** *Cryo-HAADF STEM images showing imperfections in the sample. A) Cluster of droplets with a large, partially collapsed droplet. B) Large droplet cluster near the grid bar. The higher ice thickness near the grid bars can accommodate much larger droplets (and droplet clusters) compared to the centre of the grid square, but the sample thickness here makes proper sample analysis problematic. Total electron fluences: A) 10 $e^-/Å^2$, B) 1 $e^-/Å^2$.*

The impact of the droplet size was examined by studying the hexadecane-in-water Pickering emulsion with a droplet size larger than 1 µm. This was prepared for cryo-TEM using plunge freezing and variable results were obtained. As seen from cryo-HAADF STEM images in Figure 5.7-A and Figure 5.7-B, large droplets (diameter >500 nm) are deformed, with single droplets appearing “squashed” and elongated, while droplets in clusters collapse on each other. In Figure 5.7-C smaller droplets within a cluster are also deformed, while droplets that are not part of a cluster remain mostly unaffected (see the top-right droplet in Figure 5.7-C).

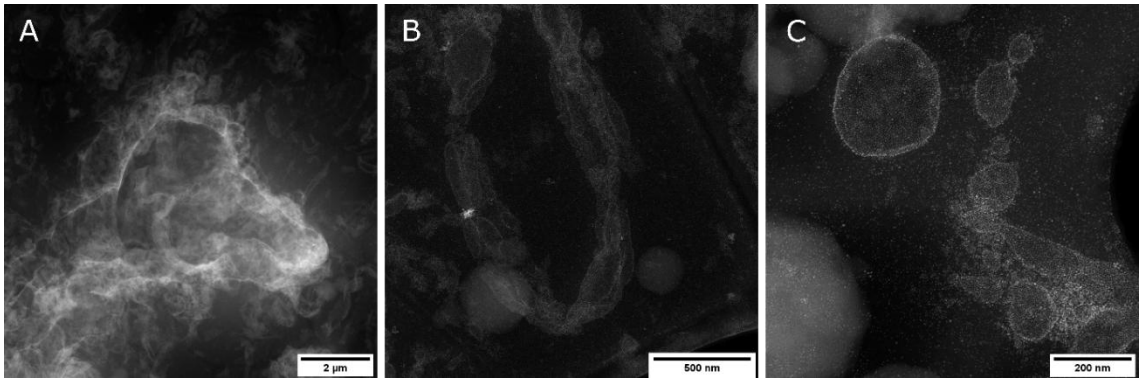


***Figure 5.7 –*** *Cryo-HAADF STEM of a hexadecane oil Pickering emulsion with large droplet size (>1 µm) after plunge-freezing. A), B) and C) all show droplets of different sizes at a range of magnifications. The droplets in this sample appeared to be deformed, an occurrence that seems to be more pronounced in larger droplets (>500 nm) or droplet clusters. Total electron fluences: A) 2 $e^-/Å^2$, B) 22 $e^-/Å^2$, C) 90 $e^-/Å^2$.*

Cryo-EELS was used for the elemental analysis of area of the sample with thickness up to the mean inelastic free path of vitreous ice, as can be seen in Figure 5.8. The EEL carbon K edge signal map in Figure 5.8-B shows that carbon is not only present in the droplet, but also ubiquitous to the entire analysed area irrespective of the presence of visible droplet remains. This could be a result of large clusters being deformed, together with the high sample concentration as a result of the blotting step. These results show that initial droplet size information needs to be known prior to selecting a cryo-preparation methods as techniques such as plunge-freezing are only suitable for smaller droplets, with other characterisation techniques such as DLS, optical microscopy, and cryo-SEM being possible alternatives depending on the specific sample size and analysis needs.

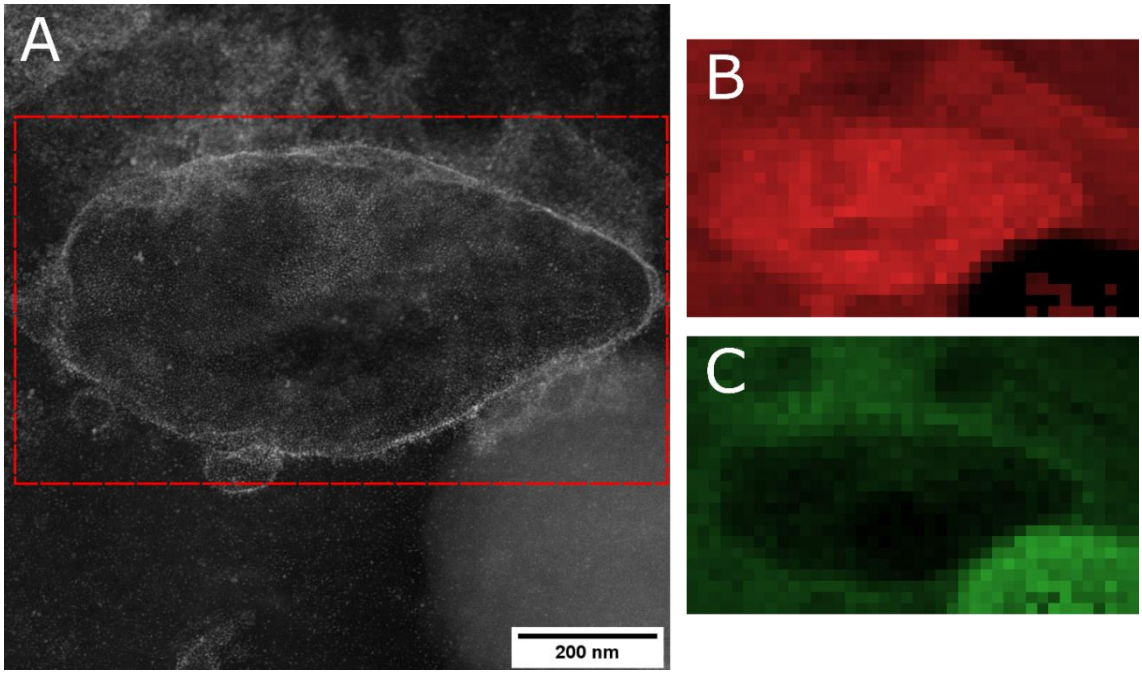


***Figure 5.8 –*** *EELS elemental maps of a plunge-frozen Pickering emulsion sample with large droplets. A) Cryo-HAADF STEM images of the plunge-frozen sample with highlighted area of interest. The droplet collapse together with the high sample thickness means the sample is often difficult to image and droplets are difficult to visualise. B) and C) EELS elemental maps of the area in A) showing the carbon K edge signal (B) and oxygen K edge signal (C). Due to the droplet collapse, it is possible to find areas where the oil can be found in the droplets and also around them (as is the case with (B), which shows carbon around the droplet). Total electron fluence: 100* $e^-/Å^2$.

### 5.2.2 Comparisons Between Dry and Cryo-Prepared Samples

It was seen from initial imaging that the sample structure was visibly different following drop casting as compared to plunge-freezing. Drop casting soft matter samples (e.g. biological samples, surfactant solutions, etc.) for conventional TEM imaging will cause drying artefacts affecting the sample's structure and morphology. Initial visual comparisons between drop cast and plunge-frozen samples in Figure 5.9 how that under the vacuum of the TEM, the emulsion droplets have burst, leaving only the Pt-NPs deposited on the supporting film (Figure 5.9-A and Figure 5.9-B). As expected from a dry Pickering emulsion sample, the droplets in Figure 5.9-A present a variable morphology, with most droplets not being circular. Conversely, the emulsion droplets

in the cryo-fixed sample in Figure 5.9-C and Figure 5.9-D are circular, implying the spherical shape of the droplets is maintained within the vitreous ice.

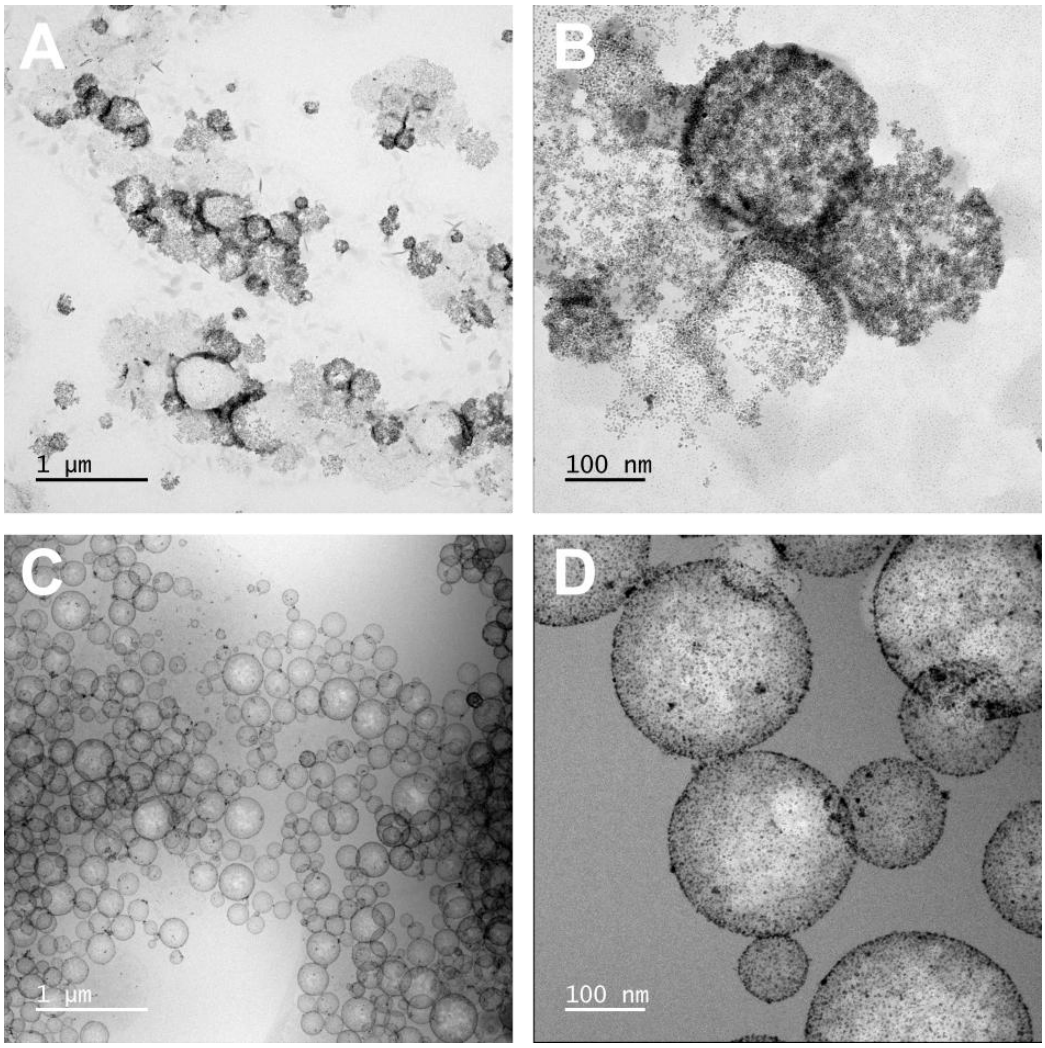


***Figure 5.9 –*** *Comparison between dry and plunge-frozen sunflower oil Pickering emulsions. A) and B) TEM images of a drop cast sample. C) and D) Cryo-TEM images of a plunge-frozen sample. Comparisons between the two sample preparation methods clearly show the spherical shape of the droplets being retained after cryogenic preparation. Total electron fluences: C) 41 $e^-/Å^2$, D) 781 $e^-/Å^2$ [236].*

The diameter of the emulsion droplets was measured for both the dry and plunge-frozen sample to compare the effects of the two preparation methods on droplet structure. 500 droplets were manually measured from (S)TEM images of both samples; the average droplet diameter in the drop cast sample was found to be 340 nm (with droplet sizes ranging from 98 nm to 1089 nm), while the average droplet

diameter was found to be 183 nm for the plunge-frozen sample (with droplet sizes ranging from 45 nm to 514 nm), as seen in Figure 5.10-A. The variability in the diameter measurements for the dry sample are extreme, with a mean diameter much greater than the bulk DLS measurement (Figure 5.1), but with only a small increase in mean diameter measured from the cryo-prepared sample compared to the same DLS results. The circularity of the droplets was measured by overlapping an ellipsoid with the droplets and adjusting it to the droplet such that the droplet diameter coincides with the ellipsoid's major axis. This was done do partially account for droplets with only partial outlines as seen in Figure 5.9-B. Circularity is given by the equation:

$$Circ = \frac{Perimeter^2}{4\pi \text{ x } Area} \tag{5.1}$$

Where circularity ranges from 1 for a perfect circle, and higher than 1 as the shape approaches an infinitely elongated polygon. A plot of circularity against droplet diameter for cryo-prepared and dry emulsion droplets in Figure 5.10-B shows the drop casted droplets present a large range in circularity (from 2.82 to 1.01), while the cryo-prepared droplets are more consistently circular (1.22 to 1.01).

These results suggest that the cryo-prepared sample retains both the droplet size and shape that would be expected in its aqueous state. However, this analysis is limited to two dimensions and cannot detect deformation in the direction normal to the viewing plane as a result from blotting the sample during plunge-freezing. In fact, the flattening of large samples was also observed by Wills *et al*. [239] in nanoparticle dispersions cryogenically frozen by plunge-freezing and subsequently dried under a high vacuum, where agglomerates were shown to be flattened [239]. By using electron tomography and acquiring images at multiple tilt angles, it is possible to observe these droplets in 3D space, therefore confirming whether the droplet shape is maintained through the sample preparation steps.

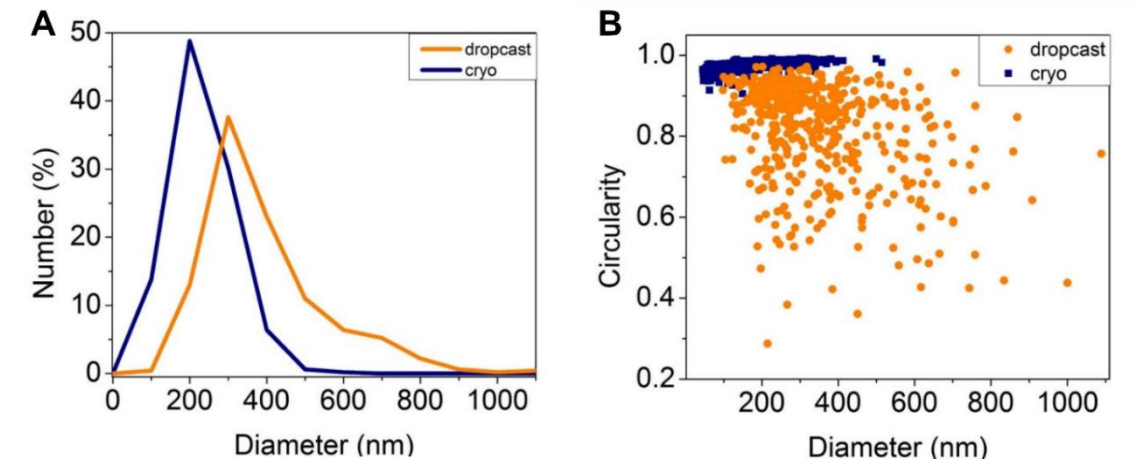


***Figure 5.10 –*** *Graphs showing the size distribution and circularity of 500 Pickering emulsion droplets prepared through drop casting and plunge-freezing. A) Size distribution of the droplets across the two samples. B) Circularity of the droplets versus the droplet diameter across the two samples. Droplet morphology appears to change as the droplets collapse during the drying process. The average droplet size for the drop cast sample was measured to be ~342 nm, compared to ~183 nm for the plunge-frozen sample [236].*

Initial sample imaging using (S)TEM clearly showed the usefulness of plunge-freezing as a cryo-preparation technique for Pickering emulsion samples, ensuring the emulsion droplet structure is maintained during imaging (Figure 5.11-A and Figure 5.11-B). However, it is also evident from the imaging of large plunge-frozen sample droplets such as Figure 5.11-C that plunge-freezing can only be applied to a narrow sample size range, with droplets >1 μm in diameter collapsing or deforming during sample preparation, It is therefore important to keep in mind that larger Pickering emulsion droplets will require alternative imaging techniques such as optical microscopy or cryo-SEM for optimal characterisation.

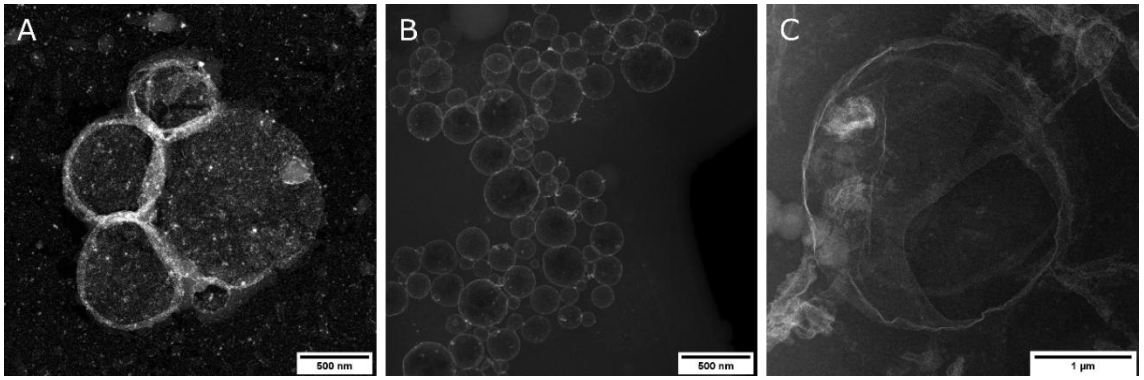


***Figure 5.11 –*** *Comparison between dry droplets and cryogenically prepared hexadecane-in-water emulsion droplets with different sizes. A) HAADF STEM image of a drop cast sample. B) Cryo-HAADF STEM image of a plunge-frozen sample. C) Cryo-HAADF STEM image of a plunge-frozen sample containing large droplets (>1 µm). Plunge-freezing is successful in preserving the droplet structure, but only for samples with appropriate droplet size; large droplets (with diameter significantly larger than the ice layer formed by plunge-freezing) will collapse. Total electron fluences: B) 14 $e^-/Å^2$, C) 1 $e^-/Å^2$.*

### 5.2.3 Spectroscopy using EELS and EDX

During cryo-(S)TEM imaging, the low contrast between the oil and water phases results in difficulties identifying the oil phase and the position of Pt-NPs relative to it. In high magnification images such as Figure 5.5-D it is not possible to clearly distinguish between the oil and water phases; while it is vaguely possible to identify the oil-water interface by following the position of the Pt-NPs, this is far from an accurate method and is based on the potentially incorrect assumption that the stabilising particles must be at the interface. In practice, the stabilising particles might also be present in the water or oil phases with Figure 5.5-D being one such case, showing Pt-NPs in the water phase. When considering different Pickering emulsions, samples using particles such as proteins as stabilisers present low contrast stabilisers that cannot be used as indicators for the purpose of identifying the oil-water interface. EELS and EDX can be used as elemental analysis techniques while in HAADF STEM mode to identify the water and oil phases through the carbon and oxygen signals respectively. Figure 5.12 shows EDX elemental maps and EDX spectra corresponding to the inside and outside of an emulsion droplet highlighted in the cryo-HAADF STEM

image in Figure 5.12-A. A composite of the carbon and platinum EDX elemental maps can be seen in Figure 5.12-B, showing the presence of carbon signal corresponding to the oil phase in the centre of the droplet, and a platinum signal located predominantly at the droplet's surface, corresponding to the position of the Pt-NPs. A challenge for the elemental analysis of this oil phase lies in distinguishing the carbon signal corresponding to the oil from the surroundings (e.g., the carbon support film). To resolve this issue, elemental analysis of the frozen sample was only performed on droplets found over holes in the carbon film.

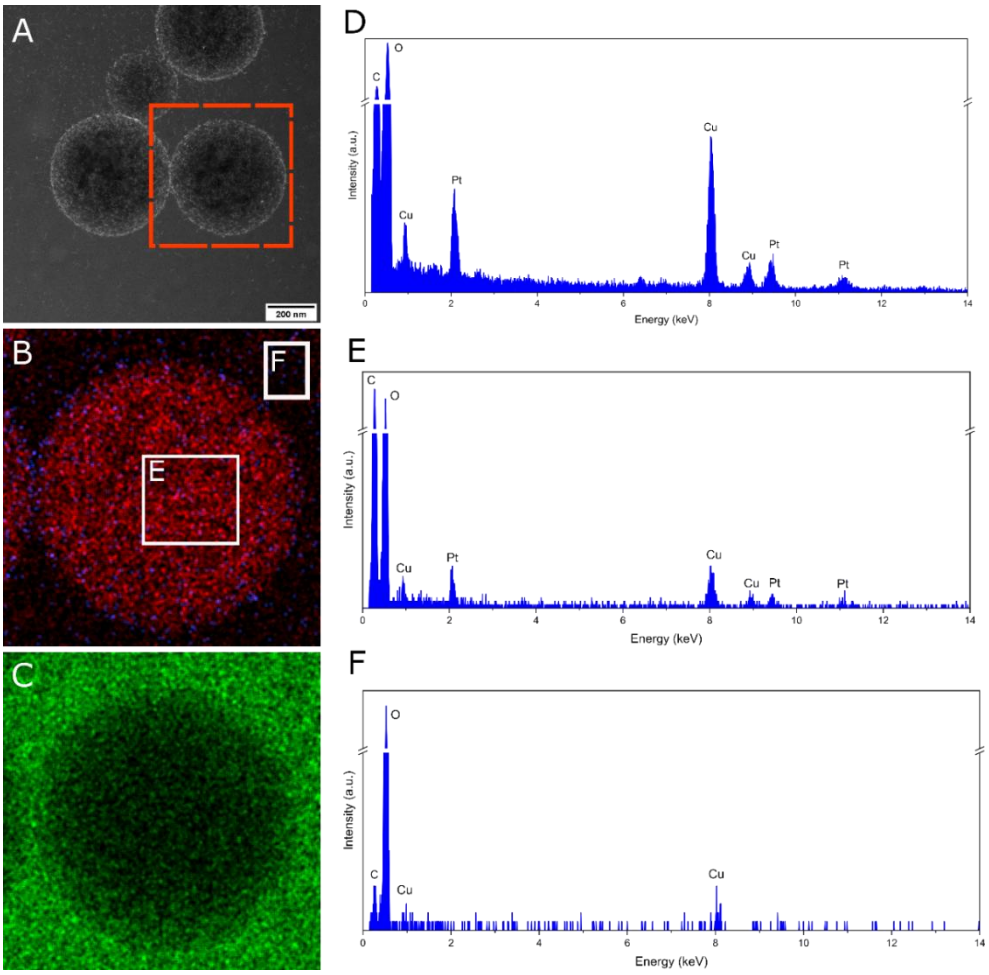


***Figure 5.12 –*** *EDX elemental analysis of a single sunflower oil-in-water emulsion droplet A) HAADF-STEM images of a cluster of Pt-NPs-stabilised Pickering emulsion droplets plunge-frozen onto lacey carbon grid, B) EDX elemental map showing the carbon (red) and platinum (blue) signals with boxes showing EDX spectra locations. C) EDX elemental map for*

*the oxygen within the vitrified ice. EDX spectra for D) the entire droplet, E) the centre of the droplet, and F) the water phase (total electron fluence: 732 $e^-$/Å).*

EELS was used to support the results obtained from the EDX analysis, generating EELS elemental maps as seen in Figure 5.13. Core-loss spectra were collected within the electron energy loss range of 200-600 eV to include carbon and oxygen edges, corresponding to the carbon in the oil phase and oxygen in the vitreous ice. This allows for the detection of the oil in the droplets and understanding what proportion of the ice thickness they occupy. The EELS maps were taken with a 0.09 s exposure time and 12 nm pixel size (resulting in a total electron fluence of 16 $e^-$/ $Å^2$), as an increase in exposure time or decrease in pixel size would result in an increase in electron fluence which would then cause damage to the sample. These parameters need to be adjusted depending on the sample and the area that is being analysed, as changes in sample size, elements present in the sample, ice thickness, and damage threshold for the sample will affect the maximum total electron fluence that can be used.

To obtain an EELS spectrum image it was found that a lower electron fluence was needed compared to an EDX map with the same pixel size and signal quality. Due to the method of signal acquisition (electron scattering in EELS versus x-ray emissions in EDX), EELS is more suitable for the analysis of elements with low atomic numbers, while EDX is more suitable for high atomic numbers. This makes EELS particularly useful for the analysis of carbon and oxygen signals in the Pickering emulsion samples. In addition, the position of the carbon and oxygen EDX peaks near each other means that differentiating between these lighter elements is more challenging, especially when signal acquisition is limited by electron fluence and sample damage. The lower electron fluence needed is especially attractive for cryo-STEM imaging, as it can allow for the use of supporting analysis techniques in the same area and could also be used in conjunction with electron tomography to generate 3D reconstructions based on the elemental maps without damaging the sample. The applicability of EELS to a given sample is given by the sample thickness (which affects the signal quality and the ability to obtain quantitative data) and presence of important major EEL edges at high energy losses, where the total electron fluence needed to obtain a sufficient signal is higher than the threshold for damage. This is the case with the Pt major edges (found at above 20000 eV) associated with the Pt-NPs, and which cannot be accessed without

damaging the sample. EELS may however be useful for the elemental analysis of different stabilising particles as long as the major edges for the elements in the particles are found at low energy loss values, as is the case with the silicon (silicon L-edge can be found near 100 eV) found in silica particles that are commonly used for Pickering emulsions [51, 57].

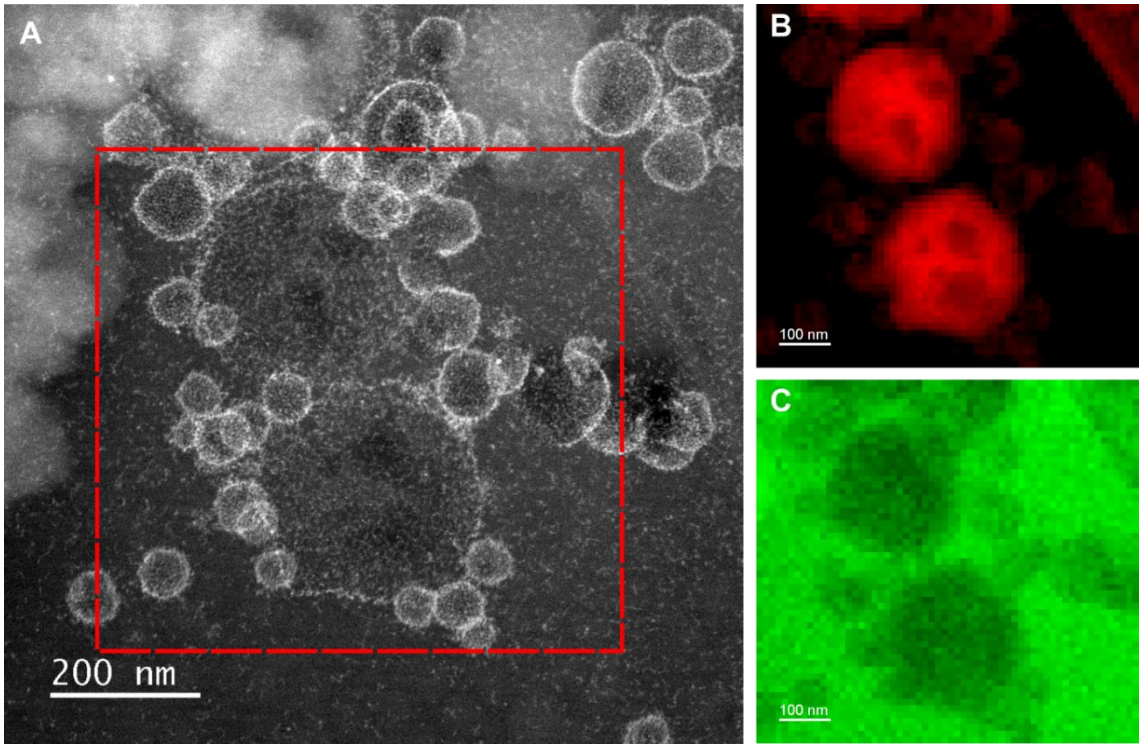


***Figure 5.13 –*** *Cryo-EELS elemental analysis of a droplet cluster. A) Cryo-HAADF STEM image of a droplet cluster. B) EEL elemental map of the carbon K edge signal and C) oxygen K edge signal. The position of the C signal maps to the position of the droplets and lacey carbon film, though smaller droplets cannot be resolved with the pixel size and dwell times used for the EEL signal collection. Total electron fluence: 16* $e^{-}/Å^{2}$ *[236].*

So far, neither EDX nor EELS can be thought of as a catch-all for elemental analysis of these Pickering emulsion samples. EELS can provide fast, single-pass, and low-dose elemental maps that can be used to quickly analyse elements within a limited electron energy loss range. This electron energy loss range imposes a limit to the elements that can be successfully analysed, as edges at high electron energy loss longer exposure time would require longer exposure times to detect a signal. This

increase in exposure time, possibly in the range of 1-10 seconds, would increase the total electron fluence by a factor of 100. Further issues arise when small image pixel sizes are needed to resolve small particles. On the other hand, EDX can be used to detect most elements despite the lower energy resolution. The 3-5 nm Pt-NPs used in these samples are challenging to analyse using both spectroscopy techniques, with EDX being able to detect a platinum signal (

Figure ***5.12***-C), but is unable to distinguish between individual NPs, and EELS being unable to reach a pixel size below 12 nm in the microscope setup used without significant damage that irreversibly changes the sample.

The absolute thickness of the sample was estimated from EEL low-loss spectra using Hyperspy, to generate height maps as shown in Figure 5.14 [240] and using a mean inelastic free path for vitreous ice of ~350 nm [217]. Thickness analysis was performed along a wide area near the centre of the TEM grid square, including areas free of sample, and areas with emulsion droplets to ensure that the ice thickness is sufficient to contain the droplets without deformation, but also thin enough to allow for cryo-HAADF STEM imaging and spectral analysis. Figure 5.14-B shows the vitreous ice within the holes in the carbon film is estimated to be approximately ~250 nm thick near the centre the grid square, with a variation in the ice thickness seen near the carbon film (~300 nm in thickness) and when approaching the copper grid. In contrast, the ice thickness in areas with droplet clusters was estimated to reach up to ~500 nm in thickness. Plunge-freezing cryo-TEM might therefore be suitable for the imaging of droplets and clusters up to a few hundreds of nanometres (<600 nm) in diameter without deformation or damage to the droplets. Larger droplet aggregates have been observed and could be suitable for cryo-(S)TEM imaging, with the only limitations being the decrease in SNR when imaging thicker sample regions and the higher likelihood of crystalline ice forming during the sample preparation in these thicker regions. For EELS analysis the droplet size limitation is more stringent: a minimum droplet size of ~50 nm could be analysed with the methods presented in this study, limited by the smallest pixel size available before beam-induced damage begins accumulating. Identifying an upper limit for EELS can be more challenging, as it is dependent on the information that needs to be extracted. The limitations for low-loss EELS and thickness estimation are less stringent and similar to those seen in regular cryo-HAADF STEM imaging, as the ice is generally thinner than 2-3 times the mean

inelastic free path. This means techniques such as EELS-based thickness estimation can be used in conjunction with other analysis techniques and as an initial step to ensure the area of interest is suitable for other techniques requiring thinner ice. On the other hand, techniques like EELS mapping and elemental quantification cannot be applied to areas where the sample thickness is much thicker than the mean inelastic free path, therefore only allowing for the analysis of single droplets or small agglomerates up to 400-500 nm in diameter.

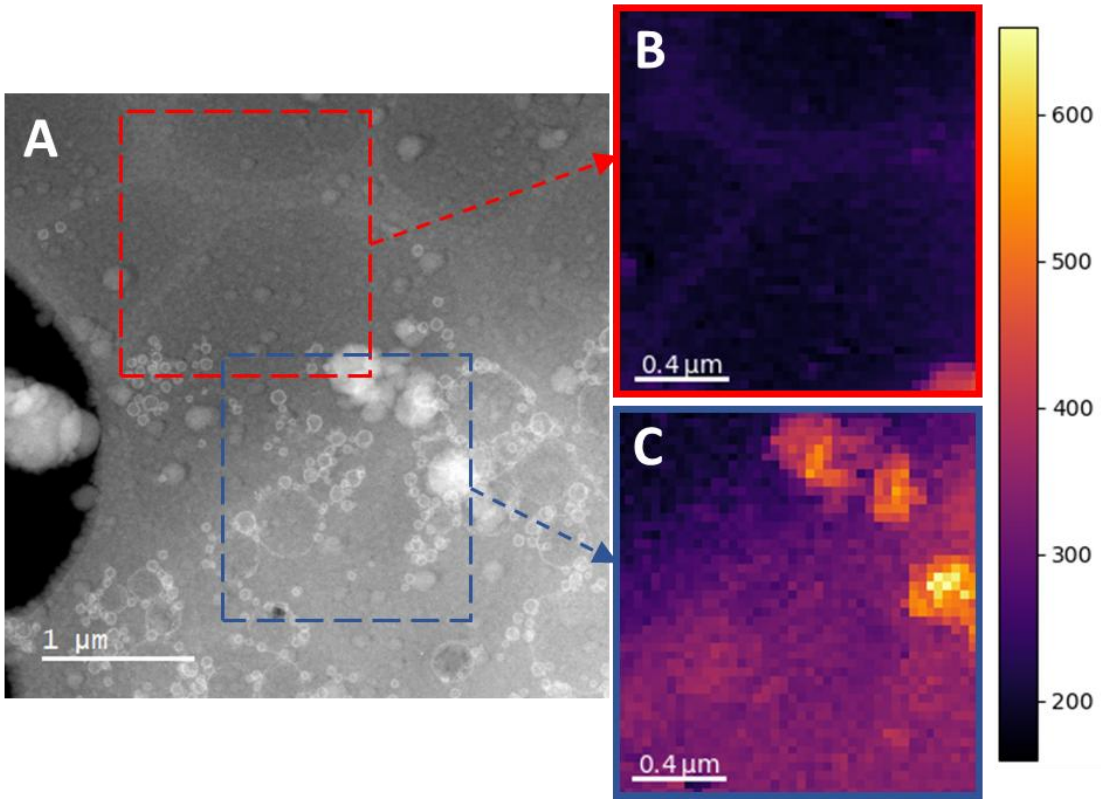


***Figure 5.14 -*** *Maps of the estimated absolute ice thickness (in nm) from EEL low-loss spectra taken from two regions of the STEM image (A). The estimated thickness maps for (B) an area without sample ($3.97x10^{-3}$ $e^-/Å^2$) and (C) an area with Pickering emulsion droplets shows that the ice thickness can vary depending on the presence of the sample (0.29 $e^-/Å^2$). Areas containing droplet clusters or larger droplets (>300 nm diameter) will feature thicker ice than what is observed in droplet-free areas [236].*

## 5.3 Electron Tomography

Electron tomography was used for the 3D visualisation of Pickering emulsion samples, to identify the 3D position and shape of the emulsion droplets and Pt-NPs. In all cases a cryo-HAADF STEM tilt series was recorded in a range from -60° to +60°, which was then reconstructed using SIRT and visualised using Imaris. Tilt series were collected in HAADF STEM mode to mitigate the beam-induced damage accumulating over the course of collecting multiple images 42[98].

Electron tomography was initially used to compare the drop cast and plunge-frozen hexadecane-in-oil emulsion samples to verify that the droplets remain spherical after cryo-fixation, while the dry droplets will completely collapse. Figure 5.15 shows HAADF STEM images of emulsion droplets taken in cryo-TEM (Figure 5.15-A) and standard dry TEM (Figure 5.15-B), and the corresponding 3D reconstructions. For both samples, tilt series were collected every 5° for a total of 25 images per tilt series. A comparison between 3D reconstructions of the two samples from a top (Figure 5.15-C and Figure 5.15-D) and side (Figure 5.15-E and Figure 5.15-F) view shows the position of Pt-NPs, which indicate that the plunge-frozen emulsion droplet retains a spherical 3D structure, while the Pt-NPs in the drop cast sample are deposited on the grid support film. Pt-NPs in the plunge-frozen sample have been colour labelled to distinguish between the particles near the main droplet's surface (coloured red) and the particles in the water phase and near the two smaller droplets (coloured green). It is notable that the Pt-NPs in the water phase and the emulsion droplets both appear to be located preferentially on the ice surface (the air-water interface).

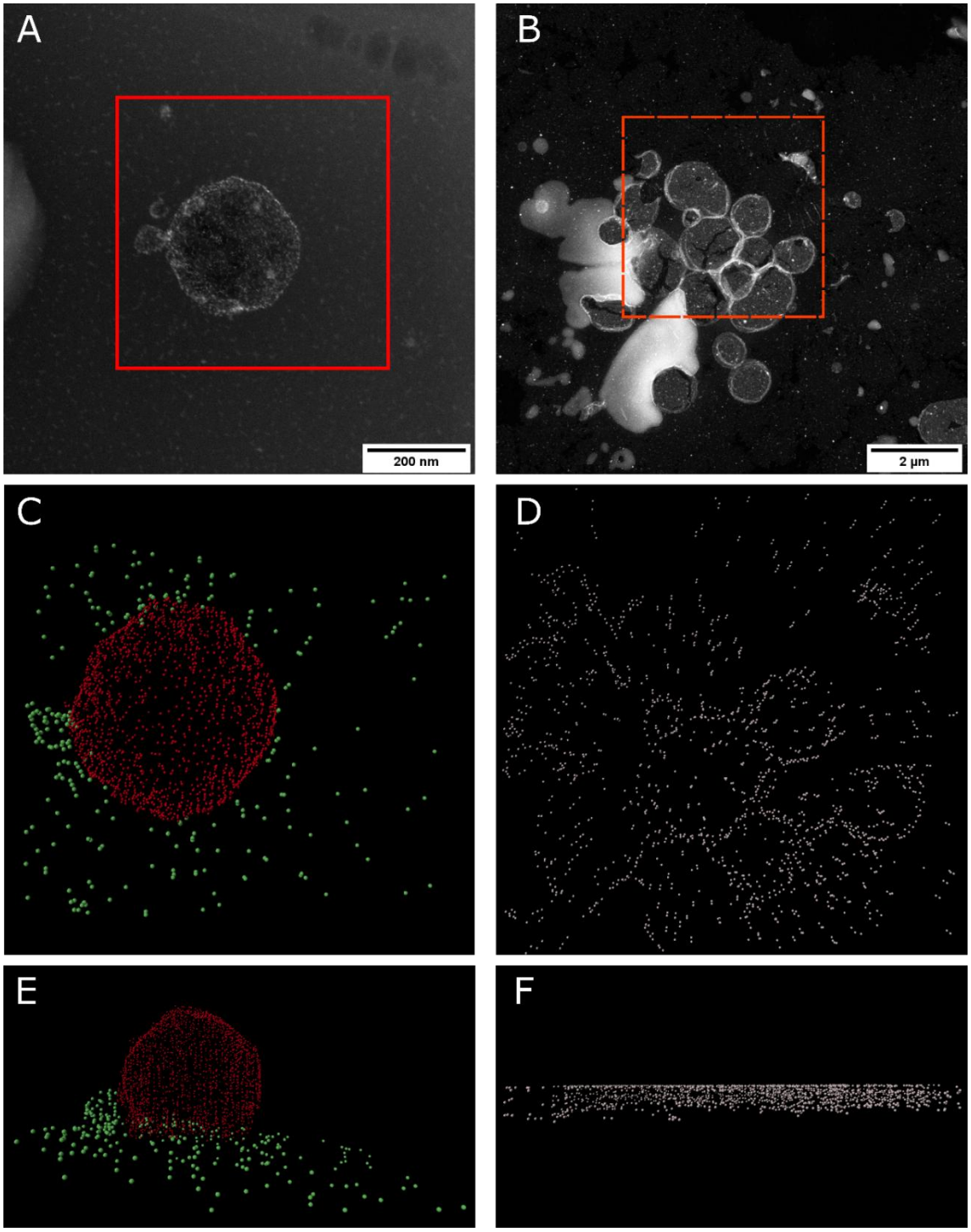


***Figure 5.15 –*** *HAADF STEM images of a plunge-frozen and drop cast emulsion samples and images from the corresponding electron tomograms. A) Cryo-HAADF STEM images of a droplet in a plunge-frozen sample. B) HAADF STEM image of a droplet cluster in a drop cast sample. C) Top view image of an electron tomogram reconstructed from a tilt series of the area in A). Pt-NPs are shown in red when found on the surface of the main droplet in A) and green when found elsewhere. D) Top view image of an electron tomogram reconstructed from a tilt series of the area in B), with*

*Pt-NPs shown in grey. E) Side view of the electron tomogram seen in image C). F) Side view of the electron tomogram seen in image D). Comparisons between E) and F) clearly show that the cryogenic sample preparation allows for the preservation of the 3D droplet structure, while all droplets appear to have collapsed in after dry sample preparation. Total electron fluence: ~2667 $e^-/Å^2$.*

Figure 5.16 shows an electron tomogram of an emulsion droplet cluster with droplets ranging from ~50 nm to ~600nm, reconstructed from a tilt series consisting of 41 images taken every 3°, using a pixel size of 1.8 nm and a probe current of 20 pA. The electron tomograms in Figure 5.16-B and Figure 5.16-C show the position of the Pt-NPs on the surface of the emulsion droplets (coloured in red) and in the water phase (coloured in green). The emulsion droplets are shown in purple; however, due to the low contrast of the oil phase, the 3D surfaces for the droplets were created manually by following the position of the Pt-NPs, assuming their position is near the oil-water interface. Similarly to the electron tomogram in Figure 5.15-E, Figure 5.16 also shows the three-dimensional nature of the droplets is retained after cryogenic preparation, as the droplets do not appear to have collapsed. The Pt-NPs can be seen both on the oil-water interface and in the water phase, where they are predominantly found near the ice surface. The presence of Pt-NPs near the ice surface might be an artefact of the sample preparation, arising from nanoparticles moving during the short time period between the sample blotting and freezing in liquid ethane. This effect has been observed in cryogenically frozen inorganic samples with nanoparticle markers being found at the ice surface; in biological samples, the presence of sample near the ice surface can induce a bias on the direction of cells, viruses, and particles, therefore affecting their characterisation [204, 217, 222, 223].

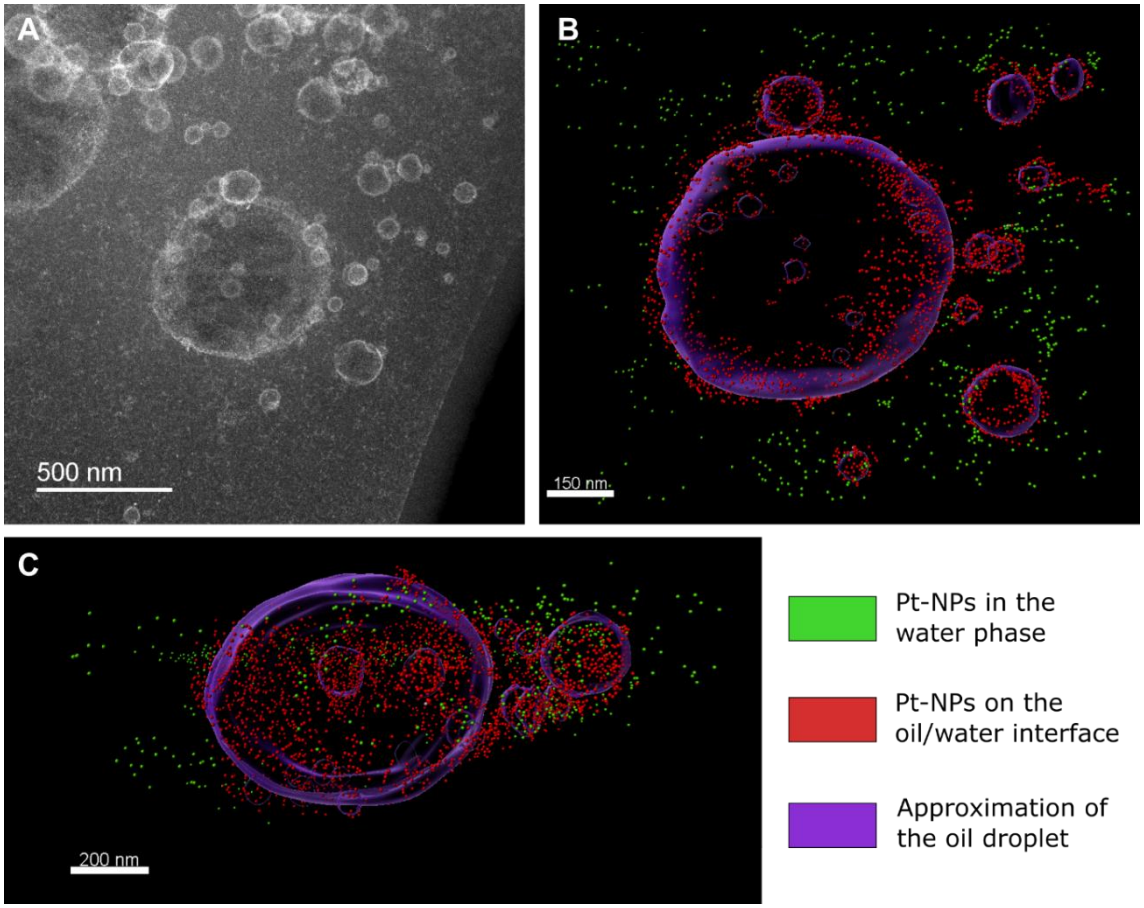


***Figure 5.16 –*** *Electron tomogram images of a droplet cluster. Cryo-HAADF STEM image of a droplet cluster and B) a top view image from the corresponding electron tomogram. Approximation for the oil droplets (in purple) were made manually based on the position of the Pt-NPs and are therefore not necessarily accurate to the position of the oil phase. C) Side view of the tomogram showing Pt-NPs in the water phase on the air-water interface, and the presence of a thicker ice layer near the large central droplet. Total electron fluence: ~1600* $e^-/Å^2$ *[236].*

As stated, electron tomograms of the Pickering emulsion samples show that similarly to other systems, the droplets and particles tend to be found near the surface of the ice [204]. A diagram representing this arrangement is shown in Figure 5.17, where Pt-NPs on the droplet surface are represented in red and those in the water phase are represented in green. Ice near large droplets becomes thicker to accommodate the droplet below an unknown critical size, above which the droplet will be partially destroyed. This increase in ice thickness can be seen by observing the position of the Pt-NPs on the ice surface in Figure 5.16-C. In this schematic, the Pt-NPs are closer

together on the right side of the image, and the gap between the top and bottom of the ice increases while nearing the large central droplet. It is unfortunately not possible to accurately determine whether the entire droplet is preserved in 3D as the Pt-NPs on the top and bottom sections of the tomogram are absent or represented inaccurately due to the missing wedge artefacts. Additionally, imaging these larger droplets becomes especially difficult as they are the first features in the sample that will incur beam-induced damage. Smaller droplets in a cluster near larger droplets can be found at any position within the ice, which functions as a shield to beam damage as more ice is required to sublime before reaching these droplets.

Following the diagram in Figure 5.17, damage to the sample was seen to progress as follows: initial damage affects the entire sample, leading to small displacements of smaller particles such as the Pt-NPs in this system. This can be observed as a displacement of particles near the ice surface and expansion of the droplets. As electron fluence increases, the ice begins to sublime, causing the particles near the ice surface to move further. This was seen to first affect the particles in the water phase (as these tend to be in contact with the ice surface) and large droplets, causing them to burst. Smaller droplets near the middle of the ice cross-section will be shielded from this until the ice sublimes further. The effects of beam-induced sample damage during the collection of tilt series are further discussed in Section 5.5 “Observations on Sample Damage“.

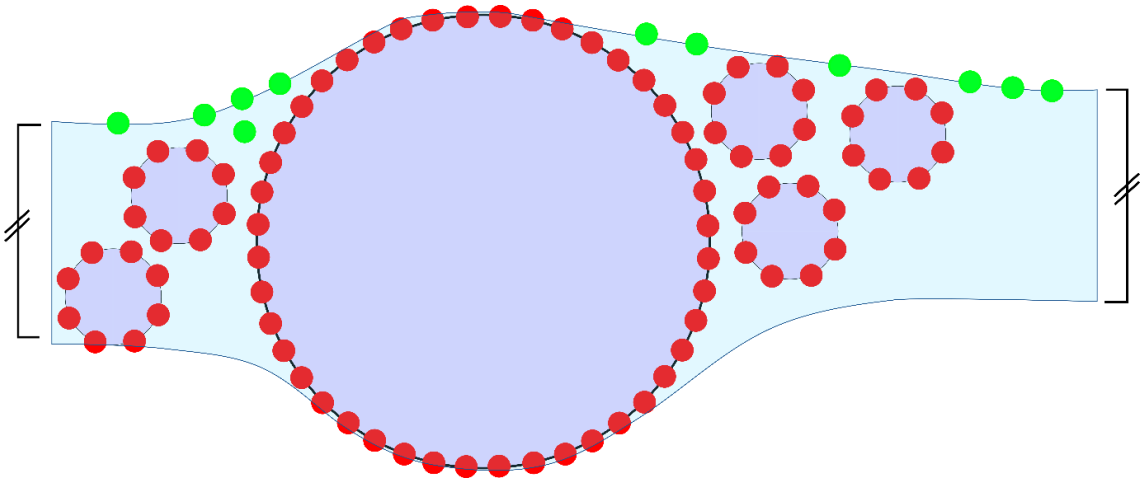

***Figure 5.17 –*** *Schematic showing a cross-section of ice containing the Pickering emulsion sample. Droplets are highlighted in purple; NPs on the oil-water interface are shown in red while NPs in the water phase are shown in green. In cases where*

*droplets have a diameter slightly larger than the ice thickness, they can still be found while being not collapsed. In these cases, the local ice near the large droplet will be thicker than usual (even when located far from the TEM grid bars). Both droplets and particles will be preferentially found near or at the ice surface, though both can be found in the middle of the ice within clusters.*

The 3D reconstruction results obtained show that HAADF STEM imaging with atomic number contrast allows for straightforward analysis of the Pt-NPs in 3D space. However, in this imaging mode the oil phase does not generate enough contrast to be successfully imaged, and it is therefore not possible to locate the position of the oil-water interface. As was seen in the $TiO_2$ case study in Chapter 4, simultaneous cryo-ET and elemental analysis can be performed to obtain 3D elemental information for a sample with poor contrast, as is the case with the Pickering emulsion's oil phase.

### 5.3.1 Considerations for Electron Tomography

Controlling beam-induced damage to the sample during the acquisition of the tilt series remains a key issue that must be balanced with the overall imaging quality. The use of HAADF STEM mode for tilt series acquisition was taken as an initial step in reducing sample damage was taken, but additional parameter can further decrease the total electron fluence. Beam current, dwell time, pixel size, and number of images in the tilt series all affect the total electron fluence and can be fine-tuned on a sample-by-sample basis. Lowering the beam current and dwell time will decrease the electron fluence but will result in a lower signal. An increase in pixel size will likewise decrease the electron fluence but will also decrease the image resolution which in this sample resulted in cases where the pixel size was too large to resolve individual Pt-NPs (see Figure 5.16, where the imaging pixel size was 1.8 nm per pixel, too large to resolve individual ~3 nm Pt-NPs) but is a vital trade-off to ensure sample subliming does not happen during imaging. Lastly, the number of tit steps can be decreased to lower the number of images taken per tilt series, but also affecting the quality of the 3D reconstruction [191, 214, 215, 217].

A comparison between electron tomograms acquired using different parameters can illustrate this balance between damage and image quality: Figure 5.18 shows an

electron tomogram of a droplet cluster reconstructed from a tilt series acquired with a 20 pA probe current, a 5° tilt step, but a pixel size of ~0.6 nm per pixel. Although the higher tilt step used for this electron tomogram compared to the tomogram in Figure 5.16, the smaller pixel size of ~0.6 nm per pixel result in an overall higher electron fluence per image taken. This resulted in visible damage to the sample which can be seen in the form of Pt-NPs being displaced from the droplet surface due to ice subliming (Figure 5.18-B and Figure 5.18-C). Sample damage occurring during the acquisition of the tilt series will inevitably result in an inaccurate reconstruction. In addition to mitigating beam-induced damage, using HAADF STEM for tomography is advantageous as it will limit any diffraction contrast that would otherwise be evident in cryo-TEM imaging and therefore limit any 3D reconstruction.

STEM pixel size and dwell time are not the only parameters to be considered when collecting a tilt series in cryo-(S)TEM: not only is the number of tilt steps in a series a major contributor to the total electron fluence, but so are the focusing and tracking steps. Both of these steps can be automated depending on the software used, allowing for focusing and tracking at lower pixel sizes. Unfortunately, due to the inability to simultaneously focus on all Pt-NPs on emulsion droplets due to the spherical shape of said droplets, all focusing had to be performed manually, therefore increasing the overall electron fluence. Sample focusing can be approached by either directly focusing on the area of interest or by moving the beam to focus on a nearby feature. Neither strategy can be thought as a catch-all solution for this system, as the former allows for accurate focusing but is more energy intensive, while the latter fully prevents damage to the area of interest but requires the presence of nearby features along the tilt axis. This requirement is often not met, as in this system droplets found in clusters tend to be near thicker ice, and therefore less suitable for collecting a tilt series. Improvements in the focusing strategy and user ability, together with a decrease in the probe current and pixel size used for imaging are the factors that had the greatest contributions in lowering the total electron fluences for the collection of a tilt series. Among the electron tomograms presented in this chapter, it is possible to see a decrease in total electron fluence required for a tilt series from ~2600 $e^{-}/Å^{2}$ to less that ~1000 $e^{-}/Å^{2}$ to obtain tomograms of similar quality, an improvement that was mostly possible through an increase in user experience allowing for faster and more accurate focusing to obtain images at lower probe currents.

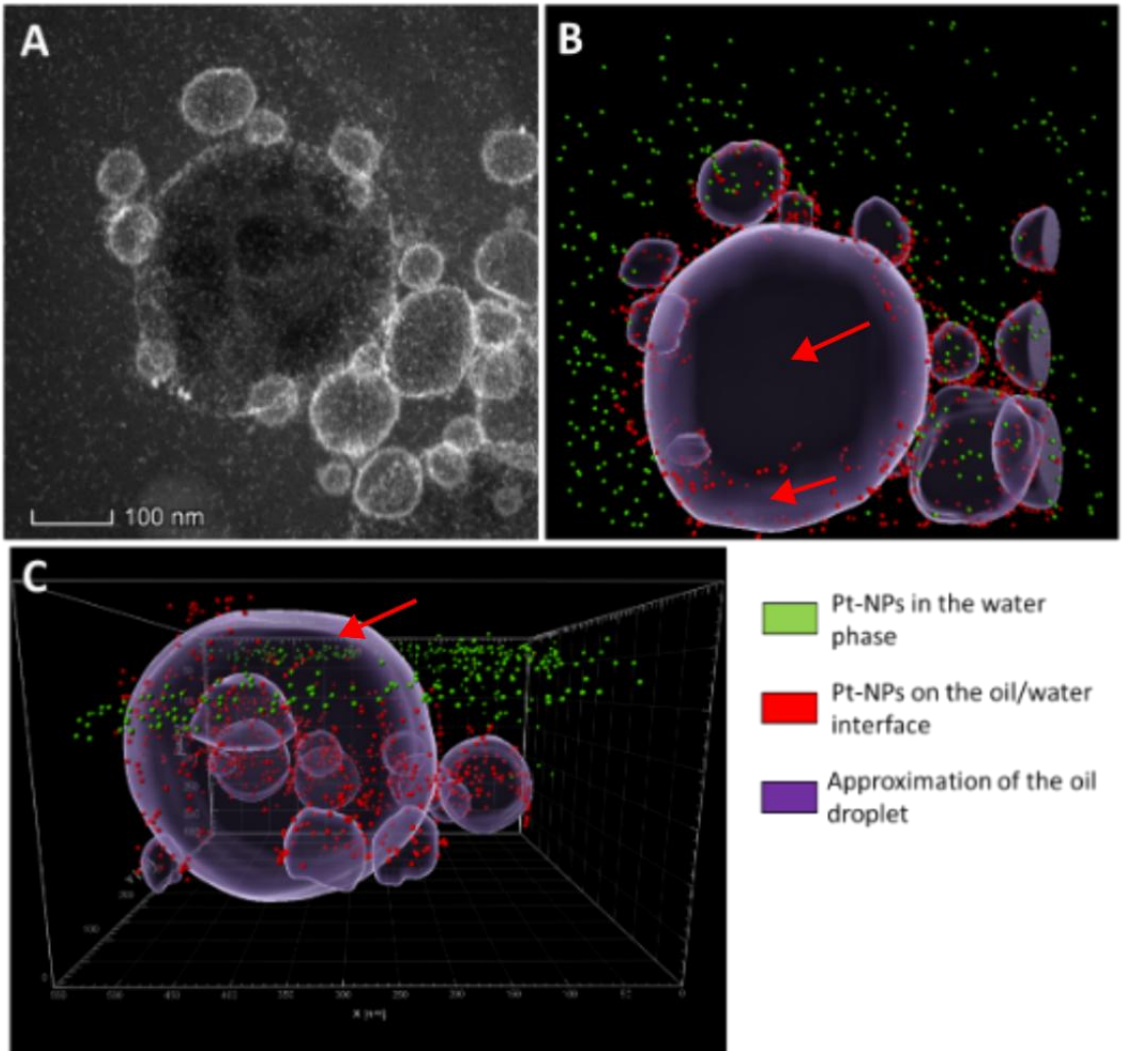


***Figure 5.18 –*** *Electron tomogram images of a droplet cluster that has received significant beam-induced damage. A) Cryo-HAADF STEM image of the droplet cluster featured in Figure 5.22 and B) a top view image of the corresponding electron tomogram with arrows pointing to areas where the Pt-NPs on the droplet surface were displaced due to ice subliming. C) Side view image of the electron tomogram showing the damage occurring at the ice surface. Total electron fluence: A) ~67 $e^-/Å^2$, B) ~2600 $e^-/Å^2$ [236].*

Increasing the tilt angle will increase the distance travelled by the electron beam through the sample, therefore making the sample more difficult to image and requiring a higher electron dose to obtain a sufficient SNR. If the thickness of the ice is assumed to be uniform (Figure 5.19), the increase in distance through the sample travelled by the electrons increases with sample tilt following:

$$l = \frac{l_0}{cos\theta} \quad \textbf{(5.2)}$$

Where:

$l_0$: Sample thickness

$l$: Length of the path travelled by the electron beam

$\theta$: Tilt angle

The cryo-TEM holder used for this study allowed for a maximum tilt of ±60°. Accounting for this, the effective sample thickness at maximum tilt can be calculated to be:

$$l = \frac{l_0}{cos60°} = 2l_0 \quad \textbf{(5.3)}$$

An increase in sample thickness by a factor of 2 can have a large effect on the imaging quality and further analysis techniques. When accounting for this thickness increase, the amount of suitable areas for electron tomography decreases; when imaging this system, areas with large droplet clusters often could not be used for electron tomography due to the potential thickness of the sample at high tilt angles, despite the abundance of droplets in these regions. In areas where the sample is present within the ice, the ice thickness tends to be thicker than the average, sample-free, regions (see Figure 5.17 and Figure 5.19-C). Likewise, depending on the sample morphology, the increase in effective thickness at high tilt angles can be larger than the calculated $2l_0$. This increase in thickness is not homogeneous throughout the sample and predicting it can be complicated, making choosing the ideal area for electron tomography a difficult endeavour. A potential strategy for determining suitable areas consists of the collection of an EEL low-loss spectrum near or at the interested area(s). This allows the user to estimate the sample thickness before beginning the tilt series collection, although this procedure will contribute to the total electron fluence for the area.

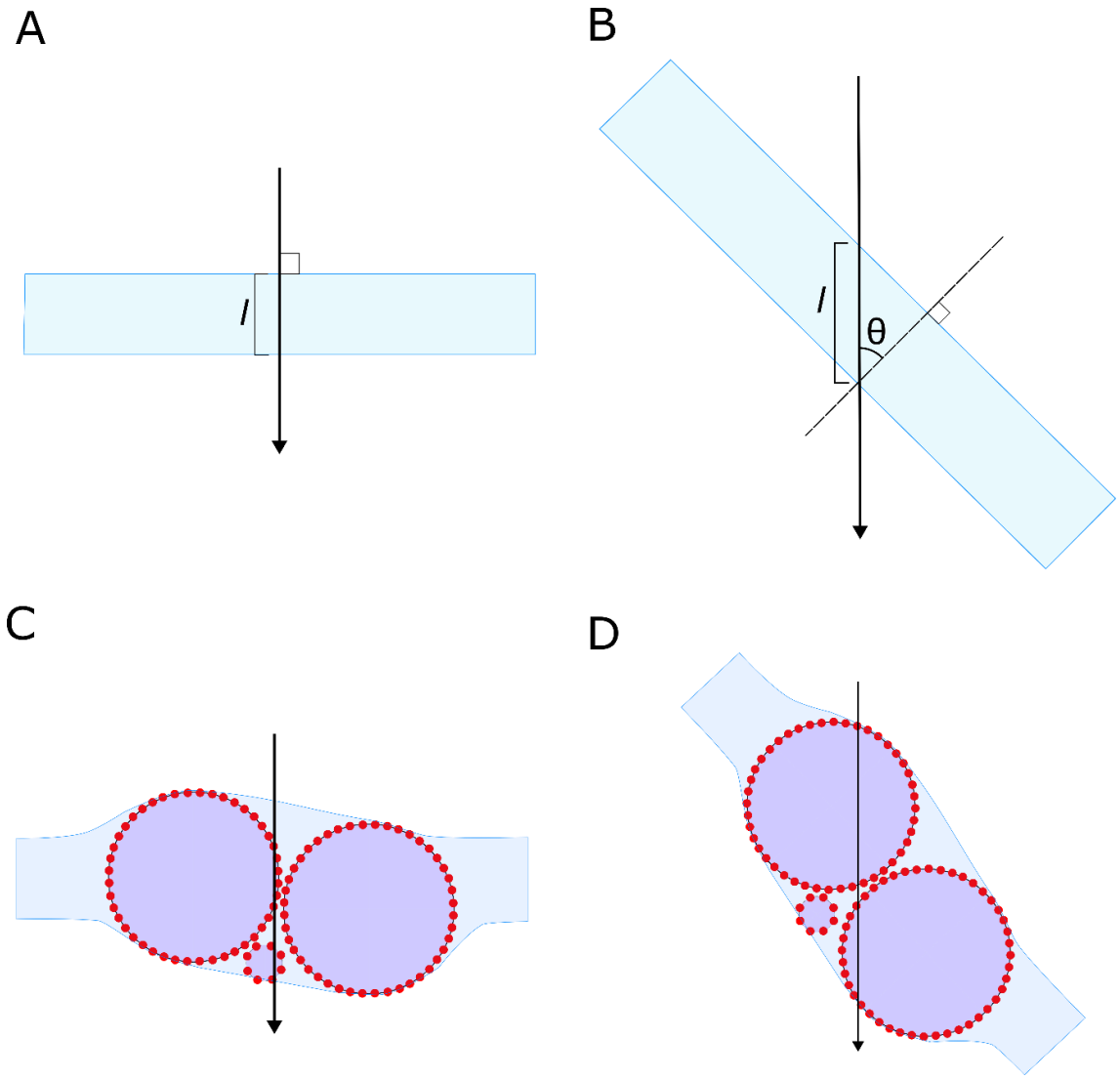


***Figure 5.19 –*** *Schematic showing the change in distance travelled by the beam through the sample after tilting. A) Electron beam passing through the sample at 0° tilt; here the distance travelled l is the same as the sample thickness. B) Electron beam passing through the sample at a tilt angle θ; as the sample tilt approaches 90°, the distance travelled by the beam (l) increases. C) Electron beam passing through a Pickering emulsion sample containing a droplet cluster. In cases where large droplets are preserved, the sample thickness can be higher than the average thickness of the ice as shown here. D) Electron beam passing through a tilted Pickering emulsion sample. Depending on the size and position on the droplets within the ice, the distance travelled by the beam might increase by an even greater extent, which cannot be easily calculated as the local sample morphology might be completely different depending on the area imaged.*

## 5.4 Cryo-EELS Tomography

Electron tomograms reconstructed from HAADF STEM images alone do not show sufficient contrast to distinguish the oil phase from the surrounding ice. In the tomograms shown in Section 5.3, the shape of emulsion droplets was generated from the position of Pt-NPs assuming their closeness to the oil-water interface. However, the success in identifying the oil phase in the emulsion droplets using EEL spectroscopy as an elemental analysis technique that required a low total electron fluence, shows an opportunity for the use of electron tomography and EELS simultaneously to obtain 3D elemental data.

EEL low-loss and core-loss spectra were collected at various tilt angles alongside a HAADF STEM tilt series. A total of 9 EELS elemental were thus acquired at tilt angles 0°, ±18°, ±27°, ±39°, and ±51°, while 51 HAADF STEM images were acquired with a 3° tilt step and ~3 nm/px pixel size at ~10 pA. A lower number of EEL spectra were collected compared to the HAADF STEM images to decrease the total electron fluence and prevent damage during data acquisition. After generating elemental maps using the carbon K edge signal in Hyperspy, the EELS tilt series was aligned and reconstructed into a tomogram using the same process outlined in Section 5.3 (see Figure 5.20). The tomograms reconstructed from the HAADF STEM and EELS signals were then superimposed in Imaris using the 0° HAADF STEM and ADF images, which were collected simultaneously with the EEL signal. Figure 5.20-D shows that the tomogram generated from the carbon K edge map aligns with the approximated position of the oil droplets.

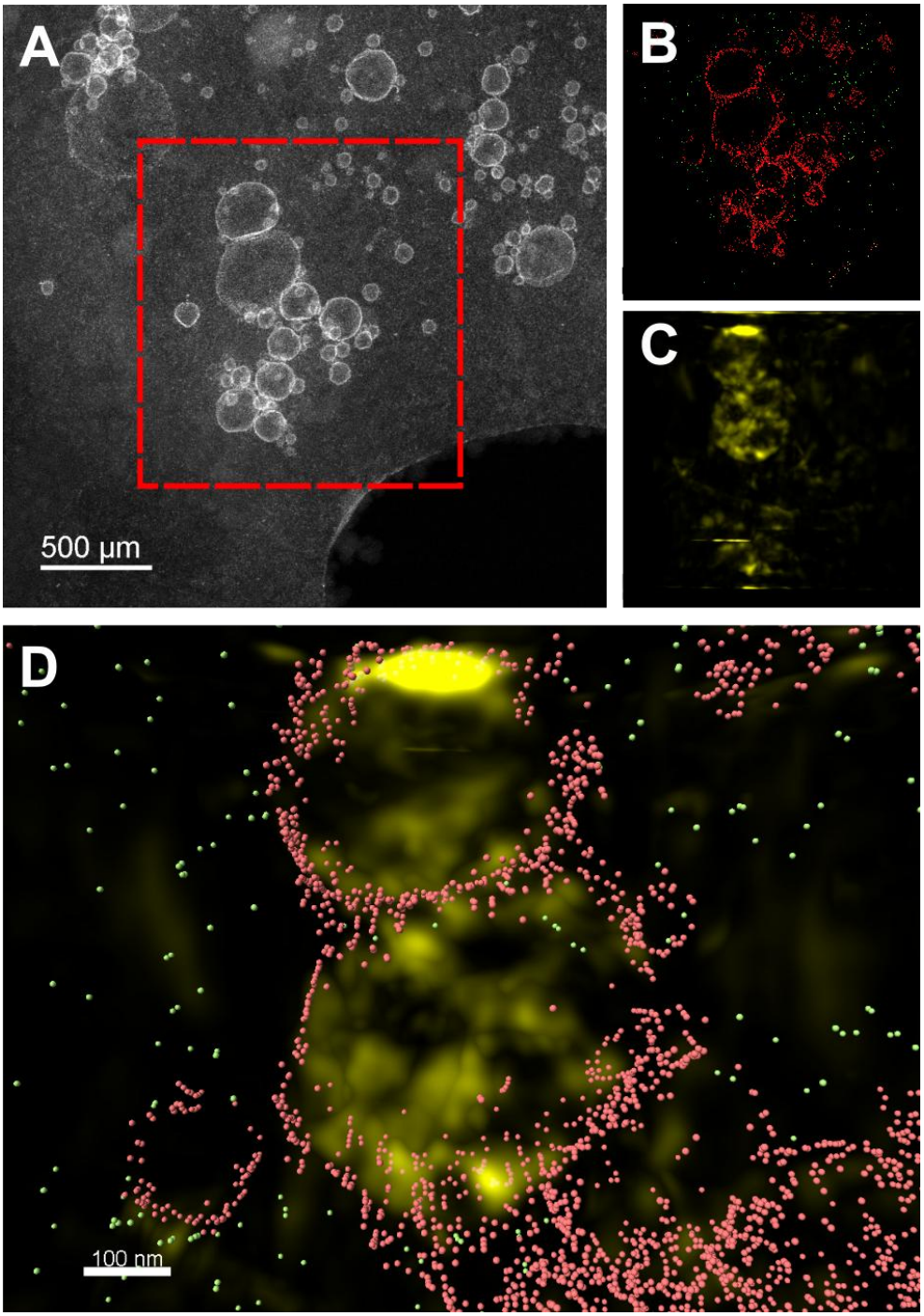


***Figure 5.20 –*** *Images from an electron tomogram including reconstructions from cryo-HAADF STEM and EELS signals. A) Cryo-HAADF STEM image of a droplet cluster. B) Top view of an electron tomogram reconstructed from cryo-HAADF STEM images of the area highlighted in A). Pt-NPs near the oil-water interface are shown in red and Pt-NPs in the water phase are shown in green. C) top view of an electron tomogram reconstructed from EEL maps of the carbon K edge signal in the highlighted area in A). D) top-view image showing the HAADF STEM and EEL signals superimposed. The*

*carbon K edge signal aligns with the two larger droplets seen in D), though the pixel size was insufficient to resolve other smaller nearby droplets. Total electron fluence: ~551 $e^-/Å^2$ [236].*

The requirement to collect multiple EELS elemental maps drastically increases the total electron fluence needed (by at least a factor of 10), and therefore pixel sizes below 12 nm cannot be used for EELS elemental maps without damage occurring during the tilt series. This limits the use of this technique to larger droplets (>300 nm) and can only give qualitative information on the position of the stabilising nanoparticles. This size limit creates a narrow size range for suitable droplets, with the lower limit being given by the pixel sized needed for EELS and an upper limit given by the sample thickness. It is therefore possible to determine the general position of the particles and whether they are embedded within the oil-water interface, but it is not possible to determine their exact position at the interface (e.g. determine the contact angle for the particles, which is a difficult task for systems where the particles stabilising the interface are <50nm).

Despite the improvements in tilt series collection methodology, some sample damage was still observed when collecting the EELS and HAADF STEM tilt series. Selected tilt series images in Figure 5.21 show some of the issues encountered during data acquisition. Initial sample damage (similar to the droplet “expansion” observed in Figure 5.25) was seen during imaging. Further issues can be found when selecting suitable regions for collecting EELS series; not only is the increase in effective ice thickness at higher tilt angles potentially problematic for obtaining a sufficiently strong EELS signal, but additionally, the supporting carbon film can partially block the sample. This can be seen highlighted in Figure 5.21-F, where the carbon film is partially blocking the droplet cluster. This issue can be solved by performing an EELS analysis at 0° to obtain information on the ice thickness and presence of carbon film (which may be difficult to see near droplet clusters).

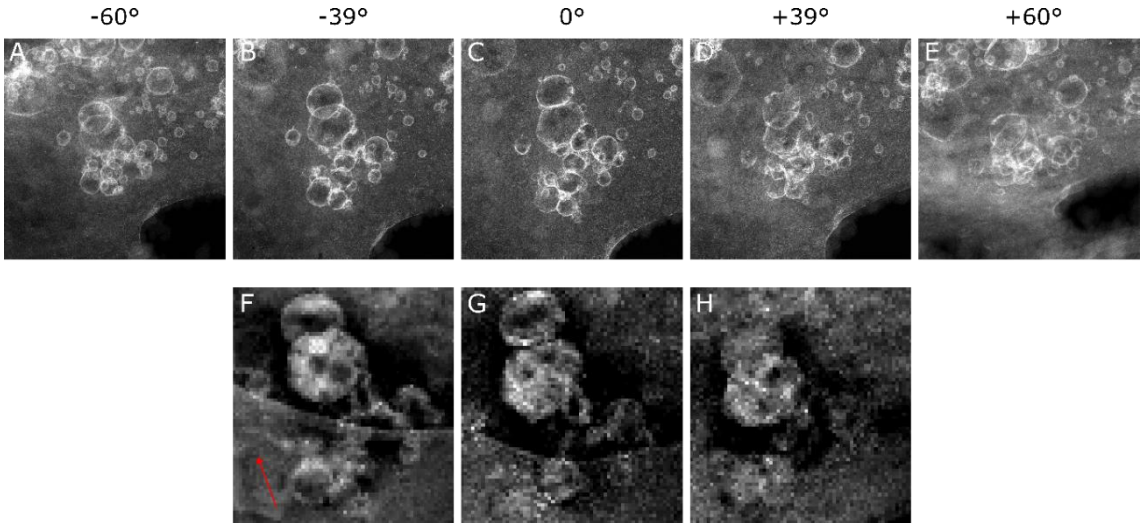


***Figure 5.21 –*** *Selection of images from the tilt series used for Figure 5.20. A) through E) tilt series images collected in cryo-HAADF STEM; as the series progresses it is possible so see some initial displacement of Pt-NPs due to beam damage. F) through H) EEL elemental maps showing the carbon K edge signal. The red arrow shows part of the lacey carbon film covering a section of droplet cluster within the area of interest.*

The techniques presented in this section were successful as a proof of concept for the use of low dose electron tomography in conjunction with spectroscopy to effectively perform 3D elemental analysis of cryo-preserved samples. This process is, however, not always necessary, as collecting a single EELS (or EDX) elemental map might be enough to provide sufficient elemental information for 3D analysis in cases where the structures of interest have clear contrast within the tilt series (see Chapter 4). This approach will cause far less beam-induced damage while being more accessible to users.

## 5.5 Observations on Sample Damage

Sample damage during cryo-EM imaging has been shown to affect not only biological samples, but also inorganic soft matter samples such as nanoparticle dispersions [241-243]. The high total electron fluence associated with repeated high-resolution imaging, especially when collecting image series causes of this damage and its visual appearance. Figure 5.22 shows a large droplet before and after the collection of a HAADF STEM tilt series, amounting to a total cumulative electron fluence of ~2600 $e^-/Å^2$ (see Section 5.3.1 for details on tilt series acquisition). The post-tilt series result in Figure 5.22-B shows the large central droplet being damaged, with its surface appearing to have burst, while the nearby smaller droplets appear to be unaffected. Images from the tilt series of the area in Figure 5.23 clearly shows the progression of the damage to the droplet, highlighted by the red arrows pointing at the forming hole. This type of damage occurs frequently and is likely due to the ice subliming; given the importance of managing sample damage, more work was done to better understand the mechanisms through which the Pickering emulsion system is affected by the electron beam.

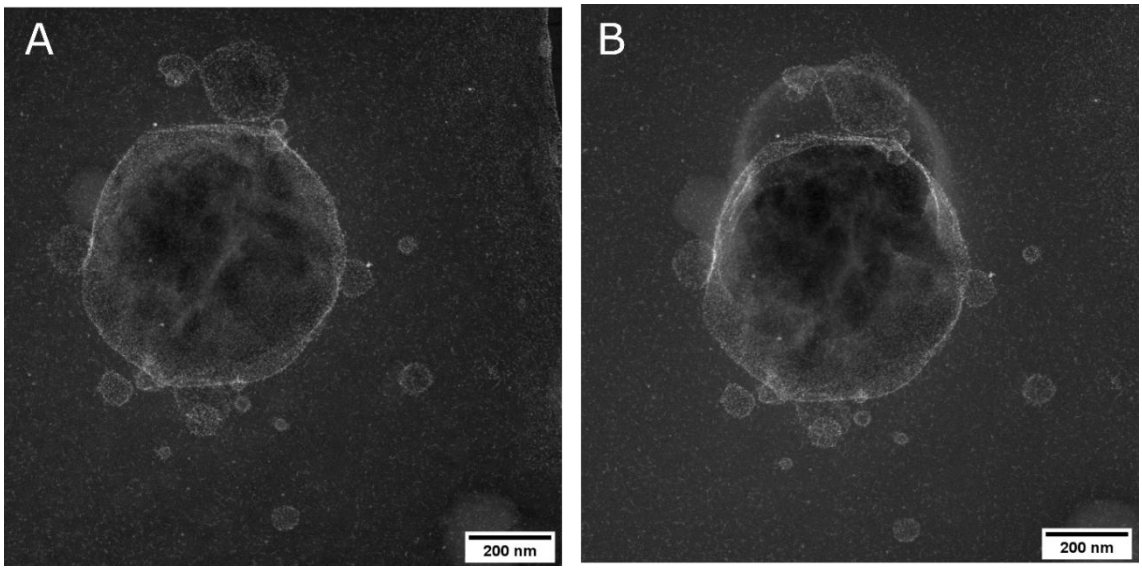


***Figure 5.22 –*** *Cryo-HAADF STEM images showing beam-induced damage to a droplet. A) Image of the droplet after minimal exposure (i.e. tracking, focusing, and imaging). B) Image of the same droplet after an approximate total electron fluence of ~2600 $e^-/Å^2$. Result of beam-induced damage in the area shown in B) include the displacement of Pt-NPs on the surface of the large central droplet as a result of ice sublimation, and beam-induced carbon contamination.*

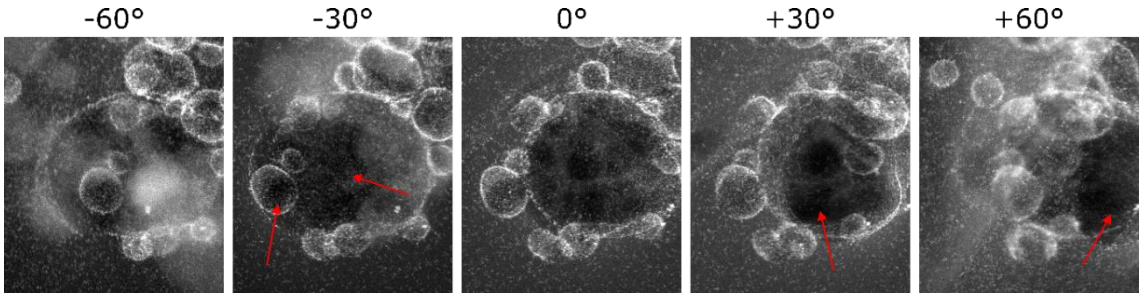


***Figure 5.23 –*** *Images from a cryo-HAADF STEM tilt series corresponding to Figure 5.22 and Figure 5.18. The image series shows the progression of sample damage (highlighted by the arrows) as the tilt series is being collected. Sample damage is evident by the displacement of Pt-NPs on the surface of the droplets closest to the ice surface (see Figure 5.18 for the position of the damage in 3D space). As the tilt series collection progresses sample imaging becomes more difficult due to the effective sample thickness increasing at high tilt angles, sample damage, and the onset of sample contamination, with the contamination becoming an issue for imaging when nearing the end of the series collection.*

EEL low-loss spectral images were taken as a selected area was irradiated with electrons to monitor the decrease in ice thickness with cumulative electron fluence (Figure 5.24 and Table 5.1). The absolute ice thickness for the irradiated region was calculated from the EEL low-loss spectra in Hyperspy. The minimum and maximum thickness values were then taken from the thickness maps for each time point and recorded in Table 5.1. Looking at the decrease in the estimated maximum and minimum values for sample thickness across the experiment in Table 5.1, no significant changes in thickness are present until the first time point. The total cumulative electron fluence of ~2600 e-/Å$^2$ before the onset of visible damage (as seen in Figure 5.24-B and Table 5.1) reflect the findings in Egerton (2019). The greatest changes in thickness begins at time point 2, which coincides with the most visual damage a seen in Figure 5.24-C, -D and -E, where the droplets begin bursting. Initial damage to the droplets begins affecting the smaller droplet to the left first and then proceeds to the central droplets. This can be explained by the position of these droplets relative to the ice surface as seen in the side view of the electron tomogram

of the area (Figure 5.15-E). Sample damage and ice thinning in Figure 5.24 is concentrated on the top-left of the image, which coincides with the beam's scanning trajectory starting on the top-left corner of the screen. This results of increased accumulated damage for an image series in this corner due to beam flyback.

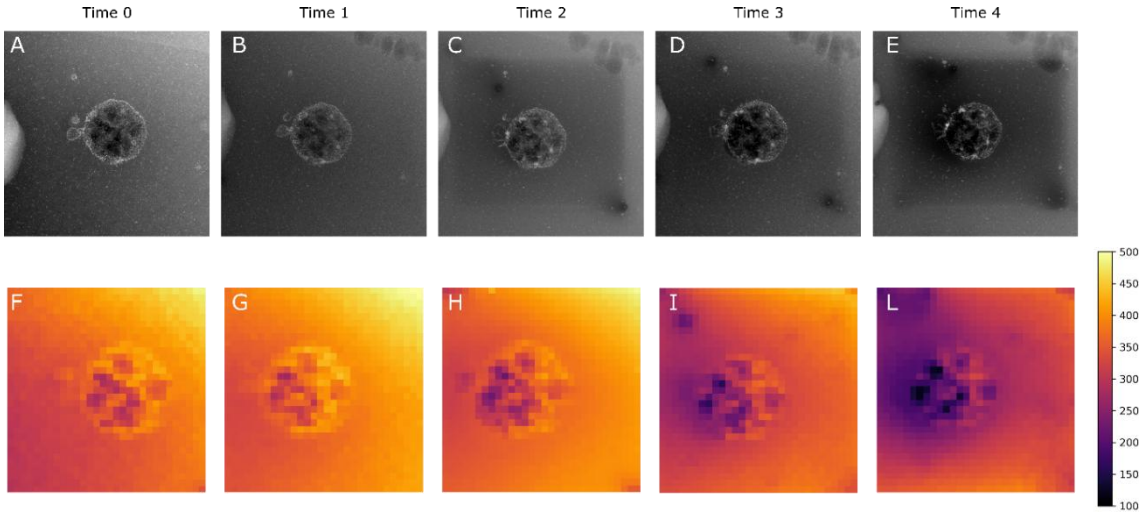


***Figure 5.24 –*** *Cryo-HAADF STEM images of a droplet after beam exposure and corresponding EEL maps of the estimated sample thickness (in nm) at different time points. A) to E) cryo-HAADF STEM images of the droplet and surrounding area showing damage to the droplet and area exposed to the electron beam. F) to L) Maps of the estimated sample thickness at the corresponding time point, using low-loss EELS. Note the values for vitreous ice were used for the inelastic mean free path and sample density, therefore the thickness estimate is inaccurate for droplet itself.*

***Table 5.1 –*** *Electron fluence values and sample thickness for the area in Figure 5.24 at different time points. Thickness at time point 0 was estimate using low-loss EELS with a total electron fluence <10* $e^-/Å^2$*. Note that fewer images were taken for time point 1, resulting in a lower electron fluence for that time point.*

| Time Point | Electron Fluence ($e^-/Å^2$) | Cumulative Electron Fluence ($e^-/Å^2$) | Max Thickness (nm) | Min Thickness (nm) |
|---|---|---|---|---|
| 0 | 10 | 10 | 486 | 282 |
| 1 | 2677 | 2677 | 500 | 272 |
| 2 | 1710 | 4387 | 493 | 220 |
| 3 | 2630 | 7017 | 444 | 159 |
| 4 | 2630 | 9647 | 389 | 118 |

At high electron fluences (>500 $e^-/Å^2$) or small pixel sizes (<2 nm/px) sample damage appears immediately in the form of a slight displacement of Pt-NPs. Initial sample damage can be seen in Figure 5.25-A to -C, where all droplets in frame appear to expand continuously. This effect is seen most evidently in the droplets labelled I and II, though movement in the Pt-NPs is present throughout the entire imaged area and in NPs that are both on the droplet surface and within the water phase. As damage progresses droplets appear to burst as shown in Figure 5.25-D to -F. Although all the imaged droplets begin expanding, only a few are seen to burst in Figure 5.25-F, with the damage mostly occurring only on one side of the droplets. Droplet bursting may occur due to the ice subliming, which forces the displacement of the Pt-NPs nearest to the ice surface. As such, most of the damage from subliming will be observed only on the droplets near the ice surface, and only on the size of the droplet in contact with it. Droplet expansion might occur through a different mechanism from droplet bursting, as all droplets in the irradiated area are seen to expand immediately independently of their size of position in the ice. This expansion might instead be caused by changes to the ice structure, with ice crystallisation possibly forcing the displacement of nanoparticles before subliming.

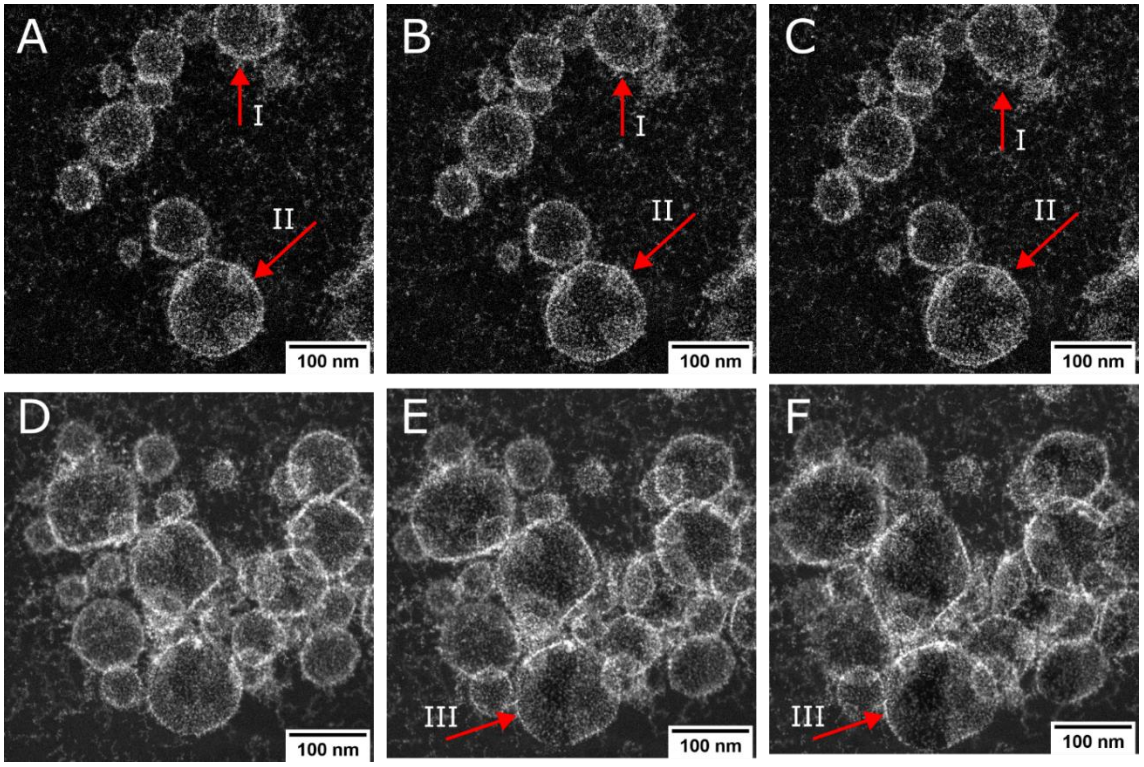


***Figure 5.25 –*** *Selection of cryo-HAADF STEM images from an image series showing droplets expanding and bursting due to beam damage. A) through C) Images showing droplets in a cluster that appear to expand as they are exposed to the electron beam, with droplets labelled I and II showing noticeable expansion. D) through F) Images showing droplets in a cluster expanding and then bursting, with the droplet labelled III showing noticeable expansion and then bursting near the area signalled by the arrow. Note that all the droplets in the two clusters imaged seemed to expand as they are exposed to the beam, but only a few of the droplets in E) and F) begin to burst, likely droplets that are near the ice surface. Total electron fluences for the full image series: (top) 2400 $e^-/Å^2$, (bottom) 1600 $e^-/Å^2$. Total fluence for images (A, D) 50 $e^-/Å^2$, (B, E) 800 $e^-/Å^2$, (C, F) 1600 $e^-/Å^2$.*

Damage to the Pickering emulsion sample when exposed to the electron beam in STEM mode for repeated imaging was observed to follow the following mechanism, illustrated in Figure 5.26. After initial exposure to the electron beam, the emulsion droplets seem to “expand” regardless of their position within the ice, even without being affected by the ice sublimating (Figure 5.26-B). The ice begins thinning as it sublimates because of the electron beam. The stabilising nanoparticles within the

sublimated volume will then appear to be displaced, as can be seen in the droplet shown in the tilt series in Figure 5.23. Only the particles near the affected ice surface are displaced, while the nanoparticles and droplets in regions of the ice that are not being sublimated will appear unaffected (Figure 5.26-C).

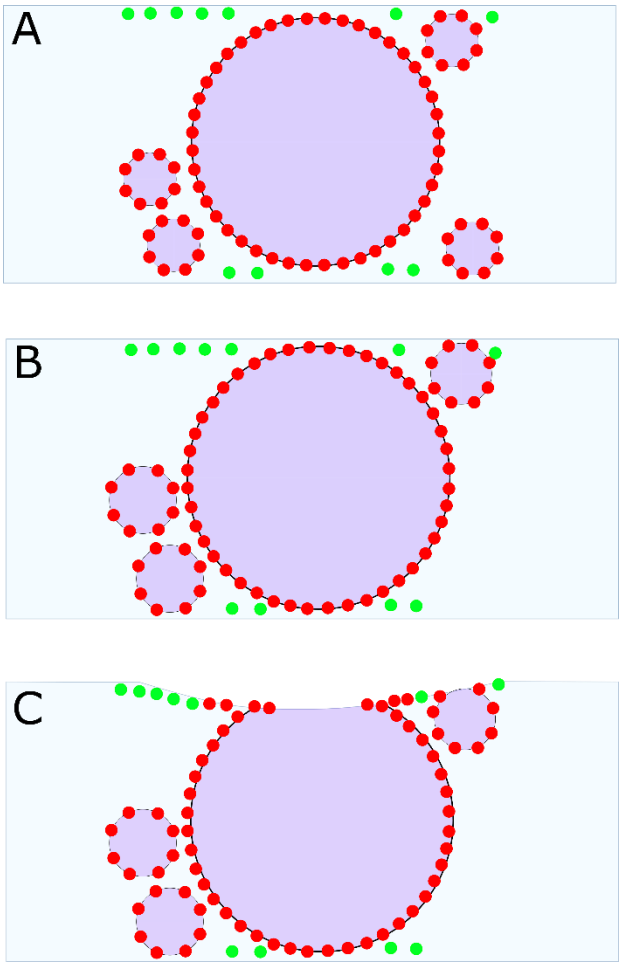


***Figure 5.26 –*** *Schematic showing the speculated mechanism for droplet deformation due to beam-induced damage. This diagram is based on observations of the sample being damaged by the beam. A) Cross-section of an ice section containing emulsion droplets of various sizes and NPs in the water phase before any damage occurs (see Figure 5.16). B) After minimal exposure to the beam, but before ice sublimation visibly begins affecting the sample, the droplets appear to "expand" (see Figure 5.25). C) The ice begins sublimating, causing the nanoparticles near the affected ice surface to be displaced (see Figure 5.23).*

## 5.6 Limits to the sample analysis and future directions for cryo-imaging and analysis of Pickering emulsions

Using the current electron microscope setup (detailed in the Materials and Methods), limits in the effective imaging resolution were encountered when attempting to analyse the Pt-NPs due to the low electron fluence needed to prevent sample damage, with the images collected having low SNR at high magnifications. The solution shown in this study was to simply work at lower magnifications (×20k to ×80k) whenever high total electron fluence was required, as was the case with electron tomography. When using electron tomography with EELS, this approach results in the inability to resolve individual Pt-NPs on the droplet surface, therefore being unable to analyse their contact angle, which is a characteristic of interest for Pickering emulsions. For the two Pickering emulsions in this study, each with the same Pt-NPs stabilising a different oil (hexadecane and sunflower oil), it would be interesting to examine the precise location of the stabilising NPs with respect to the oil–water interface, as this effective contact angle measurement is a useful indicator of stability [57]. An automated cryo-EM tomography procedure to limit exposure but push resolution to as low as possible could achieve this and such systems are currently being used and developed within other scientific fields. Moving forward applying these techniques to the system analysed here would be the logical next step [244, 245].

Furthermore, the use of improved equipment such as a direct electron detection system rather than a CCD camera could help resolve such small NPs during low dose imaging [244, 246, 247]. In addition, characterisation of the sample through cryo-scanning electron microscopy using techniques such as focus ion beam milling would offer a future opportunity to image a larger sample volume and therefore image larger droplet clusters or systems with larger droplet sizes or to select a site of interest to prepare a lamella to cryo-transfer to the cryo-(S)TEM [136, 175, 184].

## 5.7 Summary

One of the challenges of analysing Pickering emulsion systems with nano-sized stabilising particles lies in the difficulty of simultaneously analysing both the stabilising particles and the emulsion droplets. Here it was shown the possibility of successfully analysing oil-in-water Pickering emulsion samples stabilised by 3-5 nm Pt-NPs using

plunge-freezing to cryo-prepare the sample and using cryo-(S)TEM, EDX and EELS analysis for imaging and elemental analysis.

Cryo-HAADF STEM allowed for high-resolution imaging and elemental analysis using EDX and EELS while maintaining low electron fluences and minimising damage to the sample and vitreous ice. Cryo-HAADF STEM allowed for easy identification of the Pt-NPs due to their high atomic number while permitting for a higher total electron fluence before the onset of beam-induced damage to the sample. EDX and EELS were successfully used to obtain carbon, oxygen, and platinum signals in the sample which were used to identify the oil and water phases and the stabilising Pt-NPs.

The collection of EELS spectrum images alongside cryo-HAADF STEM tilt series allowed for the 3D reconstruction of the sample volume while also providing 3D elemental data. This technique provided information on the oil phase, which would otherwise be inaccessible in cryo-HAADF STEM, without the need to stain the sample. Improvements on the efficiency of the tilt series collection are needed to decrease the electron fluence per tilt angle, therefore allowing for a higher number of images per tilt series and higher resolution tomograms. The small size of the of the stabilising particles in the samples used resulted in a high electron fluence requirement for electron tomography while being able to resolve the Pt-NPs. This made the current experimental approach unsuitable to identify the exact position of the Pt-NPs on the water-oil interface. Future work may include the use of Pickering emulsion systems with larger stabilising NPs to decrease the pixel resolution requirements when collecting tilt series or elemental maps.

Plunge-freezing was found suitable for the preparation of the Pickering emulsion samples with ~100 nm droplet diameter, with the droplets retaining their spherical structure as observed using both cryo-(S)TEM for 2D imaging and cryo-ET for 3D imaging. Droplets with diameter below ~600 nm were found with no visible evidence of deformation, though larger droplets were found to be partially collapsed, making plunge-freezing unsuitable for the imaging of emulsion samples with larger droplet sizes, or where droplet clusters and interactions between droplets need to be studied. Alternate cryo-preservation technique will be required for these larger samples, with cryo-FIB-SEM being a potential alternative due to the ability to image a larger sample surface compared to TEM, while block face tomography can analyse larger 3D

volumes compared to tilt. Additionally, FIB milling allows for the generation of frozen lamellae that can be transferred to a TEM with cryogenic capabilities to access the high-resolution imaging.

# Chapter 6 Cryo-SEM Analysis of Pickering Emulsion-Based Systems

Results from Chapter 5 showed size limitations for the imaging of Pickering emulsion samples in cryo-TEM when prepared by plunge-freezing. Alternate strategies are needed to prepare and image larger sample volumes and samples with larger volumes. In this chapter, two systems were used: a gold nanocapsule sample prepared from a sunflower-in-oil Pickering emulsion with 3-5 nm Pt-NPs, and a hexadecane-in-water Pickering emulsion stabilised by 3-5 nm Pt-NPs. Both systems have droplet / nanocapsule sizes >1 μm in diameter and are not suitable to be directly imaged in cryo-TEM, and therefore have been examined here using cryo-FIB-SEM. The samples were frozen in slush nitrogen and transferred to a cryo-FIB-SEM, where FIB-milling was used create new surfaces for imaging. FIB-milling was further used for the collection of 3D “slice and view” datasets, and for the fabrication of a thin (150-400 nm) electron-transparent lamella suitable for cryo-lift out and transfer to the cryo-TEM. Ideally high pressure freezing would be preferrable for the preparation of vitreous ice, but for this thesis slush nitrogen was used due to the unavailability of a high pressure freezer.

Although Pickering emulsions are often used as stabilised emulsions, they can also be used as a template for the fabrication of capsules and porous materials [248-250]. Hitchcock *et al.* [40] shows the preparation and analysis of gold nanocapsules from the nano-sized sunflower oil-in-water Pickering emulsion droplets shown in Chapter 5. These nanocapsules were used for controlled drug delivery, and as such their size and shape of these nanocapsules and the thickness of the gold layer are important to gauge the samples performance, with the capsule thickness being important for the long-term retention of drugs within the capsules. In this thesis, plunge-freezing and cryo-(S)TEM were employed in Chapter 5 to image emulsion droplets with ~100 nm diameter; however beyond this size cryo-FIB-SEM is a more suitable imaging technique for the imaging of larger samples, with FIB allowing for the milling of sample cross-sections for the analysis of capsule thickness.

The Pickering emulsion sample and nanocapsule sample were prepared by the research group of Dr Olivier Cayre, in the School of Chemical and Process Engineering, University of Leeds.

## 6.1 Cryo-FIB-SEM Analysis of Pickering Emulsion-Based Systems

The plunge-freezing procedure and cryo-(S)TEM imaging used for analysing the Pickering emulsion samples in Chapter 5 demonstrated that it can only be used for very limited emulsion droplet sizes. The upper range for droplet diameters was estimated to be near ~600 nm before risking damage to the droplets as a result of the blotting step during plunge-freezing. The Pickering emulsion samples presented through most of Chapter 5 had droplets of a range of sizes, however most were below 600 nm. Pickering emulsions can have droplets with much larger sizes [49, 57, 64, 68]. Cryo-SEM is an alternative for imaging these samples in cryogenic conditions. Larger sample volumes can be cryo-fixed using high pressure freezing or plunging in liquid nitrogen slush [172]. Moreover, SEM as a surface imaging technique is more suitable for large samples compared to TEM where it is required for the electron beam to penetrate and transmit through the sample. Moreover, the high sensitivity of BSE to elements with high atomic numbers is useful for the imaging of platinum and gold within the ice [168-170].

### 6.1.1 FIB Milling and “Slice and View”

Cryo-SEM allows for the imaging of larger sample volumes than what is possible with cryo-(S)TEM and can therefore be used to image Pickering emulsion samples with larger droplet sizes (> 1 µm diameter) and droplet agglomerates. However, in standard cryo-SEM, the larger volume available for imaging is offset by the ability to only image the sample surface, which effectively reduces the amount of the sample that can be viewed.

This issue can in part be resolved by increasing the sample concentration before freezing and imaging to increase the likelihood of the sample being present at the imaging surface, as was the case with the ZnO NPs imaged in Chapter 4. Even when the sample is at the surface however, larger structures such as droplet agglomerates can be encased within the ice, with only a single droplet or a small group of droplets being visible on the ice surface while the remaining droplets are not visible. This may not be an issue when imaging small samples, but larger samples such as the Pickering

emulsion-based droplets presented in this study cannot be fully imaged this way, as it is impossible to view the full droplet size and shape by only imaging the fractured ice surface. Solutions to this issue can be found in the form of cryo-microtomy and focused ion milling, both of which allow for the imaging of a cross-section of the frozen sample [81, 88, 251].

In this thesis, the use of a focused ion beam within a cryo-SEM allowed for the milling of the frozen Pickering emulsion-based sample to identify areas of interest containing emulsion droplet within a larger volume than what can be accessed through cryo-SEM imaging alone. However, finding the sample during FIB milling can be difficult even after increasing the sample concentration. A larger cross-section can be milled to increase the likelihood of finding the sample, but this can quickly increase the time spent milling. A further challenge that might arise during this process is over-milling past the sample either during the initial milling procedure or while cleaning the surface prior to imaging. A possible solution can be found in the use of the “slice and view” method, consisting of FIB milling the sample to expose a sample cross-section for imaging, directly following by imaging the cross-section. After an image is taken, the imaged face is milled to produce another slice. By repeating this milling and imaging process it is possible to build an image series of all the slices, showing a view of the entire volume that was milled.

Once a suitable region for imaging was found, the cryo-SEM stage was tilted to 52° allow for FIB-milling. A rectangular section of the ice was milled to expose a cross-section containing emulsion droplet. This section was further cleaned using the FIB to ensure the sample cross-section is fully visible and free of redeposited material (Figure 3.8 and Figure 3.9 show the FIB-milled trench setup used) [81, 89]. Two parallel channels were milled to the sides of the sample to create a 39 x 52 μm area that will later be imaged. After imaging, a slice of this surface was milled to expose a new cross-section; this imaging and milling process was repeated until the entire volume of material was imaged.

Selected slices from the “slice and view” image series of the nanocapsule sample can be seen in Figure 6.1, showing images for slice 1, slice 250, and slice 500 from a 501-slice image series. A total volume of 39 x 52 x 32 μm was imaged through this process, with each slice being 50 nm thick. The sample seen here consists of a sunflower oil in

water Pickering emulsion stabilized by Pt-NPs, with droplets covered in a gold film. As seen in Figure 6.1, droplets with diameter above 10 μm are fully visible, a sample size that would be unsuitable for imaging in cryo-(S)TEM.

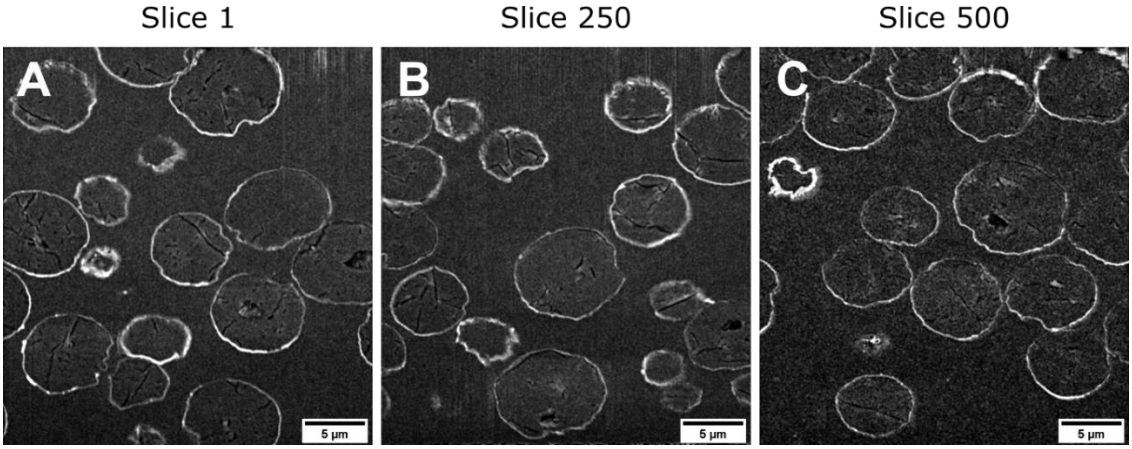


***Figure 6.1 –*** *BSE images from a "slice and view" image series. A) Slice 1, B) slice 150 and C) slice 500 of a 501-slice image series that was stabilised and cropped to isolate the emulsion droplets. The brightness in the images shown here has been corrected to minimise the effects of sample charging, though curtaining artefacts are still visible in the upper portion of images A), B), and C).*

Observing the sample using only a cross-section or an individual slice gives only partial information on the sample. From the slices in Figure 6.1 it could be possible to observe a droplet size and cross-sectional circumference, but as it is difficult to establish the droplet centre from slices alone information on the maximum droplet size is unavailable. "Slice and view" image stacks can be aligned and used to create a tomogram of the imaged volume, therefore eliminating this issue. FIB-milling is also subject to other issues besides the difficulty to obtain representative sample slices. Curtaining, thermal damage from the ion beam and sample charging are all well-known challenges in cryo-FIB-SEM imaging [81, 175]. Curtaining is often seen during FIB-milling as a result of local variations in ion scattering along the sample surface and can distort the features in the sample, as can be seen in the top region of the slices in Figure 6.1.

### 6.1.2 “Slice and View” Tomography

The image stack obtained from FIB-milling the Pickering emulsion-based sample in the previous section was reconstructed in 3D to allow for the full visualisation of the imaged volume. After aligning the image stack and correcting the brightness and contrast of the images, the stack was visualised in 3D using the Imaris software. The voxel size of the resulting 3D reconstruction is 33 x 42 x 50 nm. 3D surfaces were created using the thresholding tools in the Imaris software, used as a form of 3D segmentation to better visualise the nanocapsules and to separate individual nanocapsules. Figure 6.2-A is a 3D visualisation of the image stack, which shows a frontal view (at the same angle as the slices in Figure 6.1) of the full stack, isolating the BSE signal corresponding to the Pt-NPs and gold layer. 3D models for the nanocapsules were generated following the signal from the gold layer, which allowed to isolate individual nanocapsules and small groups for better viewing. Figure 6.2-B and Figure 6.2-C show 3D surfaces created in Imaris for a group of nanocapsules, each individual droplet textured with a different colour. The droplets here appear to be in contact with each other, with the capsule surface being distorted when in contact with other capsules. Measurements of the nanocapsules showed an average diameter of 7.8 μm (taken form the longest dimension of the nanocapsules, standard deviation: 1.3 μm) and an average sphericity of 0.955 (standard deviation: 0.013). The capsules in this samples are generally spherical, but the tomogram in Figure 6.2 also shows an uneven surface. These surface features may suggest that external forces might be able to flatten them, or possibly through damage from either sample preparation or imaging. The irregularity of the droplet surface is also visible in Figure 6.2-D and Figure 6.2-E, which show views of an individual droplet from different angles. In these images it is also evident that there are some holes in the droplet surface. It is unclear through cryo-SEM imaging alone whether these holes are the result of area on the droplet surface with poor gold coverage, or if they coincide with portions of the droplet surface with a thin enough layer to be difficult to detect with the imaging resolution used in cryo-SEM and therefore leading to poor contrast in the 3D visualisation.

The voxel size for the tomogram (33 x 42 x 50 nm) provides a limit to the ability to resolve features in the sample such as the thickness of the gold layer. Measurements of the gold layer thickness ranged from a maximum of ~200 nm to less than 80 nm. Some area of the nanocapsules appear to be thinner than this, appearing as “holes”

in the capsules which are visible in Figure 6.2-B, Figure 6.2-C, and Figure 6.2-C. Nanocapsule thickness measurements in smaller nanocapsules in Hitchcock *et al.* [40] show that the gold layer could be as thin as 15-20 nm (with an average of ~50 nm), which is below the voxel size. This means that the “holes” in the nanocapsules might instead be thin regions with thickness below the tomogram voxel size, making comprehensive measurements of the nanocapsule thickness impossible with the current imaging and milling parameters.

Imaging challenges during FIB-milling are not limited to the image pixel (or voxel) resolution, as the ion beam can directly damage the sample through a variety of mechanisms. Morphological deformations to the samples have been observed as a result of beam-induced heating and radiolysis as the ion beam is rasterised across the sample during milling, which can result in sample heating and warping [252, 253]. Other artefacts induced by the ion beam include curtaining (observable in the images in Figure 6.1) and ion implantation on the sample which can affect imaging and spectroscopy analysis [252, 254]. These artefacts can be mitigated by cleaning the sample surface with the ion beam using low voltages to remove the affected surface [252], though this approach can be of limited use during the automated serial block face milling.

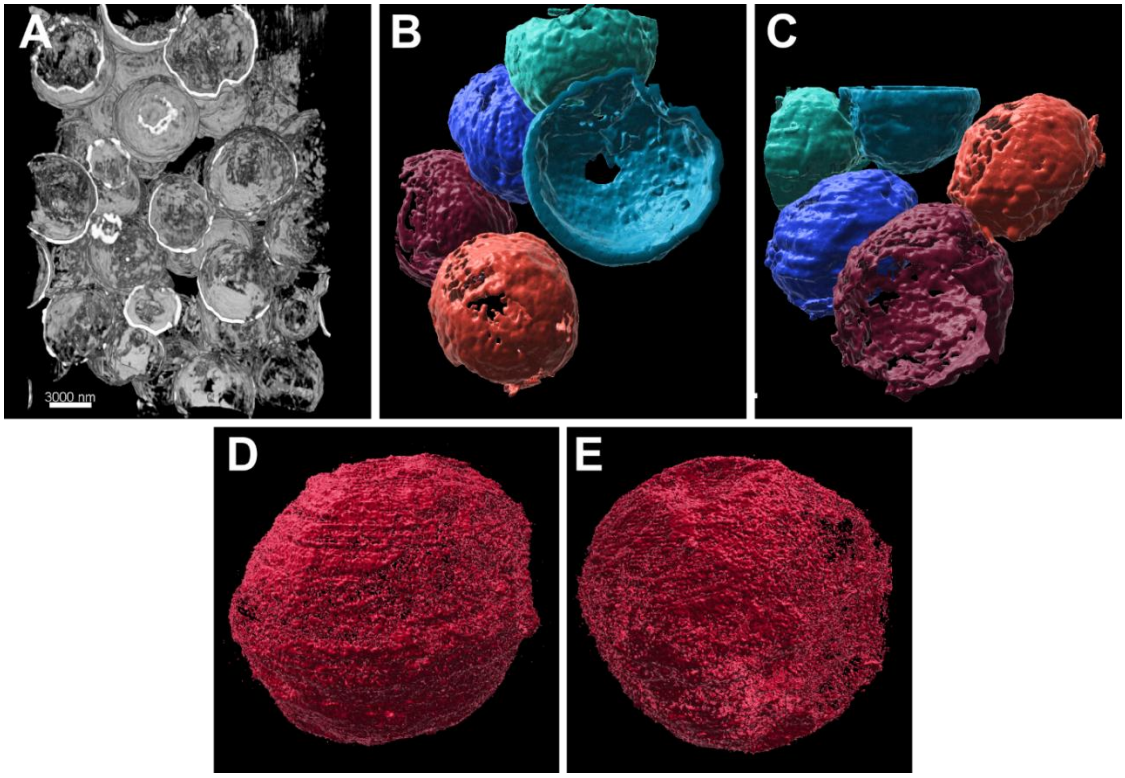


***Figure 6.2 –*** *Stills of 3D models from the "slice and view" dataset. A) Front view of the "slice and view" stack showing the signal from the Pt-NPs. B) and C) Front and side views of a group of droplets. D) and E) Front and side views of an individual droplet.*

The "slice and view" process was successful in obtaining a 3D dataset of the >1 μm droplets and allowing for the visualisation of both individual droplets and agglomerates in 3D. When compared to the results shown in Chapter 5, the approximately spherical 3D structure of the droplets appears to be retained in the cryo-FIB-SEM dataset. Sample deformation was not observed after preparation for cryo-FIB-SEM. Cryo-FIB-SEM has already been successfully used to image soft matter samples in this size range [129, 174, 175], though in Pickering emulsions freeze-fracture is a more commonly used method for exposing the sample compared to FIB-milling [57, 66, 255]. Exceptions to this are found when the main scope of the study is imaging the interfacial interaction in the sample, as seen in Elbers *et al.* [69], where FIB milling was used to obtain an image series of a Pickering emulsion sample to visualise the interfacial interaction between the droplets and stabilisers both in 2D and 3D. In these cases FIB-milling is used to create new surface cross-sections, as the ion beam is suitable for the milling of a variety of samples. On the other hand, freeze-fracture alone

forms a new surface along existing particles or sample structures, thus limiting the possible imaging areas. In addition, serial block face tomography allows for the collection of 3D datasets for much larger volumes compared to tilt tomography (which is limited to samples up to a few hundred nanometres thick), despite the trade-off in imaging resolution.

Although this was useful to obtain information on the droplets, the slice thickness (and resulting voxel resolution) was insufficient to properly visualise the 3-5 nm Pt-NPs. For this, the high-resolution imaging found in cryo-(S)TEM is still needed to visualise the stabilising Pt-NPs. Studies such as Antoniou *et al.* [129] and Parmenter *et al.* [130] have successfully shown the possibility of manufacturing a cryo-FIB-SEM lamella that can be transferred to a cryo-TEM in a process known as cryo-lift out This process could also be applied to this Pickering emulsion sample, thus allowing for the preparation and imaging of large emulsion droplets using cryo-FIB-SEM and the imaging of the much smaller stabilising nanoparticles using cryo-(S)TEM.

## 6.2 Cryo Lift-Out and transfer to cryo-(S)TEM

Preparation of lamellae for TEM imaging is a technique routinely used for the analysis of a variety of samples when high-resolution imaging of a large volume samples is needed [132, 256]. Similarly, samples can be cryogenically fixed for initial imaging in cryo-SEM, where lamellae can be prepared and then transferred for cryo-(S)TEM imaging. As seen in the previous sections, freezing in slush nitrogen allows for the cryo-preservation of the large emulsion droplets. FIB-milling of this frozen sample can be used for the fabrication of a frozen lamella thin enough to allow for cryo-(S)TEM imaging. This setup has been successfully used in the life sciences [132, 134] and will be adapted to allow for high-resolution cryo-(S)TEM imaging of Pickering emulsions droplets that would otherwise be unsuitable for conventional TEM cryo-preparation techniques such as plunge-freezing (see section 5.2.1 in Chapter 5).

### 6.2.1 Cryo-SEM Imaging and Lamella Preparation

The cryo lift-out process for a hexadecane in water Pickering emulsion sample stabilised by 3-5 nm Pt-NPs is documented in Figure 6.3, which shows images taken

at different stages of preparing a lamella. The first step in the lamella preparation process consists of identifying an area on the ice surface where the sample is present. Figure 6.3-A shows the ice surface with an emulsion droplet in the middle of the image; this area was initially chosen to start FIB milling under the assumption that more droplets might be present in the nearby area below the ice surface.

After tilting the cryo-SEM stage to 52°, the FIB was used to mill a rectangular area to expose a sample cross-section. The newly exposed cross-section was milled until an emulsion droplet was found. After this, the area behind the sample was milled until a thin section (slightly thicker than ~1 µm) was obtained. The bottom and one side of the section was milled to obtain a lamella only attached to the bulk ice on one side (Figure 6.3-B) The FIB was used to clean the surfaces of the lamella to remove any material that may have redeposited during the milling process. Once the lamella was properly thinned, cryo-grippers were used to hold onto the lamella, and after the remaining side was milled, the freed lamella was lifted. The lamella was then extracted using the cryo grippers and loaded onto a TEM grid for the transfer (see section 3.2.6.3 for more details), which was temporarily glued onto a SEM shuttle. Figure 6.3-C shows the lamella in the transfer TEM grid, after further thinning and polishing to ensure the lamella has a smooth surface and is thin enough for TEM imaging. As seen in the top-view from Figure 6.3-D, the right side of the lamella where the emulsion droplet is present has been thinned in two areas, one with a thickness of ~130 nm and another with a thickness of ~400 nm. This was done to thin the lamella enough for TEM imaging while ensuring the integrity of the whole lamella remains stable during the transfer process. A hole in the ~130 nm thick section of the lamella is visible in Figure 6.1-C, created due to a milling error; care needs to be taken when thinning lamellae to prevent heat damage or compromising the structural integrity of lamella, which might result in losing the lamella during transfer.

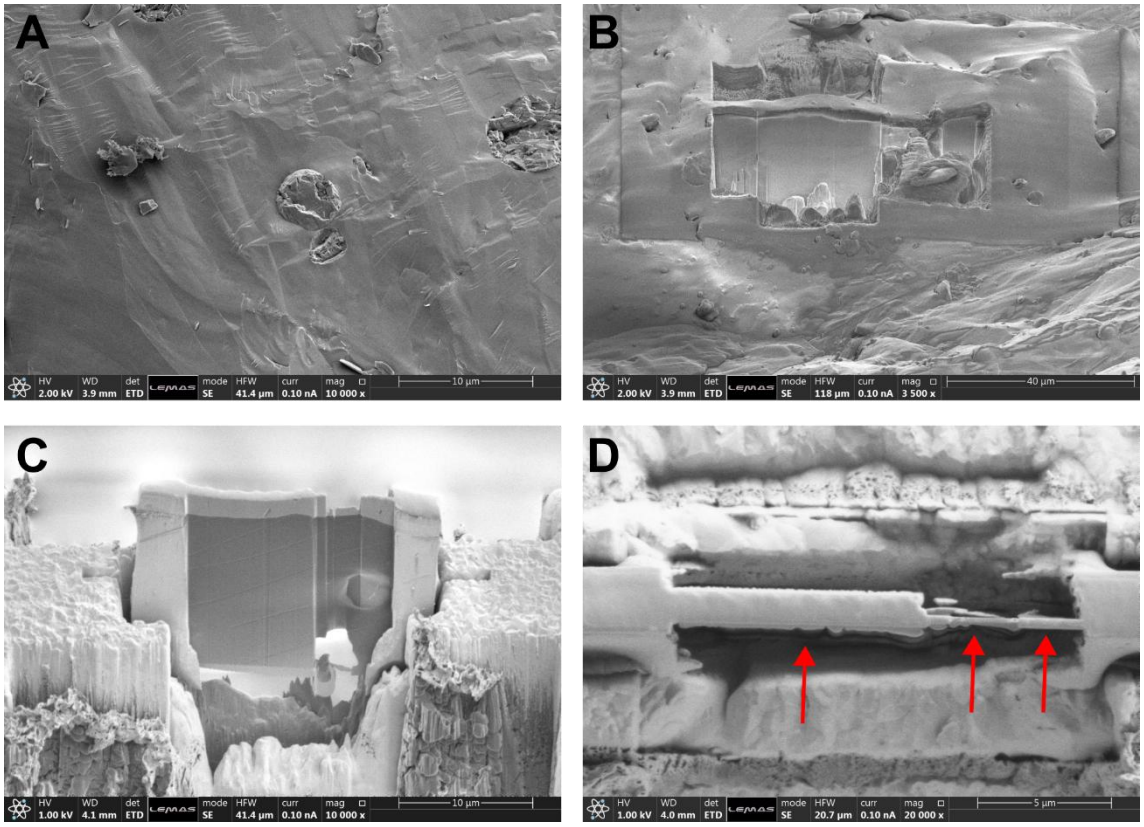


***Figure 6.3 –*** *SE images showing the process of creating a sample lamella. A) Image of the ice surface showing a droplet. B) Lamella milled using the FIB. C) Lamella loaded onto a modified TEM grid after FIB milling of the lamella surface. D) Top view of the lamella showing regions with different thickness (indicated by the red arrows from left to right: ~1 µm, ~130 nm, and ~400 nm).*

After the lamella was loaded onto the transfer TEM grid and thinned, it was removed from the cryo-FIB-SEM and immediately immersed in liquid nitrogen together with the SEM sample shuttle. The TEM grid was then transferred to a grid holder while under liquid nitrogen and stored in liquid nitrogen while the TEM cryo-holder was being cooled down and prepared for transfer. The TEM grid was then transferred to the cryo-holder under liquid nitrogen and loaded into the TEM. Grid boxes for long term storage under cryogenic conditions were not available, therefore each lamella preparation and transfer attempt had to be executed on the same day.

Due to the necessary thinning and cleaning steps, it is difficult to fabricate an ideal lamella where none of the droplet volume of interest is milled away when thinning the lamella. In the case of the Pickering emulsion lamella shown in Figure 6.3-B through

Figure 6.3-D, the central cross-section was initially visible but after the thinning and cleaning process most of the droplet was milled through, with only a smaller portion of the droplet remaining in the finished lamella. This issue can become more problematic as the sample that needs to be captured in the lamella becomes smaller, as the chance to lose important sample features through milling becomes higher. Small features such as the connection point between two emulsion droplets are therefore especially challenging.

Some of the challenges associated with the fabrication of a cryo-FIB-SEM lamella are inherent to cryo-FIB-milling, with curtaining, thermal damage and sample charging being well-known issues [252]. The cryostage temperature must be kept below -138° to avoid devitrification, which can become an especially important issue when manipulating thin lamellae. The lamellae must be kept at low temperature even during the transfer process to the cryo-TEM, where exposure of the sample to air can lead to sample contamination with the formation of frost on the sample surface and devitrification. Both issues ultimately affect cryo-TEM imaging, with surface contamination in the form of frost covering the sample while devitrification creating crystalline regions in the lamellae that disrupt imaging. Lamella transfer must therefore occur at low temperatures and in a vacuum or while submerged in liquid nitrogen to reduce the possibility of damage to the lamella. Improvements to the cryo lift-out procedure include using different strategies for the fabrication of lamellae, lift-out, and transfer to the cryo-TEM, including the use of autoloaders for cryo-ET to increase the output of useful lamellae [257-260]. An example of alternative cryo lift-out strategies can be found in Kelley *et al.* [136]. Here the sample was frozen using HPF directly on a TEM grid, then FIB-milling was used to mill multiple lamellae. The entire TEM grid containing the lamellae was then lifted-out and transferred to a cryo-TEM instead of lifting out individual lamellae, thus increasing the lamella throughput compared to conventional methods and increasing the amount of suitable lamellae reaching the cryo-TEM.

Within this work, 6 attempts were made to transfer a Pickering emulsion lamella to the cryo-(S)TEM. In most cases, challenges were encountered during the lift-out and transfer processes, with lamellae being destroyed during the thinning process and lost during the transfer process out of the cryo-FIB-SEM and into the cryo-(S)TEM. Two lamellae were successfully transferred but only one of these yielded a usable lamella,

as in the other case the Pickering emulsion sample was fully covered in frost, preventing imaging and spectroscopy.

### 6.2.2 Cryo-(S)TEM Imaging

After transferring the sample lamella to the cryo-TEM holder under liquid nitrogen, the sample was inserted into the TEM under cryogenic conditions for imaging. Initially, low magnification imaging was used to examine the state of the lamella, to ensure that the lamella was not lost during the lift-out and transfer processes, and to ensure that the lamella was not covered in frost. Figure 6.4 shows low magnification cryo-(S)TEM images of a lamella (from Figure 6.3) that was successfully transferred. It can be seen from all these images that frost crystals are present on the entire the lamella surface; in Figure 6.4-C crystals are covering part of the emulsion droplet (droplet surface indicated by a red arrow). The presence of these frost crystals is a common occurrence in cryo-(S)TEM samples due to the TEM grid being moved through the air for short distances when being transferred to the microscope. Unfortunately, the lamella in cryo lift-out samples is only a small area compared to the entirety of a TEM grid, therefore there is a higher chance for frost crystals covering the sample and rendering the entire sample preparation process fruitless. Figure 6.4-B shows the presence of eutectic ridges in the ~1 µm thick section of the lamella, appearing as parallel lines running across the lamella. These ridges are formed during the crystallisation process, and indicate that freezing with slush nitrogen was unsuccessful for the formation of fully vitreous ice. Despite this, no evidence was found of emulsion droplets being deformed or Pt-NPs being displaced during freezing.

A single emulsion droplet can be seen in Figure 6.4-C, corresponding to the droplet that was isolated during the FIB milling process in the cryo-SEM documented in Figure 6.3. The lamella thinning performed in this area allows for the cryo-(S)TEM imaging of the emulsion droplet, while minimising the area being thinned to decrease the risk of damage to the lamella during the thinning process and during transfer to the TEM. As indicated by the arrows in Figure 6.4-A, three sections of the lamella were thinned to different thicknesses (from left to right: ~1 µm, ~130 nm, and ~400 nm). The thinner sections are obviously more beam transparent and therefore more suitable for a wide

range of cryo-(S)TEM techniques, but also more fragile and at risk of damage during transfer.

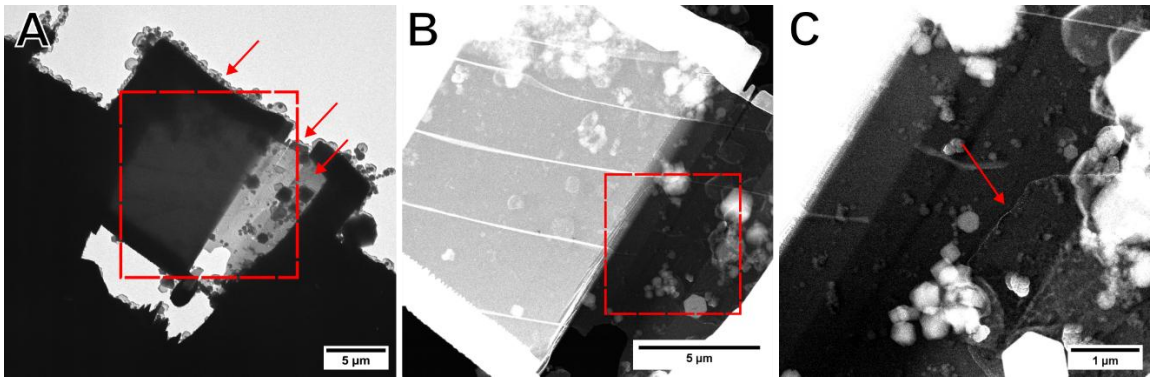


***Figure 6.4 –*** *Cryo-(S)TEM images of the lamella after being transferred to the TEM. A) Cryo-TEM image of the whole lamella, highlighting the regions with different thickness (from left to right:~>1 µm, ~130 nm, and ~400 nm). B) Cryo-HAADF STEM image of the lamella and C) magnified region of the lamella containing an emulsion droplet (highlighted by the red arrow). The image in this figure have been rotated to align with the cryo-FIB-SEM images shown in Figure 6.3. Total electron fluence: A) 0.1 $e^-/Å^2$, B) 0.8 $e^-/Å^2$, C) 7 $e^-/Å^2$.*

Higher magnification images were taken in the droplet region, as can be seen in Figure 6.5. Figure 6.5-A shows a portion of the droplet, with Pt-NPs present at the oil-water interface. It can be seen from both Figure 6.5-A and Figure 6.5-B that the Pt-NPs are only present near the (presumed) oil-water interface, and are completely absent deep within the water and oil phases. Despite this, the Pt-NPs seem to be organised in a layer which can be observed in all high magnification images; this likely suggests the oil-water interface is curved towards the centre of the droplet, while the regions with different concentrations of Pt-NPs (see Figure 6.5-B and Figure 6.5-C) suggest that the droplet interface curvature is not smooth. The spots in the water phase in Figure 6.5-B and Figure 6.5-C might be a result of implantation of the $Ga^+$ ions during FIB-milling [252], though this could not be confirmed through EDX as the overall signal was not high enough to distinguish a possible Ga EDX peak.

As was discussed in Chapter 5, damage to the ice will inevitably cause movement of the Pt-NPs as the ice sublimes; given the proximity of the Pt-NPs to the ice surface, it

is expected for some damage to appear immediately in both the areas with ~130 nm and ~400 nm thickness.

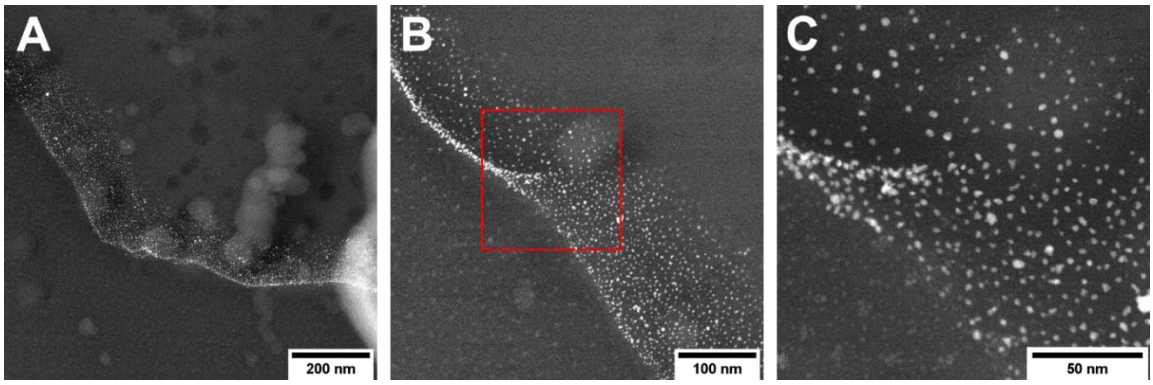


***Figure 6.5 –*** *Cryo-HAADF STEM images of the droplet and Pt-NPs in the sample lamella. A) Surface of the droplet within the ~130 nm thick region. B) Section of the droplet and C) higher-magnification image from the region in (B) showing individual Pt-NPs. Total electron fluence: A) 2 $e^-/Å^2$, B) 8 $e^-/Å^2$, C) 60 $e^-/Å^2$.*

EDX mapping was performed in four separate areas at the droplet surface. Two datasets were collected in the ~130 nm thick region of the lamella, while two other datasets were collected in the ~400 nm thick region. Figure 6.6 shows the EDX maps of an area at the surface of the droplet and EDX spectra corresponding to different area of the mapped region. As expected from the EDX and EELS results presented in Chapter 5, Figure 6.6-B and Figure 6.6-E show the presence of an oxygen signal and a lack of a carbon signal, which corresponds to the ice in the water phase. Meanwhile, Figure 6.6-C and Figure 6.6-G show the presence of a carbon signal corresponding to the oil phase. The oxygen signal elemental map in Figure 6.6-B shows the presence of oxygen through the entire analysed area, suggesting the presence of ice both in the region corresponding to the water phase and the region containing the Pt-NPs and oil phase. This is confirmed by the EDX spectra in Figure 6.6-E, -F, and -G where the oxygen signal peak is seen to decrease when going from the water phase (top) to the oil phase (bottom). The presence of ice through the entire region can be explained by the profile of the droplet's surface (further explored in Figure 6.8).

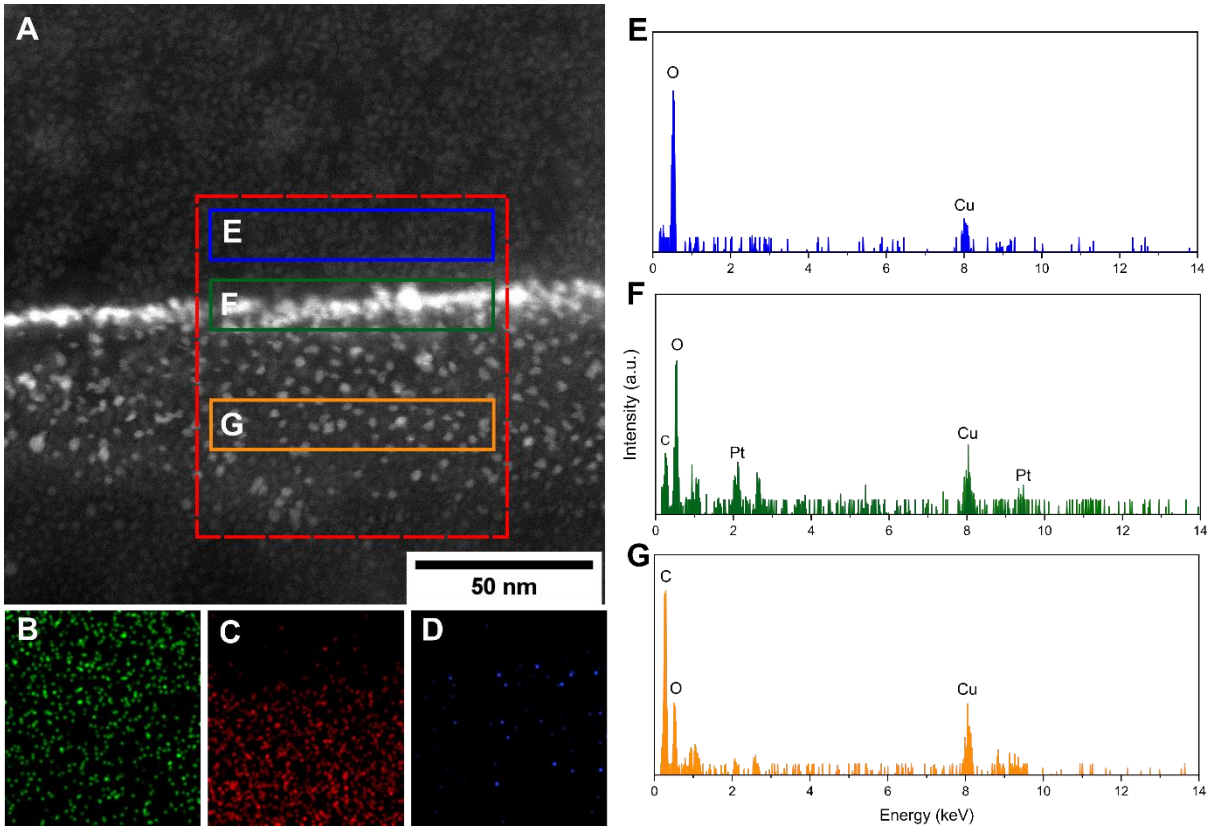


***Figure 6.6 –*** *EDX of the droplet surface in the ~400 nm thick region of the lamella. A) Cryo-HAADF STEM image of the droplet surface. EDX elemental maps showing the B) oxygen Kα C) carbon Kα and D) platinum Kα signals. E), F) and G) EDX spectra from the water phase, droplet surface, and carbon phase. The chlorine Cl Kα in F) is likely the result of the synthesis process for the Pt-NPs. The red box indicated the full area that was analysed using EDX. Total electron fluence: 600* $e^-/Å^2$.

Unfortunately, only the dataset presented in Figure 6.6 contained a sufficient EDX signal for elemental analysis (collected in the ~400 nm thick area). Difficulties collecting an EDX dataset were twofold:

- As discussed in Chapter 5, total electron fluences higher than ~800 $e^-/Å^2$ result in damage to the Pickering emulsion sample due to ice sublimation. As the imaged area becomes thicker, higher total electron fluences are required before the sample is completely lost and, inversely, thinner regions (such as the ~130 nm thick region in this lamella) will be more readily affected.
- Due to the position of the Pt-NPs near the surface of the ice, it was found that the Pt-NPs would readily be displaced as soon as any damage occurred to the

ice. This resulted in difficulties mapping the Pt EDX signal as lowering the total electron fluence to minimise damage would result in a low EDX signal being collected, while at higher electron fluences the nanoparticles would be displaced, making the mapping inaccurate.

Despite possible inaccuracies in the mapping of Pt-NPs using EDX, this technique remains more approachable than EELS (for the analysis and mapping of Pt) due to the lowest energy major edge being the $M_5$ edge at 2122 eV [152]. This edge is inaccessible during cryo-EM imaging as the high dwell times needed to obtain an acceptable SNR at such high energy loss would damage the sample.

The results of sample sublimation during EDX acquisition can be seen in Figure 6.7, which shows a lower magnification image of the area in Figure 6.6-A where the EDX analysis was performed. It is immediately visible that a hole was created due to the ice subliming, causing the Pt-NPs to move and abruptly ending the EDX acquisition process.

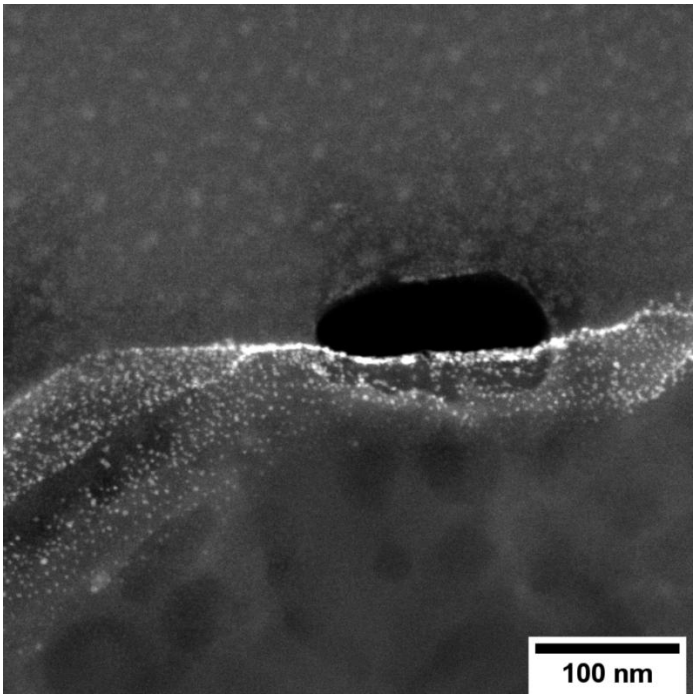


***Figure 6.7 –*** *Cryo-HAADF STEM image of the area used for EDX analysis. A hole in the ice formed in the area in the centre-right of the image, where the EDX dataset presented in Figure 6.6 was collected. Further damage can be seen in the leftmost area in the image, where Pt-NPs have been displaced due to beam-induced damage during imaging. Total electron fluence for this image: 8* $e^-/Å^2$*. Total cumulative electron fluence for the area (including EDX and HAADF STEM imaging): ~630* $e^-/Å^2$*.*

Currently, it is difficult to visualise the oil-water interface curvature due to the imaging angle and the concentration of Pt-NPs, but a possible cross-section was recreated in Figure 6.8 from the information obtained from cryo-HAADF STEM imaging and EDX elemental mapping. Figure 6.8-B and Figure 6.8-D show possible sample cross-sections of different areas of the droplet's interface. As was seen in the "slice and view" tomography in section 6.1.2, the droplets show an irregular surface rather than a perfectly "smooth" spherical surface. This is reflected in the cryo-HAADF STEM images of the droplets interface (Figure 6.8-A and Figure 6.8-C) and EDX elemental maps in Figure 6.7, which confirm the position of the oil and water phases. The ability to perform high-resolution imaging of the droplet surface could be used together with electron tomography and elemental analysis to visualise the oil-water interface and obtain information on surface interactions with the stabilising particles.

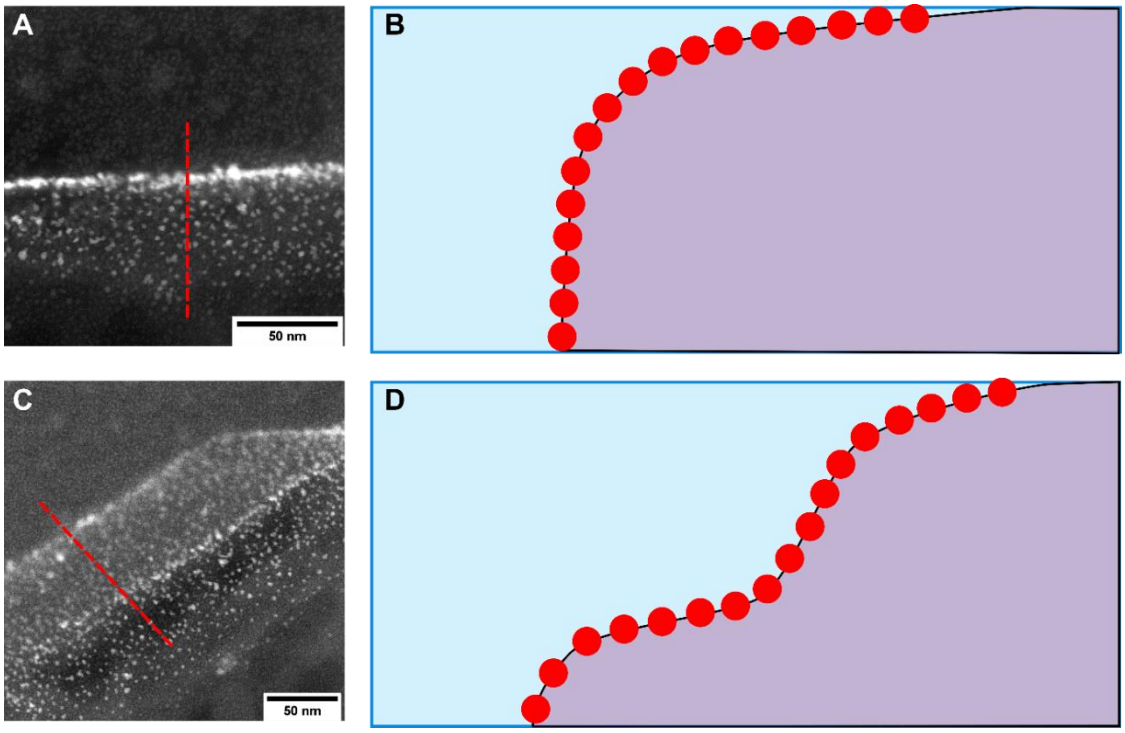


***Figure 6.8 –*** *Schematic drawing depicting the possible droplet cross-section at the droplet surface after corresponding cryo-HAADF STEM images. A) and C) are cryo-HAADF STEM images of the Pt-NPs on the droplet's surface. B) and D) are the suggested cross-sections of the droplet's surface as they would appear in the corresponding cryo-HAADF STEM image. The dotted line is the cross-section represented in the diagrams. This diagram shows the possible droplet surface profile given the information in Figure 6.5, Figure 6.6, and Figure 6.7. The oil phase is represented in purple, the water phase is represented in blue, and the Pt-NPs are represented in red. Total electron fluence: A) 60 $e^-/Å^2$, C) 30 $e^-/Å^2$.*

### 6.2.3 Cryo Lift-Out Limitations and Future Work

Due to time constraints, it was not possible to apply all the techniques shown in Chapter 5 (i.e. electron tomography, EELS elemental mapping, and EELS tomography). The ability to prepare lamellae with specific thicknesses could be used to fine-tune lamellae to ensure the sample is thin enough to allow for cryo-HAADF STEM imaging, EELS quantification and elemental maps even at high tilt angles without a significant loss in SNR. Electron tomography with simultaneous elemental analysis would be able to bring more insight into the droplet surface and the position of the stabilising nanoparticles. It was shown here that even in cases where cryo-ET

was unavailable, it is still possible to obtain information on the droplet's profile by using elemental analysis techniques. Tilt tomography of a sample in a frozen lamella can be challenging depending on the position of the sample within the lamella, orientation of the TEM grid, and presence of frost on the lamella surface. Tilt tomography was not possible in this lamella due to the position of the Pickering emulsion droplet at the edge of the lamella and near the copper grid, which prevented imaging at high tilt angles. It is clear that tilt tomography of samples within cryo lifted-out lamellae needs to be taken into consideration before the lamellae milling, as care needs to be taken to ensure a central position of the sample within the lamellae and that the TEM grid is properly orientated when loaded in the cryo-holder. Even after these considerations frost contamination from the grid transfer can cover the sample, thus preventing proper imaging at all tilt angles.

FIB-milling allows for the fine control of the lamella thickness, ensuring the sample is of an appropriate thickness for cryo-(S)TEM imaging, EDX, EELS, and tilt tomography. On the other hand, the milling of a thin sample lamella from a larger volume result in more immediate sample damage as seen in Figure 6.7. The samples prepared through plunge-freezing in Chapter 4 and Chapter 5 were often fully encased in ice and although some damage was observed as the surface of the ice sublimated, the sample fully within the ice was more resistant to damage. In the FIB-milled lamella, however, the sample is always near the air-water interface and immediately exposed to the electron beam (see Figure 6.8, where the Pt-NPs are always in contact with both the top and bottom of the lamella), thus any ice sublimation will immediately affect the sample.

Cryo lift-out was applied to this sample due to the small size of the Pt-NPs which would be otherwise difficult to resolve in cryo-FIB-SEM, though as previously mentioned, Pickering emulsion systems seen in the literature can contain stabilising nanoparticles routinely larger than 20 nm [51, 69]. For such samples, cryo lift-out might allow to not only image the stabilising nanoparticles, but also more precisely identify their position on the oil-water interface and could ultimately result in an alternative method for analysing the contact angle of the stabilising NPs in their native state.

Although cryo lift-out is a promising technique and might be tempting to apply to a wide range of samples, the many steps involved in cryo lift-out present many failure points

where the lamella may break, melt or detach, as the sample is being transfer from the cryo-SEM to the cryo-TEM. As stated earlier, after attempting this procedure six times, only two resulted with a lamella being successfully transferred to the cryo-TEM, and only in one attempt the sample was visible through the frost crystals. Despite the difficulty to carry out a lamella cryo-lift out, there have been constant improvements in various aspects of the procedure. Parmenter *et al.* [132] presents detailed instructions for the preparation of cryo-FIB-SEM lamellae, lift-out of the lamellae, and transfer to the cryo-TEM. These cryo lift-out protocols offer useful guidelines to identify possible failure areas during FIB-milling and cryo-lift out. Zachman *et al.* [261] shows the use of EDX and EELS to identify sub-surface structures in a hydrogel sample, improving the process finding suitable areas for FIB-milling and lift-out. Similar to some of the challenges encountered in this thesis, Zachman *et al.* [261] also reports a poor SNR for small sub-surface particles, but higher SNR for larger particles near the lamella surface despite a lamella thickness near 130 nm. Efforts have been made to transfer grids with multiple lamellae, thus allowing for the analysis of multiple sample areas and increasing the overall chance of delivering an uncontaminated, TEM-ready lamella. In this work, Schiøtz *et al.* [123] shows a novel approach to the preparation of multiple lamellae from a single *C. elegans* larva sample. This serial lift out of lamellae allowed for the retention of a large amount of information from the same sample.

After taking into consideration this high failure rate, it is only recommended to only use this procedure for large volume samples where the high-resolution imaging of cryo-TEM is a strict necessity.

## 6.3 Summary

It was shown here that freezing in slush nitrogen for cryo-SEM is a suitable sample preparation method for Pickering emulsion samples that are otherwise unsuitable for plunge-freezing for cryo-TEM due to large droplet sizes. The use of a focused ion beam allowed for the imaging of the droplet's cross-section and collection of an image stack that can be used to reconstruct a 3D tomogram of the imaged volume. Cryo-FIB-SEM serial block face tomography using "slice and view" allowed for the visualisation of the emulsion droplets in 3D, confirming the sample retains its structure after cryo-preparation.

The cryo-lift out procedure, though difficult to carry out successfully, is useful for the high-resolution imaging of samples that would otherwise be too large for TEM viewing. The same characterisation techniques presented in Chapter 5 are applicable to the frozen lamella after cryo-lift out, with cryo-HAADF STEM allowing for high-resolution imaging of the 3-5 nm Pt-NPs at the droplet surface. The application of electron tomography and elemental analysis techniques as seen in Chapter 5 in the future could allow for the visualisation of the droplet oil-water interface in 3D.

# Chapter 7 Conclusions and Future Work

In this chapter, the results from Chapter 4, Chapter 5, and Chapter 6 are summarised together with the original project objectives. Outcomes from these objectives and their potential for future applications and improvements are discussed. Areas for future work are then discussed, including possibilities for improving the characterisation approaches presented in this thesis, and the possibility to apply them to other systems.

## 7.1 Conclusions

The aim of this thesis project was the representative characterisation of soft matter samples, specifically Pickering emulsions, using cryo-electron microscopy techniques bridging the gaps between characterisation techniques used in biology and those used in material science. Plunge-freezing was successfully used for the cryogenic preparation of Pickering emulsions, preserving the 3D structure of emulsion droplets up to ~600 nm in diameter, and allowing for the use of cryo-TEM with HAADF STEM imaging, EDX and EELS spectroscopy, and electron tomography, characterisation techniques often used in materials science. Cryo-ET together with EELS elemental mapping consists of a novel combination of techniques used in the biological sciences and material science which has potential applications in the 3D imaging and elemental analysis of soft materials, allowing both for the detection of particles with high atomic number using HAADF STEM imaging and for the tracking of elements within the sample in 3D space.

In Chapter 4 three different systems (ZnO NP dispersions, core-satellite Au-NPs, and $TiO_2$ particles in biological media) were analysed using cryo-EM techniques to test their effectiveness of the characterisation approaches for future application on Pickering emulsion systems. ZnO NP dispersions were prepared using a range of dry and cryogenic sample preparation techniques and then imaged using dry TEM, cryo-TEM, and cryo-FIB-SEM to examine the possible effects of these preparation techniques on particle agglomeration. Particle size measurements from EM images showed similar size distributions across the different preparation methods, but with particles <100 nm being absent from cryo-FIB-SEM measurements due to limits in 3D imaging resolution related to the step size for FIB-milling. However, these results are inconclusive as this system presents a wide range of particle sizes as measured using

DLS, therefore further experiments should be performed using different, more monodisperse NP systems. Imaging of the core-satellite Au-NPs prepared using drop-casting, plunge-freezing followed by cryo-TEM and plunge-freezing followed by vacuum-drying (PF-VD) revealed changes in particle distribution that have ramifications for the measurement of particle size and nearest neighbour distances. Drop-casting was by far the simplest and fastest preparation method but could not retain the core-satellite NP structures, while both cryo-preparation methods were shown preserve these structures. Particles in samples prepared using PF-VD are deposited onto the carbon film from their position in the vitrified ice, thus retaining the core-satellite structure in 2D and allowing for easy measurements for particle size and nearest neighbour distances. Meanwhile, Au-NPs in cryo-TEM appeared to be overlapping one another, making accurate measurements more challenging. Cryo-ET of the core-satellite structures shows the overlap is due to the NPs retaining the core-satellite structure in 3D space and therefore positioned at different heights within the ice. These results show the importance of selecting suitable sample preparation methods for the given types of analysis given plunge-freezing followed by vacuum drying (PF-VD) was the most successful preparation technique to ensure proper distance and size measurements, while plunge-freezing for cryo-TEM was more successful in retaining a 3D sample structure. Overall, PF-VD was more suitable for the rapid collection of measurements across a large sample area, while cryo-ET was more suitable for the collection of measurements in small groups of particles. Cryo-HAADF STEM imaging together with EDX spectroscopy was successfully used to identify a coating containing calcium and phosphorus surrounding $TiO_2$ particles in a biological medium, which has been previously observed [232]. Cryo-ET of the coated particles showed the presence of the coating around particle agglomerates rather than around individual particles, suggesting the $TiO_2$ would have already formed agglomerates prior the growth of the coating layer during the pH treatment. This allowed us to comment on the mechanisms involved in the formation of the system, which in the future can be used to understand whether these particles could be harmful. Further cryo-ET was performed together with EDX elemental mapping of particle agglomerates to obtain 3D elemental maps of the particles and coating. Although tomograms were successfully created from the Ti Kα and Ca Kα signals, the need to maintain a low total electron fluence when collecting the EDX data resulted in a poor signal intensity and poor SNR, with the inability to obtain a strong enough

phosphorus signal for 3D reconstruction. Lastly, the thickness of vitreous ice was estimated using EELS in a sample containing only water that was prepared using plunge-freezing. The ice thickness varied across the sample, with regions thicker than 1 μm near the grid bars, and ~300-350 nm thick near the centre of the grid squares (with ice becoming thinner in the centre of holes in the carbon film). Overall, the results obtained in Chapter 4 showed the usefulness of these cryo-EM techniques for the analysis of various particle dispersions, and their potential in the characterisation of other soft matter systems such as the Pickering emulsions in Chapter 5 and Chapter 6.

In Chapter 5 a combination of DLS, cryo-(S)TEM imaging, and cryo-ET were used to successfully confirm that plunge-freezing allows for the retention of the native droplet size and spherical shape in hexadecane-in-water and sunflower-in-oil Pickering emulsion samples stabilised with 3-5 nm Pt-NPs with droplet sizes ~100 nm in diameter (with maximum droplet size below ~600 nm). Plunge-freezing was however unsuitable for the cryo-preparation of hexadecane-in-water Pickering emulsions with droplet sizes above 1 μm, as the droplets were seen to deform and collapse. Droplets with sizes within the 600 nm - 1 μm range were sometimes found in plunge-frozen samples, but were deformed or found in areas with thick ice. Cryo-FIB-SEM can be used for the analysis of a much wider range of droplet sizes with a minimum size as low as ~100 nm. However, it has to be noted that smaller droplets might be more difficult to find in cryo-FIB-SEM, especially if present in low concentrations. Cryo-HAADF STEM imaging, EDX, and EELS were successfully used for the characterisation of the emulsion droplets and stabilising NPs without incurring beam-induced damage to the sample. Cryo-electron tomograms of droplet clusters were successfully reconstructed from tilt series composed of cryo-HAADF STEM images and EELS maps, allowing for the visualisation of the sample in 3D to obtain information on the position, shape, and size of the emulsion droplets and Pt-NPs in 3D. The further use of EELS during the tilt series acquisition allowed for the identification of the oil and water phases despite poor contrast in cryo-HAADF STEM. Overall, the techniques used in Chapter 5 show the possibility of observing the size, shape, position, and agglomeration of the stabilising particles in Pickering emulsions, therefore giving information on the long-term performance of the system. Cryo-ET is a novel approach to the characterisation of Pickering emulsions allowing for high-resolution tomograms,

which when used together with spectroscopy can give elemental information and allows for the 3D tracking of elements in the sample. These techniques could be used for the analysis of the droplet interface and droplet-particle interactions in 3D which could also be applied for the analysis of other soft materials in 3D.

The cryo-FIB-SEM imaging in Chapter 6 shows alternative cryo-EM characterisation methods for Pickering emulsion samples with large droplets (> 1 μm in diameter) that would be otherwise unsuitable for plunge-freezing and cryo-TEM imaging as seen in Chapter 5. Sample preparation by plunging in slush nitrogen was suitable for freezing larger sample volumes than plunge-freezing, but future work will be needed to verify the presence of freezing artefacts. Eutectic ridges were found in samples frozen using slush nitrogen, but further work is needed to confirm damage to the sample or sample deformation resulting from the formation of crystalline ice. The use of a focused ion beam allowed the imaging of the sample beyond the fracture surface by milling the ice to expose sample cross-sections. This approach can be used to image the sample beyond the ice surface, therefore simplifying the process of finding and imaging full emulsion droplets without ice sublimation. Serial FIB-milling of a sample cross-section allowed the 3D imaging of sample volumes larger than those possible through tilt tomography in cryo-TEM, giving information on the 3D size and shape of full emulsion droplets. Although FIB-milling and SEM tomography were useful for the 3D imaging of the nanocapsules, their gold layer was at times smaller than the milling thickness, which made estimating the gold layer thickness particularly challenging. Changing the milling parameters or the cryo-TEM would be necessary for proper imaging of these features. A sample lamella containing a slice of a Pickering emulsion droplet was successfully FIB-milled and transferred from the cryo-FIB-SEM to a cryo-TEM, where it was analysed using cryo-HAADF STEM imaging and EDX. Cryo-(S)TEM imaging of the Pickering emulsion lamella allowed for the high-resolution imaging of the stabilising Pt-NPs, while future 3D analysis could give more insight into the position of the NPs relative to the droplet interface. Overall, cryo-FIB-SEM and lamella cryo lift-out allow for the imaging of emulsion droplets that would be unsuitable for more conventional cryo-TEM imaging, thus bridging the gap between higher resolution imaging of small sample volumes available in cryo-TEM and the imaging of larger volumes at lower resolution in cryo-SEM. In particular, the cryo lift-out technique can be applied to any sample that can be cryogenically frozen for cryo-FIB-SEM, effectively increasing the

size of the samples can be analysed in cryo-TEM without having to contend with issues in sample thickness.

## 7.2 Opportunities for Future Work

The most immediate opportunity for future work in the cryogenic characterisation of Pickering emulsions consists in the application of cryo-ET and cryo-ET together with spectroscopy to the cryo lift-out lamellae. This would complete the use of the techniques shown in Chapter 5 and would also allow for the 3D visualisation of the interface of larger droplets which would help understand the position on the Pt-NPs in 3D space as was proposed in the diagrams in Chapter 6.

One of the largest challenges encountered in this study is the low effective imaging resolution that is obtained as an effort to minimise total electron fluence and beam-induced damage. This is a key issue in the low-dose analysis of beam-sensitive materials including cryogenically frozen samples, with potential solutions looking to improve image collection and processing. Some of the solutions seen in other low-dose imaging studies could be adapted for the imaging of Pickering emulsions in 2D and 3D. Image collection could be improved by using serial imaging with lowered exposure time to decrease the total electron fluence while maintaining a high SNR. This could also be applied to the collection of tilt series as shown Padgett *et al.* [114] where a fast scan STEM image stack was collected at every tilt angle to obtain images with a high SNR. Machine learning (ML) methods for image processing have been developed to improve denoising and to remove missing wedge artefacts in electron tomography. Studies such as Cha *et al.* [262] show the possibility to use ML to denoise and increase the overall signal of EDX elemental maps to aid in the 3D reconstruction of tomograms from EDX data. This approach could directly benefit the cryo-ET and EDX reconstructions of the $TiO_2$ particles in Chapter 4 and might be also applicable to EELS maps, which could help improve the spatial resolution of the EELS tomograms in Chapter 5. Machine learning has also been used to aid in electron tomography reconstructions by decreasing missing wedge artefacts as seen in Wiedemann & Heckel [263] and Liu *et al.* [264] and enable accurate reconstructions with minimal projections [262-264]. These techniques could be applied to the work shown in this thesis to improve image collection in cryogenic conditions, cryo-ET, and spectroscopy.

The cryogenic freezing of samples for cryo-FIB-SEM imaging has been performed by plunging the sample in slush nitrogen. This method has been used in the literature as a better alternative to plunging in liquid nitrogen for large sample volumes due to the lower temperatures reached by the slush, but it is known that this technique is limited in the volume that can be frozen with ice crystals and phase separation appearing in samples prepared this way [206]. Therefore, a potential improvement to this work would entail the use of high pressure freezing for the cryogenic preparation of Pickering emulsion samples. HPF has been successfully used for the freezing of large volumes of biological samples without the onset of freezing-related artefacts. Moreover, HPF can be used for the freezing of samples on TEM grids which simplifies the cryo lift-out process by not requiring to move the FIB-milled lamellae to a separate TEM grid before transferring them out of the cryo-FIB-SEM, increasing the chances of successful cryo lift-outs by removing a potentially risky step [123].

Lastly, there is an opportunity to use the cryo-EM techniques presented within this thesis to analyse different Pickering emulsion systems. Currently only oil-in-water Pickering emulsion systems with small (3-5 nm) stabilising nanoparticles have been imaged, whereas Pickering emulsions found in the literature present a wide range of droplet and stabiliser shapes, sizes, and materials. In specific, oil-in-water systems with >20 nm stabilising NPs could be used as a simpler system to test electron tomography techniques, as the larger NPs would require lower magnifications for imaging and thus would allow for lower total electron fluences. This could be used to experiment with the amount of tilt images taken for electron tomography and for spectroscopy. Pickering emulsions with different droplet shapes could also be used to further test the suitability of electron tomography for 3D imaging, especially regarding the effect of missing wedge artefacts on the reconstruction of Pickering emulsion droplets. These imaging approaches could also be applied to other soft matter systems nanoparticle dispersions, hydrogels, (standard) emulsions and any other sample where analysis requires or would benefit from high-resolution 3D imaging and elemental analysis.

# References


1. Tiede, K, A B A Boxall, S P Tear, J Lewis, H David, and M Hassellöv, *Detection and characterization of engineered nanoparticles in food and the environment.* Food Additives & Contaminants: Part A, 2008. **25**(7): p. 795-821.

2. Pal, S L, U Jana, P K Manna, G P Mohanta, and R Manavalan, *Nanoparticle: An overview of preparation and characterization.* Journal of Applied Pharmaceutical Science, 2011. **1**(6): p. 228-234.

3. Douglas, S J, S S Davis, and L Illum, *Nanoparticles in drug delivery.* Critical Reviews in Therapeutic Drug Carrier Systems, 1987. **3**(3): p. 233-261.

4. Wilczewska, A Z, K Niemirowicz, K H Markiewicz, and H Car, *Nanoparticles as drug delivery systems.* Pharmacological Reports, 2012. **64**(5): p. 1020-1037.

5. He, Z, K Xiao, W Durant, D K Hensley, J E Anthony, K Hong, S M Kilbey II, J Chen, and D Li, *Enhanced Performance Consistency in Nanoparticle/TIPS Pentacene-Based Organic Thin Film Transistors.* Advanced Functional Materials, 2011. **21**(19): p. 3617-3623.

6. Osmond, M J and M J McCall, *Zinc oxide nanoparticles in modern sunscreens: An analysis of potential exposure and hazard.* Nanotoxicology, 2010. **4**(1): p. 15-41.

7. Pandurangan, M and D H Kim, *In vitro toxicity of zinc oxide nanoparticles: a review.* Journal of Nanoparticle Research, 2015. **17**(3): p. 158.

8. Youn, S M and S J Choi, *Food Additive Zinc Oxide Nanoparticles: Dissolution, Interaction, Fate, Cytotoxicity, and Oral Toxicity.* Int J Mol Sci, 2022. **23**(11): p. 1-18.

9. Rowe, R C, P J Sheskey, and M E Quinn, *Handbook of Pharmaceutical Excipients*. Sixth Edition ed. 2009, London: Pharmaceutical Press.

10. Wolf, R, D Wolf, P Morganti, and V Ruocco, *Sunscreens.* Clinics in Dermatology, 2001. **19**(4): p. 452-459.

11. Cayrol, Sarraute, Tarroux, Redoules, Charveron, and Gall, *A mineral sunscreen affords genomic protection against ultraviolet (UV) B and UVA radiation: in vitro and in situ assays.* British Journal of Dermatology, 1999. **141**(2): p. 250-258.

12. Vert, M, Y Doi, K-H Hellwich, M Hess, P Hodge, P Kubisa, M Rinaudo, and F Schué, *Terminology for biorelated polymers and applications (IUPAC Recommendations 2012).* Pure and Applied Chemistry, 2012. **84**(2): p. 377-410.

13. Hochella, M F, *Nanoscience and technology: the next revolution in the Earth sciences.* Earth and Planetary Science Letters, 2002. **203**(2): p. 593-605.

14. Mahl, D, J Diendorf, W Meyer-Zaika, and M Epple, *Possibilities and limitations of different analytical methods for the size determination of a bimodal dispersion of metallic nanoparticles.* Colloids and Surfaces A: Physicochemical and Engineering Aspects, 2011. **377**(1): p. 386-392.

15. Sokolova, V and M Epple, *Inorganic Nanoparticles as Carriers of Nucleic Acids into Cells.* Angewandte Chemie International Edition, 2008. **47**(8): p. 1382-1395.

16. Hoo, C M, N Starostin, P West, and M L Mecartney, *A comparison of atomic force microscopy (AFM) and dynamic light scattering (DLS) methods to characterize nanoparticle size distributions.* Journal of Nanoparticle Research, 2008. **10**(1): p. 89-96.

17. Dieckmann, Y, H Cölfen, H Hofmann, and A Petri-Fink, *Particle Size Distribution Measurements of Manganese-Doped ZnS Nanoparticles.* Analytical Chemistry, 2009. **81**(10): p. 3889-3895.

18. Dorofeev, G A, A N Streletskii, I V Povstugar, A V Protasov, and E P Elsukov, *Determination of nanoparticle sizes by X-ray diffraction.* Colloid Journal, 2012. **74**(6): p. 675-685.

19. Suresh, S, S Karthikeyan, and K Jayamoorthy, *FTIR and multivariate analysis to study the effect of bulk and nano copper oxide on peanut plant leaves.* Journal of Science: Advanced Materials and Devices, 2016. **1**(3): p. 343-350.

20. Ilie, A G, M Scarisoareanu, I Morjan, E Dutu, M Badiceanu, and I Mihailescu, *Principal component analysis of Raman spectra for TiO[sub 2] nanoparticle characterization.* Applied Surface Science, 2017. **417**: p. 93-103.

21. Titus, D, E James Jebaseelan Samuel, and S M Roopan, *Chapter 12 - Nanoparticle characterization techniques*, in *Green Synthesis, Characterization and Applications of Nanoparticles*, A K Shukla and S Iravani, Editors. 2019, Elsevier. p. 303-319.

22. Cho, E J, H Holback, K C Liu, S A Abouelmagd, J Park, and Y Yeo, *Nanoparticle Characterization: State of the Art, Challenges, and Emerging Technologies.* Molecular Pharmaceutics, 2013. **10**(6): p. 2093-2110.

23. Bootz, A, V Vogel, D Schubert, and J Kreuter, *Comparison of scanning electron microscopy, dynamic light scattering and analytical ultracentrifugation for the sizing of poly(butyl cyanoacrylate) nanoparticles.* European Journal of Pharmaceutics and Biopharmaceutics, 2004. **57**(2): p. 369-375.

24. Ostrowski, A, D Nordmeyer, A Boreham, C Holzhausen, L Mundhenk, C Graf, M C Meinke, A Vogt, S Hadam, J Lademann, E Rühl, U Alexiev, and A D Gruber, *Overview about the localization of nanoparticles in tissue and cellular context by different imaging techniques.* Beilstein Journal of Nanotechnology, 2015. **6**: p. 263-280.

25. Domingos, R F, M A Baalousha, Y Ju-Nam, M M Reid, N Tufenkji, J R Lead, G G Leppard, and K J Wilkinson, *Characterizing Manufactured Nanoparticles in the Environment: Multimethod Determination of Particle Sizes.* Environmental Science & Technology, 2009. **43**(19): p. 7277-7284.

26. Deegan, R D, O Bakajin, T F Dupont, G Huber, S R Nagel, and T A Witten, *Capillary flow as the cause of ring stains from dried liquid drops.* Nature, 1997. **389**(6653): p. 827-829.

27. Dubochet, J, *Chapter 1 - The Physics of Rapid Cooling and its Implications for Cryoimmobilizaion of Cells*, in *Methods in Cell Biology*. 2007, Elsevier.

28. Michen, B, C Geers, D Vanhecke, C Endes, B Rothen-Rutishauser, S Balog, and A Petri-Fink, *Avoiding drying-artifacts in transmission electron microscopy: Characterizing the size and colloidal state of nanoparticles.* Scientific Reports, 2015. **5**(1): p. 9793.

29. Wagner, J B, F Cavalca, C D Damsgaard, L D L Duchstein, and T W Hansen, *Exploring the environmental transmission electron microscope.* Micron, 2012. **43**(11): p. 1169-1175.

30. Kirk, S E, J N Skepper, and A M Donald, *Application of environmental scanning electron microscopy to determine biological surface structure.* 2009. **233**(2): p. 205-224.

31. Sharma, R, *An Environmental Transmission Electron Microscope for in situ Synthesis and Characterization of Nanomaterials.* Journal of Materials Research, 2005. **20**(7): p. 1695-1707.

32. Malis, T F and D Steele, *Ultramicrotomy for Materials Science.* MRS Proceedings, 1990. **199**: p. 3.

33. Kuo, J, *Electron Microscopy Methods and Protocols*. 3rd Ed. ed. 2014, Totowa, NJ Humana Press.

34. Bert, W, D Slos, O Leroux, and M Claeys, *Cryo-fixation and associated developments in transmission electron microscopy: a cool future for nematology.* Nematology, 2016. **18**(1): p. 1-14.

35. Pickering, S U, *CXCVI.—Emulsions.* Journal of the Chemical Society, Transactions, 1907. **91**(0): p. 2001-2021.

36. Ramsden, W and F Gotch, *Separation of solids in the surface-layers of solutions and 'suspensions' (observations on surface-membranes, bubbles, emulsions, and mechanical coagulation).—Preliminary account.* Proceedings of the Royal Society of London, 1904. **72**(477-486): p. 156-164.

37. Wu, J and G-H Ma, *Recent Studies of Pickering Emulsions: Particles Make the Difference.* Small, 2016. **12**(34): p. 4633-4648.

38. Yang, Y, Z Fang, X Chen, W Zhang, Y Xie, Y Chen, Z Liu, and W Yuan, *An Overview of Pickering Emulsions: Solid-Particle Materials, Classification, Morphology, and Applications.* Frontiers in Pharmacology, 2017. **8**: p. 287.

39. Bao, Y, K Liu, Q Zheng, L Yao, and Y Xu, *A Review of Preparation and Tribological Applications of Pickering Emulsion.* Journal of Tribology, 2021. **144**(1): p. 1-9.

40. Hitchcock, J, A L White, N Hondow, T A Hughes, H Dupont, S Biggs, and O J Cayre, *Metal-shell nanocapsules for the delivery of cancer drugs.* Journal of Colloid and Interface Science, 2020. **567**: p. 171-180.

41. Shi, M-J, F Wang, H Jiang, W-W Qian, Y-Y Xie, X-Y Wei, and T Zhou, *Effect of enzymatic degraded polysaccharides from Enteromorpha prolifera on the physical and oxidative stability of fish oil-in-water emulsions.* Food Chemistry, 2020. **322**: p. 126774.

42. Taheri, R, B Kosasih, H Zhu, and A K Tieu, *Dispersion Stability and Lubrication Performance Correlation of Vegetable Oil-In-Water Emulsions with Nanoparticle-Shielded Oil Droplets.* 2018. **6**(2): p. 55.

43. Taheri, R, B Kosasih, H Zhu, and A K Tieu, *Dual effects of TiSiO[sub 4] composite nanoparticles on dispersion stability and lubrication performance of vegetable oil-in-water emulsions.* 2019. **31**(1-2): p. 21-39.

44. Asfour, M H, H Elmotasem, D M Mostafa, and A A A Salama, *Chitosan based Pickering emulsion as a promising approach for topical application of rutin in a solubilized form intended for wound healing: In vitro and in vivo study.* International Journal of Pharmaceutics, 2017. **534**(1): p. 325-338.

45. Bresme, F and M Oettel, *Nanoparticles at fluid interfaces.* Journal of Physics: Condensed Matter, 2007. **19**(41): p. 413101.

46. Monegier du Sorbier, Q, A Aimable, and C Pagnoux, *Influence of the electrostatic interactions in a Pickering emulsion polymerization for the synthesis of silica-polystyrene hybrid nanoparticles.* Journal of Colloid and Interface Science, 2015. **448**: p. 306-14.

47. Sjoo, M, M Rayner, and M Wahlgren, *Particle-stabilized Emulsions*, in *Engineering Aspects of Food Emulsification and Homogenization*, P Dejmek and M Rayner, Editors. 2015, CRC Press. p. 101-122.

48. Xiao, J, Y Li, and Q Huang, *Recent advances on food-grade particles stabilized Pickering emulsions: fabrication, characterization and research trends.* Trends in Food Science & Technology, 2016. **55**: p. 48-60.

49. Binks, B P, *Particles as surfactants—similarities and differences.* Current Opinion in Colloid & Interface Science, 2002. **7**(1-2): p. 21-41.

50. Nan, F, J Wu, F Qi, Y Liu, T Ngai, and G Ma, *Uniform chitosan-coated alginate particles as emulsifiers for preparation of stable Pickering emulsions with stimulus dependence.* Colloids and Surfaces A: Physicochemical and Engineering Aspects, 2014. **456**: p. 246-252.

51. Binks, B P and S O Lumsdon, *Influence of Particle Wettability on the Type and Stability of Surfactant-Free Emulsions.* Langmuir, 2000. **16**(23): p. 8622-8631.

52. Wei, Z, C Wang, H Liu, S Zou, and Z Tong, *Halloysite nanotubes as particulate emulsifier: Preparation of biocompatible drug-carrying PLGA microspheres based on pickering emulsion.* 2012. **125**(S1): p. E358-E368.

53. Fujii, S, M Okada, and T Furuzono, *Hydroxyapatite nanoparticles as stimulus-responsive particulate emulsifiers and building block for porous materials.* Journal of Colloid and Interface Science, 2007. **315**(1): p. 287-296.

54. Wu, L, Z Liao, M Liu, X Yin, X Li, M Wang, X Lu, N Lv, V Singh, Z He, H Li, and J Zhang, *Fabrication of non-spherical Pickering emulsion droplets by cyclodextrins mediated molecular self-assembly.* Colloids and Surfaces A: Physicochemical and Engineering Aspects, 2016. **490**: p. 163-172.

55. Bon, S A F, S D Mookhoek, P J Colver, H R Fischer, and S van der Zwaag, *Route to stable non-spherical emulsion droplets.* European Polymer Journal, 2007. **43**(11): p. 4839-4842.

56. Norton, J E, P J Fryer, and I T Norton, *5.2.1.2 Contact-Angle Measurements*, in *Formulation Engineering of Foods*. 2013, John Wiley & Sons.

57. Low, L E, S P Siva, Y K Ho, E S Chan, and B T Tey, *Recent advances of characterization techniques for the formation, physical properties and stability of Pickering emulsion.* Advances in Colloid and Interface Science 2020. **277**: p. 102117.

58. Binks, B P and D Yin, *Pickering emulsions stabilized by hydrophilic nanoparticles: in situ surface modification by oil.* Soft Matter, 2016. **12**(32): p. 6858-67.

59. Pal, R, *Modeling of Sedimentation and Creaming in Suspensions and Pickering Emulsions.* 2019. **4**(4): p. 186.

60. McClements, D J, *Critical Review of Techniques and Methodologies for Characterization of Emulsion Stability.* Critical Reviews in Food Science and Nutrition, 2007. **47**(7): p. 611-649.

61. Meng, Z, M Zhang, and H Yang, *Pickering emulsion droplets hosting ionic liquid catalysts for continuous-flow cyanosilylation reaction.* Green Chemistry, 2019. **21**(3): p. 627-633.

62. Dinsmore, A D, E R Weeks, V Prasad, A C Levitt, and D A Weitz, *Three-dimensional confocal microscopy of colloids.* Applied Optics, 2001. **40**(24): p. 4152-4159.

63. Kwok, M-h and T Ngai, *A confocal microscopy study of micron-sized poly(N-isopropylacrylamide) microgel particles at the oil–water interface and anisotopic flattening of highly swollen microgel.* Journal of Colloid and Interface Science, 2016. **461**: p. 409-418.

64. Douliez, J P, N Martin, T Beneyton, J C Eloi, J P Chapel, L Navailles, J C Baret, S Mann, and L Beven, *Preparation of Swellable Hydrogel-Containing Colloidosomes from Aqueous Two-Phase Pickering Emulsion Droplets.* Angewandte Chemie International Edition, 2018. **57**(26): p. 7780-7784.

65. Roncal-Herrero, T, S Micklethwaite, M Ilett, J Hitchcock, O Cayre, and N Hondow, *Analytical Cryo Electron Microscopy for Characterization of Pickering Emulsions.* Microscopy and Microanalysis, 2019. **25**(S2): p. 1706-1707.

66. Sihler, S, A Schrade, Z Cao, and U Ziener, *Inverse Pickering Emulsions with Droplet Sizes below 500 nm.* Langmuir, 2015. **31**(38): p. 10392-10401.

67. Zhai, X, D Lin, D Liu, and X Yang, *Emulsions stabilized by nanofibers from bacterial cellulose: New potential food-grade Pickering emulsions.* Food Research International, 2018. **103**: p. 12-20.

68. Cho, Y S, S H Lee, H M Seo, K Shin, M H Kang, M Lee, J Park, and J W Kim, *Structuring Pickering Emulsion Interfaces with Bilayered Coacervates of Cellulose Nanofibers and Hectorite Nanoplatelets.* Langmuir, 2021. **37**(13): p. 3828-3835.

69. Elbers, N A, J E van der Hoeven, D A de Winter, C T Schneijdenberg, M N van der Linden, L Filion, and A van Blaaderen, *Repulsive van der Waals forces enable Pickering emulsions with non-touching colloids.* Soft Matter, 2016. **12**(35): p. 7265-72.

70. Schalbart, P, M Kawaji, and K Fumoto, *Formation of tetradecane nanoemulsion by low-energy emulsification methods.* International Journal of Refrigeration, 2010. **33**(8): p. 1612-1624.

71. Klang, V, N Matsko, K Raupach, N El-Hagin, and C Valenta, *Development of sucrose stearate-based nanoemulsions and optimisation through γ-cyclodextrin.* European Journal of Pharmaceutics and Biopharmaceutics, 2011. **79**(1): p. 58-67.

72. Persson, K H, I A Blute, I C Mira, and J Gustafsson, *Creation of well-defined particle stabilized oil-in-water nanoemulsions.* Colloids and Surfaces A: Physicochemical and Engineering Aspects, 2014. **459**: p. 48-57.

73. De Carlo, S and J R Harris, *Negative staining and cryo-negative staining of macromolecules and viruses for TEM.* Micron, 2011. **42**(2): p. 117-131.

74. Ruiz, G N, K Amann-Winkel, L E Bove, H R Corti, and T Loerting, *Calorimetric study of water's two glass transitions in the presence of LiCl.* Phys Chem Chem Phys, 2018. **20**(9): p. 6401-6408.

75. Drulyte, I, R M Johnson, E L Hesketh, D L Hurdiss, C A Scarff, S A Porav, N A Ranson, S P Muench, and R F Thompson, *Approaches to altering particle distributions in cryo-electron microscopy sample preparation.* Acta Crystallographica Section D - Structural Biology, 2018. **74**(Pt 6): p. 560-571.

76. Chang, J J, A W McDowall, J Lepault, R Freeman, C A Walter, and J Dubochet, *Freezing, sectioning and observation artefacts of frozen hydrated sections for electron microscopy.* Journal of Microscopy, 1983. **132**(1): p. 109-123.

77. Schmidt-Krey, I and J L Rubinstein, *Electron cryomicroscopy of membrane proteins: Specimen preparation for two-dimensional crystals and single particles.* Micron, 2011. **42**(2): p. 107-116.

78. Pouget, E M, P H H Bomans, J A C M Goos, P M Frederik, G d With, and N A J M Sommerdijk, *The Initial Stages of Template-Controlled $CaCO_3$ Formation Revealed by Cryo-TEM.* Science, 2009. **323**(5920): p. 1455-1458.

79. Berriman, J and N Unwin, *Analysis of transient structures by cryo-microscopy combined with rapid mixing of spray droplets.* Ultramicroscopy, 1994. **56**(4): p. 241-252.

80. Heuser, J E, T S Reese, M J Dennis, Y Jan, L Jan, and L Evans, *Synaptic vesicle exocytosis captured by quick freezing and correlated with quantal transmitter release.* Journal of Cell Biology, 1979. **81**(2): p. 275-300.

81. Hayles, M F and D A M De Winter, *An introduction to cryo-FIB-SEM cross-sectioning of frozen, hydrated Life Science samples.* Journal of Microscopy, 2020. **281**(2): p. 138-156.

82. Satani, H, K Masahiko, I Hirotaka, I Toshifumi, and A and Shimizu, *Preparation of SEM hydrogel samples using a high pressure water freeze fracture method.* High Pressure Research, 2021. **41**(1): p. 97-108.

83. Nishino, Y, K Miyazaki, M Kaise, and A Miyazawa, *Fine cryo-SEM observation of the microstructure of emulsions frozen via high-pressure freezing.* Microscopy, 2021. **71**(1): p. 60-65.

84. Hooper, J, D Budhadev, D L Fernandez Ainaga, N Hondow, D Zhou, and Y Guo, *Polyvalent Glycan Functionalized Quantum Nanorods as Mechanistic Probes for Shape-*

*Selective Multivalent Lectin-Glycan Recognition.* ACS Applied Nano Materials, 2023. **6**(6): p. 4201-4213.

85. Franken, L E, E J Boekema, and M C A Stuart, *Transmission Electron Microscopy as a Tool for the Characterization of Soft Materials: Application and Interpretation.* Advanced Science, 2017. **4**(5): p. 1600476.

86. Kuntsche, J, J C Horst, and H Bunjes, *Cryogenic transmission electron microscopy (cryo-TEM) for studying the morphology of colloidal drug delivery systems.* International Journal of Pharmaceutics, 2011. **417**(1): p. 120-137.

87. Friedrich, H, P M Frederik, G de With, and N A J M Sommerdijk, *Imaging of Self-Assembled Structures: Interpretation of TEM and Cryo-TEM Images.* Angewandte Chemie International Edition, 2010. **49**(43): p. 7850-7858.

88. De Winter, D A M, C Hsieh, M Marko, and M F Hayles, *Cryo-FIB preparation of whole cells and tissue for cryo-TEM: Use of high-pressure frozen specimens in tubes and planchets.* Journal of Microscopy, 2020. **281**(2): p. 125-137.

89. Elbaum, M, *Expanding horizons of cryo-tomography to larger volumes.* Current Opinion in Microbiology, 2018. **43**: p. 155-161.

90. Holzer, L, P Gasser, A.Kaech, M Wegmann, A Zingg, R.Wepf, and B Muench, *Cryo-FIB-nanotomography for quantitative analysis of particle structures in cement suspensions.* Journal of Microscopy, 2007. **227**: p. 216–228.

91. Watt, J, D L Huber, and P L Stewart, *Soft matter and nanomaterials characterization by cryogenic transmission electron microscopy.* MRS Bulletin, 2019. **44**(12): p. 942-948.

92. Löbling, T I, J S Haataja, C V Synatschke, F H Schacher, M Müller, A Hanisch, A H Gröschel, and A H E Müller, *Hidden Structural Features of Multicompartment Micelles Revealed by Cryogenic Transmission Electron Tomography.* ACS Nano, 2014. **8**(11): p. 11330-11340.

93. Hungría, A B, J J Calvino, and J C Hernández-Garrido, *HAADF-STEM Electron Tomography in Catalysis Research.* Topics in Catalysis, 2019. **62**(12): p. 808-821.

94. Frank, J, *Single-particle reconstruction of biological macromolecules in electron microscopy – 30 years.* Quarterly Reviews of Biophysics, 2009. **42**(3): p. 139-158.

95. Ilett, M, R Brydson, A Brown, and N Hondow, *Cryo-analytical STEM of frozen, aqueous dispersions of nanoparticles.* Micron, 2019. **120**: p. 35-42.

96. Glaeser, R M, *Limitations to Significant Information in Biological Electron Microscopy as a Result of Radiation Damage.* Journal of Ultrastructure Research, 1971. **36**(3): p. 466-482.

97. Kuei, B, M P Aplan, J H Litofsky, and E D Gomez, *New opportunities in transmission electron microscopy of polymers.* Materials Science and Engineering: R: Reports, 2020. **139**: p. 1-30.

98. Ilett, M, T Roncal-Herrero, R Brydson, A Brown, and N Hondow, *Progress on Cryogenic Analytical STEM of Nanomaterials.* Microscopy and Microanalysis, 2019. **25**(S2): p. 1086-1087.

99. Ilett, M, M S'Ari, H Freeman, Z Aslam, N Koniuch, M Afzali, J Cattle, R Hooley, T Roncal-Herrero, S M Collins, N Hondow, A Brown, and R Brydson, *Analysis of complex, beam-sensitive materials by transmission electron microscopy and associated techniques.* Philosophical Transactions of the Royal Society A, 2020. **378**(2186): p. 20190601.

100. Colliex, C and C Mory, *Scanning transmission electron microscopy of biological structures.* Ultramicroscopy, 1994. **80**(2-3): p. 175-180.

101. Kirchweger, P, D Mullick, S G Wolf, and M Elbaum, *Visualization of Organelles In Situ by Cryo-STEM Tomography.* Journal of Visualized Experiments, 2023(196).

102. David, K, M Yael, H Ben, L-Z Smadar, F Deborah, G W Sharon, and E Michael, *Cryo-STEM Tomography of Intact Vitrified Fibroblasts.* AIMS Biophysics, 2015. **2**(3): p. 259-273.

103. Elbaum, M, S Seifer, L Houben, S G Wolf, and P Rez, *Toward Compositional Contrast by Cryo-STEM.* Accounts of Chemical Research, 2021. **54**(19): p. 3621-3631.

104. Aoyama, K, T Takagi, A Hirase, and A Miyazawa, *STEM tomography for thick biological specimens.* Ultramicroscopy, 2008. **109**(1): p. 70-80.

105. Hohmann-Marriott, M F, A A Sousa, A A Azari, S Glushakova, G Zhang, J Zimmerberg, and R D Leapman, *Nanoscale 3D cellular imaging by axial scanning transmission electron tomography.* Nature Methods, 2009. **6**(10): p. 729-731.

106. Wolf, S G, L Houben, and M Elbaum, *Cryo-scanning transmission electron tomography of vitrified cells.* Nature Methods, 2014. **11**(4): p. 423-428.

107. Rez, P, T Larsen, and M Elbaum, *Exploring the theoretical basis and limitations of cryo-STEM tomography for thick biological specimens.* Journal of Structural Biology, 2016. **196**(3): p. 466-478.

108. Yoshida, K, M Makihara, N Tanaka, S Aoyagi, E Nishibori, M Sakata, E D Boyes, and P L Gai, *Specific Surface Area and Three-Dimensional Nanostructure Measurements of Porous Titania Photocatalysts by Electron Tomography and Their Relation to Photocatalytic Activity.* Microscopy and Microanalysis, 2011. **17**(2): p. 264-273.

109. Egerton, R F, *Control of radiation damage in the TEM.* Ultramicroscopy, 2013. **127**: p. 100-108.

110. Miszta, K, J de Graaf, G Bertoni, D Dorfs, R Brescia, S Marras, L Ceseracciu, R Cingolani, R van Roij, M Dijkstra, and L Manna, *Hierarchical self-assembly of suspended branched colloidal nanocrystals into superlattice structures.* Nature Materials, 2011. **10**(11): p. 872-876.

111. Rajabalinia, N, S Hamzehlou, E Modin, A Chuvilin, J R Leiza, and J M Asua, *Coupling HAADF-STEM Tomography and Image Reconstruction for the Precise Characterization of Particle Morphology of Composite Polymer Latexes.* Macromolecules, 2019. **52**(14): p. 5298-5306.

112. Li, X, B Han, X Yang, Z Deng, Y Zou, X Shi, L Wang, Y Zhao, S Wu, and M Gu, *Three-dimensional visualization of lithium metal anode via low-dose cryogenic electron microscopy tomography.* iScience, 2021. **24**(12): p. 1-9.

113. Koneti, S, L Roiban, F Dalmas, C Langlois, A-S Gay, A Cabiac, T Grenier, H Banjak, V Maxim, and T Epicier, *Fast electron tomography: Applications to beam sensitive samples and in situ TEM or operando environmental TEM studies.* Materials Characterization, 2019. **151**: p. 480-495.

114. Padgett, E, N Andrejevic, Z Liu, A Kongkanand, W Gu, K Moriyama, Y Jiang, S Kumaraguru, T E Moylan, R Kukreja, and D A Muller, *Editors' Choice—Connecting Fuel Cell Catalyst Nanostructure and Accessibility Using Quantitative Cryo-STEM Tomography.* Journal of The Electrochemical Society, 2018. **165**(3): p. F173.

115. Huang, B Q and E C Yeung, *Chemical and Physical Fixation of Cells and Tissues: An Overview*, in *Plant Microtechniques and Protocols*, E C T Yeung, C Stasolla, M J Sumner, and B Q Huang, Editors. 2015, Springer International Publishing: Cham. p. 23-43.

116. Zankel, A, B Kraus, P Poelt, M Schaffer, and E Ingolic, *Ultramicrotomy in the ESEM, a versatile method for materials and life sciences.* Journal of Microscopy, 2009. **233**(1): p. 140-148.

117. Denk, W and H Horstmann, *Serial block-face scanning electron microscopy to reconstruct three-dimensional tissue nanostructure.* PLoS Biol, 2004. **2**(11): p. e329.

118. Al-Amoudi, A, J J Chang, A Leforestier, A McDowall, L M Salamin, L P Norlén, K Richter, N S Blanc, D Studer, and J Dubochet, *Cryo-electron microscopy of vitreous sections.* The EMBO Journal, 2004. **23**(18): p. 3583-3588.

119. Marko, M, C Hsieh, W Moberlychan, C A Mannella, and J Frank, *Focused ion beam milling of vitreous water: prospects for an alternative to cryo-ultramicrotomy of frozen-hydrated biological samples.* Journal of Microscopy, 2006. **222**(1): p. 42-47.

120. Do, T, G Murphy, L A Earl, G Q D Prete, G Grandinetti, G-H Li, J D Estes, P Rao, C M Trubey, J Thomas, J Spector, D Bliss, A Nath, J D Lifson, and S Subramaniam, *Three-Dimensional Imaging of HIV-1 Virological Synapses Reveals Membrane Architectures Involved in Virus Transmission.* 2014. **88**(18): p. 10327-10339.

121. Narayan, K and S Subramaniam, *Focused ion beams in biology.* Nature Methods, 2015. **12**(11): p. 1021-1031.

122. Titze, B and C Genoud, *Volume scanning electron microscopy for imaging biological ultrastructure.* Biology of the Cell, 2016. **108**(11): p. 307-323.

123. Schiøtz, O H, C J O Kaiser, S Klumpe, D R Morado, M Poege, J Schneider, F Beck, D P Klebl, C Thompson, and J M Plitzko, *Serial Lift-Out: sampling the molecular anatomy of whole organisms.* Nature Methods, 2024. **21**(9): p. 1684-1692.

124. Schaffer, M, *Development of 3D Elemental Analyis using Focused Ion Beam Microscopy and Energy Dispersive X-ray Spectrometry*, in *Institute of Electron Microscopy and Nanoanalysis*. 2008, Graz University of Technology.

125. Schertel, A, N Snaidero, H M Han, T Ruhwedel, M Laue, M Grabenbauer, and W Mobius, *Cryo FIB-SEM: volume imaging of cellular ultrastructure in native frozen specimens.* Journal of Structural Biology, 2013. **184**(2): p. 355-60.

126. Spehner, D, A M Steyer, L Bertinetti, I Orlov, L Benoit, K Pernet-Gallay, A Schertel, and P Schultz, *Cryo-FIB-SEM as a promising tool for localizing proteins in 3D.* Journal of Structural Biology, 2020. **211**(1): p. 107528.

127. Marko, M, C Hsieh, R Schalek, J Frank, and C Mannella, *Focused-ion-beam thinning of frozen-hydrated biological specimens for cryo-electron microscopy.* Nature Methods, 2007. **4**(3): p. 215-217.

128. Kuba, J, J Mitchels, M Hovorka, P Erdmann, L Berka, R Kirmse, J Konig, J De Bock, B Goetze, and A Rigort, *Advanced cryo-tomography workflow developments – correlative microscopy, milling automation and cryo-lift-out.* Journal of Microscopy, 2021. **281**(2): p. 112-124.

129. Antoniou, N, *Failure Analysis of Electronic Material Using Cryogenic FIB-SEM.* EDFA Technical Articles, 2013. **15**(3): p. 12-19.

130. Parmenter, C, M Fay, C Hartfield, G Amador, and G Moldovan, *Cryogenic FIB Lift-out as a Preparation Method for Damage-Free Soft Matter TEM Imaging.* Microscopy and Microanalysis, 2014. **20**(S3): p. 1224-1225.

131. Parmenter, C D J, M W Fay, C Hartfield, and H M Eltaher, *Making the practically impossible "Merely difficult"—Cryogenic FIB lift-out for "Damage free" soft matter imaging.* Microscopy Research and Technique, 2016. **79**(4): p. 298-303.

132. Parmenter, C D and Z A Nizamudeen, *Cryo-FIB-lift-out: practically impossible to practical reality.* Journal of Microscopy, 2021. **281**(2): p. 157-174.

133. Zens, B, F Fäßler, J M Hansen, R Hauschild, J Datler, V-V Hodirnau, V Zheden, J Alanko, M Sixt, and F K M Schur, *Lift-out cryo-FIBSEM and cryo-ET reveal the ultrastructural landscape of extracellular matrix.* Journal of Cell Biology, 2024. **223**(6): p. 1-15.

134. Schaffer, M, S Pfeffer, J Mahamid, S Kleindiek, T Laugks, S Albert, B D Engel, A Rummel, A J Smith, W Baumeister, and J M Plitzko, *A cryo-FIB lift-out technique enables molecular-resolution cryo-ET within native Caenorhabditis elegans tissue.* Nature Methods, 2019. **16**(8): p. 757-762.

135. Long, D M, M K Singh, K A Small, and J Watt, *Cryo-FIB for TEM investigation of soft matter and beam sensitive energy materials.* Nanotechnology, 2022. **33**(50): p. 503001.

136. Kelley, K, A M Raczkowski, O Klykov, P Jaroenlak, D Bobe, M Kopylov, E T Eng, G Bhabha, C S Potter, B Carragher, and A J Noble, *Waffle Method: A general and flexible approach for improving throughput in FIB-milling.* Nature Communications, 2022. **13**(1): p. 1857.

137. Churchman, A H, R Wallace, S J Milne, A P Brown, R Brydson, and P A Beales, *Serum albumin enhances the membrane activity of ZnO nanoparticles*, in *Chemical Communications journal*. 2013, University of Leeds. p. 4172-4.

138. Budhadev, D, E Poole, I Nehlmeier, Y Liu, J Hooper, E Kalverda, U S Akshath, N Hondow, W B Turnbull, S Pohlmann, Y Guo, and D Zhou, *Glycan-Gold Nanoparticles as*

*Multifunctional Probes for Multivalent Lectin-Carbohydrate Binding: Implications for Blocking Virus Infection and Nanoparticle Assembly.* Journal of the American Chemical Society, 2020. **142**(42): p. 18022-18034.

139. Basaran, R, X Ning, D Budhadev, N Hondow, Y Guo, and D Zhou, *Probing the pH-dependency of DC-SIGN/R multivalent lectin-glycan interactions using polyvalent glycan-gold nanoparticles.* Nanoscale Advances, 2024. **6**(8): p. 2198-2208.

140. Hassan, P A, S Rana, and G Verma, *Making Sense of Brownian Motion: Colloid Characterization by Dynamic Light Scattering.* Langmuir, 2015. **31**(1): p. 3-12.

141. Rabenberg, L, *Aberration-Corrected Imaging in Transmission Electron Microscopy: An Introduction.* Physics Today, 2011. **64**(7): p. 55-56.

142. Williams, D B and C B Carter, *Transmission Electron Microscopy A Textbook for Materials Science*. Second Edition ed. 2009: Springer New York.

143. Kirkland, A I and J L Hutchison, *1. Characterisation of Nanomaterials Using Transmission Electron Microscopy*, in *Nanocharacterisation*. 2007: Royal Society of Chemistry.

144. Malenica, M, M Vukomanović, M Kurtjak, V Masciotti, S dal Zilio, S Greco, M Lazzarino, V Krušić, M Perčić, I Jelovica Badovinac, K Wechtersbach, I Vidović, V Baričević, S Valić, P Lučin, N Kojc, and K Grabušić, *Perspectives of Microscopy Methods for Morphology Characterisation of Extracellular Vesicles from Human Biofluids.* Biomedicines, 2021. **9**(6): p. 603.

145. Petroski, J M, Z L Wang, T C Green, and M A El-Sayed, *Kinetically Controlled Growth and Shape Formation Mechanism of Platinum Nanoparticles.* The Journal of Physical Chemistry B, 1998. **102**(18): p. 3316-3320.

146. Rao, D V S, K Muraleedharan, and C J Humphreys, *TEM specimen preparation techniques*, in *Microscopy: Science, Technology, Applications and Education*, A Méndez-Vilas and J Díaz, Editors. 2010, Formatex.

147. Shindo, D and T Oikawa, *Energy Dispersive X-ray Spectroscopy*, in *Analytical Electron Microscopy for Materials Science*, D Shindo and T Oikawa, Editors. 2002, Springer Japan: Tokyo. p. 81-102.

148. Allen, L J, A J D'Alfonso, B Freitag, and D O Klenov, *Chemical mapping at atomic resolution using energy-dispersive x-ray spectroscopy.* MRS Bulletin, 2012. **37**(1): p. 47-52.

149. Hofer, F, F P Schmidt, W Grogger, and G Kothleitner, *Fundamentals of electron energy-loss spectroscopy.* IOP Conference Series: Materials Science and Engineering, 2016. **109**: p. 1-9.

150. Egerton, R F, *Scattering delocalization and radiation damage in STEM-EELS.* Ultramicroscopy, 2017. **180**: p. 115-124.

151. Leapman, R D and R L Ornberg, *Quantitative electron energy loss spectroscopy in biology.* Ultramicroscopy, 1988. **24**(2): p. 251-268.

152. Gatan. *EELS Atlas*. (c) 2025 [cited 2025 08/04/2025]; Available from: https://eels.info/atlas.

153. Malis, T, S C Cheng, and R F Egerton, *EELS log-ratio technique for specimen-thickness measurement in the TEM.* J Electron Microsc Tech, 1988. **8**(2): p. 193-200.

154. Gatan Inc. *EELS: Electron energy loss spectroscopy (EELS) for chemical and compositional analysis.* (c) 2023 27-01-2023]; Available from: https://www.gatan.com/techniques/eels.

155. Spoth, K A, K Ma, U Wiesner, and L F Kourkoutis, *Understanding Initial Formation Stages of Nanomaterials Using Cryo-TEM.* Microscopy Society of America, 2016. **22**: p. 1844–1845.

156. Speedy, R J and C A Angell, *Isothermal compressibility of supercooled water and evidence for a thermodynamic singularity at −45°C.* The Journal of Chemical Physics, 1976. **65**(3): p. 851-858.

157. Sgro, G G and T R D Costa, *Cryo-EM Grid Preparation of Membrane Protein Samples for Single Particle Analysis.* Frontiers in Molecular Biosciences, 2018. **5**: p. 74.

158. He, X, R Kostin, E Knight, M G Han, J Mun, I Bozovic, C Jing, and Y Zhu, *Development of a liquid-helium free cryogenic sample holder with mK temperature control for autonomous electron microscopy.* Ultramicroscopy, 2024. **267**: p. 114037.

159. Palmer, C M and J Löwe, *A cylindrical specimen holder for electron cryo-tomography.* Ultramicroscopy, 2014. **137**: p. 20-29.

160. Dutta, D, S K Sundaram, J G Teeguarden, B J Riley, L S Fifield, J M Jacobs, S R Addleman, G A Kaysen, B M Moudgil, and T J Weber, *Adsorbed Proteins Influence the Biological Activity and Molecular Targeting of Nanomaterials.* Toxicological Sciences, 2007. **100**(1): p. 303-315.

161. Zhang, J, J Milzetti, F Leroy, and F Müller-Plathe, *Formation of coffee-stain patterns at the nanoscale: The role of nanoparticle solubility and solvent evaporation rate.* The Journal of Chemical Physics, 2017. **146**(11): p. 1-11.

162. Marć, M, W Wolak, A Drzewiński, and M R Dudek, *Coffee-ring formation through the use of the multi-ring mechanism guided by the self-assembly of magnetic nanoparticles.* Scientific Reports, 2022. **12**(1): p. 20131.

163. Hondow, N, R Brydson, P Wang, M D Holton, M R Brown, P Rees, H D Summers, and A Brown, *Quantitative characterization of nanoparticle agglomeration within biological media.* Journal of Nanoparticle Research, 2012. **14**(7): p. 1-15.

164. Kizilyaprak, C, Y D Stierhof, and B M Humbel, *Volume microscopy in biology: FIB-SEM tomography.* Tissue Cell, 2019. **57**: p. 123-128.

165. Smith, K C A and C W Oatley, *The scanning electron microscope and its fields of application.* British Journal of Applied Physics, 1955. **6**(11): p. 391.

166. Vernon-Parry, K D, *Scanning electron microscopy: an introduction.* III-Vs Review, 2000. **13**(4): p. 40-44.

167. Zhou, W, R Apkarian, Z L Wang, and D Joy, *Fundamentals of Scanning Electron Microscopy (SEM)*, in *Scanning Microscopy for Nanotechnology: Techniques and Applications*, W Zhou and Z L Wang, Editors. 2007, Springer New York: New York, NY. p. 1-40.

168. Ball, M D and D G McCartney, *The measurement of atomic number and composition in an SEM using backscattered detectors.* 1981. **124**(1): p. 57-68.

169. Kowoll, T, E Müller, S Fritsch-Decker, S Hettler, H Störmer, C Weiss, and D Gerthsen, *Contrast of Backscattered Electron SEM Images of Nanoparticles on Substrates with Complex Structure.* Scanning, 2017. **2017**(1): p. 4907457.

170. Sánchez, E, M T Deluigi, and G Castellano, *Mean Atomic Number Quantitative Assessment in Backscattered Electron Imaging.* Microscopy and Microanalysis, 2012. **18**(6): p. 1355-1361.

171. Rigort, A, E Villa, F Bäuerlein, B Engel, and J Plitzko, *Integrative Approaches for Cellular Cryo-electron Tomography: Correlative Imaging and Focused Ion Beam Micromachining.* Methods in Cell Biology, 2012. **111**: p. 259-81.

172. Chandler, D E and W P Sharp, *Freeze Fracture and Freeze Etching*, in *Electron Microscopy: Methods and Protocols*, J Kuo, Editor. 2014, Springer Science+Business Media Methods in Molecular Biology. p. 96-132.

173. Studer, D, M Michel, M Wohlwend, E B Hunziker, and M D Buschmann, *Vitrification of articular cartilage by high-pressure freezing.* Journal of Microscopy, 1995. **179**(3): p. 321-322.

174. Essani, M, B Charbonnier, N Stephant, H Moussi, P Weiss, J Le Bideau, and P Abellan, *Probing the microporosity and 3D spatial distribution of calcium phosphate cement/hydrogel biomaterials using FIB/SEM at cryogenic temperatures.* Materials Advances, 2023. **4**(11): p. 2474-2486.

175. Rigort, A and J M Plitzko, *Cryo-focused-ion-beam applications in structural biology.* Archives of Biochemistry and Biophysics, 2015. **581**: p. 122-130.

176. Guehrs, E, M Schneider, C M Gunther, P Hessing, K Heitz, D Wittke, A Lopez-Serrano Oliver, N Jakubowski, J Plendl, S Eisebitt, and A Haase, *Quantification of silver nanoparticle uptake and distribution within individual human macrophages by FIB/SEM slice and view.* Journal of Nanobiotechnology, 2017. **15**(1): p. 21.

177. Li, J, T Malis, and S Dionne, *Recent advances in FIB–TEM specimen preparation techniques.* Materials Characterization, 2006. **57**(1): p. 64-70.

178. Holzer, L and M Cantoni, *Review of FIB-tomography*, in *Nanofabrication using focused ion and electron beams: principles and applications*. 2012, Oxford University Press. p. 410-435.

179. Lowe, D G, *Distinctive Image Features from Scale-Invariant Keypoints.* International Journal of Computer Vision, 2004. **60**(2): p. 91–110.

180. Stewart, P L, *Cryo-electron microscopy and cryo-electron tomography of nanoparticles.* Wiley Interdisciplinary Reviews: Nanomedicine and Nanobiotechnology, 2017. **9**(2): p. 1-16.

181. Cheng, Y, N Grigorieff, Pawel A Penczek, and T Walz, *A Primer to Single-Particle Cryo-Electron Microscopy.* Cell, 2015. **161**(3): p. 438-449.

182. Lück, S, M Sailer, V Schmidt, and P Walther, *Three-dimensional analysis of intermediate filament networks using SEM tomography.* 2010. **239**(1): p. 1-16.

183. Kübel, C, A Voigt, R Schoenmakers, M Otten, D Su, T-C Lee, A Carlsson, and J Bradley, *Recent Advances in Electron Tomography: TEM and HAADF-STEM Tomography for Materials Science and Semiconductor Applications.* Microscopy and Microanalysis, 2005. **11**(5): p. 378-400.

184. Turk, M and W Baumeister, *The promise and the challenges of cryo-electron tomography.* FEBS Lett, 2020. **594**(20): p. 3243-3261.

185. Dahmen, T, J P Baudoin, A R Lupini, C Kubel, P Slusallek, and N de Jonge, *Combined scanning transmission electron microscopy tilt- and focal series.* Microscopy and Microanalysis, 2014. **20**(2): p. 548-60.

186. Gan, L and G J Jensen, *Electron tomography of cells.* Quarterly Reviews of Biophysics, 2012. **45**(1): p. 27-56.

187. Miranda, K, W Girard-Dias, M Attias, W de Souza, and I Ramos, *Three dimensional reconstruction by electron microscopy in the life sciences: An introduction for cell and tissue biologists.* Molecular Reproduction & Development, 2015. **82**(7-8): p. 530-47.

188. Ercius, P, O Alaidi, M J Rames, and G Ren, *Electron Tomography: A Three-Dimensional Analytic Tool for Hard and Soft Materials Research.* Advanced Materials, 2015. **27**(38): p. 5638-63.

189. Hall, D H and W J Rice, *Electron Tomography Methods for C. elegans*, in *C. elegans. Methods in Molecular Biology*, D Biron and G Haspel, Editors. 2015, Human Press. p. 141–158.

190. Verguet, A, C Messaoudi, C O S Sorzano, and S Marco, *Alignment of Tilt Series*, in *Cellular Imaging*. 2018, Springer: Cham. p. 183-207.

191. Fernandez, J-J, *Computational methods for electron tomography.* Micron, 2012. **43**(10): p. 1010-1030.

192. Goris, B, T Roelandts, K J Batenburg, H Heidari Mezerji, and S Bals, *Advanced reconstruction algorithms for electron tomography: From comparison to combination.* Ultramicroscopy, 2013. **127**: p. 40-47.

193. Aarle, W v, K J Batenburg, and J Sijbers, *Automatic Parameter Estimation for the Discrete Algebraic Reconstruction Technique (DART).* IEEE Transactions on Image Processing, 2012. **21**(11): p. 4608-4621.

194. Ding, S, D L Fernandez Ainaga, M Hu, B Qiu, U Khalid, C D'Agostino, X Ou, B Spencer, X Zhong, Y Peng, N Hondow, C Theodoropoulos, Y Jiao, C M A Parlett, and X Fan, *Spatial*

*segregation of catalytic sites within Pd doped H-ZSM-5 for fatty acid hydrodeoxygenation to alkanes.* Nature Communications, 2024. **15**(1): p. 7718.

195. Mu, Q, C A David, J Galceran, C Rey-Castro, Ł Krzemiński, R Wallace, F Bamiduro, S J Milne, N S Hondow, R Brydson, G Vizcay-Barrena, M N Routledge, L J C Jeuken, and A P Brown, *Systematic Investigation of the Physicochemical Factors That Contribute to the Toxicity of ZnO Nanoparticles.* Chemical Research in Toxicology, 2014. **27**(4): p. 558-567.

196. Sun, A, S Ma, and W-X Wang, *Two-sided cellular and physiological effects of zinc oxide nanoparticles (nZnO): a critical review.* Environmental Science: Nano, 2025. **12**(2): p. 1059-1078.

197. Wallace, R, A P Brown, R Brydson, S J Milne, N Hondow, and P Wang, *Characterisation of ZnO nanoparticle suspensions for toxicological applications.* Journal of Physics: Conference Series, 2012. **371**(1): p. 012080.

198. Nobbmann, U. *Polydispersity – what does it mean for DLS and chromatography?* 2017 [cited 2025 08/04-2025]; Available from: https://www.malvernpanalytical.com/en/learn/knowledge-center/insights/polydispersity-what-does-it-mean-for-dls-and-chromatography.

199. Rudolph, A R, K L Jungjohann, D R Wheeler, and S M Brozik, *Drying Effect Creates False Assemblies in DNA-Coated Gold Nanoparticles as Determined Through In Situ Liquid Cell STEM.* Microscopy and Microanalysis, 2014. **20**(2): p. 437-444.

200. Zheng, H, S A Claridge, A M Minor, A P Alivisatos, and U Dahmen, *Nanocrystal Diffusion in a Liquid Thin Film Observed by in Situ Transmission Electron Microscopy.* Nano Letters, 2009. **9**(6): p. 2460-2465.

201. Russo, C J and L A Passmore, *Controlling protein adsorption on graphene for cryo-EM using low-energy hydrogen plasmas.* Nature Methods, 2014. **11**(6): p. 649-652.

202. Pantelic, R S, W Fu, C Schoenenberger, and H Stahlberg, *Rendering graphene supports hydrophilic with non-covalent aromatic functionalization for transmission electron microscopy.* Applied Physics Letters, 2014. **104**(13): p. 1-5.

203. Altantzis, T, D Zanaga, and S Bals, *Advanced electron tomography of nanoparticle assemblies(a).* Europhysics Letters, 2017. **119**(3): p. 38001.

204. Noble, A J, V P Dandey, H Wei, J Brasch, J Chase, P Acharya, Y Z Tan, Z Zhang, L Y Kim, G Scapin, M Rapp, E T Eng, W J Rice, A Cheng, C J Negro, L Shapiro, P D Kwong, D Jeruzalmi, A des Georges, C S Potter, and B Carragher, *Routine single particle CryoEM sample and grid characterization by tomography.* eLife, 2018. **7**: p. e34257.

205. Ilett, M, E Naveed, T Roncal-Herrero, Z Aslam, S Micklethwaite, and N Hondow, *In situ electron microscopy technqiues for nanoparticle sipersion analusis of commercial sunscreen.* Journal of Nanoparticle Research, 2023. **25**: p. 122.

206. Efthymiou, C, M A K Williams, and K M McGrath, *Revealing the structure of high-water content biopolymer networks: Diminishing freezing artefacts in cryo-SEM images.* Food Hydrocolloids, 2017. **73**: p. 203-212.

207. Serp, D, M Mueller, U von Stockar, and I W Marison, *Low-temperature electron microscopy for the study of polysaccharide ultrastructures in hydrogels. I. Theoretical and technical considerations.* Biotechnology and Bioengineering, 2002. **79**(3): p. 243-252.

208. Hayles, M F, D J Stokes, D Phifer, and K C Findlay, *A technique for improved focused ion beam milling of cryo-prepared life science specimens.* Journal of Microscopy, 2007. **226**(3): p. 263-269.

209. Müller, S, *On optimizing high-pressure freezing: from heat transfer theory to a new microbiopsy device.* Journal of Microscopy, 1998. **192**(3): p. 236-247.

210. Sosinsky, G E, J Crum, Y Z Jones, J Lanman, B Smarr, M Terada, M E Martone, T J Deerinck, J E Johnson, and M H Ellisman, *The combination of chemical fixation procedures with high pressure freezing and freeze substitution preserves highly labile tissue ultrastructure for electron tomography applications.* Journal of Structural Biology, 2008. **161**(3): p. 359-371.

211. Basaran, R, D Budhadev, A Kempf, I Nehlmeier, N Hondow, S Pohlmann, Y Guo, and D Zhou, *Probing scaffold size effects on multivalent lectin-glycan binding affinity, thermodynamics and antiviral properties using polyvalent glycan-gold nanoparticles.* Nanoscale, 2024. **16**(29): p. 13962-13978.

212. Liu, N and H-W Wang, *Better Cryo-EM Specimen Preparation: How to Deal with the Air–Water Interface?* Journal of Molecular Biology, 2023. **435**(9): p. 167926.

213. Xue, H, M Zhang, J Liu, J Wang, and G Ren, *Cryo-electron tomography related radiation-damage parameters for individual-molecule 3D structure determination.* 2022. **10**: p. 1-22.

214. McEwen, B F, K H Downing, and R M Glaeser, *The relevance of dose-fractionation in tomography of radiation-sensitive specimens.* Ultramicroscopy, 1995. **60**(3): p. 357-373.

215. Koster, A J, R Grimm, D Typke, R Hegerl, A Stoschek, J Walz, and W Baumeister, *Perspectives of Molecular and Cellular Electron Tomography.* Journal of Structural Biology, 1997. **120**(3): p. 276-308.

216. Baker, L A, E A Smith, S A Bueler, and J L Rubinstein, *The resolution dependence of optimal exposures in liquid nitrogen temperature electron cryomicroscopy of catalase crystals.* Journal of Structural Biology, 2010. **169**(3): p. 431-437.

217. Yan, R, T J Edwards, L M Pankratz, R J Kuhn, J K Lanman, J Liu, and W Jiang, *Simultaneous determination of sample thickness, tilt, and electron mean free path using tomographic tilt images based on Beer-Lambert law.* Journal of Structural Biology, 2015. **192**(2): p. 287-96.

218. Winkler, H and K A Taylor, *Accurate marker-free alignment with simultaneous geometry determination and reconstruction of tilt series in electron tomography.* Ultramicroscopy, 2006. **106**(3): p. 240-254.

219. Glaeser, R M, *Proteins, interfaces, and cryo-EM grids.* Current Opinion in Colloid & Interface Science, 2018. **34**: p. 1-8.

220. Torres-Salgado, J F, M Comas-Garcia, M V Villagrana-Escareño, A L Durán-Meza, J Ruiz-García, and R D Cadena-Nava, *Physicochemical Study of Viral Nanoparticles at the Air/Water Interface.* The Journal of Physical Chemistry B, 2016. **120**(26): p. 5864-5873.

221. Qian, H, *Major Factors Influencing the Size Distribution Analysis of Cellulose Nanocrystals Imaged in Transmission Electron Microscopy.* Polymers, 2021. **13**(19): p. 1-14.

222. Dobro, M J, L A Melanson, G J Jensen, and A W McDowall, *Chapter Three - Plunge Freezing for Electron Cryomicroscopy*, in *Methods in Enzymology*, G J Jensen, Editor. 2010, Academic Press. p. 63-82.

223. Glaeser, R M, K Downing, D DeRosier, W Chiu, and J Frank, *Electron Crystallography Of Biological Macromolecules*. 2007: Oxford University Press.

224. Noble, A J, H Wei, V P Dandey, Z Zhang, Y Z Tan, C S Potter, and B Carragher, *Reducing effects of particle adsorption to the air–water interface in cryo-EM.* Nature Methods, 2018. **15**(10): p. 793-795.

225. Feng, X, Z Fu, S Kaledhonkar, Y Jia, B Shah, A Jin, Z Liu, M Sun, B Chen, R A Grassucci, Y Ren, H Jiang, J Frank, and Q Lin, *A Fast and Effective Microfluidic Spraying-Plunging Method for High-Resolution Single-Particle Cryo-EM.* Structure, 2017. **25**(4): p. 663-670.e3.

226. Jain, T, P Sheehan, J Crum, B Carragher, and C S Potter, *Spotiton: A prototype for an integrated inkjet dispense and vitrification system for cryo-TEM.* Journal of Structural Biology, 2012. **179**(1): p. 68-75.

227. Skocaj, M, M Filipic, J Petkovic, and S Novak, *Titanium dioxide in our everyday life; is it safe?* Radiology and Oncology, 2011. **45**(4): p. 227-47.

228. Ophus, E M, L Rode, B Gylseth, D G Nicholson, and K Saeed, *Analysis of titanium pigments in human lung tissue.* Scandinavian Journal of Work, Environment & Health, 1979. **5**(3): p. 290-296.

229. Lindenschmidt, R C, K E Driscoll, M A Perkins, J M Higgins, J K Maurer, and K A Belfiore, *The comparison of a fibrogenic and two nonfibrogenic dusts by bronchoalveolar lavage.* Toxicology and Applied Pharmacology, 1990. **102**(2): p. 268-281.

230. Ribeiro, A R, S Gemini-Piperni, R Travassos, L Lemgruber, R C. Silva, A L Rossi, M Farina, K Anselme, T Shokuhfar, R Shahbazian-Yassar, R Borojevic, L A Rocha, J Werckmann, and J M Granjeiro, *Trojan-Like Internalization of Anatase Titanium Dioxide Nanoparticles by Human Osteoblast Cells.* Scientific Reports, 2016. **6**(1): p. 23615.

231. Ribeiro, A R, A Mukherjee, X Hu, S Shafien, R Ghodsi, K He, S Gemini-Piperni, C Wang, R F Klie, T Shokuhfar, R Shahbazian-Yassar, R Borojevic, L A Rocha, and J M Granjeiro, *Bio-camouflage of anatase nanoparticles explored by in situ high-resolution electron microscopy.* Nanoscale, 2017. **9**(30): p. 10684-10693.

232. Ilett, M, O Matar, F Bamiduro, S Sanchez-Segado, R Brydson, A Brown, and N Hondow, *Nanoparticle corona artefacts derived from specimen preparation of particle suspensions.* Scientific Reports, 2020. **10**(1): p. 5278.

233. Moore, T L, L Rodriguez-Lorenzo, V Hirsch, S Balog, D Urban, C Jud, B Rothen-Rutishauser, M Lattuada, and A Petri-Fink, *Nanoparticle colloidal stability in cell culture media and impact on cellular interactions.* Chemical Society Reviews, 2015. **44**(17): p. 6287-6305.

234. Vulović, M, R B G Ravelli, L J van Vliet, A J Koster, I Lazić, U Lücken, H Rullgård, O Öktem, and B Rieger, *Image formation modeling in cryo-electron microscopy.* Journal of Structural Biology, 2013. **183**(1): p. 19-32.

235. Egelhaaf, S U, P Schurtenberger, and M Müller, *New controlled environment vitrification system for cryo-transmission electron microscopy: design and application to surfactant solutions.* Journal of Microscopy, 2000. **200**(2): p. 128-139.

236. Fernandez Ainaga, D L, T Roncal-Herrero, M Ilett, Z Aslam, C Cheng, J P Hitchcock, O J Cayre, and N Hondow, *Native state structural and chemical characterisation of Pickering emulsions: A cryo-electron microscopy study.* 2025. **298**(1): p. 92-105.

237. Vignati, E, R Piazza, and T P Lockhart, *Pickering Emulsions: Interfacial Tension, Colloidal Layer Morphology, and Trapped-Particle Motion.* Langmuir, 2003. **19**(17): p. 6650-6656.

238. Egerton, R F, *Radiation damage to organic and inorganic specimens in the TEM.* Micron, 2019. **119**: p. 72-87.

239. Wills, J W, H D Summers, N Hondow, A Sooresh, K E Meissner, P A White, P Rees, A Brown, and S H Doak, *Characterizing Nanoparticles in Biological Matrices: Tipping Points in Agglomeration State and Cellular Delivery In Vitro.* ACS Nano, 2017. **11**(12): p. 11986-12000.

240. Peña, F d l, E Prestat, V T Fauske, P Burdet, T Furnival, P Jokubauskas, M Nord, T Ostasevicius, J Lähnemann, K E MacArthur, D N Johnstone, M Sarahan, J Taillon, T Aarholt, pquinn-dls, V Migunov, A Eljarrat, J Caron, T Poon, S Mazzucco, B Martineau, S Somnath, T Slater, C Francis, actions-user, M Walls, N Tappy, N Cautaerts, F Winkler, and G Donval, *hyperspy/hyperspy: Release v1.6.3*. 2021, Zenodo.

241. Russo, C J and R F Egerton, *Damage in electron cryomicroscopy: Lessons from biology for materials science.* MRS Bulletin, 2019. **44**(12): p. 935-941.

242. Knapek, E and J Dubochet, *Beam damage to organic material is considerably reduced in cryo-electron microscopy.* Journal of Molecular Biology, 1980. **141**(2): p. 147-161.

243. Koniuch, N, M Ilett, S M Collins, N Hondow, A Brown, L Hughes, and H Blade, *Structure of polymeric nanoparticles encapsulating a drug - pamoic acid ion pair by scanning transmission electron microscopy.* Heliyon, 2023. **9**(6): p. 1-13.

244. Migunov, V, H Ryll, X Zhuge, M Simson, L Strüder, K J Batenburg, L Houben, and R E Dunin-Borkowski, *Rapid low dose electron tomography using a direct electron detection camera.* Scientific Reports, 2015. **5**(1): p. 14516.

245. Schwartz, J, C Harris, J Pietryga, H Zheng, P Kumar, A Visheratina, N A Kotov, B Major, P Avery, P Ercius, U Ayachit, B Geveci, D A Muller, A Genova, Y Jiang, M Hanwell, and R Hovden, *Real-time 3D analysis during electron tomography using tomviz.* Nature Communications, 2022. **13**(1): p. 4458.

246. Levin, B D A, *Direct detectors and their applications in electron microscopy for materials science.* Journal of Physics: Materials, 2021. **4**(4): p. 042005.

247. Hart, J L, A C Lang, A C Leff, P Longo, C Trevor, R D Twesten, and M L Taheri, *Direct Detection Electron Energy-Loss Spectroscopy: A Method to Push the Limits of Resolution and Sensitivity.* Scientific Reports, 2017. **7**(1): p. 8243.

248. Yang, J, X Zhang, J Xie, J Guo, Z Wang, Y Hui, J Yang, and S Zhang, *Porous mullite ceramics with hierarchical pores constructed via vat photopolymerization of multi-phase Pickering emulsion.* Additive Manufacturing, 2024. **79**: p. 103943.

249. Zhu, Y, W Wang, H Yu, and A Wang, *Preparation of porous adsorbent via Pickering emulsion template for water treatment: A review.* Journal of Environmental Sciences, 2020. **88**: p. 217-236.

250. Bago Rodriguez, A M and B P Binks, *Capsules from Pickering emulsion templates.* Current Opinion in Colloid & Interface Science, 2019. **44**: p. 107-129.

251. He, J, C Hsieh, Y Wu, T Schmelzer, P Wang, Y Lin, M Marko, and H Sui, *Cryo-FIB specimen preparation for use in a cartridge-type cryo-TEM.* Journal of Structural Biology, 2017. **199**(2): p. 114-119.

252. Drobne, D, M Milani, V Lešer, and F Tatti, *Surface damage induced by FIB milling and imaging of biological samples is controllable.* Microscopy Research and Technique, 2007. **70**(10): p. 895-903.

253. Bassim, N D, B T De Gregorio, A L D Kilocoyne, K Scott, T Chou, S Wirick, G Cody, and R M Stroud, *Minimizing damage during FIB sample preparation of soft materials.* Journal of Microscopy, 2012. **245**(3): p. 288-301.

254. Rubanov, S and P R Munroe, *FIB-induced damage in silicon.* Journal of Microscopy, 2004. **214**(3): p. 213-221.

255. Klang, V, N B Matsko, C Valenta, and F Hofer, *Electron microscopy of nanoemulsions: an essential tool for characterisation and stability assessment.* Micron, 2012. **43**(2-3): p. 85-103.

256. Tomus, D and H P Ng, *In situ lift-out dedicated techniques using FIB–SEM system for TEM specimen preparation.* Micron, 2013. **44**: p. 115-119.

257. Wang, S, H Zhou, W Chen, Y Jiang, X Yan, H You, and X Li, *CryoFIB milling large tissue samples for cryo-electron tomography.* Scientific Reports, 2023. **13**(1): p. 5879.

258. CryoEM. *TFS Autoloaders Operating Procedure*. (c) 2025 [cited 2025 08/04/2025]; Available from: https://www.cryoemcenters.org/merit-badge/tfs-autoloaders/autoloader-use-sop/.

259. Wolff, G, R W A L Limpens, S Zheng, E J Snijder, D A Agard, A J Koster, and M Bárcena, *Mind the gap: micro-expansion joints drastically decrease the bending of FIB-milled cryo-lamellae.* bioRxiv, 2019: p. 656447.

260. Beggs, K W, T E Dougherty, A J Kassab, and L A Giannuzzi, *Heat Transfer Analysis of Cryogenic EXLO Specimen Handling.* Microscopy and Microanalysis, 2025. **31**(1): p. 1-6.

261. Zachman, M J, E Asenath-Smith, L A Estroff, and L F Kourkoutis, *Site-Specific Preparation of Intact Solid–Liquid Interfaces by Label-Free In Situ Localization and Cryo-Focused Ion Beam Lift-Out.* Microscopy and Microanalysis, 2016. **22**(6): p. 1338-1349.

262. Cha, E, H Chung, J Jang, J Lee, E Lee, and J C Ye, *Low-Dose Sparse-View HAADF-STEM-EDX Tomography of Nanocrystals Using Unsupervised Deep Learning.* ACS Nano, 2022. **16**(7): p. 10314-10326.

263. Wiedemann, S and R Heckel, *A deep learning method for simultaneous denoising and missing wedge reconstruction in cryogenic electron tomography.* Nature Communications, 2024. **15**(1): p. 8255.

264. Liu, Y-T, H Zhang, H Wang, C-L Tao, G-Q Bi, and Z H Zhou, *Isotropic reconstruction for electron tomography with deep learning.* Nature Communications, 2022. **13**(1): p. 6482.

# Appendix A



Received: 26 September 2024 | Revised: 16 December 2024 | Accepted: 21 January 2025

DOI: 10.1111/jmi.13391

Journal of Microscopy RMS

ORIGINAL ARTICLE

## Native state structural and chemical characterisation of Pickering emulsions: A cryo-electron microscopy study

**Dario Luis Fernandez Ainaga** | **Teresa Roncal-Herrero** | **Martha Ilett** | **Zabeada Aslam** | **Cheng Cheng** | **James P. Hitchcock** | **Olivier J. Cayre** | **Nicole Hondow**

School of Chemical and Process Engineering, University of Leeds, Leeds, UK

**Correspondence**
Nicole Hondow, School of Chemical and Process Engineering, University of Leeds, Leeds LS2 9JT, UK.
Email: N.Hondow@leeds.ac.uk

**Summary**

Transmission electron microscopy can be used for the characterisation of a wide range of thin specimens, but soft matter and aqueous samples such as gels, nanoparticle dispersions, and emulsions will dry out and collapse under the microscope vacuum, therefore losing information on their native state and ultimately limiting the understanding of the sample.

This study examines commonly used techniques in transmission electron microscopy when applied to the characterisation of cryogenically frozen Pickering emulsion samples. Oil-in-water Pickering emulsions stabilised by 3 to 5 nm platinum nanoparticles were cryogenically frozen by plunge-freezing into liquid ethane to retain the native structure of the system without inducing crystallisation of the droplet oil cores.

A comparison between the droplet morphology following different sample preparation methods has confirmed the effectiveness of using plunge-freezing to prepare these samples. Scanning transmission electron microscopy imaging showed that dry droplets collapse under the microscope vacuum, changing their shape and size (average apparent diameter: ~342 nm) compared to frozen samples (average diameter: ~183 nm). Cryogenic electron tomography was used to collect additional information of the 3D shape and size of the emulsion droplets, and the position of the stabilising nanoparticles relative to the droplet surface. Cryogenic energy dispersive X-ray and electron energy loss spectroscopy were used to successfully obtain elemental data and generate elemental maps to identify the stabilising nanoparticles and the oil phase. Elemental maps generated from spectral data were used in conjunction with electron tomography to obtain 3D information of the oil phase in the emulsion droplets.

Beam-induced damage to the ice was the largest limiting factor to the sample characterisation, limiting the effective imaging resolution and signal-to-noise

ratio, though careful consideration of the imaging parameters used allowed for the characterisation of the samples presented in this study. Ultimately this study shows that cryo-methods are effective for the representative characterisation of Pickering emulsions.

**KEYWORDS**
cryo-electron tomography, cryogenic electron microscopy, cryo-HAADF STEM, Pickering emulsions, plunge-freezing, spectroscopy

## 1 | INTRODUCTION

Transmission electron microscopy (TEM) is routinely used for the characterisation of nanomaterial-based systems due to the high magnification and resolution imaging, alongside associated spectroscopy techniques that are possible. Routine imaging and analysis, however, does limit specimens by both size and stability under the vacuum of the electron microscope.

This creates challenges when imaging soft matter and aqueous samples such as nanoparticle dispersions and emulsions as imaging at high resolution using TEM can lead to the loss of sample structure information, such as particle agglomeration for example, due to drying artefacts.[1,2] Consequently, representative characterisation of the sample in its native state (i.e. its original aqueous state, prior to any sample preparation needed before imaging) is not possible.[3] Alternative methods for sample preparation such as staining the sample with a metallic component or stabilising with a polymer have been previously used.[4,5] However, while these techniques can provide some useful information, neither method is successful in fully preserving the original sample morphology.

Cryogenic (cryo)-fixation techniques (e.g. plunge-freezing or high-pressure freezing followed by cryo-ultramicrotomy) provide a route for the TEM imaging of aqueous samples while maintaining their native morphology and local concentration. These techniques were developed by Dubochet et al. in the 1980s focusing on the use of cryo-EM to study viruses. Alongside, extensive studies were carried out by Talmon et al. looking at cryo-EM of soft condensed matter, lipids and surfactants.[6–10] Since then, cryo-EM has been routinely used within the life sciences and there have been significant advancements made in the technologies and methodologies used.[11,12] While these methods have been used and developed for many years within the life sciences they are now becoming successfully applied to the preparation of nonbiological samples like particle dispersions (e.g. nanoparticles within a commercial sunscreen), nanotubes and emulsions among others.[13–17] Cryo preparation is ideal for such systems due to the vitrification of liquid phases that provides the optimum conditions for observation of hydrated species in their native state since the first-order exothermic phase transition between the liquid and the solids does not occur.[18] Even after successful sample vitrification, it is important to be aware of the homogeneity across the grid and ensuring the ice is appropriately thin to allow electron transmission.

A specific type of emulsion are Pickering emulsions, which are systems composed of one liquid in the form of droplets dispersed within another immiscible liquid and stabilised by solid particles. Unlike conventional emulsions stabilised by surfactants, Pickering emulsions use solid particles adsorbed at the liquid-liquid interface that stabilise the system through a combination of steric effects and capillary forces.[19–22] The stability of these emulsions is related to the detachment energy of the stabilising particles, since particles must desorb from the interface to facilitate coalescence of the droplets into a fully separated system. Understanding and controlling the distribution of the solid particles between the bulk and the interface is essential for the manufacture of Pickering emulsions, which can be used in a wide range of application areas including lubrication, food engineering, and drug delivery.[20,23–25]

Pickering emulsions are traditionally characterised in the native state using dynamic light scattering (DLS) and light microscopy to obtain information of the size, shape, and agglomeration state of the emulsion droplets and stabilising particles.[26–30] However, the characterisation of smaller components in these systems is limited by the resolution of these techniques; emulsions stabilised with smaller nanoparticles (<100 nm) and small emulsion droplets (emulsions with droplet size <1 μm) require higher resolution when sample imaging is required. AFM and electron microscopy have been used to characterise dry samples in cases when only information of the stabilising particles was needed.[22,31–33] Sample imaging in the native state, that is, when the droplet-based system is dispersed in liquid, can be accomplished through extensive sample preparation. This includes fixation, freeze-fracture and plunge-freezing.[27,34–37] These techniques can be useful when attempting to characterise the distribution and position of the particles within the system and any possible aggregation as these factors will affect the stability of

the system. Silva et al. (2020) used light microscopy, AFM, and cryo-TEM to characterise Pickering emulsions in their native state, with cryo-TEM specifically being used to analyse the dispersion of stabilising cellulose nanofibres.[27] A range of cryo-EM imaging techniques are often used in conjunction with light microscopy or other techniques for the characterisation of Pickering emulsions, such as freeze fracture used by Chen et al. (2011) and cryo-scanning electron microscopy used by Xiao et al. (2016).[26,38]

Among these techniques, cryo-TEM allows for not only direct imaging of the Pickering emulsion samples in their native state, but also allows for a wider range of characterisation techniques to be used to complement the imaging, including electron energy loss spectroscopy (EELS) and energy dispersive X-ray spectroscopy (EDX), which provide additional elemental information for the characterisation of stabilising particles and droplet phase.[39–41]

3D characterisation techniques provide important information on the size, shape, and agglomeration of emulsion droplets that would otherwise be unattainable with conventional imaging techniques. To achieve this, tomography, that is, collection of a tilt series followed by 3D reconstruction, can be used together with different microscopy techniques including electron microscopy.[42,43]

This study examines a range of transmission electron microscopy approaches for the characterisation of platinum nanoparticle stabilised oil-in-water Pickering emulsion samples. The main aim of this study is to explore the use of cryo-(S)TEM, -tomography, and -spectroscopy for the representative characterisation of Pickering emulsions in their native state, in particular to obtain specific information of the droplet interface in the nanoscale. Bulk characterisation of the emulsion samples was first performed using DLS to measure the emulsion droplet size in the native state. Samples were then imaged in TEM both in their dry state and when cryogenically frozen using conventional TEM and high angle annular dark field scanning transmission electron microscopy (HAADF STEM) to analyse the changes in droplet shape and size resulting from the sample preparation methods. Electron tomography was used to obtain further information on the shape and distribution of the emulsion droplets in 3D space. Furthermore, EELS and EDX were used to provide spectral information related to the dispersed oil phase and stabilising particles.

## 2 | MATERIALS AND METHODS

### 2.1 | Pickering emulsion

Two similar Pickering emulsions were examined: a sunflower oil-in-water emulsion stabilised by 3 to 5 nm diameter platinum nanoparticles (Pt-NPs); and a hexadecane-in-water emulsion stabilised by the same 3 to 5 nm Pt-NPs. The oils have broadly similar properties as far as their behaviour in these emulsions are concerned. The sunflower oil emulsion was prepared by first hand-shaking a 20 mL sample tube containing 2 mL of oil and 8 mL of the pre-prepared Pt-NPs aqueous suspension. The emulsion was then immediately prepared using a sonic dismembrator ultrasonic processor (Fisher Scientific) for 1 min (40% amplitude) in a large water bath (at room temperature) to avoid dramatic increase of the sample temperature. The hexadecane emulsion was prepared by hand-shaking a 10 mL sample tube containing 20 μL of hexadecane oil and 4.98 mL of Pt-NPs in suspension. This resulted in an emulsion with 0.04 vol% oil concentration. The same Pt-NPs were used in both samples and were synthesised by the reduction of platinum salt in the presence of a reducing agent at room temperature as detailed elsewhere.[25]

### 2.2 | TEM sample preparation

For conventional, dry TEM observations, 3.5 μL of a freshly inverted Pickering emulsion sample was deposited onto a plasma cleaned lacey carbon film supported on 400 mesh copper grids (EM Resolutions) or onto a SiNx grid (EM Resolutions). For cryo-TEM observations lacey carbon films supported on 200 mesh copper grids were plasma cleaned for 20 s and 3.5 μL of the freshly inverted Pickering emulsion sample was deposited using an FEI Vitrobot© mark IV plunge freezer. The sample was blotted for 4 s at blot force 6 and then plunged into liquid ethane. The sample was transferred into a Gatan 914 cryo-holder for TEM and the temperature maintained below –170°C to prevent devitrification.

### 2.3 | Cryo-TEM

A FEI Titan Themis$^3$ TEM operated at 300 kV with a monochromator, multiple STEM detectors, Gatan OneView CCD, Super-X 4-detector silicon drift EDX system and a Gatan GIF Quantum 965 EELS was used. The monochromator allowed continuous beam current control in STEM when not excited and the X-FEG source provided an energy spread of ~ 1.1 eV (FWHM of zero loss peak) in this condition. STEM was run with a 1.4 Å probe diameter of 10 mrad convergence semi angle. HAADF images were collected over the scattering semi-angle range of 35–150 mrad. STEM-EEL spectra were collected with a 20.2 mrad collection semi-angle and were analysed using the Gatan DigitalMicrograph software and Hyperspy.[44] Probe

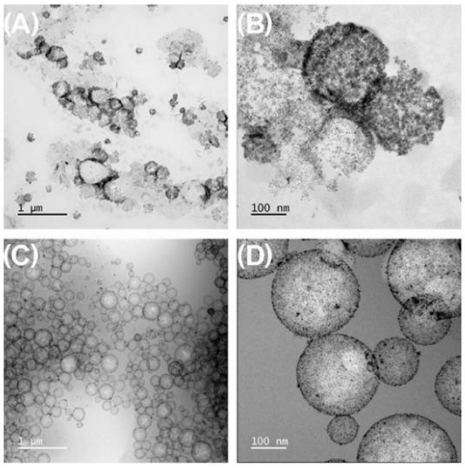


FIGURE 1 Comparison of Pt-NP-stabilised oil-in-water Pickering emulsion characterisation using TEM and cryo-TEM showing a general view of two preparation methods for the Pickering emulsion sample. In (A) and (B), the sample was drop-cast and air-dried, showing emulsion droplets that burst under the electron microscope vacuum. In (C) and (D), the sample was plunge-frozen and imaged in cryo-TEM with a total electron fluence of (C) 41 $e^-/Å^2$ and (D) 781 $e^-/Å^2$ and shows that cryogenic preparation was successful in preserving the droplets. Although the sample used is the same across all four images, the preparation method for EM characterisation greatly influences the preservation of the sample morphology.

that allows the observation of samples in their hydrated state. Electron fluence (the total number of electrons incident on the sample per unit area) and dose (the rate of electrons per unit area) are critical parameters for cryo-EM observation. A minimum amount of electrons is required to generate enough contrast, while above a critical electron fluence, significant sample damage will occur. Dose is likewise important to effectively manage the electron fluence before and during imaging; critically, this has impact on steps such as sample navigation and focusing.

Cryogenic preparation of the Pickering emulsions followed by imaging using appropriate electron fluence and doses showed significant differences compared to the drop-cast samples where the oil droplets maintained their original spherical morphology following vitrification (Figures 1 and 2). In addition cryo-analytical STEM was used alongside conventional TEM as previous work by Ilett et al. (2019) and Egerton (2019) has demonstrated that the damage due to the electron beam in cryo-analytical STEM occurs at higher electron fluences (<2000 $e^-/Å^2$) as compared to conventional cryo-TEM (<100 $e^-/Å^2$).[39,51] This is due to diffusion limited damage by the radiolysis products generated in vitreous ice.[39] Furthermore, cryo-HADDF STEM is useful when imaging this Pickering emulsion system due to atomic number contrast which is highlighted in these samples with high atomic number Pt-NPs in low atomic number oil and water (Figure 2).

The emulsion droplets imaged are circular, implying the spherical shape of the droplets is maintained within the vitreous ice. The average diameter of 500 droplets measured from the drop-cast samples was 340 nm (ranging from 98 to 1089 nm) and for the cryo-prepared sample was 183 nm (ranging from 45 to 514 nm) (Figure 3). The variability on the diameter measurements is extreme, with a measured mean diameter from drop-cast STEM measurements much greater than the bulk DLS measurement (Figure S1), and a slight increase in the mean diameter measured from the cryo-prepared sample compared to DLS. The information on emulsion size and distribution is a critical factor for the design of materials and its application and therefore bulk measurement should be interpreted carefully. The collapse of the oil droplets in the drop-cast sample is evident through the decrease in circularity as compared to the cryo-preparation (Figure 3B). This is consistent with Figure 1A and B where the emulsion droplets burst and collapsed during drop-cast and air-drying on a TEM grid. As such, for samples prepared via drop-casting the circularity ranges from 2.82 to 1.01 and for the cryo-prepared sample between 1.22 and 1.01 (Figure 3B).

These results suggest that the cryo-prepared sample retains both the droplet size and shape that would be expected in its aqueous state. The larger range in the droplet circularity in the drop-cast sample is reflected in the (S)TEM images of collapsed droplets shown in Figure 1A and B. However, this analysis is limited to two dimensions and cannot detect deformation in the direction normal to the viewing plane as a result from blotting the sample during plunge-freezing. The flattening of large samples was also observed by Wills et al. (2017) in nanoparticle dispersions cryogenically frozen by plunge-freezing and subsequently dried under a high vacuum, where agglomerates were shown to be flattened.[52] This issue was tackled by acquiring images at multiple tilt angles and creating a tomogram of the interested area to observe it in 3D and therefore confirm that the droplet shape is maintained through the sample preparation steps. The use of tomography here comes from applying developments already present and used in the life sciences where cryo-EM tomography is a common technique used in studying proteins and cells.[53–55] Drawing from these advances it is now becoming a valuable technique within materials research.

Plunge-freezing and cryo-(S)TEM imaging were successfully applied for the analysis of this Pickering

currents were varied using the monochromator and ranged from 5 to 100 pA depending on the imaging and mapping mode. EDX spectra were processed in VELOX.

### 2.4 | Cryo-STEM tomography

A tilt series of a region of interest was taken by collecting images using the FEI STEM Tomography software in cryo-HAADF STEM mode with a probe current of 5 to 10 pA. A frame was collected every 3° from $\alpha = -60°$ to $\alpha = +60°$ with a pixel resolution of 1.8 nm/pixel. The tilt series was reconstructed using simultaneous iterative reconstruction technique (SIRT) after being processed and aligned in the Inspect3D software. Renders of the reconstructed tomogram were generated after adding surfaces to represent the oil droplets and Pt-NPs using the Imaris software (version 9.5.0). Surfaces for the droplets were drawn manually using the position of the stabilising NPs as a reference outline and are therefore only an approximation of the droplet. The Pt-NPs were instead represented using the automatic spot creation function in Imaris, then manually adjusted using the original cryo-HAADF STEM images as reference.

### 2.5 | Image analysis

The shape of the emulsion droplets was measured using ImageJ in a population of 500 emulsion droplets.[45] Using the STEM images, the shape of the droplets was underlined and an ellipsoid was adjusted to the shape. In this way, the diameter of the emulsion has been chosen to be the major axis of the ellipsoid. The circularity is defined by Equation (1).

$$\text{Circ} = 4\pi \frac{\text{Area}}{\text{Perimeter}^2}. \quad (1)$$

The circularity ranges from 0 (infinitely elongated polygon) to 1 (perfect circle). Density of the Pt nanoparticles at the emulsion droplet was calculated by counting the number of Pt nanoparticles present in the central area of the spherical projection in an area equivalent to 1/3 of the diameter. Although a change in focus can be observed due to the curvature of the droplet, the particles could still be counted reliably.

## 3 | RESULTS AND DISCUSSION

### 3.1 | Bulk analysis and initial electron microscopy

Optical light microscopy is one of the simplest methods to visualise emulsions and was used in our previous work to confirm the droplet size and shape of the Pt-NPs-stabilised Pickering emulsions studied here.[18] However, the observations are limited due to the possible spatial resolution restricting the ability to image the smaller droplets (and the stabilising NPs cannot be resolved).[25] These measurements may also find difficulties due to destabilisation of the emulsion resulting in coalescence and Ostwald ripening or Brownian motion movement on the cover slips when these phenomena are not accounted for.[46,47] For the samples presented here, the smallest droplets were too small to allow for representative characterisation using a light microscope and as would be expected, this method does not provide information on the Pt particles or their distribution on the Pickering emulsion droplets. In addition to light microscopy, DLS was utilised to measure the size distribution of the emulsion droplets, with the mean diameter observed to be ~100 nm for both sunflower oil and hexadecane emulsions as seen in the number distribution DLS plot (Figures S1 and S2). However, DLS itself is limited as it measures only the hydrodynamic diameter and therefore the technique cannot distinguish between the emulsion droplets and stabilising particles.

Electron microscopy has been identified as an important technique to break through this resolution limit in cases where the stabilising nanoparticles need to be imaged.[31] However, conventional electron microscopy is prone to artefacts as seen in surfactant solutions, hydrated colloidal dispersions and biological samples.[48] Drop-casting, where a drop of the sample is placed onto a TEM grid and left to air dry, can cause drying artefacts, modifying the morphology and structure of the emulsion due to evaporation of the liquid phase. Moreover, if some of the droplets were kept intact, the vacuum in the microscope would cause shrinkage, collapse and dehydration of the sample.[1,49] These drying artefacts are seen in the drop-cast TEM images in Figure 1A and B. Under the vacuum of the TEM, the emulsion droplets have burst, with a contour marked by the Pt-NPs and with a variable morphology and size that is not in agreement with the DLS data (Figure S1), which is expected from a dry sample. EDX of the dry sample shows the presence of the platinum signal from the collapsed emulsion droplets, but the lack of a distinct carbon peak overlapping with the Pt signal suggests, as expected, that the oil phase is not contained within a spherical droplet, due to collapse, and subsequent evaporation, in the vacuum of the electron microscope.[50]

### 3.2 | Cryogenic transmission electron microscopy

Having shown a loss of structural integrity of the emulsion droplets when prepared via drop-casting for TEM analysis, cryo-TEM was investigated as an alternative technique

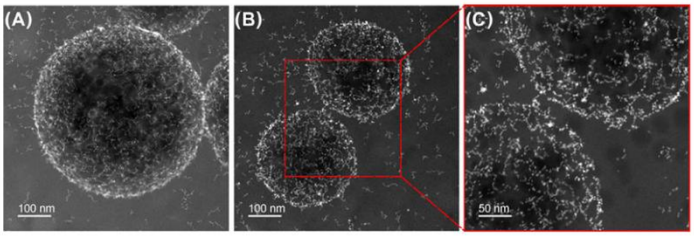


FIGURE 2 (A) Size distribution of 500 Pickering emulsion droplets measured using TEM images at various magnifications and both after drying and of cryo-preserved samples and (B) circularity and diameter of the 500 emulsion droplets measured. As it can be seen in Figure 1, the droplet morphology tends to change as the droplets dry and collapse. Droplets analysed by the drop-cast method range from 98 to 1089 nm, with an average size of ~342 nm. Cryogenically frozen droplets range from 45 to 514 nm, with an average size of ~183 nm.

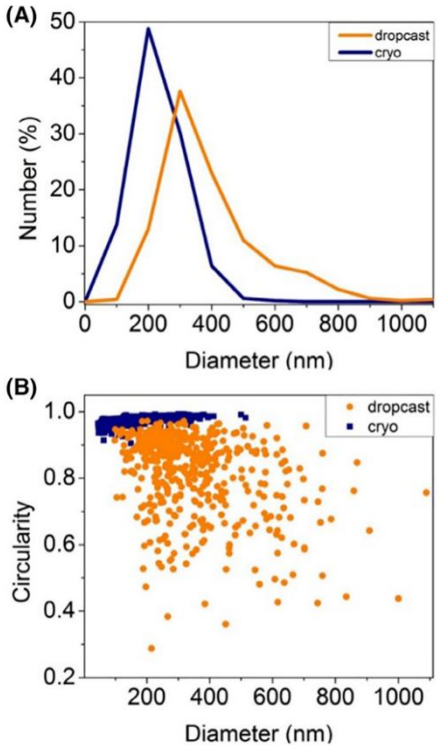


FIGURE 3 Cryo-HAADF STEM images of the hexadecane Pt-Pickering emulsion sample with total electron fluences of (A) 63 $e^-/Å^2$, (B) 66 $e^-/Å^2$ and (C) 267 $e^-/Å^2$. It was possible to obtain higher magnification images where the 3 to 5 nm Pt-NPs could be resolved as seen in (C) due to a higher total electron fluence being required to cause beam damage when using STEM.

emulsions sample, being able to image individual droplets, small droplet clusters, and Pt-NPs. Large droplet aggregates were also found near the grid bars but were often not suitable to imaging due to the excessive ice thickness. The presence of larger droplets and droplet aggregates (~600 nm) was also confirmed from Figure S2, where the DLS size distribution by volume shows a peak at ~600 nm diameter. However, cryo-(S)TEM and plunge-freezing are not suitable for the analysis of large droplets (>600 nm diameter) or droplet aggregates because these may be affected by the sample preparation and are largely inaccessible for cryo-(S)TEM imaging as they are found preferentially in area with thick, crystalline ice. For Pickering emulsion samples with large droplet sizes, or when the analysis of droplet aggregates is important, other techniques should be used (e.g. DLS, optical microscopy, cryo-scanning electron microscopy).

### 3.3 | 3D visualisation using cryogenic electron tomography

To verify the hypothesis that the emulsion droplets maintain their original 3D shape through the blotting stage, a cryo-HAADF STEM tomography tilt series was collected from −60° to +60° taking a frame every 3°. The tilt series was collected in cryo-HAADF STEM mode to mitigate the beam-induced damage that accumulates as images are taken.[56] Nonetheless, the overall quality of the tilt series is greatly limited by cumulative damage suffered by the sample. This damage can be controlled by changing the beam current, dwell time, pixel size, and number of tilt steps: lowering the beam current and dwell time will decrease the electron fluence but will also lower the signal. Increasing the pixel size will likewise decrease the electron fluence but decrease the image resolution. Lastly, the number of tilt steps can be decreased, thus decreasing the number of

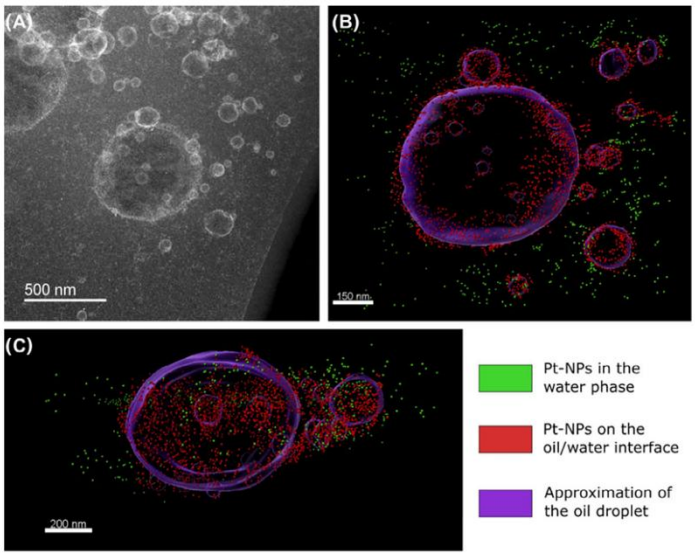


FIGURE 4 Cryo electron tomogram and corresponding cryo-HAADF STEM image of droplets. (A) Cryo-HAADF STEM image; (B, C) top-view and side-view of the of an electron tomogram taken from the area shown in (A). Although it was not possible to use a magnification high enough to consistently resolve the individual Pt-NPs without completely damaging the sample, the position of NP chains in 3D space is still visible in the tomogram. Total electron fluence: (A) 67 $e^-/Å^2$, electron tomogram 1688 $e^-/Å^2$.

images that need to be taken per tilt series, but this also affects the quality of the 3D reconstruction.[57–59] In addition to mitigating beam-induced damage, using HAADF STEM for tomography is advantageous as it will limit any diffraction contrast that would otherwise be evident in cryo-TEM imaging and therefore limit any 3D reconstruction.

A tilt series comprised of a total of 41 images (an example of which is shown in Figure 4, full tilt series in Video S1) was collected using a pixel size of 1.8 nm and a probe current of 10 pA. A tomogram was reconstructed from the tilt series using SIRT after being aligned in the Inspect3D software. Due to the low contrast for the oil phase, the 3D surfaces for the droplets were created manually and are therefore only an approximation (Figure S3). The completed 3D reconstruction in Figure 4 shows the position of the emulsion droplets and Pt-NPs. Figure 4C shows the three-dimensional nature of the droplets is retained after cryogenic preparation, as the droplets have not collapsed. The Pt-NPs are distributed mainly along the oil–water interface, but also present in the water phase on the surface of the ice. The presence of Pt-NPs on the surface of the vitreous ice might be an artefact of the sample preparation arising from the movement of the nanoparticles before the sample is plunged into the liquid ethane but it is also possible that these nanoparticles are not adsorbed to the oil–water interface and remain in the aqueous continuous phase in the emulsion sample. The former effect has been observed in inorganic samples with nanoparticle markers being found at the surface of the cryogenically-frozen sample, and in biological samples, where the effect of the interface can induce a bias on the direction of cell, viruses, and particles, and therefore affect their characterisation.[60–62]

The size of the Pt-NPs was the main limiting factor for controlling the amount of beam damage, as the need to resolve the 3 to 5 nm nanoparticles affected the minimum pixel size and magnification needed to image both the nanoparticles and oil droplets.[63] The effects of this issue can be seen in Figure 4A and B: in Figure 4B only clusters of Pt-NPs can be seen as the image resolution for the tilt series and resulting 3D reconstruction had to be decreased to limit beam damage. STEM pixel size and dwell time are not the only parameters to be considered when collecting a tilt series in cryo-(S)TEM: not only is the number of tilt steps in a series a major contributor to the total electron fluence, but so are the focusing and tracking steps (Figure S4). Tilt tracking can be accomplished with images with low pixel resolution, therefore accounting for only a small

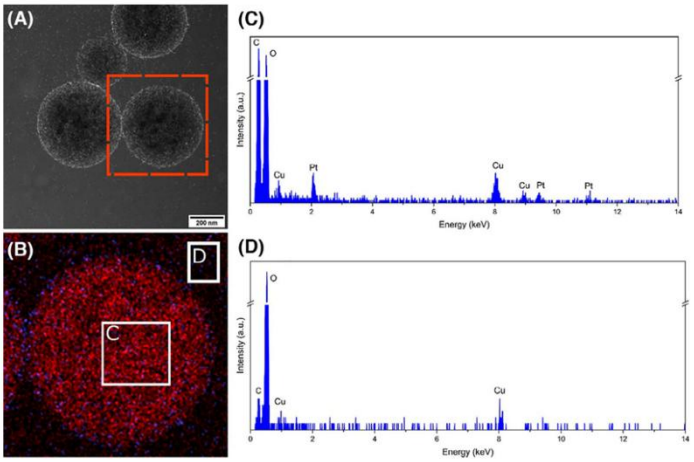


FIGURE 5 (A) HAADF-STEM images of a Pt-NPs-stabilised Pickering emulsion plunge-frozen onto lacey carbon grid and (B) EDX elemental map showing the carbon (red) and platinum (blue) signals with boxes showing EDX spectrum locations. (C, D) Corresponding EDX spectra (total electron fluence: 732 $e^-/Å$).

portion of the total electron fluence. Sample focusing can be approached by either directly focusing on the area of interest or by moving the beam to focus on a nearby feature. Neither strategy can be thought as a catch-all solution for this system, as the former allows for accurate focusing but is more energy intensive, while the latter fully prevents damage to the area of interest but requires the presence of nearby features along the tilt axis. This requirement is often not met, as in this system droplets found in clusters tend to be near thicker ice, and therefore less suitable for collecting a tilt series.

The 3D reconstruction results obtained show that HAADF STEM imaging with atomic number contrast allows for straightforward analysis of the Pt-NPs in 3D space. However, in this imaging mode the oil phase does not generate enough contrast to be successfully imaged and it is therefore not possible to locate the position of the oil–water interface.

### 3.4 | Cryo-spectroscopy EELS and EDX analysis

Elemental analysis of the frozen sample was performed using EELS and EDX mapping while in HAADF-STEM mode to provide information about both the presence of the oil phase within the emulsion droplets and the location of the stabilising Pt-NPs. The EDX elemental map of the cryo-prepared sample in Figure 5B shows a carbon signal within the droplet corresponding to the oil phase and a platinum signal localised predominantly on the droplet interface. A challenge for the elemental analysis of this oil phase lies in distinguishing the carbon signal corresponding to the oil from the surroundings (e.g. the carbon support film). To resolve this issue, elemental analysis of the frozen sample was only performed on droplets found over holes in the carbon film; the drop-cast sample was instead imaged on a SiNx grid to prevent the carbon signal from conventional carbon TEM grids which would otherwise overlap with the carbon signal from the oil phase.

EELS elemental maps (Figure 6) were collected to support the results from EDX analysis. In the EEL spectrum imaging, detection of the carbon and oxygen edges were focused on in order to detect the carbon oil phase and the oxygen in the vitreous ice, therefore permitting understanding of both the presence of the oil in the droplets and also what proportion of the ice thickness they occupy. The oxygen and carbon K edges are both found at a relatively low energy loss and are therefore possible to collect using a low total electron fluence.

The EELS maps were taken with a 0.09 s exposure time and 12 nm pixel size (resulting in a total electron fluence of 16 $e^-/ Å^2$), as an increase in exposure time or decrease in pixel size would result in an increase in electron fluence which would then cause damage to the sample. EELS exposure time and pixel size will need to be adjusted on a sample-to-sample basis depending on sample size,

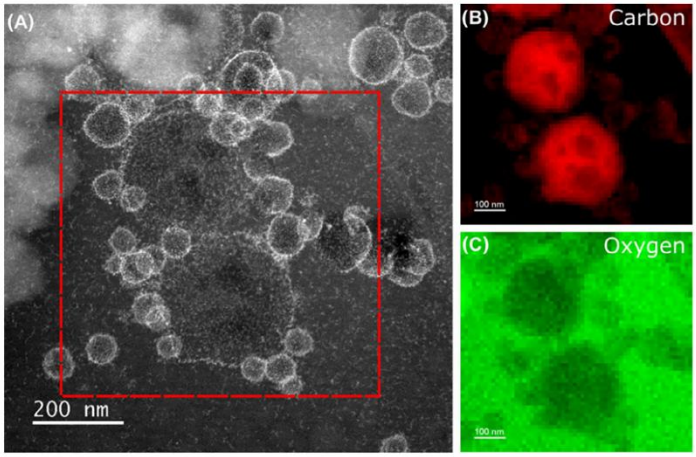


FIGURE 6 EELS elemental maps of emulsion droplets in the Pickering emulsion sample. (A) Cryo-HAADF STEM of emulsion droplets (total electron fluence of 16 $e^-/Å^2$). (B, C) Maps of the signal intensity for the C K and O K edges respectively (16 $e^-/Å^2$).

elements present in the sample, and damage threshold for the specific sample.

The lower electron fluence needed to obtain the elemental map when compared to EDX spectroscopy is especially attractive for cryo-STEM imaging, as it can not only allow for the use of multiple techniques to characterise areas of interest but could also be used in conjunction with cryo-Electron Tomography (cryo-ET) to generate 3D objects based on the elemental maps without damaging the sample. In cryo-STEM the elemental analysis provided by EELS is limited by the presence of important major edges at high energy losses, as is the case with the Pt major edges which cannot be accessed without sample damage. However, Pickering emulsion may be stabilised by a range of different particles and depending on the elemental composition of these particles, it may be possible to analyse them using EELS. For example, silica NPs may be more readily analysed using EELS due to silicon having more accessible L-edges near 100 eV.

So far, neither EDX nor EELS can be thought of as a catch-all for elemental analysis of these Pickering emulsion samples. EELS can provide fast, single-pass, and low-dose elemental maps that can be used to quickly analyse elements within a limited electron energy loss range. For the Pickering emulsion sample used here, the carbon and oxygen K-edges can be easily collected, but the major platinum edges above 2000 eV are outside of the safe detection range to prevent damage to the sample. A longer exposure time would be needed to detect the platinum signal in this system, possibly in the order of 1–10 s, therefore increasing the overall fluence by a factor of 100 before taking into consideration any increased damage from decreasing the pixel size to resolve individual nanoparticles. On the other hand, EDX can be used to detect most elements despite the lower energy resolution. The 3 to 5 nm Pt-NPs used in these samples are challenging to analyse, with EDX being unable to distinguish between individual NPs, and EELS being unable to reach a pixel size below 12 nm in the microscope setup used without significant damage that irreversibly changes the sample.

The absolute thickness of the sample was estimated from the collected EEL low-loss spectra using Hyperspy as shown in Figure S5.[44] Areas with no sample present (Figure S5B) and areas with emulsion droplets (Figure S5C) were both analysed to ensure that the ice thickness is sufficient to contain the emulsion droplets without deformation. The amorphous ice within holes in the carbon film was estimated to be approximately ~250 nm thick near the centre of the grid squares, with thickness variation present near the carbon film and approaching the copper grid. This absolute thickness calculation was done using a mean inelastic free path for vitreous ice of ~350 nm.[60] This result can be contrasted with Figure S5C, where the ice thickness was estimated to reach up to ~500 nm near clusters of emulsion droplets. Plunge-freezing cryo-TEM might therefore be suitable for the imaging of droplets and clusters up to a few hundreds of nanometres (<600 nm) in diameter without deformation or damage to the droplets. However, cryo-(S)TEM imaging can still allow for the imaging of larger droplet aggregates trapped within the ice with the

only imaging limitation being given by the presence of thicker ice near the grid bars which decreases the signal-to-noise ratio when imaging and increases the likelihood of crystalline ice forming during the sample preparation. For EELS analysis the droplet size limitation is more stringent: a minimum droplet size of ~50 nm could be analysed with the methods presented in this study, limited by the smallest pixel size available before beam-induced damage begins accumulating. Identifying an upper limit for EELS can be more challenging, as it is dependent on the information that needs to be extracted. For low-loss EELS analysis and thickness estimation, the same limits as imaging apply due to the ice being generally thinner than 2–3 times than its mean inelastic free path. However, techniques like EELS mapping and elemental quantification cannot be applied to areas where the sample thickness is much thicker than the mean inelastic free path, therefore only allowing for the analysis of single droplets or small aggregates up to 400–500 nm in diameter. Electron tomography can be applied for the imaging of large aggregates (similarly to regular cryo-(S)TEM imaging) but can only be used for samples near the centre of the grid square, as the grid bars can obstruct the sample at high tilt angles. Moreover, care needs to be taken when imaging the sample at high tilt angles as the effective sample thickness increases together with the tilt angle.

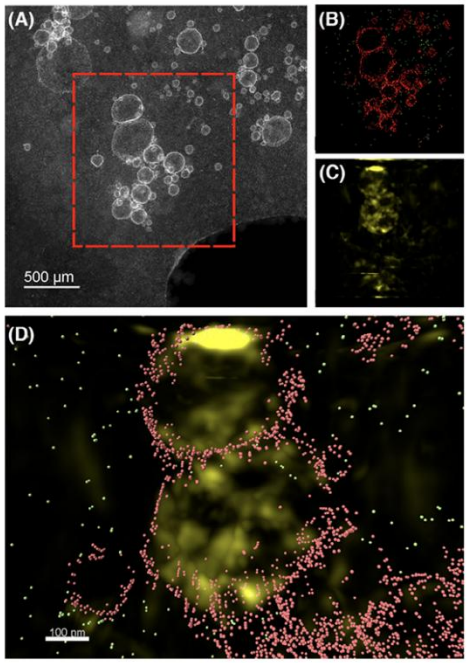


FIGURE 7 (A) Cryo-HAADF STEM image of a group of Pickering emulsions and the corresponding tomograms reconstructed from (B) a cryo-HAADF STEM tilt series and (C) a tilt series of EELS carbon signal (C K edge) maps. (B) The position (in red) of the Pt-NPs on the oil–water interface and in green Pt-NPs in the water phase. (D) A magnified superimposition of (B) and (C).

### 3.5 | Electron tomography with EELS

To compensate for the lack of information on the oil phase obtained in the HAADF STEM tomograms, EELS was used as a complementary elemental analysis technique. A total of 9 EELS elemental maps were acquired at intervals alongside the HAADF STEM tilt series (see Videos S2 and S3), making use of the tilt tracking in the Tomography STEM software. After generating elemental maps using the carbon K edge signal in Hyperspy, the EELS tilt series was aligned and reconstructed into a tomogram using the same process outlined in the electron tomography section. The tomograms obtained from the HAADF STEM and EELS signals were then superimposed in Imaris using the HAADF STEM and ADF (collected simultaneously with EELS) supporting images as references (Figure 7). As shown in Figure 7D, the tomogram generated from the carbon K edge map aligns with the approximated position of the oil droplets. The requirement to collect multiple EELS elemental maps drastically increases the total electron fluence needed (by at least a factor of 10), and therefore pixel sizes below 12 nm cannot be used for EELS elemental maps without damage occurring during the tilt series. This limits the use of this technique to larger droplets (>300 nm) and can only give qualitative information on the position of the stabilising nanoparticles. This size limit creates a narrow size range for suitable droplets, with the lower limit being given by the pixel sized needed for EELS and an upper limit given by the sample thickness. It is therefore possible to determine the general position of the particles and whether they are embedded within the oil–water interface, but it is not possible to determine their exact position at the interface (e.g. determine the contact angle for the particles, which is a difficult task for systems where the particles stabilising the interface are <50 nm).

Collecting a single EELS (or EDX) elemental map will cause less electron beam induced damage and be an alternative to provide elemental information in conjunction with a tilt series. In cases where the structures of interest provide clear contrast within the tilt series, it is possible to use EELS or EDX results to aid in segmentation. In the sample presented in Figure 7A the oil phase in the droplet cannot be distinguished from the surrounding ice using

cryo-HAADF STEM imaging alone, and this technique would therefore be unable to provide any 3D information on the oil phase.

### 3.6 | Limits to sample analysis and future directions for cryo-imaging and analysis of Pickering emulsions

Using the current electron microscope setup (detailed in the Materials and Methods), limits in the effective imaging resolution were encountered when attempting to analyse the Pt-NPs due to the low electron fluence needed to prevent sample damage, with the images collected having low signal-to-noise ratios at high magnifications. The solution shown in this study was to simply work at lower magnifications (×20k to ×80k) whenever high total electron fluence was required, as was the case with electron tomography. When using electron tomography with EELS, this approach results in the inability to resolve individual Pt-NPs on the droplet surface, therefore being unable to analyse their contact angle, which is a characteristic of interest for Pickering emulsions. For the two Pickering emulsions in this study, each with the same Pt-NPs stabilising a different oil (hexadecane and sunflower oil), it would be interesting to examine the precise location of the stabilising NPs with respect to the oil–water interface, as this effective contact angle measurement is a useful indicator of stability.[31] An automated cryo-EM tomography procedure to limit exposure but push resolution to as low as possible could achieve this and such systems are currently being used and developed within other scientific fields. Moving forward applying these techniques to the system analysed here would be the logical next step.[55,64]

Furthermore the use of improved equipment such as a direct electron detection system rather than a CCD camera could help resolve such small NPs during low dose imaging.[55,65,66] In addition, characterisation of the sample through cryo-scanning electron microscopy using techniques such as focus ion beam milling would offer a future opportunity to image a larger sample volume and therefore image larger droplet clusters or systems with larger droplet sizes or to select a site of interest to prepare a lamella to cryo-transfer to the cryo-(S)TEM.[63,67,68]

## 4 | CONCLUSION

Plunge-freezing was found to be suitable as a preparation technique for Pickering emulsion samples with average droplet sizes below 600 nm for cryo-(S)TEM imaging while retaining the native structure. At low electron fluences, cryo-STEM allows for both high-resolution imaging and elemental analysis using EDX and EELS with minimal beam-induced damage to the sample. Cryo-HAADF STEM allowed for easy identification of the Pt-NPs due to their high atomic number while permitting for a higher total electron fluence before the onset of beam-induced damage to the sample, thus allowing for imaging at higher resolutions. Although the use of EDX and EELS is limited by the damage caused at high total electron fluences, both techniques remain useful for elemental analysis. EELS can be used to confirm the presence of elements with edges at relatively low electron energy loss (e.g. oxygen, carbon, nitrogen), while EDX permits for the identification of a wider range of elements (including the platinum in the stabilising NPs).

Overall, cryo-preservation of the Pickering emulsion samples allows for not only cryo-(S)TEM imaging, but also 3D analysis through cryo-ET. Tilt series obtained in cryo-HAADF STEM mode were successful for the creation of 3D tomograms with qualitative information on droplet shape and nanoparticle distribution. Moreover, electron tomography can be combined with EELS to provide 3D information of the oil phase which would otherwise be unattainable in cryo-HAADF STEM. However, further improvements on the efficiency of the tilt series collection are needed to decrease the total electron fluence, therefore allowing for a potential increase in image resolution to obtain more quantitative data from the 3D tomograms.

## ACKNOWLEDGEMENTS

The electron microscopes used in this work were funded by the Engineering and Physical Sciences Research Council (EPSRC), UK under grant EP/M028143/1 (FEI Titan Themis). Funding is also provided by the EPSRC via a New Investigator Award (EP/R043388/1) awarded to NH. The authors gratefully acknowledge the Leeds Electron Microscopy and Spectroscopy (LEMAS) centre for their support and assistance in this work.

## ORCID

*Teresa Roncal-Herrero* https://orcid.org/0000-0002-3673-6904
*Martha Ilett* https://orcid.org/0000-0002-3111-1585
*James P. Hitchcock* https://orcid.org/0000-0003-2226-6734
*Olivier J. Cayre* https://orcid.org/0000-0003-1339-3686
*Nicole Hondow* https://orcid.org/0000-0001-9368-2538

## REFERENCES

1. Michen, B., Geers, C., Vanhecke, D., Endes, C., Rothen-Rutishauser, B., Balog, S., & Petri-Fink, A. (2015). Avoiding drying-artifacts in transmission electron microscopy: Characterizing the size and colloidal state of nanoparticles. *Scientific Reports*, *5*(1), 9793.

2. Hondow, N., Brydson, R., Wang, P., Holton, M. D., Brown, M. R., Rees, P., Summers, H. D., & Brown, A. (2012). Quantitative characterization of nanoparticle agglomeration within biological media. *Journal of Nanoparticle Research*, *14*(7), P1.
3. Brydson, R., Brown, A., Hodges, C., Abellan, P., & Hondow, N. (2015). Microscopy of nanoparticulate dispersions. *Journal of Microscopy*, *260*(3), 238–247.
4. Ganta, S., & Amiji, M. (2009). Coadministration of paclitaxel and curcumin in nanoemulsion formulations to overcome multidrug resistance in tumor cells. *Molecular Pharmaceutics*, *6*(3), 928–939.
5. Nam, Y. S., Kim, J.-W., Shim, J., Han, S. H., & Kim, H. K. (2010). Nanosized emulsions stabilized by semisolid polymer interphase. *Langmuir*, *26*(16), 13038–13043.
6. Dubochet, J., Adrian, M., Chang, J.-J., Homo, J.-C., Lepault, J., McDowall, A. W., & Schultz, P. (1988). Cryo-electron microscopy of vitrified specimens. *Quarterly Reviews of Biophysics*, *21*(2), 129–228.
7. Dubochet, J., Adrian, M., Lepault, J., & McDowall, A. W. (1985). Emerging techniques: Cryo-electron microscopy of vitrified biological specimens. *Trends in Biochemical Sciences*, *10*(4), 143–146.
8. Talmon, Y. (1985). Cryo-electron microscopy of vitrified aqueous specimens. *Ultramicroscopy*, *17*(2), 167.
9. Talmon, Y. (1986). Imaging surfactant dispersions by electron microscopy of vitrified specimens. *Colloids and Surfaces*, *19*(2), 237–248.
10. Talmon, Y., Narkis, M., & Silverstein, M. (1984). Radiation damage to latex particles as an analytical tool in polymer science. *Ultramicroscopy*, *14*(4), 380.
11. Chua, E. Y. D., Mendez, J. H., Rapp, M., Ilca, S. L., Tan, Y. Z., Maruthi, K., Kuang, H., Zimanyi, C. M., Cheng, A., Eng, E. T., Noble, A. J., Potter, C. S., & Carragher, B. (2022). Better, faster, cheaper: Recent advances in cryo-electron microscopy. *Annual Review of Biochemistry*, *91*, 1–32.
12. Guaita, M., Watters, S. C., & Loerch, S. (2022). Recent advances and current trends in cryo-electron microscopy. *Current Opinion in Structural Biology*, *77*, 102484.
13. Thompson, R. F., Walker, M., Siebert, C. A., Muench, S. P., & Ranson, N. A. (2016). An introduction to sample preparation and imaging by cryo-electron microscopy for structural biology. *Methods (San Diego, Calif.)*, *100*, 3–15.
14. Pouget, E. M., Bomans, P. H. H., Goos, J. A. C. M., Frederik, P. M., De With, G., & Sommerdijk, N. A. J. M. (2009). The initial stages of template-controlled $CaCO_3$ formation revealed by cryo-TEM. *Science*, *323*(5920), 1455–1458.
15. Edri, E., & Regev, O. (2010). Cryo-staining techniques in cryo-TEM studies of dispersed nanotubes. *Ultramicroscopy*, *110*(7), 754–760.
16. Ilett, M., Naveed, E., Roncal-Herrero, T., Aslam, Z., Micklethwaite, S., & Hondow, N. (2023). In situ electron microscopy technqiues for nanoparticle sipersion analusis of commercial sunscreen. *Journal of Nanoparticle Research*, *25*, 122.
17. Spernath, L., Regev, O., Levi-Kalisman, Y., & Magdassi, S. (2009). Phase transitions in O/W lauryl acrylate emulsions during phase inversion, studied by light microscopy and cryo-TEM. *Colloids and Surfaces A: Physicochemical and Engineering Aspects*, *332*(1), 19–25.
18. Bachmann, L., & Mayer, E. (1987). Physics of Water and Ice: Implications for Cryofixation. In Steinbrecht R. A., & Zierold, K. (Eds.), *Cryotechniques in Biological Electron Microscopy* (pp. 3–34). Springer Berlin Heidelberg: Berlin, Heidelberg.
19. Bresme, F., & Oettel, M. (2007). Nanoparticles at fluid interfaces. *Journal of Physics: Condensed Matter*, *19*(41), 413101.
20. Yang, Y., Fang, Z., Chen, X., Zhang, W., Xie, Y., Chen, Y., Liu, Z., & Yuan, W. (2017). An overview of Pickering emulsions: Solid-particle materials, classification, morphology, and applications. *Frontiers in Pharmacology*, *8*(287), 1–20.
21. Pickering, S. U. (1907). CXCVI.—Emulsions. *Journal of the Chemical Society, Transactions*, *91*(0), 2001–2021.
22. Monégier Du Sorbier, Q., Aimable, A., & Pagnoux, C. (2015). Influence of the electrostatic interactions in a Pickering emulsion polymerization for the synthesis of silica-polystyrene hybrid nanoparticles. *Journal of Colloid and Interface Science*, *448*, 306–314.
23. Yang, H., Zhao, L., Xue, S., Deng, Z., Li, J., & Zeng, X. (2019). Branch-chain length modulated graphene oxides for regulating the physicochemical and tribophysical properties of pickering emulsions. *Colloids and Surfaces A: Physicochemical and Engineering Aspects*, *579*, 123703.
24. Bao, Y., Liu, K., Zheng, Q., Yao, L., & Xu, Y. (2021). A Review of preparation and tribological applications of Pickering emulsion. *Journal of Tribology*, *144*(1), 011902.
25. Hitchcock, J., White, A. L., Hondow, N., Hughes, T. A., Dupont, H., Biggs, S., & Cayre, O. J. (2020). Metal-shell nanocapsules for the delivery of cancer drugs. *Journal of Colloid and Interface Science*, *567*, 171–180.
26. Chen, J., Vogel, R., Werner, S., Heinrich, G., Clausse, D., & Dutschk, V. (2011). Influence of the particle type on the rheological behavior of Pickering emulsions. *Colloids and Surfaces A: Physicochemical and Engineering Aspects*, *382*(1-3), 238–245.
27. Silva, C. E. P., Tam, K. C., Bernardes, J. S., & Loh, W. (2020). Double stabilization mechanism of O/W Pickering emulsions using cationic nanofibrillated cellulose. *Journal of Colloid and Interface Science*, *574*, 207–216.
28. Wan, S., Zeng, Q., Yang, S., Zhao, X., Wen, Q., Tang, H., Zhang, Y., Huang, J., Yu, G., Feng, Y., & Li, J. (2022). In situ characterization and interfacial viscoelastic properties of Pickering emulsions stabilized by AIE-active modified alginate and chitosan complexes. *ACS Sustainable Chemistry & Engineering*, *10*(31), 10275–10285.
29. Douliez, J.-P., Martin, N., Beneyton, T., Eloi, J.-C., Chapel, J.-P., Navailles, L., Baret, J.-C., Mann, S., & Béven, L. (2018). Preparation of swellable hydrogel-containing colloidosomes from aqueous two-phase Pickering emulsion droplets. *Angewandte Chemie International Edition*, *57*(26), 7780–7784.
30. Yang, H., Su, Z., Meng, X., Zhang, X., Kennedy, J. F., & Liu, B. (2020). Fabrication and characterization of Pickering emulsion stabilized by soy protein isolate-chitosan nanoparticles. *Carbohydrate Polymers*, *247*, 116712.
31. Low, L. E., Siva, S. P., Ho, Y. K., Chan, E. S., & Tey, B. T. (2020). Recent advances of characterization techniques for the formation, physical properties and stability of Pickering emulsion. *Advances in Colloid and Interface Science*, *277*, 102117.
32. Zhang, K., Wu, W., Meng, H., Guo, K., & Chen, J. F. (2009). Pickering emulsion polymerization: Preparation of

polystyrene/nano-SiO2 composite microspheres with core-shell structure. *Powder Technology*, *190*(3), 393–400.
33. Ren, G., Zheng, X., Gu, H., Di, W., Wang, Z., Guo, Y., Xu, Z., & Sun, D. (2019). Temperature and CO(2) dual-responsive Pickering emulsions using Jeffamine M2005-modified cellulose nanocrystals. *Langmuir*, *35*(42), 13663–13670.
34. Sarkar, A., Ademuyiwa, V., Stubley, S., Esa, N. H., Goycoolea, F. M., Qin, X., Gonzalez, F., & Olvera, C. (2018). Pickering emulsions co-stabilized by composite protein/polysaccharide particle-particle interfaces: Impact on in vitro gastric stability. *Food Hydrocolloids*, *84*, 282–291.
35. Ruiz, M. P., & Faria, J. A. (2022). Catalysis at the solid–liquid–liquid interface of water–oil Pickering emulsions: A tutorial review. *ACS Engineering Au*, *2*(4), 295–319.
36. Persson, K. H., Blute, I. A., Mira, I. C., & Gustafsson, J. (2014). Creation of well-defined particle stabilized oil-in-water nanoemulsions. *Colloids and Surfaces A: Physicochemical and Engineering Aspects*, *459*, 48–57.
37. Klang, V., Matsko, N. B., Valenta, C., & Hofer, F. (2012). Electron microscopy of nanoemulsions: An essential tool for characterisation and stability assessment. *Micron (Oxford, England: 1993)*, *43*(2-3), 85–103.
38. Xiao, J., Li, Y., & Huang, Q. (2016). Recent advances on food-grade particles stabilized Pickering emulsions: Fabrication, characterization and research trends. *Trends in Food Science & Technology*, *55*, 48–60.
39. Ilett, M., Brydson, R., Brown, A., & Hondow, N. (2019). Cryo-analytical STEM of frozen, aqueous dispersions of nanoparticles. *Micron (Oxford, England: 1993)*, *120*, 35–42.
40. Pfeil-Gardiner, O., Rosa, H. V. D., Riedel, D., Chen, Y. S., Lörks, D., Kükelhan, P., Linck, M., Müller, H., Van Petegem, F., & Murphy, B. J. (2024). Elemental mapping in single-particle reconstructions by reconstructed electron energy-loss analysis. *Nature Methods*, *21*(12), 2299–2306.
41. Wolf, S. G., Mutsafi, Y., Dadosh, T., Ilani, T., Lansky, Z., Horowitz, B., Rubin, S., Elbaum, M., & Fass, D. (2017). 3D visualization of mitochondrial solid-phase calcium stores in whole cells. *Elife*, *6*, e29929.
42. Baumeister, W. (2022). Cryo-electron tomography: A long journey to the inner space of cells. *Cell*, *185*(15), 2649–2652.
43. Midgley, P. A., & Dunin-Borkowski, R. E. (2009). Electron tomography and holography in materials science. *Nature Materials*, *8*(4), 271–280.
44. Peña, F. d. l., Prestat, E., Fauske, V. T., Burdet, P., Furnival, T., Jokubauskas, P., Nord, M., Ostasevicius, T., Lähnemann, J., MacArthur, K. E., Johnstone, D. N., Sarahan, M., Taillon, J., Aarholt, T., Migunov, V., Eljarrat, A., Caron, J., Poon, T., Mazzucco, S., …Donval, G. (2021). *hyperspy/hyperspy: Release v1.6.3*. Zenodo.
45. Schneider, C., Rasband, W., & Eliceiri, K. (2012). NIH to ImageJ: 25 years of image analysis. *Nature Methods*, *9*, 671–675.
46. Jumaa, M., & Müller, B. W. (1998). The effect of oil components and homogenization conditions on the physicochemical properties and stability of parenteral fat emulsions. *International Journal of Pharmaceutics*, *163*(1), 81–89.
47. Welin-Berger, K., & Bergenståhl, B. (2000). Inhibition of Ostwald ripening in local anesthetic emulsions by using hydrophobic excipients in the disperse phase. *International Journal of Pharmaceutics*, *200*(2), 249–260.
48. Egelhaaf, S. U., Schurtenberger, P., & Müller, M. (2000). New controlled environment vitrification system for cryo-transmission electron microscopy: Design and application to surfactant solutions. *Journal of Microscopy*, *200*(2), 128–139.
49. Dieckmann, Y., Cölfen, H., Hofmann, H., & Petri-Fink, A. (2009). Particle size distribution measurements of manganese-doped ZnS nanoparticles. *Analytical Chemistry*, *81*(10), 3889–3895.
50. Roncal-Herrero, T., Micklethwaite, S., Ilett, M., Hitchcock, J., Cayre, O., & Hondow, N. (2019). Analytical cryo electron microscopy for characterization of pickering emulsions. *Microscopy and Microanalysis*, *25*(S2), 1706–1707.
51. Egerton, R. F. (2019). Radiation damage to organic and inorganic specimens in the TEM. *Micron (Oxford, England: 1993)*, *119*, 72–87.
52. Wills, J. W., Summers, H. D., Hondow, N., Sooresh, A., Meissner, K. E., White, P. A., Rees, P., Brown, A., & Doak, S. H. (2017). characterizing nanoparticles in biological matrices: Tipping points in agglomeration state and cellular delivery in vitro. *ACS Nano*, *11*(12), 11986–12000.
53. Dunstone, M. A., & de Marco, A. (2017). Cryo-electron tomography: An ideal method to study membrane-associated proteins. *Philosophical Transactions of the Royal Society of London. Series B: Biological Sciences*, *372*(1726), 20160210.
54. Henderson, L. D., & Beeby, M. (2018). High-throughput electron cryo-tomography of protein complexes and their assembly. In Marsh, J. A. (Ed.) *Protein complex assembly: Methods and protocols* (pp. 29–44). Springer.
55. Migunov, V., Ryll, H., Zhuge, X., Simson, M., Strüder, L., Batenburg, K. J., Houben, L., & Dunin-Borkowski, R. E. (2015). Rapid low dose electron tomography using a direct electron detection camera. *Scientific Reports*, *5*(1), 14516.
56. Ilett, M., Roncal-Herrero, T., Brydson, R., Brown, A., & Hondow, N. (2019). Progress on cryogenic analytical STEM of nanomaterials. *Microscopy and Microanalysis*, *25*(S2), 1086–1087.
57. Fernandez, J.-J. (2012). Computational methods for electron tomography. *Micron (Oxford, England: 1993)*, *43*(10), 1010–1030.
58. McEwen, B. F., Downing, K. H., & Glaeser, R. M. (1995). The relevance of dose-fractionation in tomography of radiation-sensitive specimens. *Ultramicroscopy*, *60*(3), 357–373.
59. Koster, A. J., Grimm, R., Typke, D., Hegerl, R., Stoschek, A., Walz, J., & Baumeister, W. (1997). Perspectives of molecular and cellular electron tomography. *Journal of Structural Biology*, *120*(3), 276–308.
60. Yan, R., Edwards, T. J., Pankratz, L. M., Kuhn, R. J., Lanman, J. K., Liu, J., & Jiang, W. (2015). Simultaneous determination of sample thickness, tilt, and electron mean free path using tomographic tilt images based on Beer-Lambert law. *Journal of Structural Biology*, *192*(2), 287–296.
61. Dobro, M. J., Melanson, L. A., Jensen, G. J., & McDowall, A. W. (2010). Chapter three—Plunge freezing for electron cryomicroscopy. In Jensen, G. J. (Ed.) *Methods in enzymology* (Vol. 481, pp. 63–82). Academic Press.
62. Glaeser, R. M., Downing, K., DeRosier, D., Chiu, W., & Frank, J. (2007). *Electron crystallography of biological macromolecules*. Oxford University Press.

63. Turk, M., & Baumeister, W. (2020). The promise and the challenges of cryo-electron tomography. *Febs Letters*, *594*(20), 3243–3261.
64. Schwartz, J., Harris, C., Pietryga, J., Zheng, H., Kumar, P., Visheratina, A., Kotov, N. A., Major, B., Avery, P., Ercius, P., Ayachit, U., Geveci, B., Muller, D. A., Genova, A., Jiang, Y., Hanwell, M., & Hovden, R. (2022). Real-time 3D analysis during electron tomography using tomviz. *Nature Communications*, *13*(1), 4458.
65. Levin, B. D. A. (2021). Direct detectors and their applications in electron microscopy for materials science. *Journal of Physics: Materials*, *4*(4), 042005.
66. Hart, J. L., Lang, A. C., Leff, A. C., Longo, P., Trevor, C., Twesten, R. D., & Taheri, M. L. (2017). Direct detection electron energy-loss spectroscopy: A method to push the limits of resolution and sensitivity. *Scientific Reports*, *7*(1), 8243.
67. Kelley, K., Raczkowski, A. M., Klykov, O., Jaroenlak, P., Bobe, D., Kopylov, M., Eng, E. T., Bhabha, G., Potter, C. S., Carragher, B., & Noble, A. J. (2022). Waffle Method: A general and flexible approach for improving throughput in FIB-milling. *Nature Communications*, *13*(1), 1857.
68. Rigort, A., & Plitzko, J. M. (2015). Cryo-focused-ion-beam applications in structural biology. *Archives of Biochemistry and Biophysics*, *581*, 122–130.

## SUPPORTING INFORMATION

Additional supporting information can be found online in the Supporting Information section at the end of this article.

**How to cite this article:** Fernandez Ainaga, D. L., Roncal-Herrero, T., Ilett, M., Aslam, Z., Cheng, C., Hitchcock, J. P., Cayre, O. J., & Hondow, N. (2025). Native state structural and chemical characterisation of Pickering emulsions: A cryo-electron microscopy study. *Journal of Microscopy*, *298*, 92–105. https://doi.org/10.1111/jmi.13391

# Appendix B

ACS APPLIED NANO MATERIALS

www.acsanm.org Article

## Polyvalent Glycan Functionalized Quantum Nanorods as Mechanistic Probes for Shape-Selective Multivalent Lectin-Glycan Recognition

James Hooper, Darshita Budhadev, Dario Luis Fernandez Ainaga, Nicole Hondow, Dejian Zhou,* and Yuan Guo*

Cite This: ACS Appl. Nano Mater. 2023, 6, 4201−4213 Read Online

ACCESS | Metrics & More | Article Recommendations | Supporting Information



**ABSTRACT:** Multivalent lectin-glycan interactions (MLGIs) are widespread in biology and hold the key to many therapeutic applications. However, the underlying structural and biophysical mechanisms for many MLGIs remain poorly understood, limiting our ability to design glycoconjugates to potently target specific MLGIs for therapeutic intervention. Glycosylated nanoparticles have emerged as a powerful biophysical probe for MLGIs, although how nanoparticle shape affects the MLGI molecular mechanisms remains largely unexplored. Herein, we have prepared fluorescent quantum nanorods (QRs), densely coated with $\alpha$-1,2-manno-biose ligands (QR-DiMan), as multifunctional probes to investigate how scaffold geometry affects the MLGIs of a pair of closely related, tetrameric viral receptors, DC-SIGN and DC-SIGNR. We have previously shown that a DiMan-capped spherical quantum dot (QD-DiMan) gives weak cross-linking interactions with DC-SIGNR but strong simultaneous binding with DC-SIGN. Against the elongated QR-DiMan, DC-SIGN retains similarly strong simultaneous binding of all four binding sites with a single QR-DiMan (apparent $K_d \approx 0.5$ nM, ~1.8 million-fold stronger than the corresponding monovalent binding), while DC-SIGNR gives both weak cross-linking and strong individual binding interactions, resulting in a larger binding affinity enhancement than that with QD-DiMan. S/TEM analysis of QR-DiMan-lectin assemblies reveals that DC-SIGNR's different binding modes arise from the different nanosurface curvatures of the QR scaffold. The glycan display at the spherical ends presents too high a steric barrier for DC-SIGNR to bind with all four binding sites; thus, it cross-links between two QR-DiMan to maximize binding multivalency, whereas the more planar character of the cylindrical center allows the glycans to bridge all binding sites in DC-SIGNR. This work thus establishes glycosylated QRs as a powerful biophysical probe for MLGIs not only to provide quantitative binding affinities and binding modes but also to demonstrate the specificity of multivalent lectins in discriminating different glycan displays in solution, dictated by the scaffold curvature.

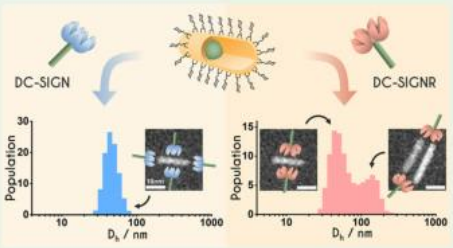


**KEYWORDS:** *multivalent interaction, quantum rod, glycoconjugate, geometry, FRET, electron microscopy*

## INTRODUCTION

Research into the effects of nanomaterial surface chemistry and scaffold design in biology has led not only to key advances in the ever-growing field of nanomedicine but also to the discovery of novel tools to answer important biological questions.[1−4] The exploration of fine-tuning nanoparticle chemistry to achieve biological functionality has been extensively investigated for over four decades; however, the study of a nanoparticle's geometric design elements, such as size and shape, and their mechanistic influences in biology remains in its infancy. Though some studies have shown that varying nanoparticle size and shape can have a strong effect on various biological processes such as cell uptake,[5−7] endocytic pathways,[8−10] cytokine/antibody production,[8,11−14] or pathogen inhibition,[15−17] the relationship between nanoparticle geometry and biological function remains a fairly underexplored topic for a lot of processes. Moreover, often little has been done to elucidate the specific mechanistic differences caused by shape variation at the molecular level, such as binding affinities or binding modes, which are essential for identifying how nanomedicines work and, perhaps more importantly, for guiding the design of more effective therapeutics.

Received: December 6, 2022
Accepted: February 24, 2023
Published: March 14, 2023





https://doi.org/10.1021/acsanm.2c05247
ACS Appl. Nano Mater. 2023, 6, 4201−4213

Multivalent lectin-glycan interactions (MLGIs) are widespread and play a pivotal role in pathogen infection, immune regulation, and cell−cell communication.[18] It is thus unsurprising that glycan-displaying nanomaterials have been widely exploited for potential antiviral and immuno-therapeutic applications due to simple polyvalent glycan functionalization. For glyconanomaterials, the geometric parameters, such as size and shape of nano-scaffolds, inevitably affect their surface glycan display. As natural lectins are often multimeric, variations in glycan display may lead to changes in the number of binding sites that can be occupied at one time, which dictates the strength and mode of lectin-glycan binding and, subsequently, biological function. A large number of glyco-nano-scaffolds with different geometries have been employed to target lectins. These include spherical scaffolds (e.g., inorganic nanoparticles, fullerenes, dendrimers, hyperbranched polymers, polymersomes, etc.),[19−29] tubular/rod-shaped structures (e.g., gold nanorods, carbon nanotubes, and cylindrical micelles),[7,17,30−33] planar sheets (e.g., graphene nanosheets),[32,34] and structures that are less well-defined (e.g., linear polymers)[16,35−39] or more complex in shape.[7,33,40−42] Since these results are obtained with scaffolds of different glycan composition, softness, size, shape, and glycan density, it is difficult to directly compare results from one another to draw general conclusions. While studies have shown that the scaffold size and shape can affect their lectin binding and pathogen inhibition properties,[7,8,15−17,31,33,43] the molecular mechanisms underlying such differences remain unclear. For example, Kikkeri's group found that, among three differently shaped mannosylated gold nanoparticles (e.g., spheres, stars, and rods), gold nanorods consistently exhibited stronger bacterial binding than the other two shapes, although no characterization of the molecular mechanisms behind such differences was presented.[7,17,33] Consequently, new tools are needed in order to identify the rationales behind these differences, allowing us to better understand the molecular mechanisms of shape dependency for such interactions. In this regard, probes that can reveal how scaffold shape affects MLGI binding mode and affinity are highly valuable, allowing us to establish a geometric design rule for glycan-nanoparticles for potent and specific targeting of MLGIs for therapeutic application.

We have recently developed densely glycosylated fluorescent quantum dots (glycan-QDs) as new mechanistic probes for MLGIs.[21,22] These glycan-QDs were able to not only quantify MLGI affinity *via* a ratiometric QD-sensitized dye Förster resonance energy transfer (FRET) readout but also dissect the exact binding modes and affinity enhancing mechanisms of MLGIs *via* hydrodynamic size analysis and STEM imaging of lectin binding-induced glycan-QD assemblies.[21,22] Here, two closely related, immunologically important tetrameric glycan-binding viral receptors, DC-SIGN and DC-SIGNR (collectively denoted as DC-SIGN/R hereafter),[44,45] were used as model lectins due to their differences in viral transmitting properties despite sharing 77% amino acid identity, the same tetrameric architecture and identical monovalent mannose-binding motifs.[46] Using QDs bearing $\alpha$-1,2-manno-biose (DiMan)-glycans (QD-DiMan) as probes, we were able to extract key structural and mechanistic information for DC-SIGN/R related MLGIs. We revealed that, although both lectins bound multivalently with QD-DiMan, it was achieved through different binding modes, resulting in very different affinities. DC-SIGN was found to simultaneously bind to the same QD-DiMan with all four carbohydrate-recognition domains (CRDs), giving rise to strong binding (apparent equilibrium binding dissociation constant, $K_d$, 2.1 ± 0.5 nM). However, DC-SIGNR was found to cross-link between QD-DiMan particles, with a much weaker affinity ($K_d \approx 633$ nM, ~300-fold weaker than that of DC-SIGN).[21] Additionally, DC-SIGN binding, monitored *via* FRET, was detected at very low protein-to-QD molar ratios (PQRs) and increased linearly with the PQR till the QD surface was fully saturated with protein. However, for DC-SIGNR, due to the low affinity and cross-linking binding nature, saturation occurred at a much higher PQR and significant binding was only observed as the PQR was increased above a certain threshold.

Compared to spherical QDs, the elongated quantum nanorods (QRs) have a higher extinction coefficient and single particle brightness, which is highly beneficial for fluorescence-based applications.[47−49] Moreover, its optical properties can be tuned by changing not only the particle size but also the aspect (length-to-width) ratio. This feature can be highly beneficial for some applications, e.g., bioluminescence resonance energy transfer (BRET), where an aspect ratio of 3 has been shown to give the highest BRET efficiency.[50,51] Furthermore, the distinct curvatures between the central cylindrical section and spherical ends make the QR an excellent platform for studying how scaffold geometry controls MLGI properties by displaying glycans polyvalently on the QR. For such glycan-QRs, the glycan displays at the ends will closely resemble those of spherical glycan-QDs, whereas, in the middle, the glycans will be presented more like a curved plane wrapped around the center of the nanorod. Therefore, each glycan-QR presents two distinct glycan displays, allowing us to probe their different effects on MLGIs using the same glycan-nanoparticle.

Here, we have densely coated a CdSe/CdS based QR with DHLA-$EG_{11}$-DiMan ligands to make the first glycan-QR probe for analyzing the shape dependency of DC-SIGN/R-related MLGIs at the molecular level in solution (Figure 1). By

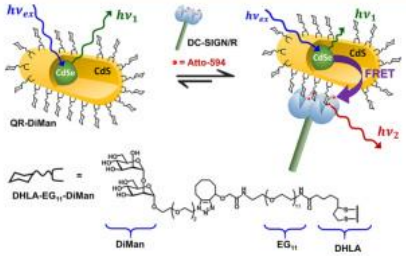


**Figure 1.** Schematic depicting the FRET readout for binding of an excited QR scaffold capped with DHLA-$EG_{11}$-DiMan ligands (chemical structure depicted beneath) with DC-SIGN labeled with an Atto-594 dye molecule.

developing a QR-FRET-based ratiometric MLGI affinity readout, together with hydrodynamic size and S/TEM analysis of lectin binding-induced QR assemblies, we show that the distinct glycan display curvatures of QR-DiMan can effectively discriminate MLGI properties between DC-SIGN and DC-SIGNR. DC-SIGN binds strongly and simultaneously to one QR-DiMan regardless of surface curvature with sub-nM $K_d$, comparable to that of QD-DiMan. In contrast, DC-SIGNR



https://doi.org/10.1021/acsanm.2c05247
ACS Appl. Nano Mater. 2023, 6, 4201−4213

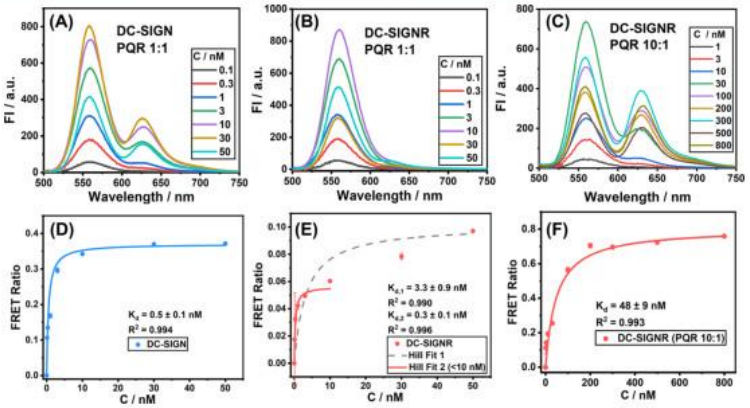


**Figure 2.** Direct excitation background-corrected fluorescence spectra of varying concentrations of QR-DiMan after binding with (A) DC-SIGN (PQR = 1), (B) DC-SIGNR (PQR = 1), or (C) DC-SIGNR (PQR = 10). The corresponding FRET ratio−concentration ($C$) relationships and Hill fits (eq 1) for QR-DiMan binding with (D) DC-SIGN (PQR = 1), (E) DC-SIGNR (PQR = 1), or (F) DC-SIGNR (PQR = 10). (Fitting parameters are summarized in Table 1; $R^2 \geq 0.99$).

binds simultaneously to the glycans displayed on the central cylindrical section of the same QR but cross-links between glycans displayed on the spherical ends of different QRs. Thus, the QR's unique geometry and its strong fluorescence and high electron microscopy contrast have allowed us to reveal how glycan-nanoparticle surface curvature affects the solution-phase binding mechanisms of target MLGIs at the molecular level.

## ■ RESULTS AND DISCUSSION

**QR-DiMan Preparation and Characterization.** A CdSe/CdS core/shell (dot in a rod) QR with maximal emission at $\lambda_{EM} \sim 560$ nm (denoted as $QR_{560}$ hereafter) was chosen to construct the QR-DiMan *via* our previously described ligand conjugation method.[53] $QR_{560}$ was chosen due to its similar core diameter to the QD scaffolds used in our previous study,[21] allowing for direct comparison of results. A dihydrolipoic acid-undeca(ethylene glycol)-$\alpha$-1,2-manno-biose (DHLA-$EG_{11}$-DiMan; Figure 1; SI, Section 2.1)-based multifunctional ligand was synthesized as described previously.[21] Each ligand contains three unique functional domains: a DHLA group for strong QR surface anchoring,[53] a flexible $EG_{11}$ linker for imposing high water solubility, stability, and resisting non-specific interactions,[54,55] and a terminal DiMan group for specific lectin binding. QR-DiMan was produced by performing cap-exchange using a deprotonated DHLA-$EG_{11}$-DiMan ligand in a homogeneous $CHCl_3$/MeOH/EtOH solution, giving rise to high cap-exchange efficiency as described previously for QD-DiMan.[21,56] QR-DiMan was found to be relatively compact, with a mean hydrodynamic diameter ($D_h$) of 20.8 ± 4.8 nm, obtained by DLS, and a mean core length and diameter of 14.7 ± 5.7 and 3.1 ± 0.7 nm, respectively, obtained by S/TEM imaging (see SI, Figure S14; all size data reported here are mean ± 1/2 full width half maximum, FWHM). The first excitonic absorption and emission peaks were observed at 541 and 560 nm, respectively, and the fluorescence quantum yield (QY) was determined as 6.2%. This represents a significant reduction from its nominal QY of ∼68% prior to cap-exchange. This result agrees well with the literature: CdSe/CdS-based QDs and QRs have shown to display significantly reduced fluorescence QY after cap-exchange.[46,49] By calculating the difference between the amount of ligand added and that which remained in the supernatant post cap-exchange, *via* phenol-sulfuric acid carbohydrate quantification, the number of DHLA-$EG_{11}$-DiMan ligands capped on each QR was estimated as 370 ± 30 (see SI, Section 2.2).[20−22]

**Binding Affinity Determination *via* FRET.** The QR's strong fluorescence was exploited as a ratiometric FRET readout to quantify the binding affinity between QR-DiMan and acceptor fluorophore-labeled DC-SIGN/R. Lectin labeling was achieved by coupling a maleimide-Atto-594 dye *via* the site-specifically introduced Q274C and R287C mutations in DC-SIGN and DC-SIGNR, respectively. These labeling sites lie close to, but not in, the glycan binding pockets, enabling us to obtain sufficient FRET signals without inhibiting the lectins' glycan binding properties, as confirmed previously.[21,22,57] The QR-Atto-594 FRET pair has good spectral overlap and a respectable Förster radius $R_0$ of 4.8 nm (see SI, Section 2.3), ensuring that efficient FRET between QR-DiMan and labeled lectins can happen upon binding. Meanwhile, there is little overlap of their emission spectra, allowing for straightforward separation of the donor and acceptor fluorescence without the need of spectral deconvolution.[57]

The affinity assays were carried out by mixing QR-DiMan with labeled lectins under different concentrations but under a fixed protein−QR molar ratio (PQR) of 1:1 in a binding buffer (20 mM HEPES, 100 mM NaCl, 10 mM $CaCl_2$, pH 7.8, containing 1 mg/mL bovine serum albumin to reduce non-specific adsorption). The resulting fluorescence spectra were recorded using a fixed excitation wavelength ($\lambda_{EX}$) of 450 nm, corresponding to the absorption minimum of the Atto-594 acceptor to reduce the dye direct excitation background. Exciting an equilibrated mixture of QR-DiMan with labeled lectins resulted in fluorescence of unbound QR (peaking at ∼559 nm) or, if binding occurred, energy transfer *via* FRET from the excited QR donor to the Atto-594 acceptor, giving rise to simultaneously quenched QR and enhanced Atto-594



https://doi.org/10.1021/acsanm.2c05247
ACS Appl. Nano Mater. 2023, 6, 4201−4213

**Table 1. Summary of Fitting Parameters Obtained from the FRET Ratio−Concentration Relationship for QR-DiMan Binding with DC-SIGN and DC-SIGNR ($R^2$ > 0.99 for All Fits)**

| protein | PQR | $F_{max}$ | $K_d^{QR}$ (nM) | $\beta^a$ | $\frac{\beta}{N}$ | $K_d^{QD\,b}$ | $K_d^{QD}/K_d^{QR\,b}$ |
|---|---|---|---|---|---|---|---|
| DC-SIGN | 1:1 | 0.37 ± 0.01 | 0.5 ± 0.1 | ~1,800,000 | ~4900 | 2.1 ± 0.5 | 4 |
| DC-SIGNR | 1:1[c] | 0.056 ± 0.003 | 0.3 ± 0.1 | ~3,000,000 | ~8100 | 633 ± 77 | 2110 |
| | 1:10 | 0.80 ± 0.03 | 48 ± 9 | ~19,000 | ~51 | | 13 |

[a]$\beta$ is the enhancement factor over the monovalent interaction (i.e., $K_d^{mono}/K_d^{QR}$), $K_d^{mono}$ = 0.9 mM for CRD-DiMan binding.[52] [b]$K_d^{QD}$ is the equilibrium binding dissociation constant between QD-DiMan and DC-SIGN (PQR 1:1) or DC-SIGNR (PQR 10:1), as reported previously.[21] $K_d^{QD}/K_d^{QR}$ signifies the enhancement in $K_d$ for the binding of QR-DiMan over that of QD-DiMan. [c]Only low concentration data points of ≤10 nM are included in the fit.

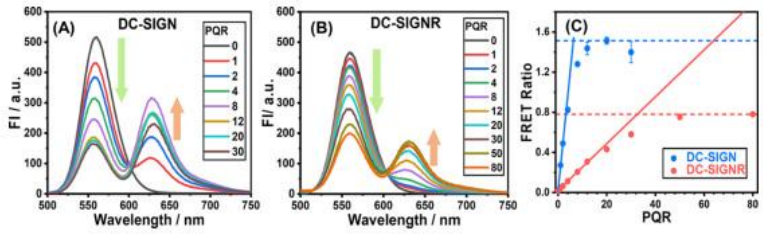


**Figure 3.** Direct excitation background-corrected fluorescence spectra corresponding to titration of (A) DC-SIGN or (B) DC-SIGNR against a fixed concentration of QR-DiMan (10 nM). (C) Plots of the corresponding FRET ratio−PQR relationships fitted with linear fits of the initial PQR data points (solid line; PQR ≤ 4 or 12 for DC-SIGN and DC-SIGNR, respectively). The fits give intercept = 0.018 ± 0.002 and 0.0194 ± 0.0006 and slope = 0.24 ± 0.01 and 0.0234 ± 0.0002 for DC-SIGN and DC-SIGNR, respectively ($R^2$ ≥ 0.99 for all fits). The intercept between the data set maxima (dotted line) and the linear fits for each protein were used to obtain the "apparent" PQRs required to achieve saturated QR binding (6.2 ± 0.3 and 32.5 ± 0.4 for DC-SIGN and DC-SIGNR, respectively).

fluorescence (at ~627 nm, Figure 1). These fluorescence spectra were corrected by subtracting dye direct excitation background spectra of the labeled lectins, without QR-DiMan, under identical conditions (Figure 2A−C). The resulting dye-to-QR fluorescence intensity ratio (apparent FRET ratio)−concentration relationship was then fitted by the Hill equation to extract the apparent binding $K_d$ values (eq 1; where $F$ is the FRET ratio, $I$ is the peak emission intensity, [P] is the protein concentration, $n$ is the Hill coefficient, and $K_d$ is the apparent equilibrium binding dissociation constant).[21,57] Here, $n$ = 1 was assumed because most binding assays were measured under a PQR of 1:1, under which most QRs should be bound by just a single lectin, and hence there should be no positive or negative influence of QR-bound lectins toward further binding of lectins to the same QR-DiMan. As the FRET ratio is proportional to the fraction of protein bound to the QR under a fixed PQR of 1:1,[21] this method is robust and can provide accurate affinity measurement of both strong and weak MLGIs.[57]

$$F = \frac{I_{dye}}{I_{QR}} = F_{max} \times \frac{[P]_{bound}}{[P]_{total}} = F_{max} \times \frac{[P]^n}{K_d^{\,n} + [P]^n} \quad (1)$$

The FRET ratio−concentration relationship for DC-SIGN binding with QR-DiMan was fitted very nicely ($R^2$ > 0.99) by the Hill equation and revealed a $K_d$ of 0.5 ± 0.1 nM at a PQR of 1:1 (Figure 2D; Table 1). This represents a massive 1.8 million-fold enhancement of affinity ($\beta$) over the corresponding DiMan-CRD monovalent binding ($K_d$ = 0.9 mM) and a per-glycan-normalized affinity enhancement ($\beta/N$) of ~4900 (Table 1).[52] Interestingly, this affinity is ~4-fold as strong as that of QD-DiMan·DC-SIGN binding, studied previously ($K_d$ = 2.1 ± 0.5 nM).[21] The sub-nanomolar $K_d$, here, demonstrates the high suitability of QR-DiMan for potent DC-SIGN targeting. The difference in affinity between QR-DiMan and QD-DiMan in DC-SIGN binding could be due to subtle changes in the inter-glycan distances and/or glycan display curvatures, allowing the former to have better spatial and/or orientation match with DC-SIGN's four binding sites to form stronger binding than the latter.

The FRET ratio for DC-SIGNR binding is considerably lower than that of DC-SIGN at PQR = 1 under equivalent conditions, implying a weaker binding compared to the former. This result is fully consistent with that of DC-SIGN/R binding with QD-DiMan reported previously.[16] The overall FRET ratio−concentration relationship for DC-SIGNR binding with QR-DiMan could be fitted by the Hill equation ($R^2$ = 0.990), giving an apparent $K_d$ of 3.3 ± 0.9 nM (gray broken line), although several data points were found to deviate considerably from the fitting curve (Figure 2E). The resulting FRET ratio−concentration relationship appeared to display biphasic binding behavior, where the concentration dependency of the FRET ratio exhibits a secondary increase at higher concentrations. By fitting only the first few data points at the low concentration range (i.e., ≤ 10 nM), a good fit ($R^2$ > 0.996) with an apparent $K_d$ of 0.3 ± 0.1 nM was obtained (Figure 2E). This $K_d$ value is comparable to that of DC-SIGN, suggesting that a similar interaction is taking place, likely involving the same degree of binding multivalency (e.g., binding of all four CRDs to the same QR-DiMan). The appearance of the broader (slower increasing signal) secondary binding phase suggests that further binding can occur with the increasing concentration *via* a relatively weak binding interaction. This may indicate the formation of cross-linking



https://doi.org/10.1021/acsanm.2c05247
ACS Appl. Nano Mater. 2023, 6, 4201−4213

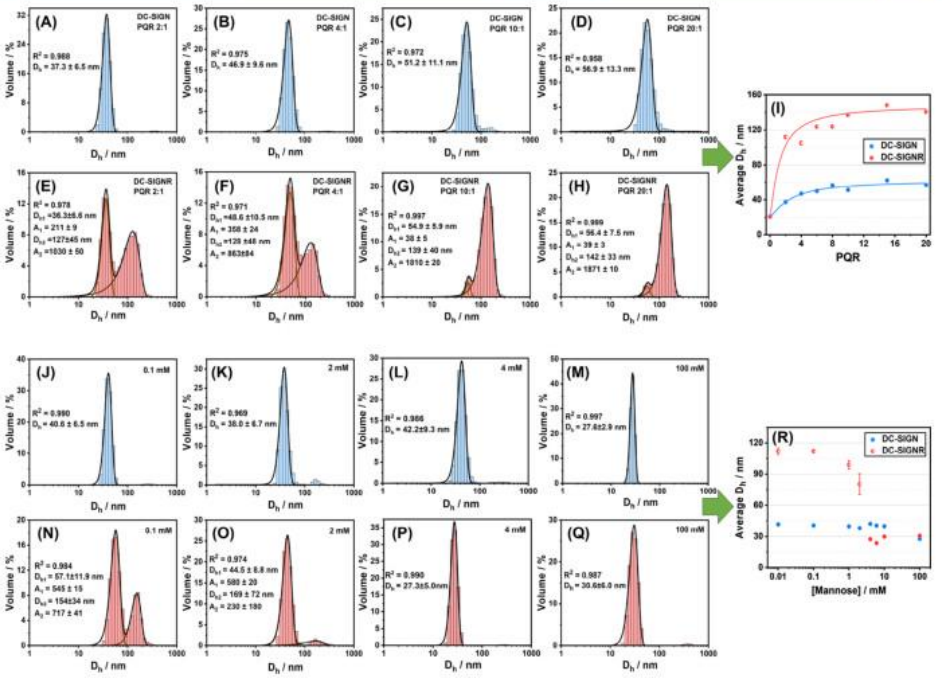

**Figure 4.** $D_h$ distribution histograms of 10 nM QR-DiMan after binding with DC-SIGN at PQRs of (A) 2:1, (B) 4:1, (C) 10:1, and (D) 20:1 or binding with DC-SIGNR at PQRs of (E) 2:1, (F) 4:1, (G) 10:1, and (H) 20:1; a pre-incubated mixture of 10 nM QR-DiMan with 40 nM DC-SIGN after addition of free mannose at concentrations of (J) 0.1, (K) 2, (L) 4, or (M) 100 mM; and a pre-incubated mixture of 10 nM QR-DiMan with 40 nM DC-SIGNR after addition of free mannose at concentrations of (N) 0.1, (O) 2, (P) 4, and (Q) 100 mM. Data were fitted with Gaussian function, and the $D_h$ values are given as mean ± 1/2 FWHM. (I) The corresponding average $D_h$–PQR relationship (average $D_h = D_{h,1} \times A_1\ \% + D_{h,2} \times A_2\ \%$ , where $A_1$% and $A_2$% are the percentage area of the Gaussian fits; filled circles: single distribution; half-filled circles: two distributions) fitted with an offset Hill function ($D_{h,\,PQR} = D_{h,0} + (D_{h,\,\infty} - D_{h,0})/(1 + (PQR_{50}/PQR)^n)$) where $D_{h,0}$ was fixed to the $D_h$ of QR-DiMan, $D_{h,\,\infty} = 62 \pm 6$ and $150 \pm 10$ nm, $PQR_{50}$ (PQR at 50% of $D_{h,\,\infty}$) = $2.7 \pm 0.8$ and $1.3 \pm 1$, and $n = 1.3 \pm 0.4$ and $1 \pm 1$, for DC-SIGN and DC-SIGNR, respectively; $R^2 \geq 0.99$). (R) Plot of the average $D_h$ against the free mannose concentration for QR-DiMan pre-incubated with DC-SIGN/R at PQR of 4:1. (DC-SIGN: blue; DC-SIGNR: red).

between QR-DiMan·DC-SIGNR assemblies, in a similar binding mode to that observed previously with QDs.

In order to obtain a more accurate overall binding affinity between DC-SIGNR and QR-DiMan, the binding assay was performed using a PQR of 10:1, which significantly improved the FRET signals (Figure 2C). Fitting the resulting FRET ratio−concentration relationship using eq 1 gave an apparent binding $K_d$ of 48 ± 9 nM (Figure 2F), which is ∼13-fold stronger than that of the QD-DiMan·DC-SIGNR binding under equivalent conditions ($K_d$ = ∼633 nM, PQR = 10).[21] The binding affinity enhancement for DC-SIGNR is more substantial than that for DC-SIGN, which is likely due to the presence of the additional high affinity 1:1 binding component observed with DC-SIGNR under a PQR of 1.

**Binding Mode Determination *via* FRET and Hydrodynamic Size Analysis.** In order to more empirically establish the binding modes between the two lectins and QR-DiMan, the effect of titrating protein against a fixed concentration of QR was analyzed using FRET and hydrodynamic size analysis. Binding of both lectins with QR-DiMan yielded an initial linear increase in the FRET ratio with an increasing PQR before reaching saturation (Figure 3). This behavior is similar to that observed previously for DC SIGN binding with QD-DiMan but is very different from the binding of DC-SIGNR with QD-DiMan, which displays a sigmoidal relationship with very little binding occurring at the low PQRs.[21] This difference agrees with the aforementioned observation that a significant amount of strong affinity, higher order multivalency complexes are established for QR-DiMan·DC-SIGNR complexation, allowing significant binding to occur even at these lower PQRs. By fitting the linear region of the FRET ratio−PQR relationship and taking the intersection with the maximum recorded FRET ratio (Figure 3C), the "apparent" PQRs required to achieve saturated QR binding (i.e., maximal FRET ratio) are estimated as ∼6 for DC-SIGN and ∼33 for DC-SIGNR. Please note that these values do not represent the actual number of lectins that are bound to each QR-DiMan but, rather, the number of lectins



https://doi.org/10.1021/acsanm.2c05247
ACS Appl. Nano Mater. 2023, 6, 4201−4213

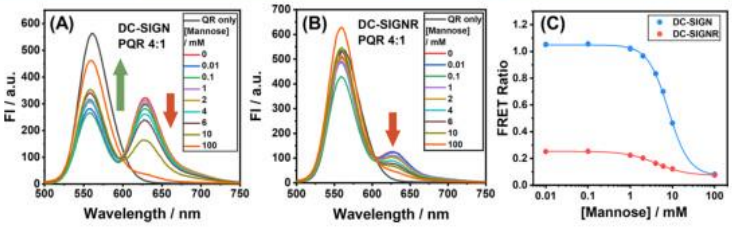


**Figure 5.** Direct excitation background corrected fluorescence spectra corresponding to increasing concentrations of free mannose ([Mannose]) to a pre-incubated 4:1 PQR mixture of 10 nM QR-DiMan with (A) DC-SIGN or (B) DC-SIGNR. (C) Plot of the relationship between the FRET ratio against the mannose concentration for the fluorescence spectra recorded in (A) and (B) fitted with an offset Hill function (eq 2; where $F_0$ = 1.049 ± 0.007 and 0.253 ± 0.001, $F_\infty$ = 0.071 ± 0.003 and 0.072 ± 0.003, $K_i$ (mannose concentration to give 50% inhibition) = 8.0 ± 0.1 and 4.2 ± 0.2 mM, and $n$ = 1.78 ± 0.05 and 1.21 ± 0.08 for DC-SIGN (blue) and DC-SIGNR (red), respectively; $R^2$ > 0.999 for both fits).

per QR required to achieve saturate binding because not all added lectins will be able to bind to the QR under the natural association/dissociation equilibrium. As the overall binding affinity of QR-DiMan with DC-SIGNR is significantly weaker than that with DC-SIGN, the proportion of added DC-SIGNR molecules that are bound to the QR would be considerably lower than that for DC-SIGN. In addition, it is also worth noting that these values are likely to be smaller than the "true" PQR required to achieve saturated protein coverage of QR. This is because, according to our previous energy-dispersive X-ray spectroscopy mapping, the CdSe fluorescent core is situated at the center of the QR.[53] Thus, only lectins bound within proximity of the central region will be close enough to engage in FRET due to the inverse sixth power dependency of the FRET efficiency to the distance between the donor and acceptor.[58]

The binding modes of the two proteins with QR-DiMan were further probed by analyzing the hydrodynamic diameters ($D_h$) of the resulting QR-lectin complexes. The apparent $D_h$ values were obtained from Gaussian fits of the $D_h$ distribution histograms over a PQR range of 0−20. For QR-DiMan·DC-SIGN complexation, only a single size distribution is observed, which plateaus at ∼60 nm after a PQR of ∼6 (Figure 4A−D,I). This value is approximately equal to the summation of the $D_h$ values of a single QR-DiMan flanked by two proteins (where QR-DiMan and DC-SIGN demonstrate individual $D_h$ values of ∼21 and ∼18 nm, respectively). This size is therefore likely to be representative of a monolayer of lectin with all CRDs simultaneously specifically bound to a single QR-DiMan particle. QR-DiMan·DC-SIGNR complexation, on the other hand, demonstrates two distinct size distributions (Figure 4E−H): one that plateaus at ∼60 nm, which matches well with that of DC-SIGN complexation, and another that plateaus at ∼140 nm. The similarity in $D_h$ values between the smaller size peak in DC-SIGNR and that observed for DC-SIGN evidently confirms the presence of simultaneous binding in DC-SIGNR. Meanwhile, the larger size distribution with DC-SIGNR is indicative of the formation of cross-linked clusters, similar to that observed previously with QDs, although the size here is somewhat smaller.[21] Fitting the average $D_h$ (weighted with respect to their integrated areas) against PQR using an offset Hill function (see Figure 4I), it is observed that the average $D_h$ plateaus at 62 ± 6 and 150 ± 10 nm for DC-SIGN and DC-SIGNR, respectively. This demonstrates that the number of DC-SIGNR clustered particles tends to increase with an increasing PQR. This result provides further evidence that the high affinity interaction observed at low concentrations for DC-SIGNR does indeed correlate with the simultaneous binding mode and the weaker affinity binding correlates with an increase in cross-linked binding at the higher PQRs. The fact that the weaker cross-linking binding mode appears to dominate, rather than being displaced, by the stronger simultaneous binding interaction at higher concentrations suggests that these two binding modes may occur at different regions of the QR.

To confirm the binding affinity-mode relationship, free D-mannose was added to compete for pre-formed QR-DiMan·DC-SIGN/R complexes prepared under a PQR of 4:1. DLS analysis showed that the amount of clustered QR-DiMan·DC-SIGNR species was decreased even with addition of just 0.1 mM mannose (Figure 4N; Figure S11B). This is a clear indication that the cross-linked clusters correspond to the weaker binding mode, which is more easily displaced than the stronger simultaneous binding. The average $D_h$ of the smaller species was also reduced to ∼30 nm with ≥4 mM mannose (Figure 4P), along with the complete disappearance of the clustered species, indicating the eventual breakdown of both binding modes. Moreover, addition of mannose to QR-DiMan·DC-SIGN/R complexes also led to a significant, dose-dependent reduction in FRET ratio (Figure 5), indicated by the simultaneous reduction of dye fluorescence and recovery of QR fluorescence. These results are fully consistent with free mannose-induced lectin·glycan-QR complex dissociation. The FRET ratio change with the mannose concentration ([Mannose]) was then fitted with an offset Hill equation to obtain the apparent-inhibition constant ($K_i$), which represents the "apparent" concentration of mannose required to inhibit binding by 50% (eq 2; where $F$ is the FRET ratio at a particular mannose concentration and $n$ represents the Hill coefficient; Figure 5C; see Figure S6 for the normalized plot).

$$F = F_0 + \frac{(F_\infty - F_0)}{1 + \left(\frac{K_i}{[\text{Mannose}]}\right)^n} \quad (2)$$

Here, an FRET minimum of ∼0.07 is observed at high mannose concentrations for both proteins. This may result from a small amount of clustering induced by high amounts of mannose, observable by the hydrodynamic size at similar concentrations (i.e., ∼30 nm, see Figure 4M,Q, *vs* ∼20 nm for unbound QR-DiMan). The apparent-$K_i$ values for DC-SIGN and DC-SIGNR were estimated as 8.0 ± 0.1 and 4.2 ± 0.2 mM, respectively. The higher $K_i$ value for DC-SIGN is a



https://doi.org/10.1021/acsanm.2c05247
ACS Appl. Nano Mater. 2023, 6, 4201−4213

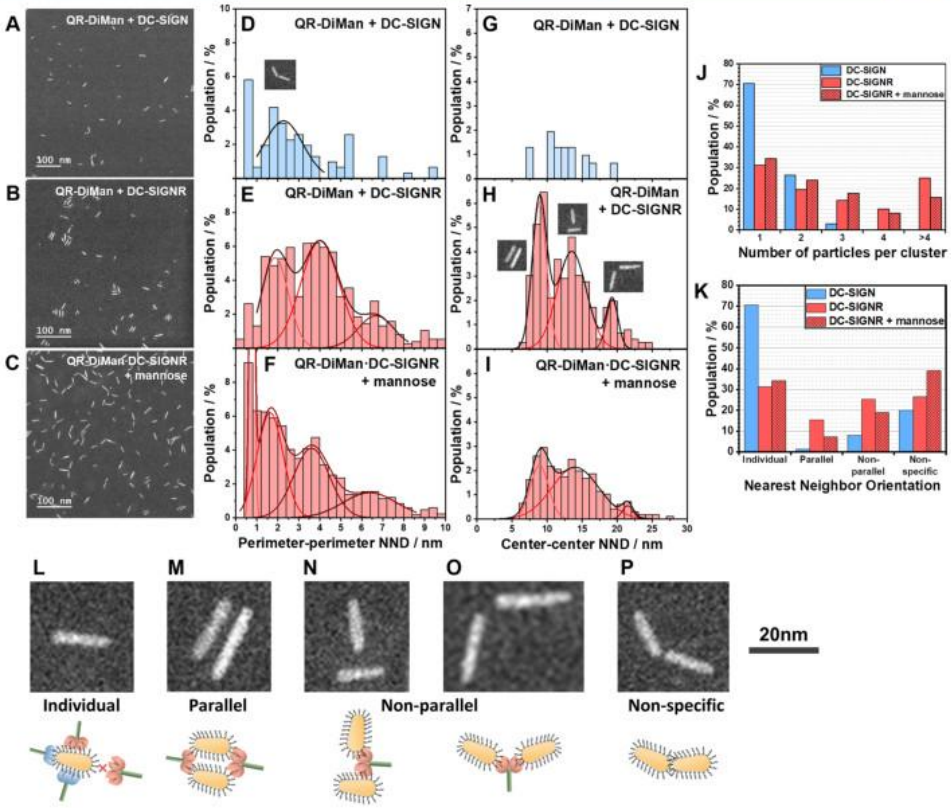


**Figure 6.** S/TEM images of cryo-prepared QR-DiMan (10 nM) after complexation with 4 molar equivalent of (A) DC-SIGN, (B) DC-SIGNR, and (C) DC-SIGNR in the presence of 2 mM mannose. Histograms of the ppNND, fitted with uni- or multimodal Gaussian fits, for QR-DiMan incubated with (D) DC-SIGN or (E) DC-SIGNR or (F) pre-incubated QR-DiMan·DC-SIGNR with 2 mM mannose. Histograms of the center−center nearest neighbor distances (ccNNDs, for 2.9 < ppNND < 7.7 nm), fitted with trimodal Gaussian fits (where applicable), for QR-DiMan incubated with (G) DC-SIGN or (H) DC-SIGNR or (I) pre-incubated QR-DiMan·DC-SIGNR with 2 mM mannose. Statistical analysis of the (J) numbers of QRs per cluster (i.e., the number of interconnected QRs with a ppNND of <7.7 nm) and (K) QR nearest neighbor orientations (individual: ppNND > 7.7 nm; parallel: the area of the first ccNND peak (or ccNND < 10 nm for DC-SIGN); non-parallel: the sum of the second and third ccNND peak areas (or ccNND > 10 nm for DC-SIGN); non-specific: ppNND < 2.9 nm). Schematics and example S/TEM images of (L) simultaneous binding of DC-SIGN (blue) to all sections of QR or DC-SIGNR (red) to the cylindrical section only; DC-SIGNR cross-linking QR-DiMan into (M) parallel stacks, (N) non-parallel perpendicular stacked QRs and (O) non-parallel adjacently stacked QRs; and (P) non-specifically adsorbed QRs (scale bar = 20 nm).

reflection of its stronger overall binding affinity with QR-DiMan and hence requires a higher concentration of mannose in order to displace 50% of binding interactions. However, DC-SIGNR displays a broader decay with increasing mannose concentrations than DC-SIGN does, evidenced by the smaller exponent ($n = 1.78 \pm 0.05$ *vs* $1.21 \pm 0.08$ for DC-SIGN *vs* DC-SIGNR). This suggests that mannose is able to displace a larger amount of bound DC-SIGNR at much lower concentrations than DC-SIGN. It is worth noting that, where the difference in the overall apparent-$K_d$ between DC-SIGN/R binding to QR-DiMan is ~100-fold, the difference in the apparent-$K_i$ with mannose is only ~2 fold. This may suggest that, for a PQR of 4:1, the simultaneous binding mode of DC-SIGNR provides a higher contribution to the apparent-$K_i$ than the crosslinking mode, where the latter contributes mainly to broadening of the decay. Interestingly, because the fluorescent core of the QR has been shown to be located in the center of the cylindrical middle section of the QR,[53] any binding at the middle section will have a larger influence on the apparent $K_i$. This result may therefore suggest that the glycan display at the central cylindrical section of the quantum nanorod is better suited to form simultaneous binding with DC-SIGNR than cross-linking interactions. Consistent with this, the decay in $D_h$ for the simultaneously bound complexes also occurs at the



https://doi.org/10.1021/acsanm.2c05247
ACS Appl. Nano Mater. 2023, 6, 4201−4213

**Table 2. Summary of Fitting Parameters Obtained from the Gaussian Fits of the Nearest Neighbor Distances (NND) of QR-DiMan Particles Binding with DC-SIGN, DC-SIGNR, or DC-SIGNR with 2 mM Mannose where ppNND is the Perimeter−Perimeter NND and ccNND is the Center−Center NND where 2.9 < ppNND < 7.7 nm**

| | perimeter−perimeter NND | | | | center−center NND | | | |
|---|---|---|---|---|---|---|---|---|
| protein | mean ppNND (nm) | FWHM (nm) | area (%) | $R^2$ | mean ccNND (nm) | FWHM (nm) | area (%) | $R^2$ |
| DC-SIGN | 2.3 ± 0.1 | 2.2 ± 0.4 | 8 ± 1 | 0.747 | | | | |
| DC-SIGNR | 1.9 ± 0.2 | 1.5 ± 0.5 | 8 ± 4 | 0.869 | 8.9 ± 0.1 | 2.4 ± 0.3 | 15 ± 2 | 0.939 |
| | 4.0 ± 0.2 | 2.2 ± 0.9 | 15 ± 6 | | 13.5 ± 0.3 | 4.9 ± 0.8 | 21 ± 3 | |
| | 6.7 ± 0.7 | 2 ± 1 | 4 ± 3 | | 19.3 ± 0.3 | 2.0 ± 0.6 | 4 ± 1 | |
| DC-SIGNR + mannose | 1.63 ± 0.09 | 1.5 ± 0.4 | 10 ± 3 | 0.987[a] | 8.9 ± 0.1 | 3.1 ± 0.4 | 7 ± 2 | 0.980 |
| | 3.6 ± 0.2 | 2.0 ± 0.6 | 9 ± 3 | | 14.0 ± 0.4 | 7.9 ± 0.9 | 18 ± 2 | |
| | 6.4 ± 0.6 | 3 ± 1 | 5 ± 2 | | 21.5 ± 0.3 | 1.8 ± 0.6 | 1.1 ± 0.4 | |

[a]An additional peak was observed at ~0.8 nm, which was an artifact of the image resolution and fit poorly to the data.

same mannose concentration range (Figure 4R). Given the previously established cross-linking character of spherical QD-DiMan with DC-SIGNR,[21] this conclusion appears reasonable as any deviation in binding mode induced by QRs with a similar radius and chemical composition is expected to occur at the central cylindrical section, where the glycan display differs the most from that of QDs.

Overall, these results collectively demonstrate that our QR-DiMan probe is able to distinguish between the strong simultaneous and weak cross-linking binding modes by combining both FRET and hydrodynamic size analyses and that these binding modes are likely to favor different regions of the quantum nanorod.

**Binding Mode Rationale *via* S/TEM Imaging.** Electron microscopy was further employed to capture "snapshot" images of the QR-lectin complexes in order to provide a more detailed understanding of their interactions. Here, QR-lectin samples, prepared with a PQR of 4:1, were plunge-frozen and then vacuum dried before being placed for S/TEM imaging. We have shown previously that this method allows for the successful capture of the native dispersion state of nanoparticle assemblies.[21,59] Binding of DC-SIGN demonstrated mostly isolated individual QRs (Figure 6A), which correlated nicely with the single $D_h$ distribution for DC-SIGN·QR-DiMan complexes observed by DLS (Figure 4B). Additionally, binding of DC-SIGNR yielded both clustered QR assemblies and non-clustered individual QRs (Figure 6B), which again agreed well with the two distinct $D_h$ species observed in DLS (Figure 4F).

To further quantify assembly formation, the inter-QR distances were analyzed by measuring the perimeter−perimeter nearest neighbor distances (ppNNDs) between each QR (i.e., the shortest distance between the perimeter of one QR with that of its nearest neighboring QR). The distributions of ppNNDs were then plotted as histograms and fitted with Gaussian distribution curves. This analysis revealed three well-defined species for QR-DiMan·DC-SIGNR assemblies with ppNNDs of 1.9 ± 0.8, 4.0 ± 1.1, and 6.7 ± 1.0 nm (mean ± 1/2 FWHM; Figure 6E; Table 2). DC-SIGN, on the other hand, displayed only one well-defined ppNND distribution at 2.3 ± 1.1 nm (Figure 6D; Table 2). These results allowed us to draw three conclusions. (1) The smallest ppNND species (~2 nm) were observed in similar amounts for both DC-SIGN and DC-SIGNR (20−27%). Such distances are comparable to the thickness of the glycan ligand coating; thus, these QR assemblies are deemed to result from non-specific interactions (depicted in Figure 6P). (2) The species with ppNNDs $\gtrsim$ 7.7 nm were found in 71% of QR-DiMan·DC-SIGN and 31% of QR-DiMan·DC-SIGNR complexes and were randomly distributed (Figure S15). These corresponded nicely to single QR-DiMan particles bound with a layer of protein, as observed by DLS, thus confirming that both DC-SIGN and DC-SIGNR were able to bind tetravalently with all CRDs with one QR-DiMan. (3) The well-defined species for DC-SIGNR binding with ppNNDs of 4.0 ± 1.1 and 6.7 ± 1.0 nm were not observed in significant amount with DC-SIGN (Figure 6D); such distances were consistent with the discrete distances expected for DC-SIGNR-bridged QRs. In addition, of the QRs with ppNNDs below ~7 nm, 49% contained >2 QRs per cluster for DC-SIGNR, whereas such assemblies were only observable in negligible amounts for DC-SIGN (<3% of QRs). These multi-QR assemblies are consistent with the larger $D_h$ sizes observed by DLS. Interestingly, these are only limited to a few QRs per cluster and thus do not resemble the extensive inter-cross-linked networks observed for QD-DiMan bridged by DC-SIGNR.[21] This is likely due to the dual simultaneous and cross-linking binding mode, which imparts a limit to the number of cross-linking interactions possible.

To investigate how mannose competes with QR-DiMan binding with DC-SIGNR, S/TEM images were performed on a sample of a pre-incubated QR-DiMan· DC-SIGNR complex with 2 mM mannose (Figure 6C,F). Here, an ~40% reduction of clusters containing >4 QRs was observed (Figure 6J), consistent with the significantly reduced mean $D_h$ observed by DLS (Figure 4O). In parallel to the decrease in cross-linking, an ~ 10% increase in the proportion of individual complexes and an ~50% increase in the proportion of non-specific interactions were observed (Figure 6K). This result may explain why the $D_h$ of QR-DiMan did not completely return to its original size after dissociation of bound proteins observed at high mannose concentrations.

Though QR-FRET and hydrodynamic size analysis were able to suggest that the different binding modes of DC-SIGNR may favor specific regions of the QR, S/TEM analysis provides a direct visual representation of how QR-DiMan particles orient themselves with respect to each other in the presence of lectin, which can be used to infer regional details regarding cross-linking. Here, inter-QR nearest neighbor orientations were analyzed by measuring the center−center nearest neighbor distance (ccNND; the shortest distance between the center of one QR with that of its nearest neighbor) for all QRs with a ppNND between 4.0 ± 1.1 and 6.7 ± 1.0 nm. As expected, no clear ccNND distribution was observed for QR-DiMan·DC-SIGN complexes (Figure 6G). In sharp contrast, for QR-DiMan·DC-SIGNR complexes, three discrete distributions were obtained with Gaussian fits with ccNNDs of 8.9 ±



https://doi.org/10.1021/acsanm.2c05247
ACS Appl. Nano Mater. 2023, 6, 4201−4213

1.2, 13.5 ± 2.4, and 19.3 ± 1.0 nm (mean ± 1/2 FWHM; Figure 6H; Table 2), respectively. These distributions are representative of QRs, which are stacked either parallel (i.e., center to center; Figure 6M), perpendicular (i.e., end to center; Figure 6N), or adjacent (i.e., end to end; Figure 6O) to one another, respectively.

If cross-linking did not discriminate between the different regions on the QR, then, based on surface area alone, the most common inter-QR orientation would be QRs stacked loosely parallel to one another. However, the ccNND distributions (Figure 6K) show that this is not case. Instead, only 15% of QRs are stacked parallel to their nearest neighbor, while 25% of QRs display non-parallel nearest neighbor orientations. This result suggests that cross-linking favors the spherical ends over the central cylindrical section of the QR. In addition, the parallel interactions were the only nearest neighbor orientation that showed a significant reduction upon addition of the mannose competitor. Therefore, it is plausible that these parallel QR stacks are composed of protein cross-linking at both QR ends, which are then either fully dissociated into isolated particles or partially dissociated into non-parallel interactions in the presence of mannose. This is feasible as further cross-linking between adjacent QR-lectin complexes within the same original QR cluster would be much more kinetically favorable than cross-linking multiple QR-lectin complexes that are freely diffusing in the solution. Based on these results, together with those observed by FRET and hydrodynamic size analyses above, three interesting conclusions can be deduced: (1) DC-SIGNR favors cross-linking upon spherical geometries (e.g., QDs or the QR end sections), (2) DC-SIGNR favors simultaneous binding upon cylindrical geometries (e.g., the central region of the QR), and (3) DC-SIGN favors simultaneous binding indiscriminately upon both spherical and cylindrical geometries.

These different binding phenomena can be rationalized by considering the relative dimensions of both binding partners. The hydrodynamic dimensions of QR-DiMan can be estimated from the summation of the average QR core dimensions obtained by S/TEM (core length, $L_{core}^{QR}$ 14.7 ± 5.7 nm; core diameter, $D_{core}^{QR}$ 3.1 ± 0.7 nm; Figure S14) and the estimated hydrodynamic surface ligand length (2.9 ± 1.1 nm; derived from the previous QD-DiMan dimensions, where $D_h^{QD}$ = 9.5 ± 0.1 nm and $D_{core}^{QD}$= 3.7 ± 2.1 nm).[21] This provided a QR-DiMan estimated terminal end $D_h$ and cylindrical height ($H$) of 8.9 ± 2.3 and 11.6 ± 5.7 nm, respectively (see SI, Figures S14 and S16). Both of these dimensions are comparable with that of the equivalent QD-DiMan ($D_h^{QD}$ = 9.5 ± 0.1 nm).[21] Due to the flexible nature of the $EG_{11}$ chain, the glycan surface density and inter-glycan distance of each glycan ligand can be assumed to be roughly the same across the whole QR. Based on these geometrical values and a surface glycan valency of ~370 per QR (see SI, Section 7), a glycan surface density of ~0.63 glycans per nm$^2$ and an average inter-glycan distance of ~1.4 nm are obtained for QR-DiMan. The crystal structure of DC-SIGNR C-terminal tetrameric fragment (PDB code: 1XAR) provides approximate dimensions of 3.8 × 8.0 nm between the primary $Ca^{2+}$ ions associated with glycan binding (see SI, Figure S17A).[60] Thus, the binding contact area of each DC-SIGNR is likely to be smaller than both the spherical and cylindrical regions of the QR-DiMan. It would cover a surface area containing ~20 glycans on QR-DiMan. These simple calculations suggest that neither the QR size nor the glycan surface density is likely to be the main factors causing the distinct binding modes for DC-SIGNR between the QR end and middle sections. Instead, the distinct DC-SIGNR binding modes are most likely to be determined by the large differences in the 3-dimensional surface curvatures between these regions. In fact, at the spherical ends of the QR, surface curvature could theoretically impart separation distances ($d$) as much as ~4 nm from the protein binding sites to the glycan surface (eq 3) where $p$ is the Ca−Ca distance between two CRDs at the furthest separation distance from the scaffold surface, which is taken as the average diagonal Ca−Ca distance ($p$:~ 8.8 nm; Figure 7 left).

$$d = \frac{D_h - \sqrt{D_h^2 - p^2}}{2} \tag{3}$$

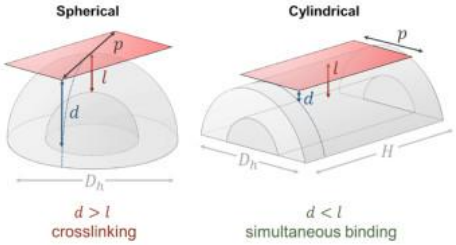


**Figure 7.** Schematic depicting the difference in separation distance between the binding contact area of DC-SIGNR (red) with either the spherical end (left) or cylindrical section (right) of the QR surface. Here, $d$ is the separation distance between the protein contact area and the QR-DiMan surface, $l$ is the maximum compression length of the surface glycan ligands, $p$ is the Ca−Ca distance between two CRDs at the furthest separation distance from the QR surface, $D_h$ is the estimated QR-DiMan hydrodynamic diameter, and $H$ is the height of the QR cylindrical section. (Not to scale).

The theoretical maximum length at which the glycan ligands may be able to be compressed ($l$) can be derived from the estimated length of flexibility in the glycan ligand, i.e., $l$ ~2.1 nm for DHLA-$EG_{11}$-DiMan (see SI, Section 7). Therefore, even with compression of the ligands, it would be impossible for all four binding sites to reach the glycan surface simultaneously. This means that the glycan displays at the QR ends are incapable of bridging all four binding sites in DC-SIGNR; thus, the protein cannot access its most stable simultaneously bound state. Instead, it is forced to find its next most favorable configuration by cross-linking with other particles to maximize binding enthalpy.[57] For the cylindrical section of the scaffold, the curvature of the round of the cylinder is the same as the spherical ends; however, along the length of the cylinder, it is roughly flat. This means that the tetrameric lectin has the opportunity to align itself with its longer length parallel to the length of the quantum rod (Figure 7, right). Therefore, only the short length of the tetramer (i.e., $p$ = 3.8 nm) needs to contribute to the separation distance ($d$) from the quantum rod surface, resulting in a $d$ of only ~0.4 nm. This is well within the maximum compression length of the ligands, therefore allowing glycans to easily bridge all four CRDs to give strong simultaneous tetravalent binding. Finally, the tetrameric model of DC-SIGN has been predicted to exhibit a more compact shape with an average diagonal inter-



https://doi.org/10.1021/acsanm.2c05247
ACS Appl. Nano Mater. 2023, 6, 4201−4213

binding site distance of 5.6 nm (Figure S17B).[61] This results in a much smaller separation distance between the protein contact area ($d \approx 1$ nm), which is smaller than the maximum compression length of the flexible surface ligands ($l = 2.1$ nm). This would therefore easily allow the QR surface glycans to bridge all 4 CRDs, regardless of the region of the QR that DC-SIGN binds to, leading to the exclusively simultaneous binding mode as observed here. These calculations therefore show that while the tetrameric structures of both lectins are still unknown, and the good agreement between the predicted and observed results suggests that the structural models for DC-SIGN/R are likely to be relatively reliable. Moreover, it also demonstrates that, by taking into account nanoscaffold curvature, estimating the $d - l$ relationship between the protein and nanoscaffold dimensions can provide a useful prediction of the binding mode for multimeric lectins.

## ■ CONCLUSIONS

In summary, we have presented a new glycan-quantum rod-based multifunctional biophysical probe for multivalent lectin-glycan interactions. By combining FRET, hydrodynamic size, and S/TEM imaging analysis, we have dissected the geometric influences of glyco-nanomaterials on the MLGI properties of DC-SIGN and DC-SIGNR, a pair of tetrameric lectin models with almost identical monovalent binding motifs but distinct binding site arrangements. We demonstrate that, given an ample polyvalent glycan density and area, nanoscale scaffold curvature has a fundamental impact on the binding modes of their MLGIs. Here, DC-SIGNR is able to distinguish between the end and middle sections of QR-DiMan, forming strong simultaneous tetravalent binding at the central cylindrical section but bis-bivalent cross-linking at the spherical ends. Meanwhile, DC-SIGN binds with strong simultaneous tetravalent binding irrespective of the QR section. We have further predicted that only curvatures affording a separation distance between the protein contact area and the glycan ligand surface ($d$) smaller than the compression length of the glycan ligands ($l$) can result in the strong simultaneous binding of all binding sites. However, if $d$ is greater than $l$, then only weak cross-linking or other lower valency binding interactions can occur.

This glycan-QR probe thus provides a powerful new tool for studying the shape-dependent binding affinities and mechanisms of multivalent lectins at the molecular level. It can provide a fundamental rationale behind the MLGI shape dependency. Such information can act as a useful guidance on the shape design of multivalent glycans for targeting specific MLGIs in a solution. These results also demonstrate how multimeric lectins like DC-SIGN/R differentiate glycan displays with different geometries, which may help explain some of their differences in virus-binding and transmitting properties in cells. Future studies will investigate the shape selectivity of such lectin receptors with glycan-coated QDs and QRs at cell surfaces to reveal the difference and correlation between MLGIs occurring in solutions and on cell surfaces. In addition, other design elements such as scaffold size, ligand density, and flexibility will also be investigated in order to design optimal glycan nanoparticles for potent and specific targeting of MLGIs in the body for therapeutic interventions.

## ■ EXPERIMENTAL SECTION

**Materials.** CdSe/CdS-elongated (dot-in-a-rod) core/shell quantum rods (QR) capped with mixed TOPO/TOP/HPA surface ligands in hexane were purchased from Centre for Applied Nanotechnology GmbH (Germany). $H_2O$ used was ultra-pure (resistance: >18.2 MΩ·cm) purified by an ELGA Purelab classic UVF system. The binding buffer consisted of 20 mM HEPES, 100 mM NaCl, 10 mM $CaCl_2$, pH 7.8, in $H_2O$. All other chemicals and reagents were purchased commercially and used as received unless stated otherwise. DHLA-$EG_{11}$-DiMan were synthesized in-house using our previously established protocols.[21] MS: calculated $m/z$ for $C_{60}H_{111}N_5O_{27}S_2$ (DHLA-$EG_{11}$-DiMan) $[M + 2H]^{2+}$: 699.84, found: 699.95.

**Preparation of QR-DiMan.**[21,22] QR-DiMan were prepared using our established quantum dot cap exchange protocol. Briefly, QR (416 μL, 2 nmol) in hexane was precipitated by EtOH (12 mL) and spun at 15,000$g$ for 5 min. After discarding the clear supernatant, the resulting QR pellet was dissolved in $CHCl_3$ (300 μL) and then a mixture of DHLA-$EG_{11}$-DiMan (273 μL, 5.4 μmol) in $CHCl_3$ and NaOH (64 μL, 6.48 μmol) in EtOH was added. MeOH (100 μL) was further added, and the resulting mixture was covered with foil and stirred at r.t. for 30 min. The resulting QRs were then precipitated by addition of hexane (600 μL) and spun at 15,000$g$ for 3 min. The resulting QR pellet was dissolved in $H_2O$ (300 μL) and washed with $H_2O$ (3×200 μL) using a 30 kDa MWCO spin filter. This yielded a stable water-dispersed QR-DiMan (1.55 nmol) in 78% yield. The supernatants and washes were combined, freeze-dried, and then used to determine the unbound ligand *via* the sulfuric acid-phenol carbohydrate quantification (SI, Section 2.2). The ligand amount bound to the QR was calculated from the difference between that added and that remaining unbound post cap-exchange,[57] yielding a mean glycan surface coverage of 370 ± 30 ligands per QR.

**FRET Assays.** All FRET studies were measured using a Cary Eclipse Fluorescence Spectrophotometer in a 0.7 mL quartz cuvette (optical path length: 10 mm). Samples were prepared by adding protein to QR-DiMan in the binding buffer containing BSA (1 mg/mL, to minimize non-specific interactions and adsorptions on surfaces) and incubated for 20 min before measurement. Samples were excited with $\lambda_{EX}$ = 450 nm (corresponding to the absorption minimum of Atto-594 to minimize dye direct excitation background), and the fluorescence spectra were recorded from 500 to 750 nm, with intervals ($\Delta\lambda$) of 1 nm. Mannose competition experiments were performed in the same way, where after addition of D-mannose, the resulting solution was incubated for a further 20 min before measurement. All fluorescence spectra were corrected by the background fluorescence of the same concentration of labeled lectin, without QR, under identical conditions. The PMT voltages and instrument slit widths were adjusted to avoid signal saturation at high concentrations. While varying instrument setups will affect the absolute fluorescence signals of both the QR and dye, it will not affect the FRET ratio used in data analysis due to its ratiometric character.[21,57]

**Hydrodynamic Size Analysis.** All hydrodynamic size studies were performed on a Malvern Zetasizer Nano using 10 mm PMMA cuvettes.[20] Samples were prepared by adding protein to QR-DiMan in the binding buffer and incubating for 20 min before measurement. The mannose competition experiment was performed the same way by adding D-mannose to pre-incubated QR-lectin samples and further incubation for 20 min. Distributions were obtained by averaging a minimum of three measurements of 10 runs of 10 s. Mean hydrodynamic diameters ($D_h$) were obtained by fitting these averaged volume hydrodynamic size distribution histograms with either unimodal or bimodal Gaussian distribution functions.[20]

**S/TEM Imaging.**[21,57] All S/TEM images were taken using an FEI Titan$^3$ Themis 300 G2 S/TEM. Samples were prepared under the same conditions as those used for $D_h$ analysis. A small sample mixture (3.5 μL) was loaded onto a plasma-cleaned TEM grid with a continuous carbon support film before being blotted and then plunge-frozen into liquid ethane. The TEM grids were then allowed to warm up to room temperature over several minutes by placing the specimens in a liquid nitrogen-cooled storage container in a rotary-pumped vacuum desiccator. The samples were plasma-cleaned (15 s) and then analyzed using high-angle annular dark field scanning transmission electron microscopy mode. S/TEM Images were



https://doi.org/10.1021/acsanm.2c05247
ACS Appl. Nano Mater. 2023, 6, 4201−4213

analyzed by using ImageJ 1.4.3.67 software to obtain perimeter−perimeter (pp) and center−center (cc) nearest neighbor distance (NND) histograms. The mean NNDs were obtained by fitting the distributions with multimodal Gaussian distribution curves.

**Data Analysis and Fitting.** All fluorescence data were analyzed using Microsoft Excel 2016. The FRET ratio data were presented as mean ± standard errors of two repeats at each concentration. The FRET ratio−concentration plots were fitted by the Origin software (version 2019b) using the relevant equations, taking into account the SEs of each experimental data point, to give the best fits (highest $R^2$ values). The results from the best fits were then listed in the relevant tables and displayed as mean ± the standard fitting errors.

## ■ ASSOCIATED CONTENT

### Supporting Information

The Supporting Information is available free of charge at https://pubs.acs.org/doi/10.1021/acsanm.2c05247.

Materials, instruments, and methods; preparation and characterization of QR-DiMan; characterization of QR-DiMan lectin hydrodynamic sizes; STEM image analysis; and curvature analysis (PDF)

## ■ AUTHOR INFORMATION


### Corresponding Authors

**Dejian Zhou** − *School of Chemistry and Astbury Centre for Structural Molecular Biology, University of Leeds, Leeds LS2 9JT, United Kingdom;* orcid.org/0000-0003-3314-9242; Email: d.zhou@leeds.ac.uk

**Yuan Guo** − *School of Food Science and Nutrition and Astbury Centre for Structural Molecular Biology, University of Leeds, Leeds LS2 9JT, United Kingdom;* orcid.org/0000-0003-4607-7356; Email: y.guo@leeds.ac.uk

### Authors

**James Hooper** − *School of Food Science and Nutrition and Astbury Centre for Structural Molecular Biology, University of Leeds, Leeds LS2 9JT, United Kingdom;* orcid.org/0000-0001-8672-1068

**Darshita Budhadev** − *School of Chemistry and Astbury Centre for Structural Molecular Biology, University of Leeds, Leeds LS2 9JT, United Kingdom*

**Dario Luis Fernandez Ainaga** − *School of Chemical and Process Engineering, University of Leeds, Leeds LS2 9JT, United Kingdom;* orcid.org/0000-0002-4634-4269

**Nicole Hondow** − *School of Chemical and Process Engineering, University of Leeds, Leeds LS2 9JT, United Kingdom*

Complete contact information is available at: https://pubs.acs.org/10.1021/acsanm.2c05247


### Author Contributions

Y.G. and D.Z. designed and supervised this study. J.H. conducted all the protein production, labeling and characterization, ligand synthesis, glycan-QR preparation, FRET and DLS experiments and data analysis. D.B. synthesized DiMan-$N_3$. N.H. and D.F.A. performed the S/TEM imaging. This manuscript was written by J.H., D.Z. and Y.G. All authors have read and approved the final version of the manuscript.


### Funding

This work was supported by the UK Biotechnology and Biological Sciences Research Council (grant BB/R007829/1), the Royal Society (grant IEC\NSFC\191,397), and the School of Food Science and Nutrition, University of Leeds, *via* a PhD scholarship.


### Notes

The authors declare no competing financial interest.

## ■ ACKNOWLEDGMENTS

We thank Prof. W. Bruce Turnbull (University of Leeds) for his help in the synthesis of the azide-modified DiMan. We thank the UK Biotechnology and Biological Sciences Research Council (grant BB/R007829/1) and the Royal Society (grant IEC\NSFC\191397) for supporting this project. J.H. thanks the School of Food Science and Nutrition, University of Leeds, for funding him a PhD scholarship. We also thank Claire Jing Zhou (The Grammar School at Leeds, Leeds LS17 8GS, U.K.) for designing the cover artwork.

## ■ ABBREVIATIONS

CRD, carbohydrate recognition domain
DC-SIGN, Dendritic Cell-Specific Intercellular adhesion molecule-3-Grabbing Nonintegrin
DC-SIGNR, a DC-SIGN related lectin found on endothelial cells
$D_h$, hydrodynamic diameter
DHLA-$EG_{11}$-DiMan, dihydrolipoic acid-undeca(ethylene glycol)-$\alpha$-1,2-manno-biose
FRET, Förster resonance energy transfer
HRMS, high resolution mass spectrometry
$K_d$, apparent equilibrium binding dissociation constant
MLGI, multivalent lectin-glycan interactions
PQR, protein: QR molar ratio
QD, quantum dot
QR, quantum nanorod
S/TEM, scanning/ transition electron microscopy

## ■ REFERENCES


(1) Fruk, L.; Kerbs, A. *Bionanotechnology: Concepts and Applications.* Cambridge University Press: 2021, DOI: 10.1017/9781108690102.

(2) Zare, E. N.; Zheng, X.; Makvandi, P.; Gheybi, H.; Sartorius, R.; Yiu, C. K. Y.; Adeli, M.; Wu, A.; Zarrabi, A.; Varma, R. S.; Tay, F. R. Nonspherical Metal-Based Nanoarchitectures: Synthesis and Impact of Size, Shape, and Composition on Their Biological Activity. *Small* **2021**, *17*, No. 2007073.

(3) Albanese, A.; Tang, P. S.; Chan, W. C. W. The Effect of Nanoparticle Size, Shape, and Surface Chemistry on Biological Systems. *Annu. Rev. Biomed. Eng.* **2012**, *14*, 1−16.

(4) Liyanage, S. H.; Yan, M. Quantification of Binding Affinity of Glyconanomaterials with Lectins. *Chem. Commun.* **2020**, *56*, 13491−13505.

(5) Chithrani, B. D.; Ghazani, A. A.; Chan, W. C. W. Determining the Size and Shape Dependence of Gold Nanoparticle Uptake into Mammalian Cells. *Nano Lett.* **2006**, *6*, 662−668.

(6) Albanese, A.; Chan, W. C. W. Effect of Gold Nanoparticle Aggregation on Cell Uptake and Toxicity. *ACS Nano* **2011**, *5*, 5478−5489.

(7) Sangabathuni, S.; Vasudeva Murthy, R.; Chaudhary, P. M.; Surve, M.; Banerjee, A.; Kikkeri, R. Glyco-Gold Nanoparticle Shapes Enhance Carbohydrate-Protein Interactions in Mammalian Cells. *Nanoscale* **2016**, *8*, 12729−12735.

(8) Li, Z.; Sun, L.; Zhang, Y.; Dove, A. P.; O'Reilly, R. K.; Chen, G. Shape Effect of Glyco-Nanoparticles on Macrophage Cellular Uptake and Immune Response. *ACS Macro Lett.* **2016**, *5*, 1059−1064.

(9) Xie, X.; Liao, J.; Shao, X.; Li, Q.; Lin, Y. The Effect of shape on Cellular Uptake of Gold Nanoparticles in the Forms of Stars, Rods, and Triangles. *Sci. Rep.* **2017**, *7*, 3827.




https://doi.org/10.1021/acsanm.2c05247
ACS Appl. Nano Mater. 2023, 6, 4201−4213

(10) Ding, L.; Yao, C.; Yin, X.; Li, C.; Huang, Y.; Wu, M.; Wang, B.; Guo, X.; Wang, Y.; Wu, M. Size, Shape, and Protein Corona Determine Cellular Uptake and Removal Mechanisms of Gold Nanoparticles. *Small* **2018**, *14*, No. 1801451.
(11) Kersting, M.; Olejnik, M.; Rosenkranz, N.; Loza, K.; Breisch, M.; Rostek, A.; Westphal, G.; Bünger, J.; Ziegler, N.; Ludwig, A.; Köller, M.; Sengstock, C.; Epple, M. Subtoxic Cell Responses to Silica Particles with Different Size and Shape. *Sci. Rep.* **2020**, *10*, 21591.
(12) Niikura, K.; Matsunaga, T.; Suzuki, T.; Kobayashi, S.; Yamaguchi, H.; Orba, Y.; Kawaguchi, A.; Hasegawa, H.; Kajino, K.; Ninomiya, T.; Ijiro, K.; Sawa, H. Gold Nanoparticles as a Vaccine Platform: Influence of Size and Shape on Immunological Responses In Vitro and In Vivo. *ACS Nano* **2013**, *7*, 3926−3938.
(13) Guo, S.; Li, H.; Ma, M.; Fu, J.; Dong, Y.; Guo, P. Size, Shape, and Sequence-Dependent Immunogenicity of RNA Nanoparticles. *Mol. Ther.−Nucleic Acids* **2017**, *9*, 399−408.
(14) Toraskar, S.; Madhukar Chaudhary, P.; Kikkeri, R. The Shape of Nanostructures Encodes Immunomodulation of Carbohydrate Antigen and Vaccine Development. *ACS Chem. Biol.* **2022**, *17*, 1122−1130.
(15) Reuter, J. D.; Myc, A.; Hayes, M. M.; Gan, Z.; Roy, R.; Qin, D.; Yin, R.; Piehler, L. T.; Esfand, R.; Tomalia, D. A.; Baker, J. R. Inhibition of Viral Adhesion and Infection by Sialic-Acid-Conjugated Dendritic Polymers. *Bioconjugate Chem.* **1999**, *10*, 271−278.
(16) Bhatia, S.; Lauster, D.; Bardua, M.; Ludwig, K.; Angioletti-Uberti, S.; Popp, N.; Hoffmann, U.; Paulus, F.; Budt, M.; Stadtmüller, M.; Wolff, T.; Hamann, A.; Böttcher, C.; Herrmann, A.; Haag, R. Linear Polysialoside Outperforms Dendritic Analogs for Inhibition of Influenza Virus Infection In Vitro and In Vivo. *Biomaterials* **2017**, *138*, 22−34.
(17) Toraskar, S.; Gade, M.; Sangabathuni, S.; Thulasiram, H. V.; Kikkeri, R. Exploring the Influence of Shapes and Heterogeneity of Glyco-Gold Nanoparticles on Bacterial Binding for Preventing Infections. *ChemMedChem* **2017**, *12*, 1116−1124.
(18) Brown, G. D.; Willment, J. A.; Whitehead, L. C-type lectins in immunity and homeostasis. *Nat. Rev. Immunol.* **2018**, *18*, 374−389.
(19) Thodikayil, A. T.; Sharma, S.; Saha, S. Engineering Carbohydrate-Based Particles for Biomedical Applications: Strategies to Construct and Modify. *ACS Appl. Bio Mater.* **2021**, *4*, 2907−2940.
(20) Budhadev, D.; Poole, E.; Nehlmeier, I.; Liu, Y.; Hooper, J.; Kalverda, E.; Akshath, U. S.; Hondow, N.; Turnbull, W. B.; Pöhlmann, S.; Guo, Y.; Zhou, D. Glycan-Gold Nanoparticles as Multifunctional Probes for Multivalent Lectin-Carbohydrate Binding: Implications for Blocking Virus Infection and Nanoparticle Assembly. *J. Am. Chem. Soc.* **2020**, *142*, 18022−18034.
(21) Guo, Y.; Nehlmeier, I.; Poole, E.; Sakonsinsiri, C.; Hondow, N.; Brown, A.; Li, Q.; Li, S.; Whitworth, J.; Li, Z.; Yu, A.; Brydson, R.; Turnbull, W. B.; Pöhlmann, S.; Zhou, D. Dissecting Multivalent Lectin−Carbohydrate Recognition Using Polyvalent Multifunctional Glycan-Quantum Dots. *J. Am. Chem. Soc.* **2017**, *139*, 11833−11844.
(22) Guo, Y.; Sakonsinsiri, C.; Nehlmeier, I.; Fascione, M. A.; Zhang, H.; Wang, W.; Pöhlmann, S.; Turnbull, W. B.; Zhou, D. Compact, Polyvalent Mannose Quantum Dots as Sensitive, Ratiometric FRET Probes for Multivalent Protein−Ligand Interactions. *Angew. Chem., Int. Ed.* **2016**, *55*, 4738−4742.
(23) Nazemi, A.; Haeryfar, S. M. M.; Gillies, E. R. Multifunctional Dendritic Sialopolymersomes as Potential Antiviral Agents: Their Lectin Binding and Drug Release Properties. *Langmuir* **2013**, *29*, 6420−6428.
(24) Bes, L.; Angot, S.; Limer, A.; Haddleton, D. M. Sugar-Coated Amphiphilic Block Copolymer Micelles from Living Radical Polymerization: Recognition by Immobilized Lectins. *Macromolecules* **2003**, *36*, 2493−2499.
(25) Luczkowiak, J.; Muñoz, A.; Sánchez-Navarro, M.; Ribeiro-Viana, R.; Ginieis, A.; Illescas, B. M.; Martín, N.; Delgado, R.; Rojo, J. Glycofullerenes Inhibit Viral Infection. *Biomacromolecules* **2013**, *14*, 431−437.
(26) Buffet, K.; Gillon, E.; Holler, M.; Nierengarten, J.-F.; Imberty, A.; Vincent, S. P. Fucofullerenes as Tight Ligands of RSL and LecB Two Bacterial Lectins. *Org. Biomol. Chem.* **2015**, *13*, 6482−6492.
(27) Rísquez-Cuadro, R.; García Fernández, J. M.; Nierengarten, J.-F.; Ortiz Mellet, C. Fullerene-sp2-Iminosugar Balls as Multimodal Ligands for Lectins and Glycosidases: A Mechanistic Hypothesis for the Inhibitory Multivalent Effect. *Chem. − Eur. J.* **2013**, *19*, 16791−16803.
(28) Arosio, D.; Chiodo, F.; Reina, J. J.; Marelli, M.; Penadés, S.; van Kooyk, Y.; Garcia-Vallejo, J. J.; Bernardi, A. Effective Targeting of DC-SIGN by α-Fucosylamide Functionalized Gold Nanoparticles. *Bioconjugate Chem.* **2014**, *25*, 2244−2251.
(29) Bernardi, A.; Jiménez-Barbero, J.; Casnati, A.; De Castro, C.; Darbre, T.; Fieschi, F.; Finne, J.; Funken, H.; Jaeger, K. E.; Lahmann, M.; Lindhorst, T. K.; Marradi, M.; Messner, P.; Molinaro, A.; Murphy, P. V.; Nativi, C.; Oscarson, S.; Penadés, S.; Peri, F.; Pieters, R. J.; Renaudet, O.; Reymond, J. L.; Richichi, B.; Rojo, J.; Sansone, F.; Schäffer, C.; Turnbull, W. B.; Velasco-Torrijos, T.; Vidal, S.; Vincent, S.; Wennekes, T.; Zuilhof, H.; Imberty, A. Multivalent Glycoconjugates as Anti-Pathogenic Agents. *Chem. Soc. Rev.* **2013**, *42*, 4709−4727.
(30) DiLillo, A. M.; Chan, K. K.; Sun, X.-L.; Ao, G. Glycopolymer-Wrapped Carbon Nanotubes Show Distinct Interaction of Carbohydrates With Lectins. *Front. Chem.* **2022**, *10*, No. 852988.
(31) Kim, B.-S.; Hong, D.-J.; Bae, J.; Lee, M. Controlled Self-Assembly of Carbohydrate Conjugate Rod−Coil Amphiphiles for Supramolecular Multivalent Ligands. *J. Am. Chem. Soc.* **2005**, *127*, 16333−16337.
(32) Chen, Y.; Vedala, H.; Kotchey, G. P.; Audfray, A.; Cecioni, S.; Imberty, A.; Vidal, S.; Star, A. Electronic Detection of Lectins Using Carbohydrate-Functionalized Nanostructures: Graphene versus Carbon Nanotubes. *ACS Nano* **2012**, *6*, 760−770.
(33) Chaudhary, P. M.; Sangabathuni, S.; Murthy, R. V.; Paul, A.; Thulasiram, H. V.; Kikkeri, R. Assessing the Effect of Different Shapes of Glyco-Gold Nanoparticles on Bacterial Adhesion and Infections. *Chem. Commun.* **2015**, *51*, 15669−15672.
(34) Koukalová, T.; Kovaříček, P.; Bojarová, P.; Guerra, V. L. P.; Vrkoslav, V.; Navara, L.; Jirka, I.; Cebecauer, M.; Křen, V.; Kalbáč, M. Reversible Lectin Binding to Glycan-Functionalized Graphene. *Int. J. Mol. Sci.* **2021**, *22*, 6661.
(35) Tanaka, T.; Ishitani, H.; Miura, Y.; Oishi, K.; Takahashi, T.; Suzuki, T.; Shoda, S.-I.; Kimura, Y. Protecting-Group-Free Synthesis of Glycopolymers Bearing Sialyloligosaccharide and Their High Binding with the Influenza Virus. *ACS Macro Lett.* **2014**, *3*, 1074−1078.
(36) Suzuki, K.; Koyama, T.; Yingsakmongkon, S.; Suzuki, Y.; Hatano, K.; Matsuoka, K. Synthesis and Biological Evaluation of Sialic Acid Derivatives Containing a Long Hydrophobic Chain at the Anomeric Position and Their C-5 Linked Polymers as Potent Influenza Virus Inhibitors. *Bioorg. Med. Chem.* **2012**, *20*, 446−454.
(37) Nagao, M.; Kurebayashi, Y.; Seto, H.; Tanaka, T.; Takahashi, T.; Suzuki, T.; Hoshino, Y.; Miura, Y. Synthesis of Well-Controlled Glycopolymers Bearing Oligosaccharides and Their Interactions with Influenza Viruses. *Polym. J.* **2016**, *48*, 745−749.
(38) Haldar, J.; Álvarez de Cienfuegos, L.; Tumpey, T. M.; Gubareva, L. V.; Chen, J.; Klibanov, A. M. Bifunctional Polymeric Inhibitors of Human Influenza A Viruses. *Pharm. Res.* **2010**, *27*, 259−263.
(39) Becer, C. R.; Gibson, M. I.; Geng, J.; Ilyas, R.; Wallis, R.; Mitchell, D. A.; Haddleton, D. M. High-Affinity Glycopolymer Binding to Human DC-SIGN and Disruption of DC-SIGN Interactions with HIV Envelope Glycoprotein. *J. Am. Chem. Soc.* **2010**, *132*, 15130−15132.
(40) Papp, I.; Sieben, C.; Sisson, A. L.; Kostka, J.; Böttcher, C.; Ludwig, K.; Herrmann, A.; Haag, R. Inhibition of Influenza Virus Activity by Multivalent Glycoarchitectures with Matched Sizes. *ChemBioChem* **2011**, *12*, 887−895.



https://doi.org/10.1021/acsanm.2c05247
ACS Appl. Nano Mater. 2023, 6, 4201−4213

(41) Ramos-Soriano, J.; Rojo, J. Glycodendritic Structures as DC-SIGN Binders to Inhibit Viral Infections. *Chem. Commun.* **2021**, *57*, 5111−5126.
(42) Pernía Leal, M.; Assali, M.; Cid, J. J.; Valdivia, V.; Franco, J. M.; Fernández, I.; Pozo, D.; Khiar, N. Synthesis of 1D-Glyconanomaterials by a Hybrid Noncovalent−Covalent Functionalization of Single Wall Carbon Nanotubes: a Study of Their Selective Interactions with Lectins and with Live Cells. *Nanoscale* **2015**, *7*, 19259−19272.
(43) Gestwicki, J. E.; Cairo, C. W.; Strong, L. E.; Oetjen, K. A.; Kiessling, L. L. Influencing Receptor−Ligand Binding Mechanisms with Multivalent Ligand Architecture. *J. Am. Chem. Soc.* **2002**, *124*, 14922−14933.
(44) Geijtenbeek, T. B. H.; Kwon, D. S.; Torensma, R.; van Vliet, S. J.; van Duijnhoven, G. C. F.; Middel, J.; Cornelissen, I. L. M. H. A.; Nottet, H. S. L. M.; KewalRamani, V. N.; Littman, D. R.; Figdor, C. G.; van Kooyk, Y. DC-SIGN, a Dendritic Cell-Specific HIV-1-Binding Protein That Enhances Trans-Infection of T Cells. *Cell* **2000**, *100*, 587−597.
(45) Pöhlmann, S.; Soilleux, E. J.; Baribaud, F.; Leslie, G. J.; Morris, L. S.; Trowsdale, J.; Lee, B.; Coleman, N.; Doms, R. W. DC-SIGNR, A DC-SIGN Homologue Expressed in Endothelial Cells, Binds to Human and Simian Immunodeficiency Viruses and Activates Infection in Trans. *Proc. Natl. Acad. Sci. U. S. A.* **2001**, *98*, 2670−2675.
(46) Guo, Y.; Feinberg, H.; Conroy, E.; Mitchell, D. A.; Alvarez, R.; Blixt, O.; Taylor, M. E.; Weis, W. I.; Drickamer, K. Structural Basis for Distinct Ligand-Binding and Targeting Properties of the Receptors DC-SIGN and DC-SIGNR. *Nat. Struct. Mol. Biol.* **2004**, *11*, 591−598.
(47) Fu, A.; Gu, W.; Boussert, B.; Koski, K.; Gerion, D.; Manna, L.; Le Gros, M.; Larabell, C. A.; Alivisatos, A. P. Semiconductor Quantum Rods as Single Molecule Fluorescent Biological Labels. *Nano Lett.* **2007**, *7*, 179−182.
(48) Albers, A. E.; Chan, E. M.; McBride, P. M.; Ajo-Franklin, C. M.; Cohen, B. E.; Helms, B. A. Dual-emitting Quantum Dot/Quantum Rod-Based Nanothermometers with Enhanced Response and Sensitivity in Live Cells. *J. Am. Chem. Soc.* **2012**, *134*, 9565−9568.
(49) Wu, K.; Hill, L. J.; Chen, J.; McBride, J. R.; Pavlopolous, N. G.; Richey, N. E.; Pyun, J.; Lian, T. Universal Length Dependence of Rod-to-Seed Exciton Localization Efficiency in Type I and Quasi-Type II CdSe@CdS Nanorods. *ACS Nano* **2015**, *9*, 4591−4599.
(50) Alam, R.; Fontaine, D. M.; Branchini, B. R.; Maye, M. M. Designing Quantum Rods for Optimized Energy Transfer with Firefly Luciferase Enzymes. *Nano Lett.* **2012**, *12*, 3251−3256.
(51) Alam, R.; Karam, L. M.; Doane, T. L.; Coopersmith, K.; Fontaine, D. M.; Branchini, B. R.; Maye, M. M. Probing Bioluminescence Resonance Energy Transfer in Quantum Rod-Luciferase Nanoconjugates. *ACS Nano* **2016**, *10*, 1969−1977.
(52) Holla, A.; Skerra, A. Comparative Analysis Reveals Selective Recognition of Glycans by the Dendritic Cell Receptors DC-SIGN and Langerin. *Protein Eng., Des. Sel.* **2011**, *24*, 659−669.
(53) Wang, W.; Kong, Y.; Jiang, J.; Tian, X.; Li, S.; Akshath, U. S.; Tiede, C.; Hondow, N.; Yu, A.; Guo, Y.; Zhou, D. Photon Induced Quantum Yield Regeneration of Cap-Exchanged CdSe/CdS Quantum Rods for Ratiometric Biosensing and Cellular Imaging. *Nanoscale* **2020**, *12*, 8647−8655.
(54) Zhou, D.; Bruckbauer, A.; Abell, C.; Klenerman, D.; Kang, D.-J. Fabrication of Three-Dimensional Surface Structures with Highly Fluorescent Quantum Dots by Surface-Templated Layer-by-Layer Assembly. *Adv. Mater.* **2005**, *17*, 1243−1248.
(55) Zhou, D.; Bruckbauer, A.; Ying, L.; Abell, C.; Klenerman, D. Building Three-Dimensional Surface Biological Assemblies on the Nanometer Scale. *Nano Lett.* **2003**, *3*, 1517−1520.
(56) Wang, W.; Guo, Y.; Tiede, C.; Chen, S.; Kopytynski, M.; Kong, Y.; Kulak, A.; Tomlinson, D.; Chen, R.; McPherson, M.; Zhou, D. Ultraefficient Cap-Exchange Protocol To Compact Biofunctional Quantum Dots for Sensitive Ratiometric Biosensing and Cell Imaging. *ACS Appl. Mater. Interfaces* **2017**, *9*, 15232−15244.
(57) Hooper, J.; Liu, Y.; Budhadev, D.; Ainaga, D. F.; Hondow, N.; Zhou, D.; Guo, Y. Polyvalent Glycan Quantum Dots as a Multifunctional Tool for Revealing Thermodynamic, QKinetic, and Structural Details of Multivalent Lectin−Glycan Interactions. *ACS Appl. Mater. Interfaces* **2022**, *14*, 47385−47396.
(58) Förster, T. Zwischenmolekulare Energiewanderung und Fluoreszenz. *Ann. Phys.* **1948**, *437*, 55−75.
(59) Hondow, N.; Brydson, R.; Wang, P.; Holton, M. D.; Brown, M. R.; Rees, P.; Summers, H. D.; Brown, A. Quantitative Characterization of Nanoparticle Agglomeration Within Biological Media. *J. Nanopart. Res.* **2012**, *14*, 977.
(60) Feinberg, H.; Guo, Y.; Mitchell, D. A.; Drickamer, K.; Weis, W. I. Extended Neck Regions Stabilize Tetramers of the Receptors DC-SIGN and DC-SIGNR*. *J. Biol. Chem.* **2005**, *280*, 1327−1335.
(61) Tabarani, G.; Thépaut, M.; Stroebel, D.; Ebel, C.; Vivès, C.; Vachette, P.; Durand, D.; Fieschi, F. DC-SIGN Neck Domain Is A pH-Sensor Controlling Oligomerization: SAXS and Hydrodynamic Studies of Extracellular Domain. *J. Biol. Chem.* **2009**, *284*, 21229−21240.



https://doi.org/10.1021/acsanm.2c05247
ACS Appl. Nano Mater. 2023, 6, 4201−4213

# Appendix C

nature communications

Article

https://doi.org/10.1038/s41467-024-51925-2

# Spatial segregation of catalytic sites within Pd doped H-ZSM-5 for fatty acid hydrodeoxygenation to alkanes

Received: 14 September 2023

Accepted: 21 August 2024

Published online: 04 September 2024

Check for updates

Shengzhe Ding[1,2], Dario Luis Fernandez Ainaga[3], Min Hu[1], Boya Qiu[1], Ushna Khalid[1], Carmine D'Agostino[1,4], Xiaoxia Ou[1,5], Ben Spencer[6,7], Xiangli Zhong[6,7], Yani Peng[1], Nicole Hondow[3], Constantinos Theodoropoulos[1], Yilai Jiao[8], Christopher M. A. Parlett[1,9,10,11] ✉ & Xiaolei Fan[1,5,12] ✉

Spatial control over features within multifunctional catalysts can unlock efficient one-pot cascade reactions, which are themselves a pathway to aviation biofuels via hydrodeoxygenation. A synthesis strategy that encompasses spatial orthogonality, i.e., one in which different catalytic species are deposited exclusively within discrete locations of a support architecture, is one solution that permits control over potential interactions between different sites and the cascade process. Here, we report a Pd doped hierarchical zeolite, in which Pd nanoparticles are selectively deposited within the mesopores, while acidity is retained solely within the micropores of ZSM-5. This spatial segregation facilitates hydrodeoxygenation while suppressing undesirable decarboxylation and decarbonation, yielding significant enhancements in activity (30.6 vs 3.6 $mol_{dodecane}$ $mol_{Pd}^{-1}$ $h^{-1}$) and selectivity ($C_{12}$:$C_{11}$ 5.2 vs 1.9) relative to a conventionally prepared counterpart (via wet impregnation). Herein, multifunctional material design can realise efficient fatty acid hydrodeoxygenation, thus advancing the field and inspiring future developments in rationalised catalyst design.

Cascade reactions, particularly catalytic cascades, are powerful strategies for complex multistep chemical processes within pharmaceuticals[1], agrochemicals[2], and biorefining[3,4]. Such synthetic approaches can reduce the number of product isolation steps while also permitting alternative reaction pathways that may not otherwise be feasible, for example, where an unstable intermediate prevents its isolation[5,6]. This reduction in chemical separations increases the overall energy and atom efficiency, benefiting process economics[7]. One-pot catalytic cascades typically require coupling of at least two individual catalytic materials or combining two or more catalytic species on a single material, i.e. multifunctional materials[8–11]. The latter, in particular, is already showing great potential, including for reactions such as Fischer-Tropsch[12,13], transesterification[9,14] and xylose valorisation to γ-valerolactone[15,16]. These have necessitated the amalgamation of a range of different pairs

[1]Department of Chemical Engineering, The University of Manchester, Manchester M13 9PL, UK. [2]Institute of Catalysis Science, Beijing Research Institute of Chemical Industry, Sinopec, Beijing 100013, China. [3]School of Chemical and Process Engineering, University of Leeds, Leeds LS2 9JT, UK. [4]Dipartimento di Ingegneria Civile, Chimica, Università di Bologna, 40131 Bologna, Italy. [5]Nottingham Ningbo China Beacons of Excellence Research and Innovation Institute, Ningbo 315100, China. [6]Henry Royce Institute, The University of Manchester, Manchester M13 9PL, UK. [7]Department of Materials, The University of Manchester, Manchester M13 9PL, UK. [8]Shenyang National Laboratory for Materials Science, Chinese Academy of Sciences, Shenyang 110016, China. [9]Diamond Light Source, Harwell Science and Innovation Campus, Didcot, Oxfordshire OX11 0DE, UK. [10]University of Manchester at Harwell, Harwell Science and Innovation Campus, Didcot, Oxfordshire OX11 0DE, UK. [11]UK Catalysis Hub, Rutherford Appleton Laboratory, Harwell, Oxfordshire OX11 0FA, UK. [12]Institute of Wenzhou, Zhejiang University, Wenzhou 325006, China. ✉e-mail: christopher.parlett@manchester.ac.uk; xiaolei.fan@manchester.ac.uk

of active sites, including metal and acid, acid and base, and Lewis and Brønsted acids. The combined sites either act alone, with one site for each distinct step of the cascade[17], or synergistically to promote one step[18] or the entire cascade[19]. Furfural upgrading to γ-valerolactone, is an example of the former, with transfer hydrogenation of the carbonyl group over Lewis acid sites and subsequent hydrolytic ring-opening over Brønsted acid sites[20]. Conversely, phenol hydroalkylation requires the interaction of metal and acid sites[21,22]. The rational design of multifunctional catalysts for cascade processes, therefore, requires attention regarding the reaction sequence and the mechanisms of each step. Furthermore, the order in which the distinct catalytic species are encountered within the cascade process is also critical if there is the potential for side reactions or unwanted interactions[9]. Thus, consideration of whether a random distribution of sites is acceptable or if the cascade dictates that careful engineering of the spatial location of different active sites (i.e. segregated) is needed is also imperative.

A core-shell structure has shown to be beneficial towards Fischer-Tropsch synthesis, with intermediate olefins (>$C_5$), produced at a metallic core, further converted to aromatic species within the microporous zeolite shell. The micropores give rise to prolonged diffusion, which assists the final step of the process[11,23]. Alkane isomerisation and cracking can likewise be tuned from nanoscale active site separation either within a core-shell architecture or on a binder zeolite composite, with control over metal deposition sites of the latter based on the difference between isoelectric points of alumina and zeolites[24,25]. Spatially orthogonal catalysts based on a hierarchical porous network have also resulted from their nanoscale design, with the mesopores and macropores of a silica framework selectively functionalised with two different catalytic species to govern the catalytic reaction sequence[9,26]. However, basing the design on duel templated mesoporous macroporous silicas can require controlled selective extraction of the two different pore templating agents individually.

Biofuels, preferably from feedstocks that do not compete with food supplies, have the potential to, in part, address carbon emissions through the replacement of fossil fuels. The aviation sector is one critical sector where biofuels can play a key role, given the steady growth of global air traffic demand (~5% per year) and the lack of other fuel alternatives at appropriate technology maturity[27,28]. Hydrodeoxygenation (HDO) of fatty acids (and triglycerides) to alkanes, ideally under mild reaction conditions (<300 °C), provides one of the most promising economically viable solutions under investigation[29,30]. Much of the focus to date has encompassed the union of noble metal catalytic sites with strong acidity, the latter vital to driving the HDO process. For example, Pd/C and Pd/$Al_2O_3$ strongly favour decarboxylation/decarbonylation ($DCO_x$), releasing $CO_2$ and CO as by-products, when operating at high process temperatures (>300 °C)[29]. Pd/$SiO_2$ and Pd/$TiO_2$ are active for succinic acid HDO, although selectivity often favours (slightly) the cyclic γ-Butyrolactone, which can be envisaged as an intermediate of the diol, with Pd particle size a critical parameter[31,32]. Adding acidity to the catalytic system, either by employing alumina silicates or through grafting heteropolyacids, is beneficial, introducing a propensity for HDO while simultaneously promoting fatty acid conversion[33–35]. The reaction pathway, based on experimental and kinetic modelling of biomass-derived species, is considered a multistep cascade process. Carboxylic acids are sequentially reduced to the corresponding alcohol, via the aldehyde intermediate, over metal sites. Subsequent alcohol dehydration yields alkenes, which in turn can undergo facile hydrogenation to saturated hydrocarbons while retaining the original carbon chain length. The alcohol intermediate may also undergo direct hydrogenation to the alkane, attributed to the absence of alkene detection, although this may reflect the significant low activation energy of C=C hydrogenation, while the formation of esters, ethers and aldol condensation products are other potential side reactions[36,37]. These latter pathways provide a circular route via their conversion back into the constituent species. Decreased carbon chain length species result from decarboxylation and decarbonylation, with the intermediate aldehyde a potential candidate for the latter, for which Ni/ZSM-5 has shown high and tunable selectivity towards[37,38]. Overall, catalyst composition governs the propensity towards this array of different reactions (e.g. HDO, $DCO_x$, coupling), with choice of metal, acidity (including that of the support) and mass transfer, either singularly or combined, controlling factors[37,38]. Bimetallic systems, specifically incorporating Lewis acid sites (e.g. $MoO_x$, $Nb_2O_5$, $ReO_x$) into Pd or Pt based catalysts, also show potential for HDO through switching off the $DCO_x$ pathway[39,40]. Nevertheless, in the case of Re, an optimal promoter, the synthesis condition can be critical due to the multi-oxidation state species reported to be responsible, the necessity for the two metals to be adjoined[41], and the potential for Re leaching from the final catalyst[42]. Furthermore, Brønsted acidity may need to be added, achievable through a physical mixture with a zeolite, if alkane production is to be realised[43], while low operating temperatures of the bimetallic system, typically less than 200 °C, can take a toll on activity.

Here, we report the development of a simple strategy to prepare multifunctional catalytic materials with spatially segregated metal and acidic sites based on industrially relevant zeolite materials. Hierarchical mesoporous-microporous ZSM-5 zeolite is deployed as both catalysts, given its inherent acidity, and catalyst support to host deposited metal sites. The combination of Brønsted acid sites and Pd has shown the capacity for HDO, but to date, not within spatially orthogonal systems. Active site location is governed by size exclusion effects, with acid sites selectively extracted from the mesopores and replaced with preformed Pd metal nanoparticles (NPs). The choice of a mono-metallic Pd species over a bimetallic system was to entrench a degree of simplicity within what is already a multistep synthesis, albeit one amenable to scale-up. The spatial segregation of these two distinct catalytic active species shows profound benefit for the one-pot cascade HDO of the lauric acid to $C_{12}$ alkanes, a model reaction for catalytic HDO fatty acid upgrading to biofuel equivalents of diesel and kerosene. This design strategy represents a generic platform for multifuncional materials, including catalysts of industrial interest, in particular for producing those in which spatial separation of different chemical functionalities is desired.

## Results and discussion

### Controlling Pd site location within hierarchical ZSM-5

Hierarchical $H^+$ form ZSM-5 (H-MZSM5) arises from the post-synthetic treatment of the parent zeolite (H-ZSM-5) with NaOH, evidenced by a characteristic Type IV isotherm, Barrett–Joyner–Halenda (BJH) pore size analysis, and electron microscopy, as shown in Fig. 1 and Supplementary Fig. 1. The formation of mesopores, with an average diameter of 8.6 nm (Fig. 1b), gives rise to a fivefold increase in mesopore volume, while a relative crystallinity of 80.6% and comparable micropore volume confirm preservation of micropore network (Supplementary Table 1 and Supplementary Fig. 1b). The presence of mesopores is subsequently exploited for the selective deposition of metal NPs solely within these domains through size exclusion, as illustrated in Fig. 1a. Pd NPs, possessing an average diameter of 4.6 ± 1.3 nm (Supplementary Fig. 2), are deposited exclusively outside of the micropores of the hierarchical architecture (PdNP/H-MZSM5). This spatial control is governed by the difference in pore diameter, 8.6 nm (meso) vs 0.54–0.56 nm (micro), thus, preformed Pd NPs can reside only at the external surface and/or within the mesopores of H-MZSM5. Furthermore, spatial separation of Pd and acid sites is realised with Brønsted acid sites (i.e. Al-$O^{(H)}$-Si) principally located within the retained micropores. Conversely, conventional impregnation and thermal processing of a Pd salt ($Pd_{imp}$/H-MZSM5) cannot achieve this active site spatial separation (Fig. 1).

High-angle annular dark-field scanning transmission electron microscopy (HAADF-STEM) of PdNP/H-MZSM5 and $Pd_{imp}$/H-MZSM5 shows a distinct difference in the distribution and size of Pd within the

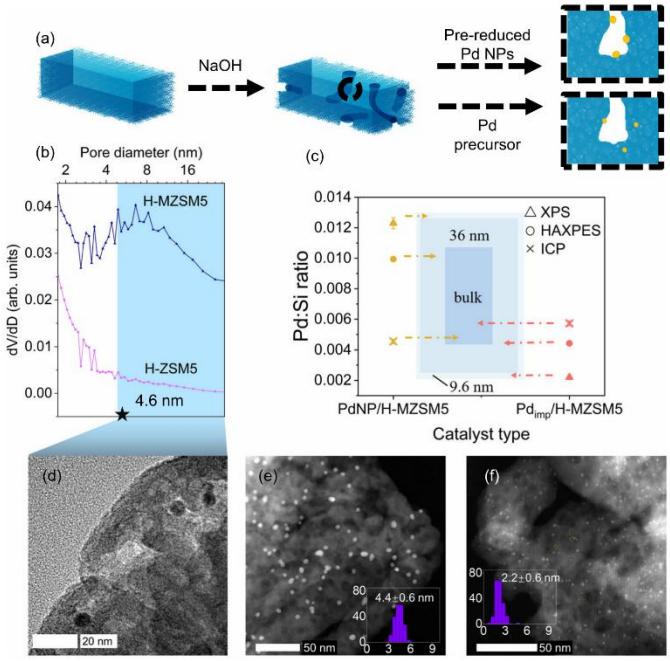


**Fig. 1 | Catalyst synthesis and physicochemical properties. a** Graphic illustration of catalyst synthesis. **b** Pore size distribution based on the BJH method with Faas correction using the adsorption branch of $N_2$ physisorption isotherms. **c** Pd:Si molar ratio by X-ray photoelectron spectroscopy (XPS), hard X-ray photoelectron spectroscopy (HAXPES) and inductively coupled plasma optical emission spectroscopy (ICP). **d** TEM image of PdNP/H-MZSM5. **e** HAADF-STEM image of PdNP/H-MZSM5 (inset: Pd particle size distribution). **f** HAADF-STEM image of Pd$_{imp}$/H-MZSM5 (inset: Pd particle size distribution). The error on the average particle sizes reported is the standard deviation of the dataset.

porous support framework. The conventional preparation route, namely Pd$_{imp}$/H-MZSM5, produces highly dispersed small Pd NPs (2.2 ± 0.6 nm) in conjunction with sub-1-nm Pd clusters, as shown in Fig. 1f and Supplementary Fig. 1. These species are randomly distributed throughout the three-dimensional hierarchical ZSM-5 skeleton, including within micropores, as confirmed by HAADF-STEM energy dispersive x-ray spectroscopy (EDX), consistent with previous investigations in which metal nanoparticles larger than the micropore diameter have been confirmed inside the zeolite framework[44]. Thus, such a synthesis approach endorses Pd integration within the micro and mesopores, i.e. uncontrollably across the entire hierarchical pore network and hence non-selectively[45]. The combination of Pd NPs and clusters results in a Pd dispersion of 26.5% (Supplementary Table 2). In contrast, PdNP/H-MZSM5 displays only Pd NPs, with an average diameter of 4.4 ± 0.6 nm (Fig. 1e), which are consistent with the parent unsupported NPs and naturally possess a lower dispersion (11.9%, Supplementary Table 2). Therefore, given their sizes and the size of the two distinct pore domains, and in conjunction with the imaging, Pd NPs reside selectively and exclusively in the mesopores and outer surface of the support matrix, as evidenced by Fig. 1d, e, for PdNP/H-MZSM5, whilst Pd is present in the micro and mesopores in Pd$_{imp}$/H-MZSM5 (Fig. 1f). It is worth pointing out that incorporating Pd, via either route, does not lead to micropore blockage. Comparable micropore properties to the parent zeolite (Supplementary Table 1) provides evidence of the highly accessible hierarchical framework structure.

Further evidence of the difference in Pd distribution within the two catalysts is afforded through the combination of inductively coupled plasma (ICP) (Supplementary Table 2), X-ray photoelectron spectroscopy (XPS) and hard X-ray photoelectron spectroscopy (HAXPES) (Fig. 1c and Supplementary Fig. 3). Bulk elemental analysis (ICP) confirms comparable Pd:Si ratios, 0.0045 for 0.81 wt% PdNP/H-MZSM5 and 0.0057 for 1.02 wt% Pd$_{imp}$/H-MZSM5, respectively. Due to the inherent sampling depths of XPS and HAXPES, ~9.6 nm for Al Kα vs ~36 nm for Ga Kα, for which 63% of the signal originates from the top 3.2 and 12 nm, respectively, they provide pseudo surface vs pseudo bulk analysis[46], i.e. they probe depth-dependence of Pd species across the two catalysts. A significantly higher Pd concentration at the surface (external and within directly accessible mesopores) is identified by XPS for PdNP/H-MZSM-5, whilst HAXPES reveals an intermediate Pd:Si ratio of the three techniques. This trend completely flips for Pd$_{imp}$/H-MZSM5, with comparable ratios for HAXPES and ICP and a significant drop for XPS, indicative of significant levels of Pd migration into the bulk of the zeolite skeleton during impregnation, a feat not observed of PdNP/H-MZSM5. Both catalytic materials consist of Pd metal, with only a trace amount of PdO detected in Pd$_{imp}$/H-MZSM5, again reflecting the smaller NP size and, thus, increase in surface-to-bulk ratio and, therefore, greater surface PdO concentration[47].

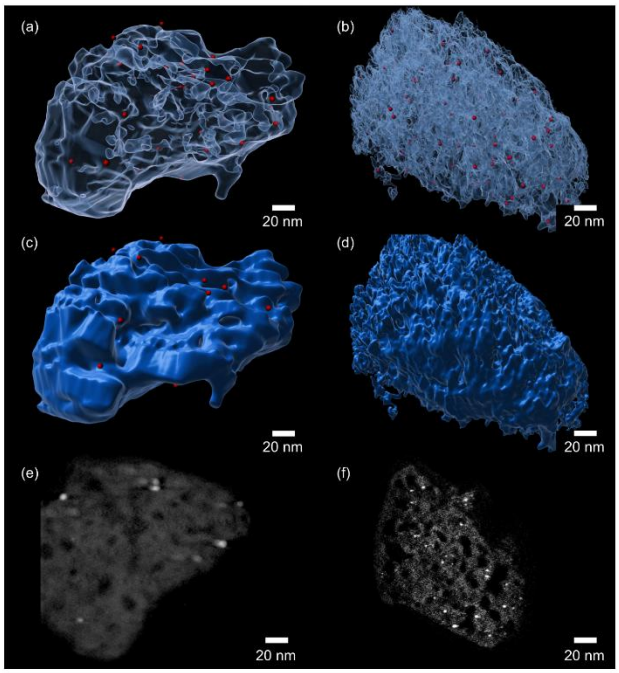


**Fig. 2 | STEM tomogram reconstructions. a**, **c** PdNP/H-MZSM5 and **b**, **d** $Pd_{imp}$/H-MZSM5, with the Zeolite set as semi-transparent in (**a**, **b**) and non-transparent in (**c**, **d**). Cross-section slices from the centre of the catalyst are presented in **e** PdNP/H-MZSM5 and **f** $Pd_{imp}$/H-MZSM5.

Three-dimensional tomography reconstructions of PdNP/H-MZSM5 and $Pd_{imp}$/H-MZSM5, produced from tilt-series HAADF-STEM imaging, were established to study the distribution of Pd NPs through the two catalysts (Fig. 2 and Supplementary Videos 1–4) and further validate the distinct difference in Pd location between the two catalysts. Semi and non-transparent rendering of the zeolite framework, Fig. 2a–d, shows a degree of Pd located on the external surface within PdNP/H-MZSM5, whilst the same is not apparent in $Pd_{imp}$/H-MZSM5. Consistent with our expected deposition locations within the two systems, Pd within $Pd_{imp}$/H-MZSM5 is more uniformly distributed through the meso and micropores, while Pd in PdNP/H-MZSM5 is compartmentalised at external sites and within directly accessible mesopores. Cross-section slices through the reconstructions (Fig. 2e, f and Supplementary Fig. 4), taken from the centre of the zeolite particle, reinforce our deduction that Pd in PdNP/H-MZSM5 is located within mesopores close to the external surface of the zeolite crystal, whereas $Pd_{imp}$/H-MZSM5 comprises Pd NPs within the interior region of the framework, with species present within the micropores and mesopores. For Pd residing within the micropores, the NPs can span multiple micropores or can induce the partial collapse of the localised framework. Thus, Pd NPs larger than a single micropore exists but are encapsulated within the micropore framework, i.e. accessible only via a micropore[44]. Identification of Pd in the same location in the cross-section slices above and below those in Fig. 2, as shown in Supplementary Fig. 4, verifies our identification of Pd within the tomogram and the corresponding slices.

### Mutually exclusive sites within hierarchical ZSM-5

Having developed a protocol to selectively deposit Pd NPs within mesopores of hierarchical ZSM-5, the attention can turn to the intrinsic Brønsted acid sites within ZSM-5. The aim to truly segregate the two different sites is complicated given the capacity for mesopores, in addition to micropores, to accommodate surface acid sites, both Brønsted and Lewis, the latter due to extra-framework aluminium species[48]. Therefore, removing such surface acidity within the mesopores is paramount to completely segregating two active species. The deployment of a bulky chelating agent, diethylenetriaminepentaacetic acid (DPTA), with a molecule diameter of ~0.9 nm (Supplementary Fig. 5) permits selective extraction of Al species (via complexation) from the mesopores/outer surface areas only[49,50], as depicted in Fig. 3a. Post-DPTA treatment (H-MZSM5-DA) crystallinity and porosity of the zeolite framework are unaffected, as evidenced by XRD and $N_2$ porosimetry (Supplementary Fig. 6 and Supplementary Table 1). Furthermore, this dealumination treatment restores Si:Al close to that of the parent ZSM-5, 34 (H-MZSM5-DA) and 40 (H-ZSM-5), an increase from 24 for H-MZSM5 (resulting from the initial desilication).

Acid-base titration using 2,6-ditertbutylpyridine (DTBPy), 3,5-dimethylbenzylamine (DBAM in acetone), and ethylenediamine (EDA) enables either partial or total titrations of the acid sites within the hierarchical zeolite catalysts due to steric limitations for DTBPy and DBAM relative to EDA. The large molecular dimension of DTBPy, kinetic diameter of 1.05 nm[51], limits its interaction to solely acid sites within the mesopores and on the external surface. Attenuated total

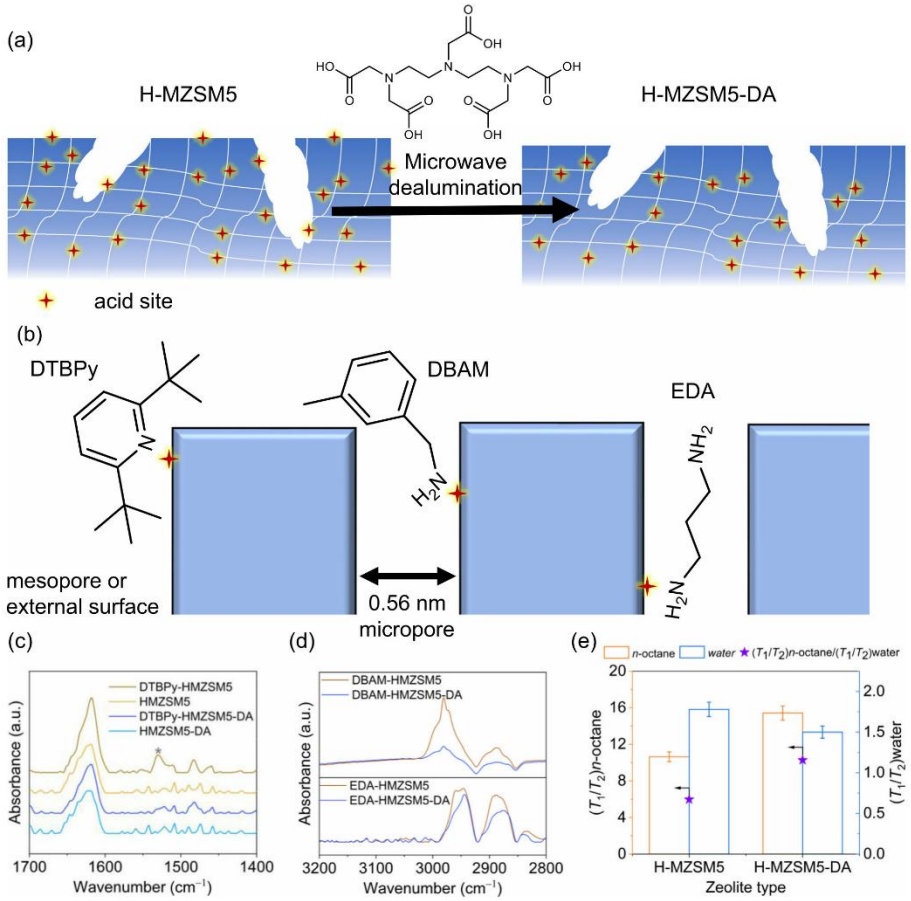


**Fig. 3 | Investigation of acid site location in H-MZSM5 and H-MZSM5-DA.** **a** Schematic of H-MZSM5 dealumination. **b** Schematic of using 2,6-di-tert-butylpyridine (DTBPy), 3,5-dimethylbenzylamine (DBAM) and ethylenediamine (EDA) as probes to titrate acid sites. **c** ATR-IR spectra for the DTBPy-titrated H-MZSM5 and H-MZSM5-DA and their pure zeolite equivalents. **d** ATR-IR spectra for DBAM- and EDA-titrated H-MZSM5 and H-MZSM5-DA. **e** NMR relaxation $T_1/T_2$ ratios of *n*-octane and water in H-MZSM5 and H-MZSM5-DA and corresponding $(T_1/T_2)_{n\text{-octane}}/(T_1/T_2)_{water}$. The relative error on $T_1/T_2$ measurements is ~±5%.

reflection infrared (ATR-IR), shown in Fig. 3c, confirms DTBPy only adsorbs on H-MZSM5. The band at ~1530 $cm^{-1}$ is attributed to the $DTBPyH^+$ ion[52] from the interaction of DTBPy with Brønsted acid sites[53], thus validating the absence of acid sites at the external surface and within mesopores for the DPTA-treated zeolite (H-MZSM5-DA). In comparison, in addition to titrating external and mesopore-bound acid sites, DBAM, based on the pendant amine chain length, probes acid sites at a depth of up to ~0.3 nm into a micropore (Fig. 3b). CH stretching bands are observed in the region of 2800–3000 $cm^{-1}$ by ATR-IR, shown in Fig. 3d, with the intensity of these bands for H-MZSM5-DA greatly reduced relative to the parent material. This reduced acid site density is consistent with the successful removal of the mesopore and external surface acidity, with DBAM adsorbed at acid sites within the micropores close to the mesopores and external surface, i.e. within the first zeolite cage from the mesopores or external surface. In contrast, EDA is unselectively adsorbed, titrating sites in the micropores, mesopores, and outer surfaces. CH stretch intensities reveal only a slight drop post-DPTA treatment (Fig. 3d), which again is consistent with the selective removal of sites from the mesopores and external surface only. Based on the combined results from the acid-base titrations, it can be concluded that DPTA treatment of H-MZSM-5 selectively extracts acidity from the mesopores and external surfaces only, with the characteristic micropore acidity of the zeolite, even in the micropores adjoining the mesopores and external zeolite surface, retained.

$NH_3$-TPD (Supplementary Fig. 6c) further confirms the decrease in total acidity. Weak and strong acid peak intensity, evaluated by desorption below and above 300 °C, respectively, reveals H-MZSM5-DA

possesses lower weak (0.219 vs 0.320 mmol $g^{-1}$) and strong acidity (0.340 vs 0.396 mmol $g^{-1}$), with the loss of weak site symptomatic of the removal of Al from outside the micropore framework. A side effect of removing acidity is the potential change in the hydrophobic-hydrophile nature of the material[54], with NMR relaxation used to probe internal hydrophobicity/hydrophilicity[55,56]. As shown in Fig. 3e, Supplementary Fig. 7, and Supplementary Table 3, T1 and T2 NMR relaxation times of water and *n*-octane in H-MZSM5 and H-MZSM5-DA probed variations in hydrophobicity. After post-treatment with DPTA, the zeolite framework becomes more hydrophobic, confirmed by a 16% reduction of the $T_1/T_2$ of water, i.e. 1.5 vs 1.8. Conversely, the interaction with the organic non-polar hydrocarbon probe, *n*-octane, is enhanced, with a $T_1/T_2$ ratio of 15.4 for H-MZSM5-DA vs 10.6 for H-MZSM5. The subsequent ratio of the $T_1/T_2$ values of *n*-octane to water is indicative of the relative surface affinity towards hydrocarbons relative to water[57,58]. As shown in Fig. 3e, DPTA removal of Al increases hydrophobicity (and correspondingly the affinity for hydrocarbons), which has been shown to be beneficial for catalytic reactions in which water is the by-product through its displacement from the catalyst[59–61]. The interaction of a model substrate and intermediate, 1-nonanoic acid and 1-nonanol, respectively, with the zeolites (H-MZSM5 and H-MZSM5-DA) can be considered to arise from a combination of the non-polar hydrocarbon chain and polar functional group, i.e. an intermediate of the two initial probes (water and n-octane) rather than one dominating over the other (shown in Supplementary Fig. 8 and Supplementary Table 3). Dealumination results in an increase in interaction for both model substrate and intermediate, reflecting a significant affinity between the hydrocarbon chain and the increased hydrophobic mesopore surface rather than a decreased interaction due to the repulsion of the polar functional group.

Having successfully extracted acidity from the mesopores and external surface to produce H-MZSM5-DA, the selective deposition of Pd, via the route deployed for PdNP/H-MSM5, yields a spatially orthogonal system with true active site compartmentalisation, i.e. acid sites only in micropores and Pd solely in mesopores and on external surfaces (PdNP/H-MSM5-DA). Supplementary Fig. 9 and Supplementary Table 1 reveal its analogous nature to its parent zeolite (where applicable) and PdNP/H-MZSM-5, with equivalent porosity (surface areas, pore volumes and pore diameter), PdNP size (4.5 ± 0.9 nm from HAADF-STEM), and Pd:Si atomic ratios from surface, semi-bulk, and bulk analysis (0.0125 for XPS, 0.0118 for HAXPES, and 0.0048 for bulk analysis, to be compared with Fig. 1c) substantiating their comparable physicochemical nature. However, close inspection of the Pd *3d* XPS reveals a subtle shift to lower binding energy. Given the identical Pd particle sizes for PdNP/H-MSM5 and PdNP/H-MSM5-DA, this shift in energy must arise from the interaction with the acid site and is not a result of size effects. This shift results from interactions between the mesopore-located acid sites (both Brønsted and Lewis) and the Pd NPs within PdNP/H-MZSM-5. The acidity imparts an δ+ charge on the Pd NPs, and hence a higher binding energy[62,63]. Thus, removing these acid sites eradicates this influence on the electronic nature of the deposited Pd NPs, i.e. further evidence of the absence of mesopore acid sites in PdNP/H-MSM5-DA. XPS of $Pd_{imp}$/H-MZSM5 reveals a larger impact on Pd binding energy, attributed to the smaller PdNP size, here being both a particle size effect and a greater Pd-acid site interaction. $PdNP_{small}$/H-MZSM5 (Supplementary Fig. 9), prepared using pre-reduced Pd NPs with a diameter of only 2.7 ± 0.5 nm, shows an identical degree of mesopore acid site influence.

### Catalytic cascade HDO of Lauric acid to alkanes

We propose that the spatial segregation within the reported catalytic systems should be beneficial to a cascade hydrodeoxygenation that proceeds stepwise as follows: reduction (carboxylic acid to alcohol) in the mesopores over Pd, dehydration (alcohol to alkene) in the micropores over acid sites, and finally hydrogenation (alkene to alkane) over Pd in the mesopores, with the alkane product diffusing to the bulk reaction media, i.e. cascade intermediates are contained within the zeolite framework and subsequently consumed until the final product is generated. The stepwise cascade pathway is illustrated in Fig. 4, which is also observed for Ni/ZSM-5 and Mo/ZSM-22[64,65]. Observing cascade intermediate species is dependent on the catalyst configuration and species reactivity, e.g. carbonyl and alkene intermediates are often not observed due to rapid conversion[36,37], i.e. they are consumed before they can accumulate in the bulk solution.

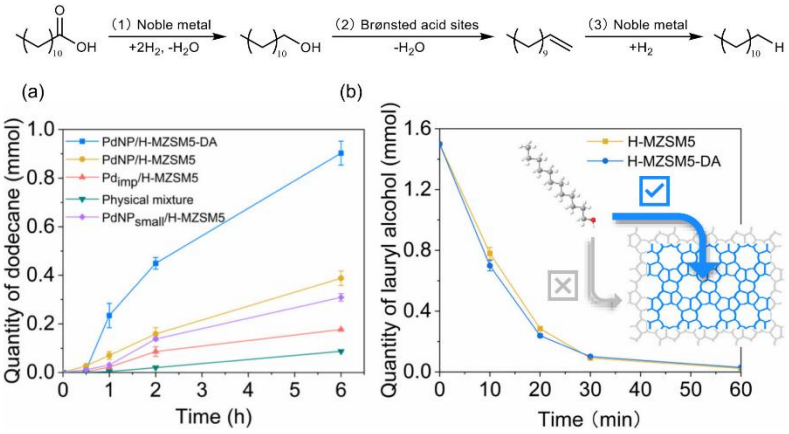


**Fig. 4 | HDO cascade reaction pathway of lauric acid to dodecane. a** HDO of lauric acid monitored from dodecane yield over PdNP/H-MZSM5-DA, PdNP/H-MZSM5, $Pd_{imp}$/H-MZSM5, $PdNP_{small}$/H-MZSM5 and physical mixture of H-MZSM5 + PdNP/Na-MZSM5. Reaction conditions: 100 mg 1 wt% Pd-doped catalyst, 300 mg lauric acid, 0.1 $cm^3$ of nonane as the internal standard, 40 $cm^3$ of hexane as the solvent, at 200 °C, 30 bar and 1000 rpm for 6 h. **b** Dehydration of lauryl alcohol of H-MZSM5 and H-MZSM5-DA to evaluate the rate of intermediate conversion, with the inset showing the location of dehydration reactions within the zeolite. Error bars in (**a**, **b**) correspond to the standard deviation of the average taken over at least two independent measurements.

**Table 1 | Lauric acid HDO performance over conventional prepared and spatial compartmentalised catalysts.[a]**

| Catalysts | Acid Conv., % | $C_{12}$ Sel., % | $C_{11}$ Sel., % | Productivity [b] ($mol_{C12}$ $mol_{Pd}^{-1}$ $h^{-1}$) | TON[c] |
|---|---|---|---|---|---|
| H-MZSM5 | 0 | 0 | 0 | 0 | 0 |
| PdNP/Na-MZSM5 | 2.2 | 27.3 (alcohol) | 0 [d] | 0.05 (alcohol) | 29 |
| H-MZSM5 + PdNP/Na-MZSM5 [e] | 20.6 | 28.1 | 2.1 | 1.7 | 278 |
| PdNP/H-MZSM5 | 51.0 | 51.8 | 9.9 | 11.9 | 689 |
| $Pd_{imp}$/H-MZSM5 | 31.2 | 38.4 | 20.5 | 3.6 | 187 |
| PdNP/H-MZSM5-DA | 94.1 | 64.9 | 12.6 | 30.6 | 1272 |
| $Pd_{imp}$/H-MZSM5-DA | 70.9 | 39.9 | 18.2 | 11.3 | 426 |
| $PdNP_{small}$/H-MZSM5 | 50.9 | 40.4 | 14.9 | 9.9 | 688 |
| $PdNP_{small}$/H-MZSM5-DA[f] | 71.5 | 59.3 | 24.4 | 28.1 | 1205 |

[a]Reaction conditions: 100 mg 1 wt% Pd-doped catalyst, 300 mg lauric acid, 0.1 $cm^3$ of nonane as the internal standard, 40 $cm^3$ of hexane as the solvent, at 200 °C, 30 bar and 1000 rpm for 6 h.
[b]Production rate was calculated based on the yield of n-$C_{12}$ + iso-$C_{12}$ in 2 h, as shown in Fig. 4a. The unit is $mol_{dodecane}$ $mol_{Pd}^{-1}$ $h^{-1}$, in which the quantity of Pd is based on Pd loading from ICP.
[c]TON calculated based on moles of lauric acid converted at 6 h by surface Pd.
[d]The concentration of $C_{11}$ is below the GC detection limit.
[e]Physical mixture of 100 mg H-MZSM5 and 100 mg PdNP/Na-MZSM5.
[f]80 mg 1 wt% Pd-doped catalyst. The errors of conversion and selectivity are within ±3%, whereas yields and production rates are within ±5%.

HDO of lauric acid (dodecanoic acid) evaluates the effectiveness of PdNP/H-MZSM-5 and PdNP/H-MZSM5-DA relative to $Pd_{imp}$/H-MZSM5 and a physical mixture of monofunctional catalysts, H-MZSM5 (acid only) and PdNP/Na-MZSM5 (Pd only). The latter was prepared by applying the same synthesis strategy as PdNP/H-MZSM5 to the $Na^+$ form equivalent zeolite, which possesses similar Pd properties (Supplementary Table 2 and Supplementary Fig. 10), albeit with a reduced Pd binding energy due to electron donation from the alkali metal[66]. Optimised reaction conditions are established on dodecane total yield (combination of *n*-dodecane, *n*-$C_{12}$, and *iso*-dodecane, *iso*-$C_{12}$), shown in Supplementary Table 4 and Supplementary Fig. 11. The process also yields undecane ($C_{11}$), through undesirable $DCO_x$, this being the main by-product detected (Supplementary Fig. 12), while trace amounts of lauryl laurate from the esterification reaction between the fatty alcohol and acid are also detected. The concentration of the latter does not increase significantly over the duration of the reaction, suggesting that its formation is a minor pathway. The impact of pressure shows at ≤20 bar, only selectivity is influenced whilst conversion is comparable, whereas increasing pressure to 30 bar drives up conversion while maintaining higher $C_{12}$ selectivity. The impact of stirring rate shows no effect, as presented in Supplementary Fig. 11, ruling out bulk mass diffusion effects.

The synergy between the two sites, viz. metal and acid, is paramount to enabling HDO. Control experiments over one-site-only systems, i.e. H-MZSM-5 and PdNP/Na-MZSM5 (Table 1), reveal acidity alone is unable to convert the starting substrate. In comparison, the sole deployment of Pd via PdNP/Na-MZSM5 produces only the first intermediate product (1-dodecanol) at low levels, consistent with the initial reduction step of the cascade[67]. A physical mixture of these two materials does produce a $C_{12}$ alkane yield (Fig. 4a), thus confirming the criticality of a union of metal and acid sites for the catalytic cascade HDO. While also demonstrating the power of coupling these two sites in driving the cascade reaction forward, i.e. consumption of the alcohol by the acid sites drives the equilibrium increasing acid reduction, hence higher lauric acid conversion relative to PdNP/Na-MZSM5. However, a physical mixture does not permit governance over the order in which the different catalytic active species are encountered and is thus far from optimal[9,24–26]. When this reaction parameter is controlled by deploying PdNP/H-MZSM5, it yields a significant enhancement, with dodecane yield increasing by ~20% and a sevenfold increase in production rate, a direct consequence of dictating the reaction sequence of the cascade. Decreasing PdNP size whilst retaining spatial compartmentalisation, i.e. $PdNP_{small}$/H-MZSM5, does not reveal an anticipated kinetic enhancement from the increased Pd dispersion, i.e. faster lauric acid conversion from increased surface Pd sites. In fact, it results in reduced $C_{12}$ selectivity. Thus, decreasing Pd particle size harms overall HDO performance. This correlation between HDO performance and PdNP size is further evident from the further reduced HDO performance of $Pd_{imp}$/H-MZSM5, with a greater impact, at least partially, due to accessibility, i.e. Pd in micropore being less accessible. The drop in the capacity towards HDO, including lauric acid conversion, is in conjunction with an increase in $C_{11}$ selectivity. The latter arising from the proximity, i.e. adjacent, of Pd and acid sites, with their interaction favouring decarboxylation over HDO[68], and the decrease in Pd size[69]. Thus, decreasing Pd particles is detrimental to overall HDO performance, exacerbated by contiguous Pd and acid sites, i.e. when co-located within the micropores or mesopores of the zeolite framework. However, comparing HDO performance for materials with comparable average particle sizes, impregnation vs small Pd NPs, further highlights the benefit of spatial segregation on the HDO cascade process, with reduced $C_{11}$ formation resulting from suppressing interaction between Pd and acid sites.

While it is expected that compartmentalisation of Pd into the mesopores of PdNP/H-MZSM5 is likely beneficial for substrate diffusion, given the dimension of lauric acid (Supplementary Fig. 13), we acknowledge that a degree (albeit minor based on the $NH_3$-TPD) of acid sites co-exist within the mesopores. This raises the question regarding which sites are responsible for the alcohol dehydration step, i.e. acid sites within mesopores or micropores. The dehydration of lauryl alcohol over H-MZSM5 and H-MZSM5-DA (acid only zeolites), as shown in Fig. 4b, reveals almost identical reaction rates (1.62 and 1.74 mmol $h^{-1}$, respectively), confirming that Brønsted acid sites within the micropores of the zeolite framework drive dehydration. Thus, Pd and acid sites separated at the nanoscale operate individually for their respective steps within the cascade process but collaborate for overall optimal HDO performance. Furthermore, as shown in Fig. 4b and Supplementary Fig. 14, the rate of dehydration is significantly greater than that of lauric acid consumption (~0.3 mmol $h^{-1}$) for PdNP/H-MZSM5. The initial reduction step of the acid to the alcohol is, therefore, slower than the subsequent alcohol dehydration step, which is further supported given that cascade intermediate species are not observed, i.e. intermediates are consumed rapidly within the pore architecture of the bifunctional catalysts as substrates for the subsequent step in the cascade before having time to diffuse into the bulk reaction media. Likewise, alkene hydrogenation is another facile step in the cascade and is thus consumed before building up in the reaction media[36,37].

HDO activity further escalates with true active site compartmentalisation, with PdNP/H-MZSM5-DA showing the highest rate of dodecane production (30.6 $mol_{dodecane}$ $mol_{Pd}^{-1}$ $h^{-1}$), a 2.5-fold increase on

PdNP/H-MZSM5, and $C_{12}$ selectivity. Furthermore, the rate of lauric acid consumption increases by a comparable factor (~2). As previously observed in the non-dealumianted system, the incorporation of small Pd NPs ($PdNP_{small}$/H-MZSM5-DA) with a greater number of surface sites is not conducive to improved activity relative to its larger NP equivalent (PdNP/H-MZSM5-DA). Likewise, it induces increasing $C_{11}$ formation, although now solely due to reduced NP size[69]. That said, achieving true compartmentalisation once again is highly beneficial, as evident by the amplified activity and conversion relative to the impregnated and non-dealuminated equivalents ($Pd_{imp}$/H-MZSM5-DA and $PdNP_{small}$/H-MZSM5, respectively). While $PdNP_{small}$/H-MZSM5 does give rise to a significant increase in performance relative to $Pd_{imp}$/H-MZSM5, it does not reach the level of PdNP/H-MZSM5-DA or $PdNP_{small}$/H-MZSM5-DA, confirming the benefit of spatial orthogonality of active species on catalytic HDO. The origin of the enhancement from spatial separation of the active species resulting from the removal of the mesopore acidity is attributed to the coeffect of; (i) the elimination of the undesirable interaction between acid sites and Pd NPs, and (ii) the increased mesopore hydrophobicity, which aids the expulsion of water (the by-product of acid reduction), driving the localised equilibrium forward increasing alcohol production. Furthermore, $H_2$ dissociation on the PGM sites has been shown to be hindered by the presence of water[70]. Concurrently, increasing hydrophobicity within PdNP/H-MZSM5-DA does not negatively impact interaction with the fatty acid (discussed above) and, thus, would not negatively impact cascade process efficiency. The inherent benefit of active site spatial compartmentalisation within PdNP/H-MZSM5-DA is further evident from its capacity for HDO of other fatty acids, including palmitic (C16) and stearic (C18) (Supplementary Table 5).

Catalyst recycling studies show that PdNP/H-MZSM5-DA exhibits good recyclability (Supplementary Figs. 15, 16) without requiring reactivation between runs, whilst PdNP/H-MZSM5 shows reasonable recyclability (TON drop from 688 to 574 over three cycles). In contrast, PdNP/H-ZSM-5, comprising Pd NPs deposited on the external surface of micropore-only ZSM-5, exhibits poor catalyst recyclability, deactivating by ~90% over only two runs. HAADF-STEM imaging confirms Pd agglomeration is the root cause of this, which arises from the lack of mesopore confinement of the Pd NPs. Thus, the catalyst configuration possessed by PdNP/H-MZSM5 and PdNP/H-MZSM5-DA bestows yet another highly beneficial asset on our catalytic materials. Moreover, the formation of coke, another common deactivation pathway in zeolite catalysis, can also be ruled out. Thermogravimetric analysis of PdNP/H-MZSM5-DA (Supplementary Fig. 17) shows mass losses only below 300 °C, which we attributed to arise from the desorption of adsorbed substrate (dodecanoic acid b.p. 299 °C), intermediates (dodecanal b.p. 242 °C, dodecanol b.p. 259 °C, and dodecene b.p. 213 °C), and product (dodecane b.p. 216 °C), whereas combustion of coke species requires temperatures ≥500 °C. So, while species are adsorbed, which accounts for some of the mass balance of the process (the remaining missing mass may reflect low solubility and precipitation of the substrate during sampling), it is reasonable to assume they remain as species that partake in the cascade process. This varies from studies into unsaturated triglycerides where coking and oligomerisation are apparent due to reactivity from unsaturation in the initial substrate[71].

To further explore this approach and evaluate the impact of intrinsic zeolite acidity, the optimal synthetic route was applied to ZSM-5 with Si:Al ratios of 25 and 15. Increasing the inherent acidity of the catalytic system shows little effect on overall conversion (Supplementary Table 6), note the higher substrate concentration and lower metal loading, with only a decrease observed at the lowest Si:Al ratio. In contrast, selectivity towards HDO is compromised by the increasing acidity, which negatively impacts $C_{12}$ alkane productivity. Furthermore, switching to other zeolite frameworks, namely USY and Beta, further demonstrates the generic nature of the approach for catalyst synthesis. While resulting in superior acid conversion, it is at the expense of $C_{12}$ alkane selectivity.

In conclusion, the successfully developed a hierarchical ZSM-5 catalyst involving spatial compartmentalisation of Pd (mesopores) and acid (micropores) sites, and its influence over the one-pot HDO of lauric acid to dodecane has been demonstrated. Compared with conventional catalyst production, via impregnating with Pd salts, Pd within the spatially separated catalysts resides within mesopores and on the outer surfaces, as evidenced by electron tomography. This facilitates greater accessibility for the initial acid reduction step of the cascade, whereas the dehydration of lauric acid, the second step in the cascade, is shown to occur over acid sites within the micropores of hierarchical ZSM-5, potentially within micropores bordering mesopores. Furthermore, the segregation of Pd and acid sites impedes undesirable side reactions, i.e. decarboxylation and decarbonylation, while the elimination of mesopore acidity, tunes the hydrophobicity of the mesopores and interactions between Pd and acid sites, which further accelerates overall HDO performance. Moreover, this approach prohibits Pd blocking/binding to the acid sites, another undesirable aspect of producing such bifunctional materials. However, we do point out that here, within our $Pd_{imp}$/H-MZSM5, the acid site of the parent zeolite significantly outweighs the amount of Pd impregnated, and thus, the resulting surface Pd atoms could, in theory, only block a maximum of 3.5% of the acid sites present, i.e. the impact of such an effect can be considered inconsequential.

The benefit of employing a spatially orthogonal catalyst, through active site compartmentalisation, for lauric acid HDO is further evident when it is benchmarked against the current state-of-the-art HDO catalysts (Supplementary Table 7), in which Pd is deployed either as an active species, promotor or stabiliser. Compared with mono-metallic Pd systems[29], the higher selectivity of the catalyst reported here drives greater HDO performance, as while higher reaction temperatures deployed in the literature enhance conversion, this is at the expense of favouring $DCO_x$ over HDO. Furthermore, the benefit of spatial orthogonality within PdNP/H-MZSM5-DA is further evident from its superior performance to Pd supported randomly on acidic alumina silicates (Pd/Al-SBA-15, Pd@Al-$SiO_2$)[29,33], and zeotype materials (Pd/SAPO-31)[29], which again is due to superior selectivity. However, relative to acidity co-deposited on silicas (Pd-$Nb_2O_5$/$SiO_2$ and Pd/HPA-$SiO_2$)[34,72] and bimetallic systems (Pd/CuZnAl + ZSM-5 and Pd-Re/C + zeolite A)[40,43] it is the greater mol normalised activity of PdNP/H-MZSM5-DA that gives rise to greater HDO productivity. Comparisons are also made with Pt-based systems, with either comparable (Pt/$Nb_2O_5$) or superior (Pt/ZSM-5, Pt/$TiO_2$, Pt-Re/$TiO_2$) alkane productivities observed. Therefore, it is a combination of activity and selectivity that results in the optimal HDO performance of PdNP/H-MZSM5-DA, which equals or outperforms the current literature demonstrating the advantage of nanoscale active species segregation in catalytic cascade HDO processes. Thus, this study should inspire future HDO catalyst development while also highlighting the potential of spatial separation of active species within multifunctional materials for one-pot cascade reactions, i.e. catalysts that can facilitate the combination of multiple steps of a chemical production process within a single reactor. Furthermore, it demonstrates a generic synthesis approach for the production of bifunctional materials, in which different functionalities are compartmentalised within two distinct regions.

## Methods

### Chemicals and materials

ZSM-5 zeolite Si:Al 40 (Zeolyst International as ammonia form, CBV 8014), ZSM-5 zeolites Si:Al 15 and 25 (Fisher Scientific), sodium hydroxide (NaOH, ACROS Organics, ≥99%), ammonium nitrate ($NH_4NO_3$, ACROS Organics, ≥98%), diethylenetriaminepentaacetic acid (DPTA, Sigma Aldrich, ≥99%), tetraaminepalladium(II) nitrate solution ($Pd(NH_3)_4(NO_3)_2$, Sigma Aldrich, 10 wt.%), ethylene glycol (EG, Fisher

Scientific, ≥99%), poly(vinyl pyrrolidone) (PVP, Sigma Aldrich, $M_w$ = ~55,000), sodium tetrachloropalladate(II) ($Na_2PdCl_4$, Sigma Aldrich, ≥98%), 2,6-di-tert-butylpyridine (DTBPy, Sigma Aldrich, ≥97%), 3,5-dimethylbenzylamine (DBAM, Sigma Aldrich, ≥98%), ethylenediamine (EDA, Fluorochem, 99.0%), hexane ($CH_3(CH_2)_4CH_3$, Sigma Aldrich, ≥95%), nonane ($CH_3(CH_2)_7CH_3$, Sigma Aldrich, ≥99%), lauric acid ($CH_3(CH_2)_{10}COOH$, Sigma Aldrich, ≥98%), and lauryl alcohol ($CH_3(CH_2)_{11}OH$, Sigma Aldrich, ≥98%). All chemicals were used as received.

### Preparation of catalysts

Hierarchical ZSM-5 was prepared by alkaline desilication as reported by ref. 73. ZSM-5 Si:Al 40 was calcinated at 550 °C for 5 h (ramp rate 5 °C $min^{-1}$) to convert to the H-form (denoted H-ZSM-5). H-ZSM-5 (6 g) was vigorously stirred in aq. NaOH (0.2 M, 180 $cm^3$) at 65 °C for 0.5 h and then washed with deionised water to neutral pH. Ion exchange was carried out using aq. $NH_4NO_3$ (0.1 M, 180 $cm^3$) at 80 °C for 3 h in triplicate. The solid was isolated by centrifugation (relative centrifugal force 3000 G, 10 min), dried at 100 °C for 6 h, and calcined in air at 550 °C for 5 h (ramp rate 5 °C $min^{-1}$) to generate the H-form hierarchical ZSM-5 (denoted H-MZSM5). $Na^+$-form hierarchical ZSM-5 (sample denoted Na-MZSM5) was prepared as above, with the ion exchange step omitted.

Mesopore and external surface acid sites were removed from H-MZSM5 by microwave-assisted chelation[50]. H-MZSM5 (1 g) was dispersed in aq. DPTA (0.16 M, 15 $cm^3$) by stirring at room temperature (20 °C). The solution was heated to 100 °C (ramp rate 25 °C $min^{-1}$) and treated isothermally for 0.25 h within an Anton Paar Monowave 400 microwave reactor, followed by washing, drying and calcination at 550 °C for 5 h (ramp rate 5 °C $min^{-1}$) to give the sample H-MZSM5-DA.

Near monodisperse Pd NPs of ~4.5 nm were prepared using a procedure reported by ref. 74. PVP (450 mg) was dissolved in EG (20 $cm^3$) at 160 °C. A second solution containing $Na_2PdCl_4$ (155 mg) dissolved in EG (10 $cm^3$) at 60 °C was added to the PVP-EG solution at 160 °C under stirring. After 3 h, acetone (60 $cm^3$) was charged into the solution to precipitate Pd NPs. The solid was separated by centrifugation and washed with water and acetone (1:3, v/v) mixture in triplicate. Pd NPs were dispersed in water (30 $cm^3$) to yield a colloidal solution. Pd NPs of ~2.5 nm were prepared using an increased mass of PVP (1550 mg).

Deposition of Pd NPs on H-MZSM5 was conducted by NP impregnation. ~4.5 nm PdNP colloid (6 $cm^3$) was mixed with H-MZM5 (1 g) to give a nominal 1 wt% Pd loading. The slurry was stirred at 20 °C for 18 h, then heated to 50 °C to isolate a solid. The solid was calcined at 400 °C for 2 h (ramp rate 1 °C $min^{-1}$) and reduced at 200 °C under $H_2$ for 2 h (ramp rate 5 °C $min^{-1}$, $H_2$ 100%, flow rate 100 $cm^3$ $min^{-1}$) to yield PdNP/H-MZSM5. An identical approach was deployed for the following supports: H-ZSM-5, Na-ZSM-5, and H-MZSM5-DA, to produce catalysts denoted as PdNP/H-ZSM-5, PdNP/Na-ZSM-5, and PdNP/H-MZSM5-DA, respectively. $PdNP_{small}$/H-MZSM5 and $PdNP_{small}$/H-MZSM5-DA were prepared as above but using the ~2.5 nm PdNP colloid.

Control catalysts were prepared via conventional wet impregnation of a Pd salt. H-MZSM5 (or H-MZSM5-DA) (1 g) was suspended in an aq. $Pd(NH_3)_4(NO_3)_2$ (3 $cm^3$) solution with Pd concentration adjusted for a nominal 1 wt% Pd loading. The slurry was stirred at 20 °C for 18 h, then heated to 50 °C to isolate a solid. The solid was calcined at 500 °C for 2 h (ramp rate 1 °C $min^{-1}$) and reduced under $H_2$ at 400 °C for 2 h (ramp rate 5 °C $min^{-1}$, $H_2$ 100%, flow rate 100 $cm^3$ $min^{-1}$). The obtained catalyst is denoted $Pd_{imp}$/H-MZSM5 ($Pd_{imp}$/H-MZSM5-DA).

### Characterisation of materials

Powder X-ray diffraction (XRD) was conducted on a Philips X'Pert-PRO theta-theta PW3050/60 diffractometer with a PW3064 sample spinner and X'Celerator 1-D detector (2.122° active length) in Bragg-Brentano geometry using a copper line focused X-ray tube with Ni Kβ absorber (0.02 mm; Kβ = 1.392250 Å) Kα radiation ($K\alpha_1$ = 1.540598 Å, $K\alpha_2$ = 1.544426 Å, Kα ratio 0.5, $K\alpha_{ave}$ = 1.541874 Å). Diffraction patterns were collected from 5 to 75 ° 2 theta at 0.0334 ° step and 1.7 s $step^{-1}$. The relative crystallinity of the zeolite materials was determined by a standard integrated peak area method using 22.5–25.0° 2 theta (Eq. S1)[75].

Nitrogen adsorption/desorption isotherms were measured on a Micromeritics ASAP 2020 porosimeter. The materials were degassed under vacuum at 350 °C for 12 h before nitrogen adsorption at −196 °C. Brunauer–Emmett–Teller (BET) surface areas ($S_{BET}$) were calculated over the relative pressure range of 0.03–0.30, the specific micropore surface area ($S_{micro}$) and volume ($V_{micro}$) were calculated over the relative pressure range of 0.3–0.5 using the *t*-plot method. Pore size distribution was calculated by the Barrett–Joyner-Halenda (BJH) method with Faas correction using the adsorption branch of the isotherms.

Ammonia temperature-programmed desorption ($NH_3$-TPD) was conducted on a Quantachrome ChemBET 3000 system. Catalysts (~50 mg) were pre-treated at 550 °C (ramp rate 5 °C $min^{-1}$) for 1 h under He. The sample was cooled to 100 °C and exposed to a $NH_3$/He (1:9 vol/vol, 30 $cm^3$ $min^{-1}$) gas mix for 1.5 h, followed by He purge (60 $cm^3$ $min^{-1}$) for 2 h to remove physisorbed $NH_3$. $NH_3$-TPD was performed from 100 to 600 °C (ramp rate 10 °C $min^{-1}$) under He (30 $cm^3$ $min^{-1}$), with desorbed $NH_3$ monitored by thermal conductivity. CO pulse chemisorption was performed using a Quantachrome ChemBET 3000 system. Samples were degassed at 150 °C for 1 h under He (20 $cm^3$ $min^{-1}$) before reduction at 100 °C for 1 h under pure $H_2$ (20 $cm^3$ $min^{-1}$). A milder reduction condition was used to avoid additional particle sintering. CO chemisorption was conducted at RT, with dispersion measurements evaluated based on CO Pd stoichiometry of 1 to 2[47].

X-ray photoelectron spectroscopy (XPS) was performed using a Kratos Axis Ultra Hybrid spectrometer with monochromated Al $K_\alpha$ radiation (1486.6 eV, 10 mA emission at 150 W, spot size 300 × 700 µm) at a base vacuum pressure of ~$5 \times 10^{-9}$ mbar. Charge neutralisation was achieved using a low-energy electron flood gun. Pass energies of 80 and 20 eV were used for the survey and high-resolution scans. The total energy resolution of high-resolution scans was 0.5 eV, which is limited by the width of the emission line from the sample, the analyser, and a Gaussian and Lorentzian contribution to the lineshape. Hard X-ray photoelectron spectroscopy (HAXPES) was performed on a Scienta Omicron GmbH HAXPES-Lab using monochromated Ga $K_\alpha$ X-ray radiation (9252 eV, 3.57 mA emission at 250 W, micro-focussed to 50 µm) and an EW-4000 high voltage electron energy analyser[76,77]. Measurements were made at a base vacuum pressure of ~$5 \times 10^{-10}$ mbar, with an entrance slit width of 0.8 mm. Pass energies of 500 and 200 eV were used for the survey and core level spectra, respectively, with total energy resolutions of 1.2 and 0.6 eV. Charge neutralisation was achieved using a PreVac FS40A low-energy electron flood source. In all tests, binding energy scale calibration was performed using Si *2p* photoelectron peak at 103.4 eV. Analysis and curve fitting was performed using CasaXPS, with a Shirley background and an asymmetric lineshape of LA(1.9,7,2) for Pd(0) and a symmetrical line of LA(1.53,243) for all other components[78].

Transmission electron microscopy (TEM) was conducted with an FEI Tecnai F30 FEG-AEM TEM operating at 300 kV. High-angle annular dark-field scanning transmission electron microscopy (HAADF-STEM) images were recorded on an FEI Titan3 Themis G2 operated at an accelerating voltage of 300 kV, equipped with a Schottky field-emission gun (X-FEG) operating at an extraction voltage of 4.5 kV, a monochromator (energy spread ~0.25 eV) and an FEI Super-X 4-detector EDX system. The HAADF-STEM tilt series were performed using the FEI STEM Tomography set-up with images collected at 5° intervals over a ±70° range. The tilt series images were aligned and reconstructed in Inspect 3D (version 9.5.0) using the simultaneous

iteration reconstruction technique (SIRT). The reconstructed model was then visualised using Imaris to obtain the cross-section images and generate three-dimensional surfaces to aid in visualising the position of the nanoparticles.

Attenuated total internal reflection infrared spectroscopy (ATR-IR) was conducted on a Bruker Vertex 70 spectrometer with a deuterated triglycine sulfate detector and platinum ATR accessory. Samples were measured at room temperature under air. Spectra of adsorbed amine probe molecules (DTBPy, DBAM, and EDA) are an average of 64 scans with a resolution of 4 $cm^{-1}$, with air recorded as a background.

Nuclear magnetic resonance (NMR) relaxation measurements were carried out in a Magritek SpinSolve benchtop NMR spectrometer operating at a $^1H$ frequency of 43 MHz. $T_1$ relaxation experiments were performed using an inversion recovery pulse sequence[79], acquiring 16 experimental points for each experiment with time delay values between 1 ms and 1000 ms, 16–64 scans and a repetition time of 1000 ms. $T_2$ relaxation experiments were performed with the CPMG (Carr Purcell Meiboom Gill) pulse sequence[80], with an echo time of 250 µs, using 16 steps with a number of echoes per step varying in the range 30–70, 64–128 scans and a repetition time of 1000 ms. Samples were prepared by soaking the solid in the relevant probe liquid for 48 h. Excess external liquid was removed by placing the solid on pre-soaked filter paper. The solids were placed in 5 mm NMR glass tubes, and measurements were made at 20 °C ± 0.5 °C under atmospheric pressure.

Thermogravimetric analysis (TGA) was conducted on a TA Instruments TGA 550. TGA analysis was conducted under flowing air (40 $cm^3$ $ml^{-1}$) from room temperature to 800 °C (ramp rate 10 °C $min^{-1}$).

### Catalytic testing

Catalyst (~0.1 g) was charged into hexane (20 $cm^3$) in a 100 $cm^3$ Parr 4598 autoclave reactor and reduced under $H_2$ (30 bar) at 200 °C for 2 h with stirring (at 1000 RPM). After reduction, the reactor was purged to 5 bar and depressurised five times before the addition of lauric acid (0.3 g) in hexane (20 $cm^3$) and nonane (0.1 $cm^3$) as an internal standard. The system was pressurised with $H_2$ and heated to the desired reaction temperature. Once at temperature, reactions were initiated by agitation, with aliquots (<1 $cm^3$) extracted for reaction profiling, with analysis by gas chromatography. It is important to note that due to the potential for precipitation of the fatty acid substrate at room temperature, sampling should be conducted at the reaction temperature, and the sampling system should be flushed prior to sample collection to avoid carryover. Loss of the substrate during sampling will impact solely on the conversion reported. There are no issues with regard to product solubility. The dehydration of lauryl alcohol was conducted under identical conditions, with the omission of the pre-treatment. For catalyst recycle studies, additional lauric acid (0.3 g), hexane (3 $cm^3$) and nonane (0.015 $cm^3$) were added into the reactor without discharging the previous reaction media[81]. The system was returned to reaction conditions to commence the subsequent catalytic cycle.

## Data availability

Raw data that further supports and underpins the manuscript can be found in the supplementary information, with all raw data available via the online digital repository Figshare https://doi.org/10.48420/22722229 or from the corresponding authors upon reasonable request.

## References


1. Li, Y. et al. Applications and perspectives of cascade reactions in bacterial infection control. *Front. Chem.* **7**, 861 (2019).
2. Grondal, C., Jeanty, M. & Enders, D. Organocatalytic cascade reactions as a new tool in total synthesis. *Nat. Chem.* **2**, 167–178 (2010).
3. Pritchard, J., Filonenko, G. A., van Putten, R., Hensen, E. J. & Pidko, E. A. Heterogeneous and homogeneous catalysis for the hydrogenation of carboxylic acid derivatives: history, advances and future directions. *Chem. Soc. Rev.* **44**, 3808–3833 (2015).
4. Robinson, A. M., Hensley, J. E. & Medlin, J. W. Bifunctional catalysts for upgrading of biomass-derived oxygenates: a review. *ACS Catal.* **6**, 5026–5043 (2016).
5. Enders, D., Huttl, M. R. M., Grondal, C. & Raabe, G. Control of four stereocentres in a triple cascade organocatalytic reaction. *Nature* **441**, 861–863 (2006).
6. Climent, M. J., Corma, A., Iborra, S. & Sabater, M. J. Heterogeneous catalysis for tandem reactions. *ACS Catal.* **4**, 870–891 (2014).
7. Climent, M. J., Corma, A. & Iborra, S. Heterogeneous catalysts for the one-pot synthesis of chemicals and fine chemicals. *Chem. Rev.* **111**, 1072–1133 (2011).
8. Wei, J. et al. Directly converting CO2 into a gasoline fuel. *Nat. Commun.* **8**, 1–9 (2017).
9. Isaacs, M. A. et al. A spatially orthogonal hierarchically porous acid–base catalyst for cascade and antagonistic reactions. *Nat. Catal.* **3**, 921–931 (2020).
10. Yamada, Y. et al. Nanocrystal bilayer for tandem catalysis. *Nat. Chem.* **3**, 372–376 (2011).
11. Xu, Y. et al. Yolk@Shell FeMn@Hollow HZSM-5 nanoreactor for directly converting syngas to aromatics. *ACS Catal.* **11**, 4476–4485 (2021).
12. Gao, P. et al. Direct conversion of CO2 into liquid fuels with high selectivity over a bifunctional catalyst. *Nat. Chem.* **9**, 1019–1024 (2017).
13. Jiao, F. et al. Selective conversion of syngas to light olefins. *Science* **351**, 1065–1068 (2016).
14. Guo, H. et al. Fabricating different coordination states of cobalt as magnetic acid-base bifunctional catalyst for biodiesel production from microalgal lipid. *Fuel* **322**, 124172 (2022).
15. Li, X. et al. Catalytic production of γ-valerolactone from xylose over delaminated Zr-Al-SCM-1 zeolite via a cascade process. *J. Catal.* **392**, 175–185 (2020).
16. Song, S. et al. Meso-Zr-Al-beta zeolite as a robust catalyst for cascade reactions in biomass valorization. *Appl. Catal. B Environ.* **205**, 393–403 (2017).
17. Bui, L., Luo, H., Gunther, W. R. & Román-Leshkov, Y. Domino reaction catalyzed by zeolites with Brønsted and Lewis acid sites for the production of γ-valerolactone from furfural. *Angew. Chem. Int. Ed.* **125**, 8180–8183 (2013).
18. Wang, W., Liu, C.-J. & Wu, W. Bifunctional catalysts for the hydroisomerization of n-alkanes: the effects of metal–acid balance and textural structure. *Catal. Sci. Technol.* **9**, 4162–4187 (2019).
19. Huang, J., Zhang, F. & Li, H. Organometal-bridged PMOs as efficiency and reusable bifunctional catalysts in one-pot cascade reactions. *Appl. Catal. A Gen.* **431**, 95–103 (2012).
20. Zhu, S. et al. Integrated conversion of hemicellulose and furfural into γ-valerolactone over Au/ZrO2 catalyst combined with ZSM-5. *ACS Catal.* **6**, 2035–2042 (2016).
21. Shi, Y. et al. Recent progress on upgrading of bio-oil to hydrocarbons over metal/zeolite bifunctional catalysts. *Catal. Sci. Technol.* **7**, 2385–2415 (2017).
22. Zhao, C., Camaioni, D. M. & Lercher, J. A. Selective catalytic hydroalkylation and deoxygenation of substituted phenols to bicycloalkanes. *J. Catal.* **288**, 92–103 (2012).
23. Xiao, J. et al. Tandem catalysis with double-shelled hollow spheres. *Nat. Mater.* **21**, 572–579 (2022).
24. Ben Moussa, O. et al. Heteroaggregation and selective deposition for the fine design of nanoarchitectured bifunctional catalysts: application to hydroisomerization. *ACS Catal.* **8**, 6071–6078 (2018).

25. Zecevic, J., Vanbutsele, G., de Jong, K. P. & Martens, J. A. Nanoscale intimacy in bifunctional catalysts for selective conversion of hydrocarbons. *Nature* **528**, 245–248 (2015).
26. Parlett, C. M. et al. Spatially orthogonal chemical functionalization of a hierarchical pore network for catalytic cascade reactions. *Nat. Mater.* **15**, 178–182 (2016).
27. Deane, J. P. & Pye, S. Europe's ambition for biofuels in aviation - a strategic review of challenges and opportunities. *Energy Strat. Rev.* **20**, 1–5 (2018).
28. O'Connell, A., Kousoulidou, M., Lonza, L. & Weindorf, W. Considerations on GHG emissions and energy balances of promising aviation biofuel pathways. *Renew. Sustain. Energy Rev.* **101**, 504–515 (2019).
29. Ding, S., Parlett, C. M. A. & Fan, X. Recent developments in multifunctional catalysts for fatty acid hydrodeoxygenation as a route towards biofuels. *Mol. Catal.* **523**, 111492 (2022).
30. Tanzil, A. H., Brandt, K., Wolcott, M., Zhang, X. & Garcia-Perez, M. Strategic assessment of sustainable aviation fuel production technologies: yield improvement and cost reduction opportunities. *Biomass. Bioenergy* **145**, 105942 (2021).
31. Chung, S. H., Park, Y. M., Kim, M. S. & Lee, K. Y. The effect of textural properties on the hydrogenation of succinic acid using palladium incorporated mesoporous supports. *Catal. Today* **185**, 205–210 (2012).
32. Tapin, B. et al. Study of monometallic Pd/TiO2 catalysts for the hydrogenation of succinic acid in aqueous phase. *ACS Catal.* **3**, 2327–2335 (2013).
33. Cao, X. et al. Al-modified Pd@mSiO2 core-shell catalysts for the selective hydrodeoxygenation of fatty acid esters: Influence of catalyst structure and Al atoms incorporation. *Appl. Catal. B Environ.* **305**, 121068 (2022).
34. Liu, H. et al. Catalytic hydrodeoxygenation of methyl stearate and microbial lipids to diesel-range alkanes over Pd/HPA-SiO2 catalysts. *Ind. Eng. Chem. Res.* **59**, 17440–17450 (2020).
35. Shahinuzzaman, M., Yaakob, Z. & Ahmed, Y. Non-sulphide zeolite catalyst for bio-jet-fuel conversion. *Renew. Sustain. Energy Rev.* **77**, 1375–1384 (2017).
36. Hočevar, B., Grilc, M., Huš, M. & Likozar, B. Mechanism, ab initio calculations and microkinetics of straight-chain alcohol, ether, ester, aldehyde and carboxylic acid hydrodeoxygenation over Ni-Mo catalyst. *Chem. Eng. J.* **359**, 1339–1351 (2019).
37. Žula, M., Grilc, M. & Likozar, B. Hydrocracking, hydrogenation and hydro-deoxygenation of fatty acids, esters and glycerides: mechanisms, kinetics and transport phenomena. *Chem. Eng. J.* **444**, 136564 (2022).
38. Ojeda, M. et al. Conversion of palmitic acid over Bi-functional Ni/ZSM-5 catalyst: effect of stoichiometric Ni/Al molar ratio. *Top. Catal.* **61**, 1757–1768 (2018).
39. Toyao, T., Hakim Siddiki, S. M. A., Kon, K. & Shimizu, K. I. The catalytic reduction of carboxylic acid derivatives and $CO_2$ by metal nanoparticles on Lewis-acidic supports. *Chem. Rec.* **18**, 1374–1393 (2018).
40. Ullrich, J. & Breit, B. Selective hydrogenation of carboxylic acids to alcohols or alkanes employing a heterogeneous catalyst. *ACS Catal.* **8**, 785–789 (2017).
41. Takeda, Y., Tamura, M., Nakagawa, Y., Okumura, K. & Tomishige, K. Hydrogenation of dicarboxylic acids to diols over Re-Pd catalysts. *Catal. Sci. Technol.* **6**, 5668–5683 (2016).
42. Ly, B. K. et al. In situ preparation of bimetallic ReOx-Pd/TiO2 catalysts for selective aqueous-phase hydrogenation of succinic acid to 1,4-butanediol. *Catal. Today* **355**, 75–83 (2020).
43. Guo, Z. et al. Highly selective conversion of natural oil to alcohols or alkanes over a Pd stabilized CuZnAl catalyst under mild conditions. *Green. Chem.* **21**, 5046–5052 (2019).
44. Zecevic, J., van der Eerden, A. M. J., Friedrich, H., de Jongh, P. E. & de Jong, K. P. Heterogeneities of the nanostructure of platinum/zeolite Y catalysts revealed by electron tomography. *ACS Nano* **7**, 3698–3705 (2013).
45. Sun, Q., Wang, N. & Yu, J. Advances in catalytic applications of zeolite-supported metal catalysts. *Adv. Mater.* **33**, e2104442 (2021).
46. Shinotsuka, H., Tanuma, S., Powell, C. J. & Penn, D. R. Calculations of electron inelastic mean free paths. X. Data for 41 elemental solids over the 50 eV to 200 keV range with the relativistic full Penn algorithm. *Surf. Interface Anal.* **47**, 871–888 (2015).
47. Parlett, C. M. A., Bruce, D. W., Hondow, N. S., Lee, A. F. & Wilson, K. Support-enhanced selective aerobic alcohol oxidation over Pd/mesoporous silicas. *ACS Catal.* **1**, 636–640 (2011).
48. Groen, J. C. & Moulijn, J. A. & Pérez-Ramírez, J. Desilication: on the controlled generation of mesoporosity in MFI zeolites. *J. Mater. Chem.* **16**, 2121–2131 (2006).
49. Linstrom, P. J. & Mallard, W. G. *NIST Chemistry WebBook, NIST Standard Reference Database Number 69* (National Institute of Standards and Technology, 2022).
50. Abdulridha, S. et al. An efficient microwave-assisted chelation (MWAC) post-synthetic modification method to produce hierarchical Y zeolites. *Microporous Mesoporous Mater.* **311**, 110715 (2021).
51. Liu, H., Diao, Z. H., Liu, G. Z., Wang, L. & Zhang, X. W. Catalytic cracking of n-dodecane over hierarchical HZSM-5 zeolites synthesized by double-template method. *J. Porous Mat.* **24**, 1679–1687 (2017).
52. Corma, A. et al. 2,6-di-tert-butyl-pyridine as a probe molecule to measure external acidity of zeolites. *J. Catal.* **179**, 451–458 (1998).
53. Milina, M., Mitchell, S., Michels, N.-L., Kenvin, J. & Pérez-Ramírez, J. Interdependence between porosity, acidity, and catalytic performance in hierarchical ZSM-5 zeolites prepared by post-synthetic modification. *J. Catal.* **308**, 398–407 (2013).
54. Eckstein, S. et al. Influence of hydronium ions in zeolites on sorption. *Angew. Chem. Int. Ed.* **58**, 3450–3455 (2019).
55. Robinson, N., Bräuer, P., York, A. P. & D'Agostino, C. Nuclear spin relaxation as a probe of zeolite acidity: a combined NMR and TPD investigation of pyridine in HZSM-5. *Phys. Chem. Chem. Phys.* **23**, 17752–17760 (2021).
56. D'Agostino, C., York, A. P. & Bräuer, P. Host-guest interactions and confinement effects in HZSM-5 and chabazite zeolites studied by low-field NMR spin relaxation. *Mater. Today Chem.* **24**, 100901 (2022).
57. D'Agostino, C. et al. Solvent inhibition in the liquid-phase catalytic oxidation of 1, 4-butanediol: understanding the catalyst behaviour from NMR relaxation time measurements. *Catal. Sci. Technol.* **6**, 7896–7901 (2016).
58. D'Agostino, C. et al. Adsorbate/adsorbent interactions in microporous zeolites: mechanistic insights from NMR relaxation and DFT calculations. *Mater. Today Chem.* **29**, 101443 (2023).
59. Dacquin, J. P. et al. Interdependent lateral interactions, hydrophobicity and acid strength and their influence on the catalytic activity of nanoporous sulfonic acid silicas. *Green. Chem.* **12**, 1383–1391 (2010).
60. Song, D., An, S., Sun, Y. & Guo, Y. Efficient conversion of levulinic acid or furfuryl alcohol into alkyl levulinates catalyzed by heteropoly acid and ZrO2 bifunctionalized organosilica nanotubes. *J. Catal.* **333**, 184–199 (2016).
61. Ji, K. et al. Highly selective production of 2, 5-dimethylfuran from fructose through tailoring of catalyst wettability. *Ind. Eng. Chem. Res.* **58**, 10844–10854 (2019).
62. Tsud, N., Johanek, V., Stara, I., Veltruska, K. & Matolin, V. CO adsorption on palladium model catalysts: XPS Pd-Al2O3 interaction study. *Surf. Sci.* **467**, 169–176 (2000).

63. He, Y. F. et al. Pd nanoparticles on hydrotalcite as an efficient catalyst for partial hydrogenation of acetylene: effect of support acidic and basic properties. *J. Catal.* **331**, 118–127 (2015).
64. Kumar, P., Yenumala, S. R., Maity, S. K. & Shee, D. Kinetics of hydrodeoxygenation of stearic acid using supported nickel catalysts: effects of supports. *Appl. Catal. A Gen.* **471**, 28–38 (2014).
65. Shi, Y. et al. Upgrading of palmitic acid to iso-alkanes over bifunctional Mo/ZSM-22 catalysts. *Green. Chem.* **18**, 4633–4648 (2016).
66. Pitchon, V., Guenin, M. & Praliaud, H. X-ray photoelectron spectroscopic study of the electronic state of palladium in alkali-metal doped pd/sio2 solids. *Appl. Catal.* **63**, 333–343 (1990).
67. Falorni, M., Giacomelli, G., Porcheddu, A. & Taddei, M. A simple method for the reduction of carboxylic acids to aldehydes or alcohols using H-2 and Pd/C. *J. Org. Chem.* **64**, 8962–8964 (1999).
68. Arroyo, M., Briones, L., Hernando, H., Escola, J. M. & Serrano, D. P. Selective decarboxylation of fatty acids catalyzed by Pd-supported hierarchical ZSM-5 zeolite. *Energy Fuels* **35**, 17167–17181 (2021).
69. Ishida, T. et al. Efficient decarbonylation of furfural to furan catalyzed by zirconia-supported palladium clusters with low atomicity. *ChemSusChem* **9**, 3441–3447 (2016).
70. Yang, G. et al. The nature of hydrogen adsorption on platinum in the aqueous phase. *Angew. Chem. Int. Ed. Engl.* **58**, 3527–3532 (2019).
71. Oh, M. et al. Importance of pore size and Lewis acidity of Pt/Al2O3 for mitigating mass transfer limitation and catalyst fouling in triglyceride deoxygenation. *Chem. Eng. J.* **439**, 135530 (2022).
72. Shao, Y., Xia, Q. N., Liu, X. H., Lu, G. Z. & Wang, Y. Q. Pd/Nb2O5/SiO2 catalyst for the direct hydrodeoxygenation of biomass-related compounds to liquid alkanes under mild conditions. *ChemSusChem* **8**, 1761–1767 (2015).
73. Groen, J. C., Peffer, L. A. A., Moulijn, J. A. & Perez-Ramirez, J. On the introduction of intracrystalline mesoporosity in zeolites upon desilication in alkaline medium. *Microporous Mesoporous Mater.* **69**, 29–34 (2004).
74. Wang, Y. et al. One-pot synthesis of single-crystal palladium nanoparticles with controllable sizes for applications in catalysis and biomedicine. *ACS Appl. Nano Mater.* **2**, 4605–4612 (2019).
75. Ou, X. et al. Creating hierarchies promptly: microwave-accelerated synthesis of ZSM-5 zeolites on macrocellular silicon carbide (SiC) foams. *J. Chem. Eng.* **312**, 1–9 (2017).
76. Regoutz, A. et al. A novel laboratory-based hard X-ray photoelectron spectroscopy system. *Rev. Sci. Instrum.* **89**, 073105 (2018).
77. Spencer, B. et al. Inelastic background modelling applied to hard X-ray photoelectron spectroscopy of deeply buried layers: a comparison of synchrotron and lab-based (9.25 keV) measurements. *Appl. Surf. Sci.* **541**, 148635 (2021).
78. Moulder, J. F. & Chastain, J. *Handbook of X-ray Photoelectron Spectroscopy: A Reference Book of Standard Spectra for Identification and Interpretation of XPS Data* (Physical Electronics Division, Perkin-Elmer Corporation, 1992).
79. Fukushima, E. *Experimental Pulse NMR: A Nuts and Bolts Approach* (CRC Press, 2018).
80. Carr, H. Y. & Purcell, E. M. Effects of diffusion on free precession in nuclear magnetic resonance experiments. *Phys. Rev.* **94**, 630–638 (1954).
81. Anbarasan, P. et al. Integration of chemical catalysis with extractive fermentation to produce fuels. *Nature* **491**, 235–239 (2012).


## Acknowledgements

This project has received funding from the European Union's Horizon 2020 research and innovation programme under grant agreement No 872102. M.H. thanks the China Scholarship Council (CSC, file no. 201806340224) for supporting her research. B.Q. thanks to the China Scholarship Council (CSC, file no. 202006240076) and the University of Manchester for the joint PhD studentship to support her research. X.O. thanks the Zhejiang Provincial Natural Science Foundation for funding (LQ23B060005). U.K. thanks the Punjab Educational Endowment Fund (PEEF). B.S. thanks the EPSRC grants EP/R00661X/1, EP/P025021/1, and EP/P025498/1. X.F. and Y.J. acknowledge the Key Project on Intergovernmental International Science, Technology and Innovation (STI) Cooperation/STI Cooperation with Hong Kong, Macao and Taiwan of China's National Key R&D Programme (2019YFE0123200) and the National Natural Science Foundation of China (No. 22378407) for supporting the collaboration. C.M.A.P. thanks the UK Catalysis Hub for the resources and support provided via our membership of the UK Catalysis Hub Consortium and funded by EPSRC grants EP/R026939/1 and EP/R027129/1. The authors thank the EPSRC grant EP/S021531/1 for TEM analysis at The University of Manchester. C.D. and X.F. also acknowledge the EPSRC (grant no. EP/V026089/1) for supporting the research.

## Author contributions

C.M.A.P. and X.F. conceived the work. C.M.A.P., X.F. and S.D. planned the experiments. S.D. synthesised materials under guidance from X.F. and C.M.A.P. S.D., Y.P. and U.K. performed catalytic testing. S.D., D.L.F.A., M.H., B.Q., X.O., B.S., C.D., X.Z., Y.J. and N.H. undertook materials characterisation. S.D., C.D., N.H., B.S., X.F., C.T., U.K. and C.M.A.P. analysed the data. S.D., X.F. and C.M.A.P. wrote the manuscript, with contributions from all other co-authors.

## Competing interests

The authors declare no competing interests.

## Additional information

**Supplementary information** The online version contains supplementary material available at https://doi.org/10.1038/s41467-024-51925-2.

**Correspondence** and requests for materials should be addressed to Christopher M. A. Parlett or Xiaolei Fan.

**Peer review information** *Nature Communications* thanks Kang Cheng, Tejas Goculdas, and the other, anonymous, reviewer(s) for their contribution to the peer review of this work. A peer review file is available.